Characterization and Stabilization of Atmospheric Pressure DC Microplasmas and their Application to Thin Film Deposition

Volume 1

A Thesis

Submitted to the Faculty

of

Drexel University

by

David Alexander Staack

in partial fulfillment of the

requirements for the degree

of

Doctor of Philosophy

December 2008

Acknowledgements

I would like to convey my gratitude to both my advisers Prof. Bakhtier Farouk and Prof. Alexander Fridman whose help, support and guidance were appreciated throughout my graduate studies. Together their experience and expertise made my time at Drexel successful and enjoyable. I also would like to express my deep appreciation to the most dedicated Prof. Alexander Gutsol with whom I had pleasure to work with on this project. I feel thankful for the innovative research environment they created in our weekly meetings at the Drexel Plasma Institute. I additionally thank Prof. Nicholas Cernansky, Prof. Gennady Friedman and Prof. Yury Gogotsi for their valuable remarks and guidance in the various projects we have collaborated on.

I am grateful for the financial support that I received during my graduate study especially from the NSF grant DMII-0423409, the Koerner Family Fellowship and the NSF-IGERT Program. I am thankful to the Department of Mechanical Engineering and Mechanics at Drexel University for providing an excellent graduate education and friendly environment. I would like to thank all my colleagues at DPI and in the CFF group for their camaraderie in the laboratory over the years; especially Tanvir Farouk. I am thankful to all my committee members and other professors for their constructive remarks and suggestions.

I am very grateful to all my family and especially to my wife Andrea and son Nikolas for their patience and support.

Table of Contents

Volume 2

List of Tables

List of Figures

Chapter 6.

Chapter 12.

Abstract

A comprehensive study was carried out to examine the feasibility of depositing thin films using atmospheric pressure DC and RF microplasma discharges. Atmospheric pressure plasmas for material processing are desirable because of the lower costs, higher throughput, continuous processing, and potentially novel applications obtainable by not using vacuum systems. However, several major concerns exist because of the higher pressures. These are related to: 1) discharge stability, 2) non-thermal operation, 3) non-uniformities, and 4) particle formation. These concerns were investigated using DC and RF microplasmas for atmospheric pressure plasma enhanced chemical vapor deposition (AP-PECVD) of thin films. The DC discharges were fundamentally characterized in Air, helium, nitrogen, argon, hydrogen, methane and mixtures thereof by: 1) voltage-current measurements, 2) current density measurements, 3) microscopic visualization and manipulation of the discharges, and 4) extensive spectroscopic measurements. Measurements were made for breakdown, transitional and stable regimes in current ranges from 0 mA to 40 mA, and discharge gaps sizes from 20 μm to 10 mm. The main focus of the optical emission spectroscopy (OES) was the measurements of rotational and vibrational temperature measurement made by the fitting of experimental data to spectral models of the N_2 2nd positive system (N_2 $C^3\Pi_u \rightarrow B^3\Pi_g$), though the N_2^+ 1st negative system, the NO β, γ, δ, and ε systems, and the atomic emissions lines were also used for additional temperature measurements, species identification, and measurements of relative concentrations. The structure, electric field, current density and voltage-current measurements indicated that the DC microplasmas operate as density scaled version of the low-pressure normal glow discharge regime with notable exceptions. Spectroscopic

measurements show the gas temperatures to vary from ambient to 2000K depending on conditions and to be non-equilibrium discharges, $T_{gas} < T_{vib}$. An analysis of the thermodynamics and stability of these discharges revealed that these discharges are in thermal balance because of their small size and can be stabilized through careful design of the external circuit. These stability requirements were analyzed in detail both experimentally and through mathematical modeling using a linearized perturbation analysis. The tailored discharges were used in the AP-PECVD of hydrogenated amorphous carbon film (a-C:H) from H_2, CH_4 precursors. Regimes of particle formation and thin film deposition were found. The characteristics of the deposits were measured with profilometry, Raman spectroscopy and other techniques. The films deposited are uniform thin films though very localized by the small size of the discharge. More commonly used atmospheric pressure RF capacitively coupled plasmas (CCP) utilizing helium buffering for stabilization were also investigated for AP-PECVD. Characterization revealed that the high concentrations of helium were required to maintain low current densities and prevent alpha to gamma mode transition and instabilities. Comparisons were made between the DC, and RF atmospheric pressure deposition system and results from the literature. Properties in general are similar to those achieved by other techniques with the structure of the amorphous carbon films ranging from more polymeric-like-carbon to more diamond-like-carbon. In comparison to the RF deposition, the DC system could deposit more durable films, likely due to higher power densities and ion energies, but the discharge was more sensitive to the substrate properties. The DC microplasma system could also deposit thin films with significantly less helium buffering as helium was not necessary for stabilization.

1. Introduction

1.1. Background

The following sections give a brief background on plasmas and plasma processing necessary to place the motivations of this research in context.

1.1.1. Plasmas

Plasmas are often termed the "fourth state of matter;" the other three being solid, liquid, and gas. Simply stated, plasma is an ionized gas which conducts electricity. It is formed (typically electrically) by the addition of energy to a gas, which separates electrons from neutral gas molecules and atoms. Plasmas consist of charged particles including free electrons, as well as negative and positive ions, which respond to applied electric and magnetic fields. Laboratory plasmas are generated by electrical discharges.[1]

Plasma discharges come in two main varieties, thermal and non-thermal.[2] Thermal kinds are typically equilibrium systems with temperatures in excess of 10,000K. Non-thermal types, in contrast, are in a thermodynamic and chemical non-equilibrium with the temperature of the electrons (>10,000K) greatly in excess of the gas temperature (~300K).

Non-thermal atmospheric pressure plasmas are the focus of this research. Their non-equilibrium nature allows for the creation of active species without generating excessive heat, which may damage surfaces or cause excessive dissociation. Also, the chemical processes which occur in the non-equilibrium plasma are beyond those which are accessible by the addition of only thermal energy.[3] Non-thermal plasmas thus find

many diverse applications in the controlled treatment of materials. Operation at atmospheric pressure allows for ease of use and lower costs, among other advantages. However, there are important challenges to using non-thermal, atmospheric pressure plasmas. Principally, they (for example, lightning) are very unstable and "want" to be thermal.

1.1.2. *Plasma Processing and Plasma Enhanced Chemical Vapor Deposition*

There are many important applications of non-thermal plasmas to the manufacturing of materials. Most notable is the processing of semiconductors for the manufacturing of microelectronics and integrated circuits. As much as 30% of all steps in the manufacturing of integrated circuits involve plasmas, while purchases of plasma-processing equipment account for about 5% of the 260 billion dollar semiconductor industry.[4, 5] Other areas in which plasma processing is important include automotive, textile processing, and biomedical applications.[6] Plasma-processing techniques include: removal of material through etching, the addition of matter through plasma-enhanced chemical vapor deposition, and, without significant addition or removal of material, the modification of surface chemical bonds and functionality.[7]

Plasma-enhanced chemical vapor deposition (PECVD) is a type of plasma processing in which material is deposited onto surfaces in the form of thin films. It is a variant of thermal CVD in that a plasma, rather than temperature, is used to activate the chemical processes. In the plasma, the precursors (species from which the deposition products are formed) are partially dissociated or otherwise chemically activated. The precursor undergoes a chemical change at a solid surface, leaving a solid layer typically

as an amorphous or crystalline homogeneous and uniform film. Almost all industrial applications of this processing occur in low-temperature, non-thermal plasma systems generated at low pressures.[6] This is because the necessary plasma conditions are easier to maintain at pressures of 10's of milliTorrs to a few Torrs. This dissertation investigates atmospheric pressure, plasma-enhanced, chemical vapor deposition (AP-PECVD), which has several advantages and challenges in comparison to traditional PECVD.

1.2. Thesis Statement

This dissertation details a project that focuses on the application of atmospheric pressure microplasma discharges to thin film deposition. Simply put, this thesis states that *"atmospheric pressure DC microplasmas can be stable, non-thermal and used in thin film deposition."* The demonstrative approach of this engineering thesis includes an analysis of why instabilities arise, how they can be suppressed, and how the non-equilibrium balance is maintained in microplasmas.

The present study has two parts: the first is a fundamental study of a novel type of microplasma; and second is the application of this microplasma to the manufacturing process of thin film deposition. For the purposes of this thesis, more emphasis is placed on the first part as the plasma conditions necessary for thin film deposition are well known from studies on materials processing in low-pressure plasma systems. The requirements are that the plasma be uniform, stable, non-equilibrium and low in temperature. Thus, the research focuses on 1) measuring and attaining these conditions

within the microplasma and 2) demonstrating that they meet the criteria for thin film deposition manufacturing processes.

Atmospheric pressure direct current (DC) plasma discharges with characteristic dimensions of less than 1 mm were studied. This small size gives rise to the term microplasma. A micrograph of one of the DC microplasma used is shown in Figure 1.1. Several operating modes for the microplasma were discovered and a suite of diagnostic methods was developed to study these discharges. These include microscopic visualizations, electrical diagnostics, and detailed spectroscopic diagnostics for measurements of species present and non-equilibrium temperatures. Insights gained from these measurements allowed for the characterization of these discharges as a type of "normal glow" within the rubric of plasma discharges. Conditions for controlling instabilities and temperature within the discharge were also found and analyzed.
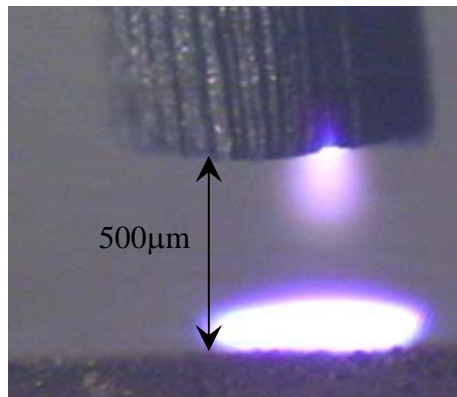
Figure 1.1: Images of glow discharge in atmospheric pressure air at 0.5 mm electrode spacing, 430V, and 10 mA. Anode is at the top of the image and cathode is at the bottom.

With regard to thin film deposition, literally hundreds of materials are created through the process of plasma enhanced chemical vapor deposition (PECVD). The

present study of deposition processes focused on proof of concept studies and verification of the necessary plasma characteristics. Specifically, the deposition of amorphous carbon films from methane precursors was studied. The most important criterion to satisfy was that particle free thin films generally similar to those achieved in low pressure processing were deposited. The improvements in film quality are illustrated in the two micrographs shown in Figure 1.2. The first illustration (A) shows typical results at the inception of this research, indicating a rough particle comprised film; after applying the stability and temperature control methods developed here, smooth thin films could be deposited as shown in the second illustration (B). Some detailed materials characterizations, including Raman analysis, were also performed to determine if the film properties were similar to those attained in more common low-pressure processing systems. Various modes of the microplasma discharges were compared and the novel characteristics of the deposition system with specific regard to the micro scale of the discharge were studied.
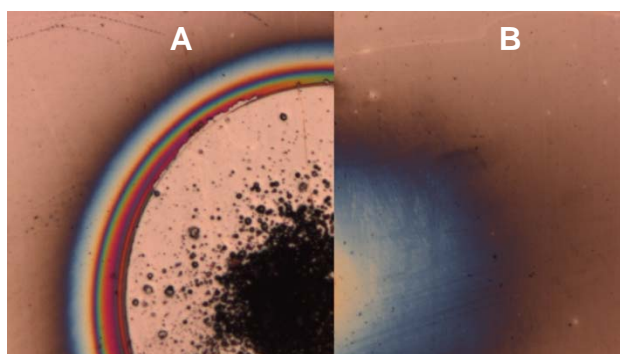
Figure 1.2: Micrographs of deposited amorphous carbon (aC:H) from atmospheric pressure $CH_4/H2$ mixture (1%/99%) in the case of (A) unstabilized and (B) external circuit stabilized microplasmas. Scale in both images is the same.

1.3. Motivation

This research was performed under the auspices of an NSF grant "Atmospheric-Pressure Plasma Microdischarges for High-Rate Deposition and Microfabrication". The present study has two main aspects with regard to general motivations and impact. The first aspect is the application of PECVD at atmospheric pressure, and the second is the study of novel microscale plasma discharge.

1.3.1. *Atmospheric Pressure Plasma Enhanced Chemical Vapor Deposition (AP-PECVD)*

Plasma-enhanced chemical vapor deposition (PECVD) is widely used to coat thin films onto materials using plasmas in gas mixtures. These films serve many purposes.[8] For example, silicon dioxide and silicon nitride layers are essential components of integrated circuits. Diamond-like coatings increase the wear and corrosion resistance of metal parts. Nanocoatings of glass onto plastic sheeting prevent oxygen and moisture penetration. Thicker coatings may be used for scratch protection on structural plastics. Polymer coatings are used as dielectrics or temporary masks in integrated circuits.

Most thin film PECVD processes[4] take place in vacuum-based plasma reactors. Performing PECVD at atmospheric pressure has several advantages: firstly, microfabrication is less expensive as there is no need for expensive vacuum pumps; secondly, the process uses less energy and is more environmentally-friendly because operating at ambient pressure and temperature satisfies "Green Chemistry"[9] principles; thirdly, free from the constraints of a vacuum chamber, the processing takes place in

continuous rather batch mode and can treat any size shape or object. Similarly, non-vacuum compatible substrates can be treated by operating at an atmospheric pressure. Lastly, due to the higher operating gas densities, deposition rate is likely be higher allowing for more rapid processing.

While the benefits of atmospheric pressure plasma processing are well documented, significant challenges still exist. The requirements for thin film deposition by PECVD are that the plasma be 1) uniform, 2) stable, and 3) non-thermal. Using traditional technologies, such plasma can only be generated in low-pressure systems. This is because, at atmospheric pressure caused by the increased collisionality and decreased stabilizing effect of the reactor walls, instabilities arise that prevent a uniform and non-thermal discharge to be maintained. Depending on the type of discharge, these instabilities include 1) glow-to-arc transition (GAT), 2) ionization overheating thermal instability, 3) α-mode to γ-mode transition, and 4) streamer formation. The first three of these types eventually lead to thermalization of the plasma discharge, and the last type leads to spatial non-uniformities.

1.3.2. *Fundamental Study of Novel Atmospheric Pressure Microplasmas*

Historically, the multiple challenges preventing the generation of plasma discharges suitable for atmospheric pressure PECVD (AP-PECVD) have been overcome only on a piecemeal basis. Typically using discharge configurations that depart significantly from the relatively simple parallel plate, CCP configuration used effectively in low pressure plasma systems. Traditional atmospheric pressure systems include the corona, dielectric barrier discharge (DBD), and plasma arc torch. The corona and DBD

maintain a non-thermal plasma but are not spatially uniform. The torch can be uniform but is a thermal discharge. In the past decade, various new and improved atmospheric pressure plasma configurations have been studied that attempt to simultaneously be uniform, stable, and non-thermal. These include pulsed corona discharges, glow mode DBD, and the atmospheric pressure plasma jet.[10] To date, the two that have successfully demonstrated AP-PECVD of thin films are: 1) the helium-based radio frequency (RF) capacitevely coupled plasma (CCP) discharges commonly referred to as atmospheric pressure plasma jets (APPJ)[11]; and 2) the helium-based uniform dielectric barrier discharges (DBD) commonly referred to as the atmospheric pressure glow (APG).[12] The first started 10 years ago and the second started 20 years ago. The extensive use of helium (typically >99% of processing gas must be helium) has always been a major drawback of these solutions. Helium detracts from some of the benefits of AP-PECVD because of its high cost.

At the inception of this study (as detailed in the literature review), atmospheric pressure microplasmas had only been attempted in one study of PECVD,[13] and growing interest in atmospheric pressure microscale plasmas only began as recently as the late 1990s.[14, 15] Microplasma discharges were novel but it was not clear if they could meet the conditions for thin film PECVD (uniform, stable, and non-thermal). The largest concern was whether the discharge was non-thermal; early experiments revealed temperatures above 2000K for operations in air. One of the main motivations of this dissertation was to determine if it was possible to better measure and define the characteristics of microplasmas. The present paper seeks to determine if they can operate in non-thermal regimes, and if the discharges are sufficiently non-thermal and stable to

generate the desired thin films? To cut a long story short, the answer, as detailed herein, is yes. This research has sought to study the microplasma discharge using simple geometries within the context of well-known low-pressure plasma discharges. The results help to refine the definition of microplasma, discover its limitations, and thus ascertain its potential applications, including but not limited to atmospheric pressure plasma enhanced chemical vapor deposition AP-PECVD.

1.4. Thesis Overview

Chapter 1 introduces the thesis topic and explains the motivations for the research. Chapter 2 covers introductory information and background for those less familiar with plasmas and the context of the research. This includes an introduction to some basic and advanced concepts in plasma discharges discussed later in this dissertation. Chapter 2 also includes a detailed literature review of both microplasma research and atmospheric pressure thin film deposition.

The presentation of results begins in Chapter 3 and largely follows the chronological order of seven papers published (4) or submitted (3) to journals as part of this research. The characteristic of useful PECVD systems is that the plasma must be 1) Non-thermal, 2) stable, and 3) uniform, and the chapters of this thesis basically address each of these issues. Chapters 3-6 address the non-thermal characteristics of DC microplasmas. Initial characterizations of microplasma in the air are detailed in Chapter 3. Global temperature measurements and thermal balance is discussed in Chapter 4. Spatially resolved and microscopic temperature measurements and thermal balance is discussed in Chapter 5. The general characteristics and temperature measurements for

microplasmas in various gases is described in Chapter 6. Chapter 7 addresses instabilities in DC microplasma both from an experimental and an analytical point of view. These fundamental studies are brought together and applied in Chapter 8, which focuses on using the discharges for PECVD addressing three issues: 1) discharge stability, 2) particle formation (i.e. non-thermal) and 3) deposition uniformity. The unique applications of microplasmas related to their small size are also presented. Chapter 9 compares AP-PECVD with this DC microplasma source to deposition with an RF source similar to the APPJ and with results from the relative literature. Finally, Chapter 10 summarizes and concludes the dissertation with a discussion on the impact of this research, limitations and future work that might be undertaken. The Appendix section covers some of the data analysis algorithms developed and also a detailed mathematical stability analysis of the microplasma.

As mentioned, each of these chapters is based on published or submitted papers and corresponds to a single set of experiments. As such, the chapters are somewhat self-contained; introductions, experimental setup, and conclusions corresponding to each experiment are given in each chapter along with the results. Each chapter builds on the next and each begins with a paragraph that gives context to the results presented within the framework of this dissertation.

2. Background and Literature Review

2.1. Summary

This chapter introduces plasmas describes several relevant phenomena and summarizes some prior research in the fields of microplasmas and atmospheric pressure PECVD. The background material on plasmas attempts to be self contained but of course is brief as an extensive amount of material is available in text books on plasma physics, plasma engineering and plasma processing. Some more fundamental plasma physics phenomena are discussed since the study of the microplasma is fundamental in nature. Also covered are more specific phenomena necessary to understand many of the discussions in later chapters. These topics are also reintroduced in later chapter but here are given in more detail. A literature review is also given on microplasmas, and atmospheric pressure plasma enhanced chemical vapor deposition.

2.2. Introduction to Plasmas

Plasmas are often termed the "fourth state of mater", the other three being solid, liquid, and gas. Simply stated, a plasma is an ionized gas which conducts electricity. It is formed by the addition of energy to a gas, which separates electrons from neutral gas molecules and atoms. Plasmas consist of charged particles including free electrons, negative ions, and positive ions which respond to applied electric and magnetic fields. A plasma is a distinct state of matter containing a significant number of electrically charged particles to affect its electrical properties and behavior.

In many cases interactions between the charged particles and the neutral particles are important in determining the behavior and usefulness of the plasma. The type of atoms in a plasma, the ratio of ionized to neutral particles and the particle energies all result in a broad spectrum of plasma types, characteristics and behaviors. These unique behaviors cause plasmas to be useful in a large and growing number of applications important to our lives and to the world around us.

2.2.1. History

Werner von Siemens in 1857 patented the first technological use of plasma, an ozonizer. This utilized DBD discharges though little at the time was known about the nature of the electric discharge. The theory of plasmas began to develop as Sir William Crookes, an English physicist, first identified this "radiant matter" created in glow discharge tubes as the fourth state of matter, now called plasma, in 1879. Though ancient recognition of a 4th state of matter dates back at least to Empedocles' (ca. 490–430 BC) cosmogenic theory of the four classical elements: Earth, Water, Wind and Fire (a weak plasma).

Johannes Starks text book "Electricity in Gases" published in 1902 is considered the first account of gas discharge physics. The word "plasma" (from the Greek word *plassein*, to form or mold) was first applied to ionized gas by Irving Langmuir in 1929. Though other early researcher into electricity and ionized gases such as Benjamin Franklin (1706-1790), G. C. Lichtenberg (1752–1799), V. V. Petrov (1761—1834), Humphrey Davy(1778- 1829), and Michael Faraday (1791–1867), were the earliest investigators of plasmas.

Raizer[1] asserts that the development of atomic physics around the turn of the 20th century went hand in hand with that of gas discharge physics. During the latter half of the 20th century, plasma research has been directed towards thermonuclear fusion and space plasma physics. Glow discharges (low-temperature non-equilibrium plasmas) became important in electronic materials processing applications in the mid 1970's. Other interests to develop for glow discharges include gas discharge lasers and lamps.

Today plasmas are widely used in materials processing industry and lighting applications. Popular lighting applications are fluorescent and neon bulbs, plasma televisions, and gas discharge lamps. High temperature plasmas are used to melt rocks and metals in refining and welding applications. Lower temperature, vacuum based plasmas are extensively used to deposit and etch materials in the integrated circuit (IC), solar cell, and microfabrication industries. Low temperature atmoshepric pressure plasmas such as coronas and dielectric barrier discharges are also widely in ozonizer and web treatment of materials. In addition to being important in many aspects of our industries and daily lives, plasmas are estimated to constitute more than 99 percent of the visible universe and are widely researched in astrophysics. The most significant university and governmental research into plasmas still focuses on nuclear fusion and astrophysical research. Though, with the turn of the 21st century, interest has increased in low temperature plasmas, and specifically in low temperature atmospheric pressure plasmas. In fact non-thermal and chemically reacting atmospheric pressure plasma are considered to be the most worthwhile and necessary research directions for the future.[6]

2.2.2. *Definition of a Plasma*

The statement that a plasma is an ionized gas is over simplified. To some degree all gases have some small fraction of ionized particles and free electrons due to 1) their finite temperature which will lead to a small fraction of particles having sufficient internal energy to be ionized as described by the Saha equation and 2) cosmic sources of ionizing radiation. Yet not all gases are plasmas. From a physical perspective plasmas are said to occur when there are a sufficient number of charged particles for collective behavior to be observed. This occurs when the charged particles are close enough together that each particle influences many nearby charged particles, rather than just interacting with the closest particle. The collective behavior is call the *plasma approximation* and is valid when the number of electrons (or charged particles) within the sphere of influence of a particular particle is large.

The spheres of influence radius is given by the Debye length, which is the scale over which mobile charge carriers (e.g. electrons) screen out electric fields in plasmas and other conductors. In other words, the Debye length is the distance over which significant charge separation can occur. The Debye length, λ_d, is derived in many introductory plasma physics text[16] for an idealized system assuming a Boltzmann distribution of an equal number of ions and electrons around a charge and then using Poisson's equation to solve for the resulting space potential. The characteristic dimension of the solution is the Debye Length, $\lambda_d = (\varepsilon_o k T_e / n_e e^2)^{1/2}$, where T_e and n_e are the electron temperature and density, and e is electron charge, ε_o is the permittivity of free space, and k is Boltzmann's constant. The average number of particles in the Debye sphere is given by the plasma parameter, Λ.

The defining characteristic of a plasma are that 1) the Debye length is smaller than the plasma size, 2) there should be many particles in a Debye sphere, $\Lambda = n_e 4/3\pi\lambda_d{}^3$ >> 1 and 3) there is *quasineutrality* (both ion and electron densities are present in approximately equal number in the bulk plasma). Within any plasma system there are regions where these characteristics do not hold. Most notably are the physical boundaries of the plasma where the Debye length is comparable to the distance to the wall. This plasma boundary layer is called the *sheath*.

2.2.3. Plasmas in Nature

As stated, plasmas are thought to constitute over ninety-nine percent of the visible universe though terrestrially there are fewer plasmas. Lightning and the Auroras, see Figure 2.1, are two naturally occurring terrestrial plasmas. The Aurora is generated by energetic particles originating from the sun which are directed by the earth's magnetic field to the poles where they collide with atoms and molecules in the Earth's upper atmosphere. In the low densities of the upper atmosphere the plasma generated though luminous is low temperature. Lightning is formed when charge separation and charge accumulation in clouds continues until the electrical potential becomes sufficient to cause the air to breakdown, initiating the lightning. In contrast to the Aurora, lightning which is formed at near atmospheric pressure is a very high energy density, high temperature plasma. These two discharges are natural examples of high temperature (thermal) and low temperature (non-thermal) plasma discharges.

Figure 2.1: (a) Lightning strikes over Oradea in Romania[17], (B) the Aurora Borealis, or northern lights, above Bear Lake Alaska[17].

2.2.4. *Laboratory Plasmas & Electrical Breakdown*

In laboratory, residential and industrial devices plasmas are generated artificially. Considering that plasma's are considered to be the 4th state of matter one approach to artificially generate plasmas is to add thermal energy to a gas until a temperature is reached such that the number of free electrons as described by Saha's equilibrium is sufficiently high. This occurs when temperatures reach about 10000K, is very impractical and will only generate thermal equilibrium plasmas.

The more common approach to generate plasmas uses externally applied electric fields as might be generated between parallel plates shown in figure 2.2. This approach relies on the fact that all gases have some small fraction of ionized particles and free electrons already present. In the presence of an electric field an electron will gain kinetic energy as it is accelerated by the field. Since the electron is in a dense gas it will collide with a particle as it travels towards the anode. If it has sufficient energy it will ionize the atom or molecule producing a positive ion and an additional electron. These two

electrons are then in turn accelerated and can additionally ionize particles. If the multiplication of electrons exceeds all losses the plasma density will geometrically increases, in what is termed an electron avalanche, see Figure 2.2.
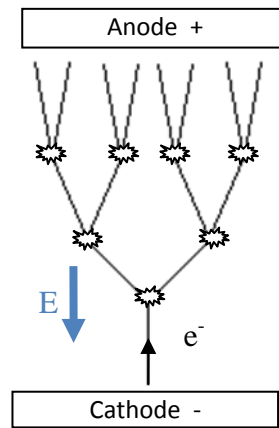
Figure 2.2: Electron avalanche in an applied electric field, E.

The increase in electron density during avalanche growth is written as: $dn_e/dx = \alpha n_e$, $n_e(x) = n_{e0}exp^{\alpha x}$. Where x is distance and α is a termed the first Townsend coefficient. The coefficient gives the probability of an ionization event per unit path length of an electron. The parameter of concern in determining α and the formation of an electron avalanche is, ε, the average energy gained by the electron between collisions. Conveniently ε is written as a product of the electric field, E, and the electron mean free path, λ_e. The mean free path is inversely proportional to the density of the collision partner, $\lambda = \left(\sqrt{2}\sigma n\right)^{-1}$, in this case n is the neutral gas density, and σ is the collision cross section. Thus the energy gain between collisions can be written as $\varepsilon \sim E/n$. This parameter E/n (called the reduced electric field) is the most important parameter in gas

discharge physics and many scaling laws for discharges are based upon it. *E/n* is also often written as *E/p* with the assumption that the gas temperature is near room temperature (T_0), though if a scaling law is based upon *E/p* any deviations in temperature, *T*, need to be taken into account using an effective pressure $p_{eff} = pT_0/T$.

If *E/n* is sufficiently high an electron avalanche occurs and the plasma density will increase. This process however, requires an initial electron and is not self sustained. The discharge in this case will be limited by the spontaneous formation of free electrons (i.e. Saha equilibrium) and by free electron generated by cosmic rays collectively called primary electrons. In certain situations there may be electrons existing from previous discharges as in the case of high frequency pulsed or alternating current operation. Electrical discharges which rely on preexisting electrons are so called a Townsend discharge or an alpha mode discharges. This is named after α, the first Townsend ionization coefficient, expressing the number of ion pairs generated per unit length (e.g. meter) by an electron moving from cathode to anode.

In order to be self sustained electrons must be generated at the cathode of the discharge. Generally there are two mechanisms by which the discharge can become self sustained the first is secondary electron emission (SEE) and the second is thermionic emission (TE). Secondary electron emission a processes wherein an energetic ion from the plasma strikes the cathode and due to its kinetic energy causes an electron to be ejected from the surface. SEE is not a very probable process typically only about 1 in 1000 ions produce a secondary electron. Typically this ratio of the flux of incoming ions to outgoing electrons is called the secondary electron emission coefficient, and is given the symbol γ. Discharges sustained by secondary electron emission are called gamma-

mode discharges. γ is a function of the electrode material, ion energy, and is weakly dependant on surface temperature. Thermionic emission occurs when the electrode becomes sufficiently hot (either by external heating or by bombardment from plasma species) that electrons are thermally liberated from the surface. TE is a function of the electrode temperature and the work function of the electrode material.

Electrical breakdown specifically refer to the transition of a medium from a poor conductor to a good conductor. For electrical breakdown of gases this occurs when the discharge transitions to a self sustained mode. In the self sustained mode the electron density and electrical conductivity of the plasma is much higher. In the consideration of DC discharge between parallel plates as show in figure 2.2 the breakdown occurs when one secondary electron produces a sufficient number of ions to replace the original secondary electron. This condition is given by the Townsend formula as shown in equation 2.1, where i is the total current in the discharge, i_0 is the current of primary electrons.

$$i = \frac{i_0 \exp{(\alpha d)}}{1 - \gamma[\exp(\alpha d) - 1]} \qquad (2.1)$$

From this formula we see as the amount of electron multiplication, α, increases the denominator will tend to zero and the current will dramatically increase. α/p is another similarity parameter which is exponentially dependant on the reduced electric field E/p, $\alpha/p = A exp\left(-B / \frac{E}{p}\right)$. Where A and B are the gas specific numerical parameters of Townsend. The reduced electric field required for breakdown can thus be written as a function of the similarly parameter pd (pressure times discharge gap length), resulting in a familiar relationship exemplified by the Paschen curve. Figure 2.3, shows the Paschen curves[1] for air, nitrogen, hydrogen, helium and argon. Similar to how E/p is

related to collisional processes (the energy gain per mean free path, ε), the parameter *pd*
is simply proportional to ratio of the discharge gap length to the mean free path or the
inverse of the Knudsen number. There is a minimum breakdown voltage on the Paschen
curve, V_{min} and corresponding pd_{min}). To the left of the minimum the discharge gap is so
small that there is an insufficient number of mean free paths in the discharge gap to ignite
a discharge. To the right the required voltage is higher since the gap is longer, although
the required E/p is lower.
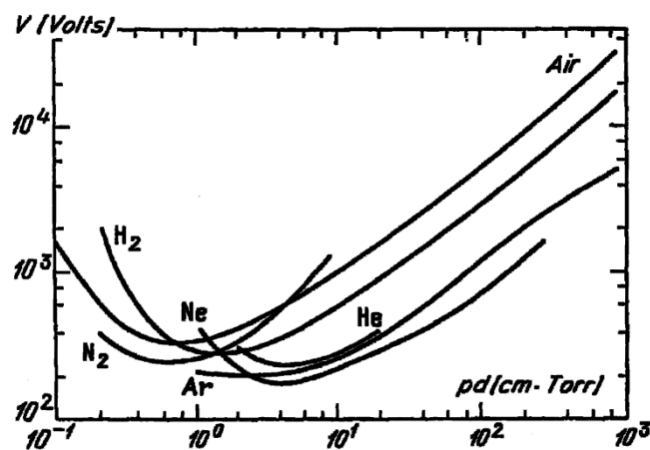
Figure 2.3: Paschen curves for different atomic and molecular gases.

With the electrical breakdown there is a dramatic change in the operating regime
of the discharge. As might be expected from equation 2.1 when the discharge becomes
self sustained the current will increase approaching infinity. In practice there are some
physical limitations which prevent this. The most important limitation is that the power
supply which initiated the discharge can only supply a finite current. The current can thus
be limited by the power supply or some electrical circuit in conjunction with the power

supply. Alternatively the power supply can be pulsed, operate at some frequency alternating current, or otherwise turned on or off. Other methods to limit the current include resistive or dielectric barriers on the electrodes to limit the current as in dielectric barrier discharges (DBD). If the power supply is not the limitation it may occur that the power will be so high as to initiate thermionic emission and or melt the electrodes.

All these different methods of applying and controlling the discharge power are what differentiate one type of plasma discharge from another. A brief summary of the common types of plasma follows.[2]

2.2.5. Examples of common industrial/commercial plasma

Many different type of plasma discharges exist. Here only the most relevant and general are mentioned.

2.2.5.1. *Low-pressure discharges*

Gamma mode glow plasmas: non-thermal plasmas generated by the application of DC or low frequency RF (<100 kHz) electric field to the gap between two metal electrodes. Probably the most common plasma; this is the plasma generated within fluorescent light tubes. Used in materials processing and manufacturing in parallel with CCPs to modify ion energies, in sputter sources like magnetrons, and for physical mechanism of surface modification.

Capacitively coupled plasma (CCP): similar to glow discharge plasmas, but generated with high frequency RF electric fields, typically 13.56 MHz. At these high frequencies the discharges operate continuously but in an alpha mode. These differ from glow

discharges in that the sheaths and power densities are much less intense. These are widely used in the microfabrication and integrated circuit manufacturing industries for plasma etching and plasma enhanced chemical vapor deposition.

Inductively coupled plasma (ICP): similar to a CCP and with similar applications but the electrode consists of a coil wrapped around the discharge volume which inductively excites the plasma. ICP are widely used in conjunction with CCP in IC manufacturing to intensify the plasma discharge.

Wave heated plasma: similar to CCP and ICP in that it is typically RF (or microwave), but is heated by both electrostatic and electromagnetic means. Examples are helicon discharge, electron cyclotron resonance (ECR), and ion cyclotron resonance (ICR). These typically require specific magnetic field geometry for wave propagation.

2.2.5.2.   Atmospheric pressure discharges

Arc discharge: this is a high power thermal discharge of very high temperature ~10,000 K sustained by thermionic emission. It can be generated using various power supplies. It is commonly used in metallurgical processes. For example it is used to melt rocks containing Al_2O_3 to produce aluminum.

Corona discharge: this is a non-thermal discharge generated by the application of high voltage to sharp electrode tips. The sharp tip creates a electric field sufficient for breakdown only in the vicinity of the tip the remaining region of discharge gap remain

dark. Coronas are very weak discharges they are commonly used in ozone generators and particle precipitators.

Dielectric barrier discharge (DBD): this is a non-thermal discharge generated by the application of high voltages across small gaps wherein a non-conducting coating prevents the transition of the plasma discharge into a self sustained glow or arc. Breakdown occurs in the form of streamers and charges build up on the electrodes during the discharge. A low frequency AC field <100 kHz is used to cycle the discharge and maintain. It is often mislabeled 'Corona' discharge in industry and has similar application to corona discharges. It is also widely used in the web treatment of fabrics in roll to roll configuration. The application of the discharge to synthetic fabrics and plastics functionalizes the surface and allows for paints, glues and similar materials to adhere.

Novel Atmospheric Pressure Discharges): These are covered in more detail later and do not have any widespread industrial applications yet. They include the atmospheric pressure plasma jet, helium based CCPs, microhollow cathodes, micro-glow discharges (the subject of this study), 'uniform' dielectric barrier discharges, and nano-second dielectric barrier discharges.

2.2.6. Thermodynamics of Plasmas

In materials processing one of the most important aspects of the plasma is that it be low temperature and non-thermal. This section reviews what these terms mean are and how such plasmas are attained.

2.2.6.1.   Thermal Plasmas

A thermal plasma is what is commonly referred to as the 4th state of matter in high school text books. It is a high temperature gas in which the temperature is so high that a significant number of neutral atoms have sufficient internal energy to ionize. The type of plasmas consists of free electrons, negative ions, and positive ions, as well as neutral species. During a collision between two neutral molecules or atoms the electrons that are normally bound to the atom in orbits around the nucleus will be ejected from the atom and will join the free electron gas. In general all of the species are in thermal equilibrium having the same temperature and energy is equally partitioned among the internal energies. As such the state of the system can be described by equilibrium statistical thermodynamics. A description for such a system can be found in many textbooks on statistical thermodynamics and is referred to as the Saha equilibrium and described by the Saha equation of which a simplified version is shown in 2.2, here n_e is electron density, n is neutral gas number density, Λ the electron thermal de Broglie wavelength, g_1 and g_0 are the degeneracies of the ionized and ground states, I is the energy required for ionization, k is Boltzmann constant and T is the equilibrium gas temperature. This form of the equation only applies to weakly ionized plasma with long Debye lengths and for a simplified atomic system with only a single ionization level. The most important factor is the exponential dependence of ionization degree (n_e/n) on temperature which persists in more complex version of the equation. Temperature is controlled by the power density of the discharge system. Arcs are the most common type of thermal plasma. The most important difference between thermal plasmas and other plasmas is the method of

ionization. In thermal plasmas ionization occurs through the transfer of a small amount of additional energy to an already energetic neutral atom (referred to a thermal ionization).

$$\frac{n_e^2}{n-n_e} = \frac{2}{\Lambda^3}\frac{g_1}{g_0}exp\left[\frac{-I}{kT}\right] \qquad (2.2)$$

Thermal plasma discharges are the hottest man made things with typical temperatures in excess of 10000K. The applications for thermal plasmas are both defined and limited by their high temperatures. They are typically used to destroy or melt surfaces they are in contact with, or are used with active cooling and convective flows to direct the thermal damage. They find applications in welding, in ore refining, and as sprays for molten material. Because of their high temperature most of the species in thermal discharges are atomized as all of the chemical bonds are broken. They are thus also used for decomposing materials or wastes.

2.2.6.2. *Non-thermal plasmas*

In stark constant to thermal plasmas are non-thermal plasmas. In these discharges the species are not in equilibrium. Energy is not equally partitioned between the various kinetic and internal degree of freedom of the system. In order to facilitate discussions and although the distribution among state may not be Boltzmann, temperatures are used to describe the average energies in the various energy modes. Non-thermal plasmas (also cold plasmas) are characterized by their effective electron kinetic temperature (T_e), and

neutral gas electronic excitation temperature (T_{elex}), vibrational temperature (T_{vib}), rotational temperature (T_{rot}) and translational temperature (T_{trans}). In non-thermal plasmas created by externally applied electric fields typically $T_e > T_{elex} > T_{vib} > T_{rot} = T_{trans}$. The energy in a non-thermal plasma is not equally distributed among the various internal and kinetic energies of the system.

In non-thermal plasmas the basic mechanism of ionization is through electron impact ionization: $e^- + A \rightarrow A^+ + 2e^-$. The condition for electron impact ionization is that the electrons have energy in excess of the atom's ionization potential. Considering that typically ionization energies are 10 eV to 15 eV and the electrons have a Boltzmann distribution of energies at a given temperature, rates of ionization are typically sufficiently high to sustain a plasma when the electron temperature is about 1eV. Gas temperatures in non-equilibrium plasmas can vary significantly depending on the specific heat balance but are typically near room temperature due to cooling of the neutral molecules on the electrodes or chamber walls which are at or near room temperature.

Similar to Townsend avalanches and breakdown phenomena non-thermal discharges require a sufficient amount of electron energy to maintain a high electron energy and ionization. The behavior of non-thermal plasmas are thus governed by the reduced electric field *E/n* (which is related to the electron's energy gain per mean free path, ε). This is in contrast to thermal plasmas which are controlled only by the equilibrium temperature as dictated by the discharge's power density.

The non-equilibrium nature of non-thermal plasma discharges allows for the creation of active species without generating excessive heat which may damage substrates or cause excessive dissociation. Also the chemical processes which occur in

the non-equilibrium plasma are beyond those which are accessible by the addition of only thermal energy. Non-thermal plasmas thus find many diverse applications in the treatments of materials. The applications generally fall into two categories those which rely on physical mechanisms of the plasma and those which rely on chemical mechanisms.

2.2.6.3.   *Energy Transfer in Non-Equilibrium Discharges*

The non-equilibrium nature of non-thermal discharge can be maintained because the plasma discharge is sustained by an electric field. The energy directed into the system does not interact will all of the particles but only couples with the ions and the electrons. The neutral atoms essentially do not feel the electric field whereas the charged particles are accelerated by it. A flow diagram indicating the flow of energy in a plasma sustained by an electric field is shown in Figure 5. This flow diagram is very important to understand because it is the relative rates of these energy flows and reverse energy flows which determine if the non-equilibrium can be sustained. In the consideration of the applicability of microplasma glow discharges for PECVD one of the most important conditions to meet is that the discharge be non-thermal.
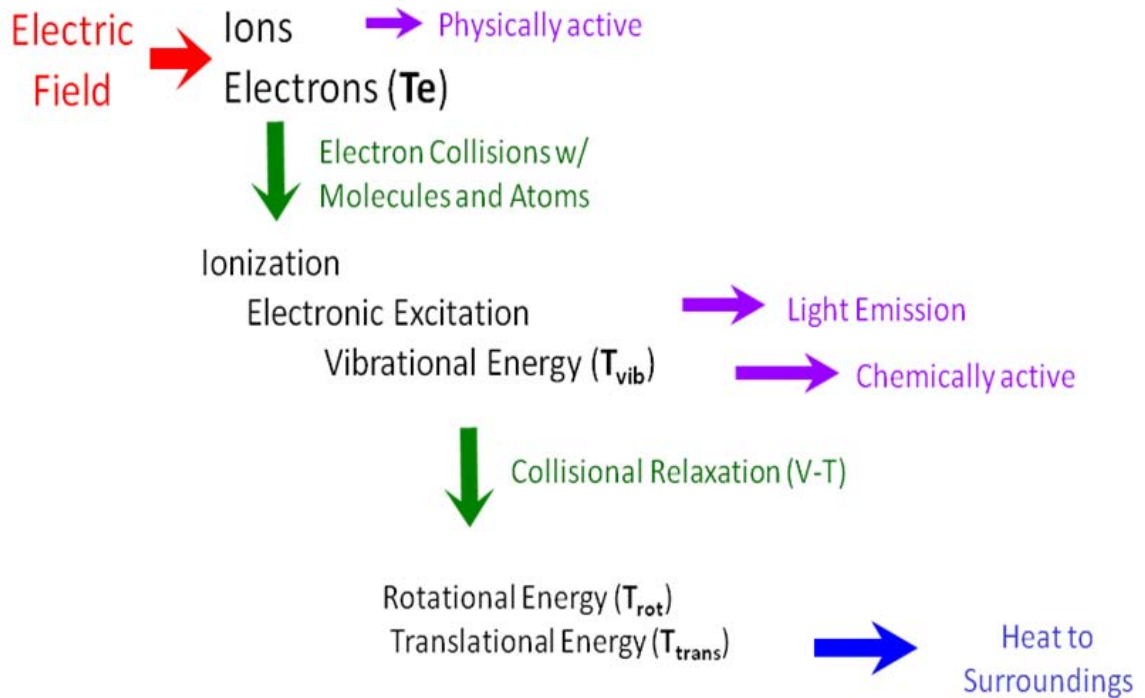
Figure 2.4: Energy flow diagram for non-thermal plasmas.

The electric field only directly couples with ions and electron through the Lorentz Force, $F = qE$, where F is the force on the particle, q is the charge and E is the local electric field. The energy given to the particle of mass, m, is a product of the force and displacement and after some time, t, a particle starting from rest with have and energy, $\varepsilon = \epsilon = \frac{q^2 E^2}{2m} t^2$. Considering the large disparity in mass between electrons and ions $m_{ion}/m_e = 5.1 \times 10^4$ most of the discharge power in the plasma is converted into the energy of the electrons. Some energy does go to the ions and in specifically tailored discharges this can be maximized and for sputtering and other physical modifications of the substrate.

The majority of energy goes to the electrons. The electrons in turn collide with the neutral molecules and atoms. Various types of collisions occur which affect the transfer

of energy in the system, including for example: momentum transfer, rotational excitation, vibrational excitation, electronic excitation, ionization, dissociation, and attachment. Atoms of course do not have internal degrees of freedom and so do not experience rotational excitation, vibrational excitation, or dissociation. The relative importance for each of these mechanisms of energy transfer is dependent on E/n. For typical electric fields in the range of 0.1 to 1 times the breakdown E/n the importance of each type of electron collision is summarized below.

Momentum Transfer: Energy is transferred very inefficiently by this process. This is because very little momentum and energy can be transferred due to the disparity in masses between the electron and heavy neutral particle (in terms of relative masses, $m_{ion}/m_e = 5.1 \times 10^4$, consider it as a collision between a ping pong ball and a gorilla). These numerous collisions serve mainly to scatter the electrons thermalizing their energies. Some energy though is transferred by momentum transfer collisions and in atomic gases this may be the only and main route.

Rotational Excitation: Rotational excitation is an insignificant portion of the energy flow as the characteristic energy of rotational modes is only about 5 K (4×10^{-4} eV) and thus will not transfer significant energy per collision.

Vibrational Excitation: In molecular gases the main transfer of energy from electron to neutral atom occurs through vibrational excitation. These collisions are less probable than momentum transfer collisions however they can be resonant and a significant amount of energy can be transferred. This is because the characteristic energy of vibrational modes in molecules typically 2000K to 5000K (0.2eV to 0.5 eV) is close to energy of the

electrons typically about 1 eV. Depending on the specific value of *E/n* typically as much as 80% of the energy may flow from the electrons to vibrational modes. Vibrational modes additionally relax through chemical processes (i.e. stepwise dissociation, or lowering of activation energies in endothermic reactions) or through collision with neutral atoms resulting in effective vibrational-translation (V-T) energy transfer.

Electronic Excitation: Electronic excitation is responsible for light emission from the plasma discharges and may also play a role in stepwise ionization processes. For most gases the energy of the first electronic level is above 10eV. As such there are few electrons with sufficient energy to electronically excite the particles and this is not a significant mode of energy transfer. Nonetheless the electronic excitation is very important for understanding the light emitted by the discharge and for spectral analysis. A explanation of the spectroscopic techniques used in this research is given along with the experimental results and some of the programming methods are detailed in appendix A. The 2nd, 3rd, 4th and higher electronically excited stated typically have energy difference of about 1eV to 2 eV and a significant number of electrons can give energy to already excited particles. However for typical conditions the lifetime of the excited electronic state relative to the time between excitation collisions with electrons is relatively short and such stepwise excitation and ionization processes are few.

Ionization: Though a very import process for generating the plasma similar to electronic excitation ionization in not a significant method of energy transfer. Ionization energies are about 14 eV in Air and as high as 24eV in Helium and only the small fraction of high energy electrons participate in ionization.

Dissociation: The amount of dissociation which occurs due to electron impact collision depends very much on the strength of the molecule. Nitrogen which has dissociation energy of 9.756 eV only experiences a small degree of dissociation. Methane with an energy of 4.56 eV will experience more dissociation. Though these energies are still above the average electron energy and thus do not play a significant role in energy transfer.

Attachment: Though very important for charge balance, ionization rates and charge mobility, attachment is not too important for energy transfer.

The various modes of energy transfer depicted by these different types of collisions have convenient abbreviations for electron (e), ionization (I), electronic (E), vibrational (V), translational (T) and rotational (R) energy. The most commonly used are for the dominant energy transfers namely electron to vibrational (e-V), electronic to translational (e-T) and vibrational to translational (V-T). Rotational and translational energy modes are assumed to be equal because of the high rate of R-T and T-R energy transfer. The high probability of R-T, T-R are due to the gas temperature (>290K) being significantly greater than the characteristic temperatures of the rotational and translational energy modes, approximately 5K and <1K respectively.

Some of the different paths of energy transfer in non-thermal plasma can be illustrated by looking at the energy level diagrams for two different species molecular and atom. Figure 2.5A shows the diagram for Nitrogen, and 2.5B show the diagram for helium. Electrons in the plasma have average energies of about 1 eV. The electrons do not have a maxwellian distribution of energies, see figure 2.6, though there are

similarities. This distribution occurs because a large proportion of the electron can easily interact with the vibrational modes of molecules. Electronic excitation is much less probable and ionization even less so. This correspond to the collision cross sections for e-V being significantly higher than for ionization (e-I) and electronic excitation (e-E). These cross-sections, distributions functions and energy transfer, along with estimates of electron temperature from the electric field have been well studied for low temperature plasmas and put together to calculate the fractional amount of the discharge power which goes into the various modes (Figure 2.7). As shown in this graph e-V energy transfer can account for as much as 80% of the energy transfer in these systems.

In collision with atoms though there are no ways to transfer energy to vibrational modes. Helium because of it very high ionization energy is also very hard to electronically excite of ionize. The energy for electronic excitation is in excess of 20eV and very few electrons will inelastically interact with helium. For discharge operation in helium thus the only method of energy transfer is through the inefficient e-T. As such non-equilibrium discharges are easiest to maintain in helium discharges. For this reason helium is very successfully used to stabilized discharge at atmospheric pressure. In plasma discharges with helium though any trace molecular impurity will be strongly excited as there are few other routes and the benefit of helium for stabilization go away with addition of impurities greater than about 1%.
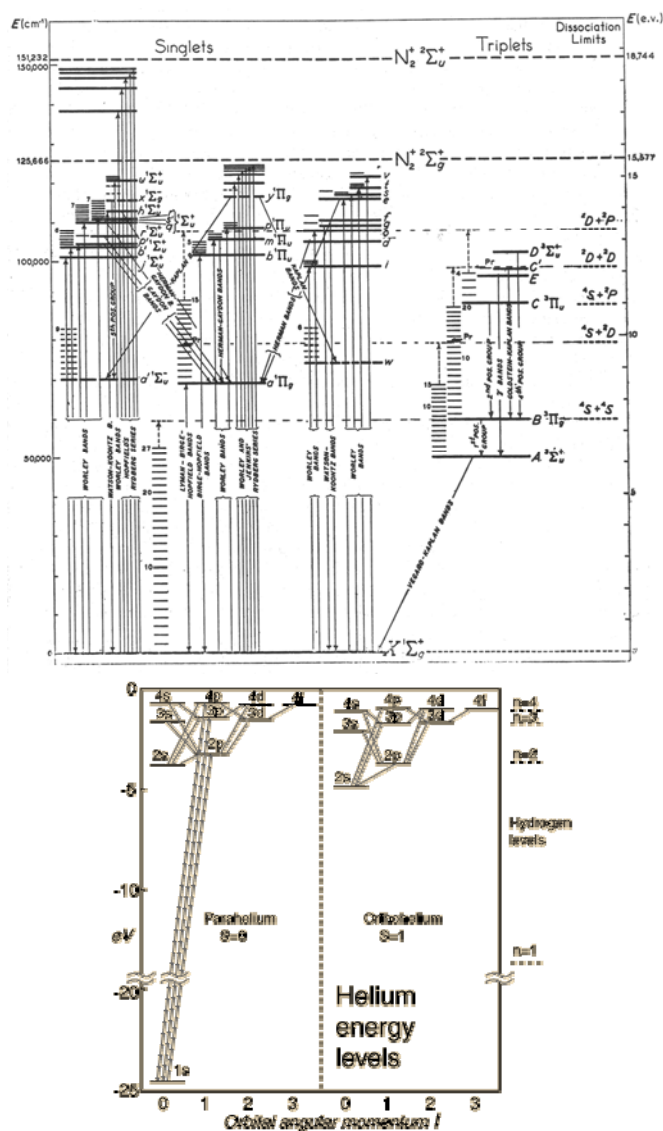
Figure 2.5: (A) energy level diagram of N2 molecule. The heavy (full) horizontal lines give the electronic states; the shorter thinner lines give the vibrational levels in each of them. The light broken horizontal lines ending in heavier lines at the right indicate dissociation limits. Transitions are labeled in the vertical and angled lines. (B) Energy level diagram for atomic helium which only has electronic excitation levels. Spin orientation of excited electron relative to inner electron indicated by para- and ortho-states. Details can be found in reference.[18]
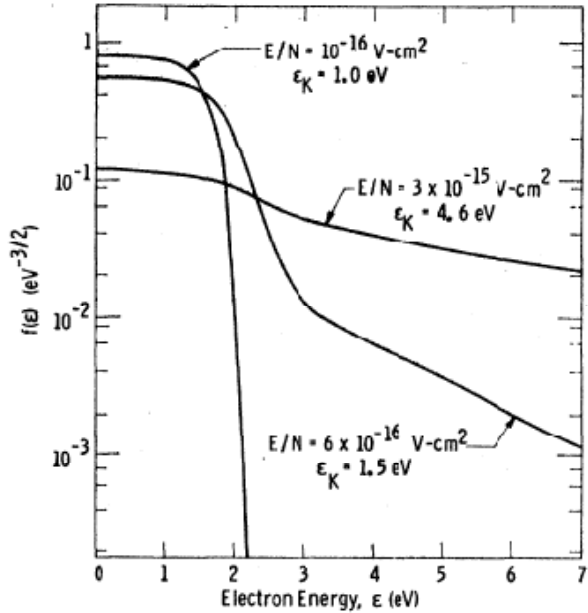
Figure 2.6: Electron energy distribution function in low temperature N_2 plasma at several

different values of Te or E/n.[19]
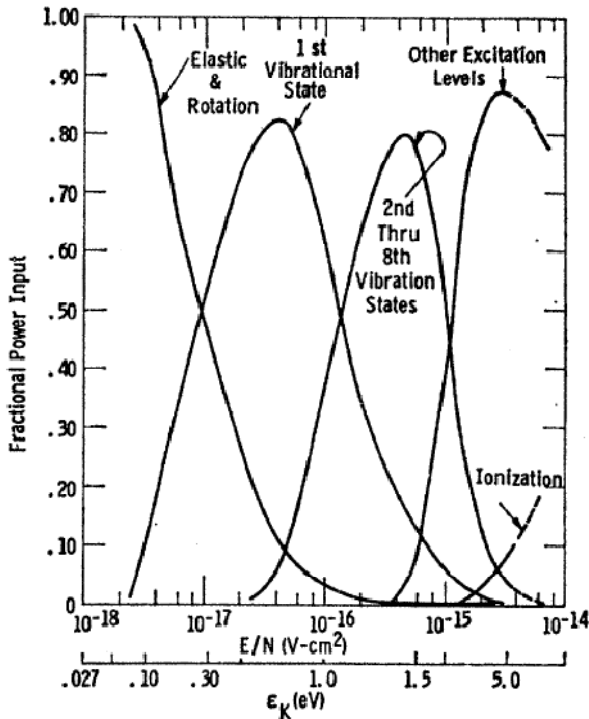
Figure 2.7: Flow of power into different modes as a function of the reduced

electric field and electron temperature.[19]

The most important path in molecular gases is the transfer of energy from the electron to vibrational energy modes. The focus here is on molecular gases because in PECVD processes the precursors are always molecular. Vibrational energy is very useful for promoting chemical reactions. Specifically endothermic reactions will have effectively lower activation energy for vibrationally excited molecules.[1] In a PECVD reactor the goal is to increase the rate of endothermic reactions without adding significant thermal energy. Although only a small portion of the discharge energy put into the electron may end up in chemical reactions the vibrational temperature must be maintained at a value higher than the translational temperature to catalyzed these endothermic reactions.

All of the e-V energy transfer does not stay in vibrational modes. There is some V-T energy transfer. Ideally in a chemically reacting plasma system V-T transfer would be minimized. Generally speaking the rates of V-T energy transfer can comparatively low which is why $T_{vib} > T_{trans}$ can be maintained in plasma. The rate of V-T energy transfer is very dependent on the respective temperature T_{vib} and T_{trans}. The closer T_{trans} is to T_{vib} the faster the V-T energy transfer. Expression for this V-T rate are given by Lifshitz [20] and there is an exponential increase in the rate of V-T relaxation with gas temperature for nitrogen as is plotted in figure 2.8.

---

[1] An illustrative description of how this works was described to me by Dr. Fridman. The potential energy surface (ϕ vs. d_{AB}, d_{AC}) of a reaction AB+C→AC+B looks like two perpendicular valleys/trenches separated by a ridge with a saddle point. Consider the analogy of trying to kick a soccer ball up from the bottom of a valley over into the adjacent valley, kicking the ball straight along the axis of the valley (translational energy) is less effective than bouncing the ball up the sides of the valley (vibrational energy), in which case it can pop over the saddle point to the adjacent valley. In exothermic reactions the saddle point is almost aligned with the axis of the initial valley and so whether the energy is translational or vibrational is not that important. In contrast for endothermic reactions the saddle point will be to the side of the axis of the initial valley and vibrational energy can help significantly.
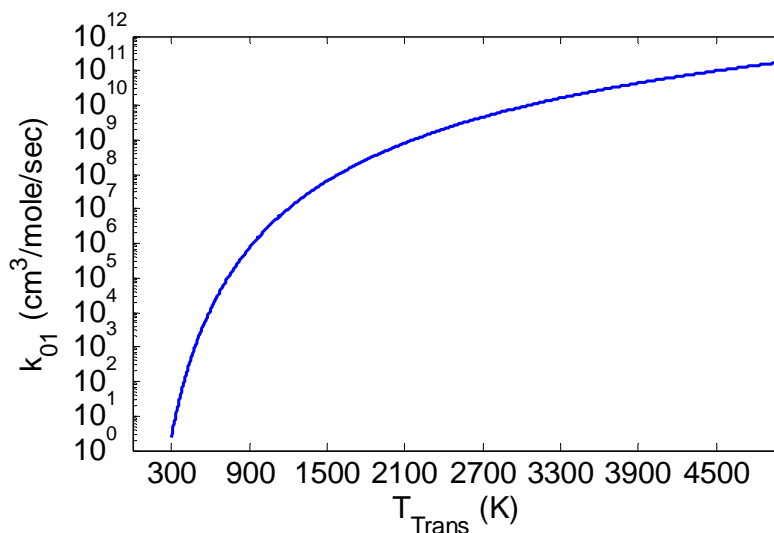
Figure 2.8: Exponential dependence of the vibrational de-excitation rate constant k_{01} on

the gas temperature.

V-T relaxation will give some of the energy to the translational modes and will

effectively increase the gas temperatures. Translational modes lose their energy through

collision will the reactor walls. The reactor walls are assumed to be at or near room

temperature and are effectively an isothermal energy sink.   This normal case of

isothermal wall will be reconsidered in our discussion of heat balance in microplasmas in

Chapter 4.

In a molecular gas the direction of most of the energy flow is thus e-V then V-T

then T-wall. This flow of energy can be met in more than one way. The rate of e-V is

always high and relatively independent of T_{vib}.[2] The rate of V-T could be high in two

cases 1) high T_{vib} (a non-equilibrium plasma), or 2) high T_{trans} (a thermal/equilibrium

plasma). In a PECVD system the goal is to have this plasma with high T_{vib} and low T_{trans}.

---

[2] An exception to this is so called super-elastic collisions wherein electron gain energy in collisions with vibrationally excited molecules. This is not typically. Though in Hydrogen discharges it is occasionally considered.

Thus a very important factor to maintain a non-equilibrium system is to have T_{trans} not increase significantly. Only if the translational energy sink is sufficiently rapid to maintain a low T_{trans} will T_{vib} increase.

2.2.6.4. *Warm Discharges*

The terms thermal, equilibrium, non-thermal, non-equilbrium are four terms which are used with specific meaning. Thermal – refers to the dominant mechanism of ionization being the thermal collisional mechanism. Non-thermal – refers to the dominant mechanism of ionization being electron impact ionization. Equilibrium refers to $T_e = T_{elex} = T_{vib} = T_{rot} = T_{rans}$. Non-equilibrium refers to any two of the temperature being unequal. Typically in plasma when a system is thermal it is also equilibrium for example a hot arc with T=10000K. When it is non-thermal it is non-equilibrium for example a glow discharge with $T_e = 11610K$, $T_{vib} = 6000K$, $T_{trans} = 400K$. There are some shades of gray though. The first is non-equibrium arcs, or arcs in stong convective flows. These have high temperatures T_{trans}~5000K and are dominated by thermal ionization but with possibly slightly higher T_e ~ 10000K. There also may be non-equilibrium system $T_e = 10000$ K, $T_{Trans} = 2500K$, $T_{vib} = 3000K$ such as transitional gliding arcs and some microplasma in which both electron impact and thermal ionization mechanisms occur and one ionization mechanism (thermal or non-thermal) is not dominant. During our research into higher current microplasma and similar gliding arcs Alexander Gutsol, Shailesh Gangoli, and myself have come up with the terminology of 'Warm discharges' to describe these systems. Summarizing these shades of gray all non-thermal discharges are

non-equilibrium, and all equilibrium discharges are thermal, though not all non-equilibrium discharges are non-thermal and not all thermal discharges are equilibrium.

2.2.6.5.   *Plasma Thermal Instability*

Returning to the ideas presented on the thermodynamics of plasmas the presence of an energy sink is a necessary condition for a non-thermal discharge. If the energy sink is insufficient the gas temperature rises and eventually will match the electron temperature. This transition is not smooth. An instability arises referred to as the ionization-overheating thermal instability [2, 21-28]. This instability is indicated in the close chain shown in equation 2.4. An incremental increase in the electron density (n_e) leads through collision to an increase in gas temperature ($T_o=T_{trans}$). The T_o increase corresponds with a decrease in neutral density, n_o, by the equation of state at constant pressure. The decrease in density corresponds to an increase in the parameter E/n assuming a constant electric field, E. The electron temperature (T_e) is largely determined by E/n and an increase in E/n causes and increase in T_e. At slightly higher T_e the ionization rate increases dramatically and causes a further increase in n_e. The chain thus has positive feedback and is unstable. This mechanism is one of the major mechanism by which a non-thermal discharge becomes a thermal discharge.

$$\uparrow n_e \Rightarrow \uparrow T_o \Rightarrow \downarrow n_o \Rightarrow \uparrow \frac{E}{n} \Rightarrow T_e \Rightarrow \uparrow n_e \qquad (2.4)$$

For clarification we address the relationship between the ionization overheating instability and the traditionally considered glow to arc transition (GAT) [10]. The

transition from a glow discharge to an arc discharge by the change from secondary electron emission to thermionic emission at the cathode does not necessarily create a thermal discharge although the two are closely related. Often, the significant increase in current density caused by transition to thermionic emission results in an increase in n_e and the onset of the overheating instability and transition to a thermal discharge. However, non-thermal discharges sustained by thermionic emission at the cathode are commonly achievable especially in low pressure conditions [Granovsky, 1971]. Likewise discharges sustained only by secondary electron emission may become thermal discharges through the ionization overheating instability. However, as the discharge is becoming thermal typically the increased temperature causes thermionic emission from the cathode. Significant limitations on the transition from a glow to an arc are often imposed by the power supply used to create the discharge. Modern power supplies typically have a current limitation to prevent catastrophic failure and may prevent the overheating instability from fully transitioning to an arc.

2.2.7. DC glow discharge

One of the most studied non-equilibrium plasma discharges is the low pressure normal glow discharge and its positive column, and descriptions of such discharges can be found in many introductory plasma texts. It is simple in geometry and easy to generate, complex in structure but describable. Figure 2.9 shows a general schematic of the circuit to generate a DC glow discharge. A power supply is connected in series to a ballast resistor and the discharge gap. When the power supply voltage is in excess of the

breakdown voltage for the gap the discharge initiates. The ballast resistor serves to stop the current from increasing too much. Consider the power supply voltage, V_{ps}, as constant and the sum of the discharge voltage V_p, and the ballast resistor voltage $V_b=IR_b$. Where I is the discharge current and R_b is the ballast resistance. At breakdown the plasma discharge has a negative differential resistance ($dV_p/dI < 0$) because as the discharge transition to a self sustained mode and the current rapidly increases the voltage required to maintain the plasma actually decreases since the gas in the discharge gap has become more conductive.
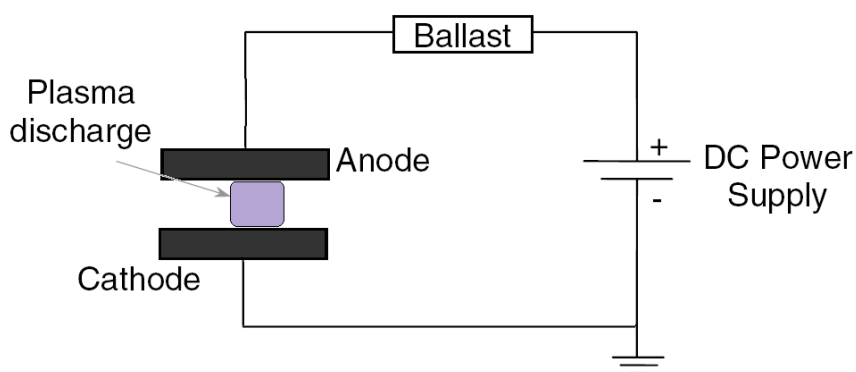
Figure 2.9: Electrical Circuit for generating and DC glow discharge.

2.2.7.1.   V-I Curve

Figure 2.10 is an illustrative plot of voltage versus current for a DC electric discharge in a gas[29] (actual plots will vary slightly depending on electrode configuration, gas, pressure, temperature and to a certain degree author (see Figure 2.11 for example). As voltage is initially applied naturally occurring free electrons provide some current (A-

B in Fig. 2.10). As the voltage is increased the electric field becomes sufficient for the electrons to gain energy and ionize some of the gas producing more electrons, but not yet creating a sufficient number to create a self sustained discharge (C-D). In a corona (D-E) a sharp electrode is used to locally increase the electric field and in the region near the sharp electrode the plasma density is higher and a glowing region is seen. The shape of C-D-E shown in Figure 2.10 is for a negative corona configuration. In a parallel plate configuration the C-D-E will actually be a flat line with voltage at the level of E as in figure 2.11.

Eventually breakdown occurs (E-F) when the discharge becomes self sustaining. Sufficient electron emission from the cathode is one of the requirements for the development of self sustained plasmas. In typical glow discharges the electron emission occurs because of secondary electron emission due to ion bombardment at the cathode surface. After breakdown at low currents the DC normal glow discharge plasma is observed (F-G). The normal discharge has several unique characteristics described in detail later. In general though the voltage is constant and an increase in current causes an increase in the diameter of the discharge.

In the normal glow regime if the current is increased and the size of the electrodes in limited the current density will increase and we have the abnormal glow discharge (G-H). The abnormal glow is initially low temperature, but as the current is increased it can transition to the high temperature arc discharge (H-J). The transition can occur by either 1) the cathode becomes overheated or thermionically emission greatly increases the current or 2) the gas temperature increases and the dominant mechanism of ionization changes from electron impact ionization to thermal ionization. The higher the density of

the gas medium the lower current at which the transition to an arc occurs. If the size of

the electrode is not limited glow to arc transition will also occur but the line G-H will be

relatively flat.
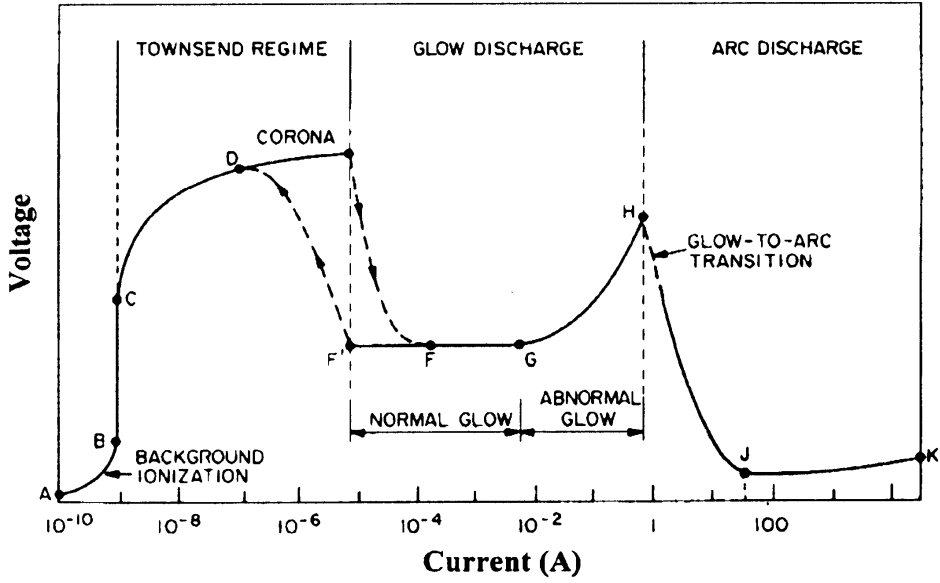
Figure 2.10: Voltage current characteristics of a typical DC discharge[29]
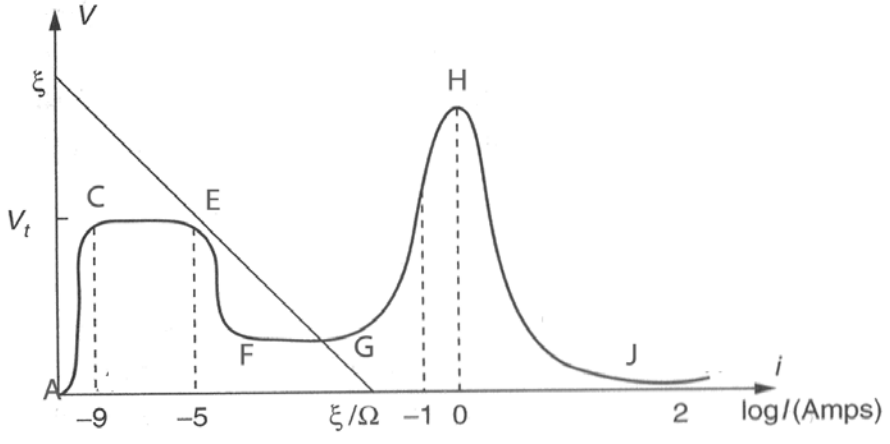
Figure 2.11: Alternate voltage current characteristic of a typical DC discharge.[2]

Shown in figure 2.11 (and not in 2.10) is a diagonal line from ξ to ξ/Ω. This line is called the load line and represents the ballast resistor in the circuit. The ξ and ξ/Ω in the notation used earlier would be V_{ps}, and V_{ps}/R_b. Graphically the interactions of the external ballast resistor and the plasma work such that the operating point of the discharge will be where the load line crosses the V-I characteristic. Depending on the value of the ballast resistor it is possible that the load line will cross multiple parts of the V-I. In such configurations the discharge may be unstable or show hysteresis between the two points.

2.2.7.2. *Structure of a Normal Glow Discharge*

Glow discharges (F-G in figure 2.10) are 'just right' for most materials processing applications. Townsend regime discharges are too weak and arc discharges are too hot. Figure 2.11 shows the structure of a typical DC normal glow discharge. This structure is well studied for low pressure DC glow discharge operation. In atmospheric pressure microplasma systems we observe some of these structures (mainly the negative glow, faraday dark space, and positive column) and were among the first researchers to report on them. The description of various structures starts at the cathode and proceeds toward the anode.
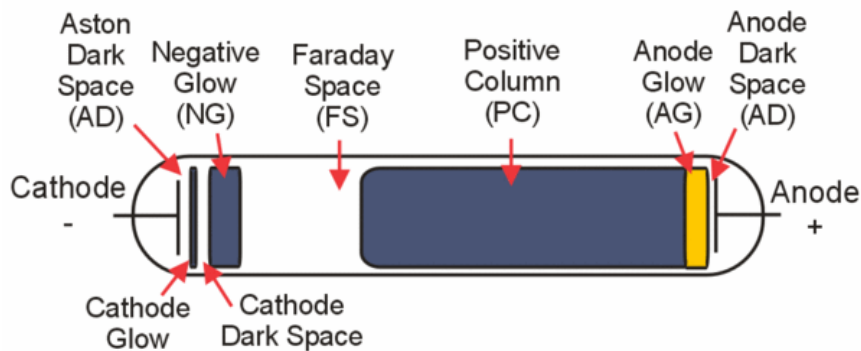
Figure 2.12: Structure of a DC glow discharge

Cathode – An electrical conductor with a secondary emission coefficient γ that is very important for the operation of the discharge tube. Electron are emitted from the cathode due to secondary electron emission due to ion flux to the surface.

Aston Dark Space – A thin region to the right of the cathode with a strong electric field. The electrons are accelerated through this space away from the cathode. The electrons are too low density and/or energy to excite the gas, so it appears dark.

Cathode Glow – The next structure to the right of Aston dark space. Here the electrons are energetic enough to excite the neutral atoms they collide with. The cathode glow has a relatively high ion density. The axial length of the cathode glow depends on the type of gas and the pressure. The cathode glow sometimes clings to the cathode and masks the Aston dark space.

Cathode (Crooks, Hittorf) dark space - Relatively dark region to the right of the cathode glow that has moderate electric field, a positive space charge and a relatively high ion density.

Negative Glow – The brightest intensity of the entire discharge. The negative glow has relatively low electric field, long, compared to the cathode glow and is the most intense on the cathode side. Electrons carry almost the entire current in the negative glow region. Electrons that have been accelerated in the cathode region to high speeds produce ionization and avalanches, and slower electrons that have had inelastic collisions already produce electronic excitations. These slower electrons are responsible for the negative glow. As these electrons slow down, energy for excitation is no longer available and Faraday dark space begins.

Cathode Region. – The cathode regions near the cathode described above. Most of the voltage drop across the discharge tube occurs between the cathode and the negative glow. The length of the cathode region, from the cathode surface to the boundary of the negative glow is d_c. The voltage drop here is V_c. Most of the discharge power is dissipated in this region. The electrons are accelerated in this region to energies high enough to produce ionization and avalanching in the negative glow, and in the regions to the right of the right of the negative glow. A discharge will adjust the axial length of its cathode region, d_c, so that the minimum value of the product d_{cp} is established, d_{cp} ~ $(dp)_{min}$. This product is the Paschen minimum. At the Paschen minimum the discharge maintains itself with a minimum cathode fall voltage V_c and minimum power dissipation. In the normal glow discharge, the current density flowing to the cathode remains approximately constant as the total current varies, as the total area of contact with the cathode increases with the total current. This value is named the normal current density j_n. Simmilar to the length of the cathode region this normal current density scale with pressure such that j_n*p^2 is a constant. Typical values in air at a pressure of 1 Torr might

be a current density of 0.3 mA/cm^2, d_c approximately 0.5 cm, and cathode fall voltage between 150 to 300 V.

Faraday dark space – The electron energy is low in this region. The electron number density decreases by recombination and diffusion to the walls, the net space charge is very low, and the axial electric field is small.

Positive Column – Quasi-neutral, small electric field, typically ~1-10 V/cm at 1 Torr. The electric field is just large enough to maintain a constant degree of ionization along its length. The electron number density at 1 Torr is about 10^{15} to 10^{16} electrons/m^3 in the positive column, and the electron temperature of 1 to 2 eV. In air the positive column plasma is pinkish blue. As the length of the discharge tube is increased at constant pressure, the length of the cathode structures remains constant (p_{dc} = constant), and the positive column lengthens. The positive column is a long, uniform glow, except when standing or moving striations are triggered spontaneously, or ionization waves are triggered by a disturbance. Incredibly long positive columns can be created as in the case of neon tubes.

Anode glow – Slightly brighter than the positive column, and not always present. This is the boundary of the anode sheath. The voltage drop and brightness depend on the electron boundary conditions. In general ions are repelled and electron are attached to the anode by a slightly higher electric field.

Anode dark space – The space between the anode glow and the anode itself is the anode sheath. It has negative space charge due to electrons traveling from the positive column

to the anode. There is a higher electric field than the positive column. The anode pulls electrons out of the positive column and acts like a Langmuir probe in electron saturation.

Striations – Moving or standing striations are traveling waves or stationary perturbations in the electron number density which occurs in partially ionized gases. In their usual form moving striations are propagating luminous bands which appear in positive columns. Standing striations can be easily photographed. Many apparently homogeneous partially ionized gasses in reality have moving striations. The longitudinal striations arise from small instabilities and are mostly benign.

2.2.8.   RF CCP

Another type of glow discharge suitable for materials processing is the radio frequency capacievly couple plasma (RF-CCP). These plasma discharges are generated in parallel plate configuration but with the application of high frequency RF electric fields, typically 13.56 MHz.   A typically electrical circuit for generating such a discharge is shown in figure 2.12. An RF generator with typical output impedance of 50 ohms is connect to a matching box and then to output of the matching box is connect to the parallel plate electrodes. The matching box is required because the impedance of the plasma may not be equal to the output impedance of the RF generator. If there is a significant mismatch in the impedances very little power will be transferred from the power supply to the plasma. The energy will be absorbed by the internal resistance of the power supply and cause the power source to overheat. The matching box serves to make the impendance of the plasma look like a 50 ohm impedance to the power supply. This is

done by using a 'L' shaped configuration of capacitor and inductor circuit elements. Typically the capacitor in series with the discharge is called the loading capacitor and the capacitor in parallel with the system is called the tuning capacitor. Depending on the values and ranges of the inductor and variable capacitors the matching circuit can be used to make a plasma with impedance in the range of 10-200 ohms look like 50 ohms to the power supply. This thus allows for sufficient energy to flow into the plasma. As the conditions of the plasma change it is necessary to change the configuration of the matching circuit to maintain a 50 ohm effective impedance.
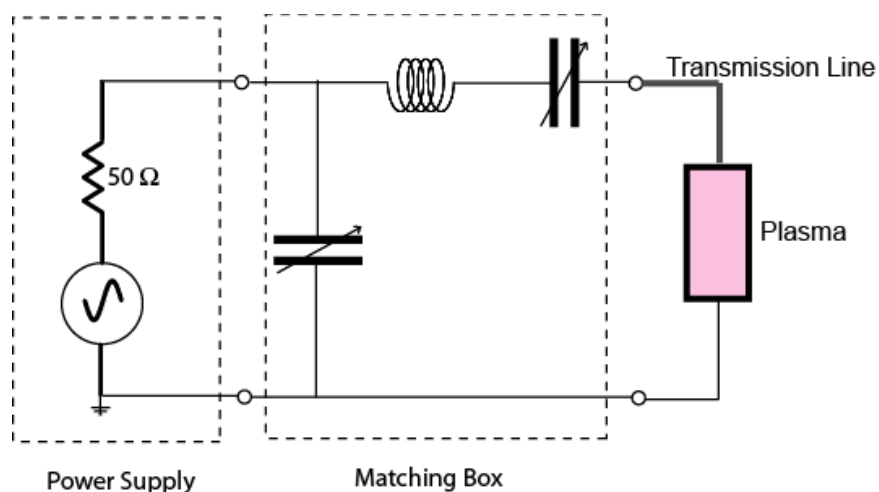
Figure 2.13: Circuit schematic for generating a RF plasma discharge

Because the frequency is so high in RF plasma discharges the ions do not have time to move from one electrode to another. As such secondary electron emission at the electrode surfaces is essentially negligible. The electrons though because of the lighter mass are accelerated from one electrode to the other and make up the discharge current.

These discharges unlike DC glow discharge thus do not operate in a gamma mode but rather operate in an alpha mode. Though they operate in alpha mode such RF discharge are self sustained because the electrons from one cycle of the discharge are still present in the discharge gap at the inception of the next cycle of the discharge. Alpha mode discharges operate at lower current densities than gamma mode discharges typically 1/100th of the current density.

Like DC glow discharge CCP discharge can operate in a normal or abnormal mode dependant on the size of the discharge relative to the electrodes. Once the discharge completely covers the electrodes and increase in current will cause an increase in the current density on the electrodes. Current density is governed by the electrode flux to the electrode and an increase in current density will require an increase in the sheaths at the electrode boundaries. This increase in sheath voltage and electric field will cause more of the ions to be accelerated toward the electrode and thus slight increases in the secondary electron emission. It is possible in abnormal CCP discharge for the sheath voltages to become sufficiently high to cause breakdown in the electrode sheath. Essentially the ion flux to the electrode will be sufficient that secondary electrons can no longer be neglected and the discharge will transition to a gamma mode. Figure 2.13 shows the characteristic light emission profiles of alpha and gamma mode RF CCP discharges. In the case of alpha mode the sheaths are not luminous and only the center of the discharge glows dimly. In the gamma mode discharge the structure is generally similar to the DC gamma mode discharge only the orientation changes every half cycle. On average a gamma mode RF discharge has the structure from one electrode to another of: negative glow, faraday dark space, positive column, faraday dark space, negative glow.
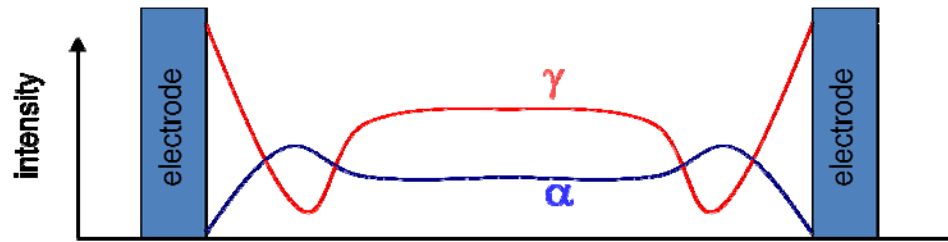
Figure 2.14: Characteristic light emission profiles for alpha mode and gamma

mode RF CCP discharges.

With the transition to gamma mode in RF CCP discharges there is a significant

increase in the current density and a contraction of the discharge area. This more intense

discharge is can often overheat the electrodes. Also the gamma mode discharge has

significantly higher impedance than the alpha mode discharge as such the matching

circuit may not be effectively matching the circuit. The transition to gamma mode is thus

often unstable resulting in failure of the power supply or overheating of the electrodes.

This alpha-gamma mode transition is thus to be avoided in operation of RF CCPs. As

$\alpha-\gamma$ transition is a breakdown phenomena the critical current density, j_{crit}, for it is

calculated for moderate pressure CCPs as shown in equation 2.2.[2] Here A and B are the

Townsend constants as before the only new parameters are ω the discharge frequency and

ε_o the permittivity of free space. Results from equation 2.3 are plotted in figure 2.12 for

air at pd =11.5. We see from this that maintaining alpha mode discharges becomes more

difficult (requires high frequency power sources) as the pressure is increased.

$$j_{crit} = \cfrac{Bp\omega\varepsilon_o}{\ln\left\{\cfrac{Apd}{3\left[\ln\left(\left(1+\cfrac{1}{\gamma}\right)\sqrt{\cfrac{\pi Apd}{4}}\right)-\cfrac{Bp\omega\varepsilon_o}{j_{crit}}\right]}\right\}} \qquad (2.3)$$
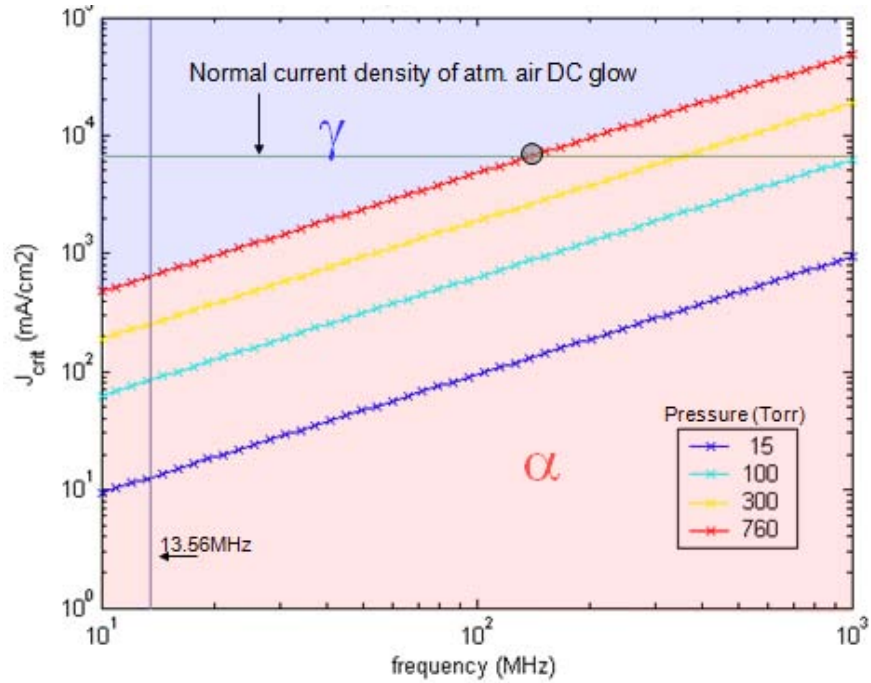
Figure 2.15: Critical current density for α–γ transition as a function of RF frequency for several different pressures of air. Alpha mode can be maintained if the current density is below the line, gamma mode if above. *pd* is taken as 11.5 cmTorr

2.2.9. Novel Atmospheric pressure plasmas

In addition to the traditional atmospheric pressure discharge (coronas, DBD and arcs) several other configurations of discharges are being studied which may have the potential for being non-thermal, low temperature discharges suitable for materials processing.

2.2.9.1.   APPJ

The atmospheric pressure plasma jet (APPJ)[11, 30] is a type of RF CCP plasma discharge operated at atmospheric pressure. Like all atmospheric pressure discharges RF CCP are susceptible to instabilities such as the ionization overheating instability and alpha to gamma mode transition. In the APPJ the systems are stabilized by operation in helium or argon. The atomic noble gas operation, as described in section 2.1., makes it significantly easier to maintain the non-equilibrium system. Such systems can be stably operated in normal and abnormal modes (up to a point) in pure helium. However, only a very minor faction of precursor gases can be added. In SiO_2 deposition for example typically only as much as 2% oxygen may be added and even less ~0.1% of the HDMSO precursor may be added. The drawback of using helium is that it is very costly. None-the-less this technology has been able to deposition thin films and commercial developed and is seeing success by the company spun off by the inventors of this technology (http://www.surfxtechnologies.com/)[31]

2.2.9.2.   Uniform DBD

Traditional continuous wave DBDs[32] are typically seen as unsuitable for PECVD materials processing because of streamer formation. Streamers arise in DBDs because the avalanche formation is non-uniform and certain branches of the avalanches will become

preferentially intensified. Eventually this leads to spatial non-uniformities in the discharge which also lead to spatial non-uniformities in deposited films. In operation in helium it has been observed that these non-uniformities do not occur. The precise reason for this is still unclear. However, like the APPJ, very high purity helium is required. There has been some success in depositing uniform thin films.[33] Another opportunity to generate uniform DBD is to use pulsed rather than continuous wave excitation to apply the electric field sufficiently fast and with high over voltage to generate more uniform avalanches and thus prevent streamer formation. [34]

2.2.9.3.   Microplasma

Microplasmas are pressure scaled versions of the common low pressure discharges. The similarity parameter E/p and pd form the basis of understanding plasmas in terms of pressure scaling. Considering first pd as you increase the pressure at which a discharge is operating to achieve the same conditions the size should be reduced. For example a fluorescent tube which has an interior pressure of about 1 Torr and a length of about 100 cm.[35] To achieve a discharge similar in structure to in a fluorescent tube at atmospheric pressure, 760 Torr, a discharge gap of 1.3 mm would be required. Fluorescent tubes are relatively long discharges. The size of a discharge corresponding pd_{min} (the Paschen minimum) at atmospheric pressure in air would be 9 μm. This small characteristic size for plasma operation at atmospheric pressures naturally gives rise to the study of microplasmas. Because the scaling parameters in a microplasma are the same as for a low pressure plasma many of the operating conditions are similar.

2.2.10. Literature Review on Microplasmas

Growing interest in atmospheric pressure microscale plasmas only began as recently as the late 1990s[14, 15]. Schoenbach et Al.[15] approached work on microplasmas by looking into the operation of hollow-cathode discharges at higher pressures. Hollow cathodes are a type of DC discharge in which the cathode is arranged as a hollow cylinder and the geometry is chosen such that the diameter of the cylinder is on the order of d_{min} from the Paschen pd_{min} at a given design pressure. This arrangement of the negative glow on the axis of the hollow cylinder allows for a very high intensity stable plasma source to be generated. Schoenbach's original application was to use the stable hollow cathode as a source in creating larger volume stable atmospheric pressure discharges. His initial experiments showed interesting regimes of operation but the $d_{min} \sim 9\mu m$ required for true micro-hollow cathode operation was not achieved.

Several others have expanded on this research as in covered in the review on microplasmas by Becker et. Al.[36]. This review though only focuses on microcavity geometries (shown in Figure 2.16) similar to those of Schoenbach's. In terms of nomenclature many of these were initially called by the name micro-hollow cathode devices although as has since been shown by modeling of these geometries that few of these devices actually exhibit hollow-cathode behavior.[37] The term 'microplasma' is more generally applied now as is the name 'microcavity' plasma for those with a cavity geometry similar to hollow cathodes. The term 'microdischarge' is also used by some in the literature but I prefer not to as this lead to some ambiguity between the stable

microplasmas discussed here and the transient microdischarges and streamers generated in DBDs.
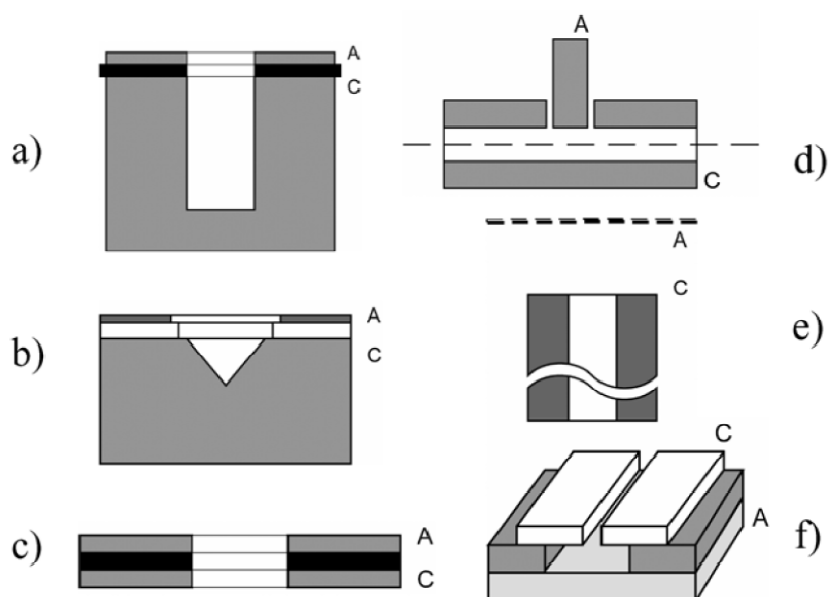
Figure 2.16: Various micro-cavity geometries. A denote anode C denote cathode.

In addition to the micro-cavity configurations simpler parallel plate configurations have also recently been investigated as early as 2000 in helium [14] (as with several following works) in applications for molecular emission detector in micro-total analysis systems. This work identified that scaling laws predict that normal discharges can exist at atmospheric pressure, though no such specific features were measured. The earliest publications on DC discharge in parallel plate systems at atmospheric pressure though dates back much earlier to the late 1930's and 1950's [38-40]. These earlier fundamental works focused on higher current discharges (10 mA -100 mA, rather than 1-10 mA) and the unstable glow to arc transition. The difference in modern works has been the lower current operation, and the use of micro-scale electrodes and discharge gaps.

Microcavity microplasmas as reviewed in ref.[36] and [41]3 have enabled the generation of stable glow discharges in a wide variety of gases at atmospheric pressure. Applications discussed therein include as light sources, for the destruction of VOCs, [42] as elemental detectors and as plasma reactors. As light sources, of note is the generation of excimer light sources which specifically utilized the high density operation to allow for the three body collisions to form significant numbers of excimer species. As elemental detectors the microplasmas are able to detect trace elements from nL volumes. In the destruction of VOCs they were very effective.

The use as plasma reactors includes applications in molecular decomposition[43], etching, fuel conversion, and materials depositions. Focusing on materials deposition: Sankaran shows diamond particle deposition at 100-500 Torr operation [44]; Guo shows deposition of amorphous carbon thin films using helium discharges and RF microplasmas [45]; and Ito[13] shows deposition of amorphous carbon (or unknown particle/film quality) at 300 Torr.

With regards to applications like deposition, in general microplasma discharges were novel and promising but it was not clear if they could meet the conditions for thin film PECVD (uniform, stable, and non-thermal). The largest concern was whether the discharge was non-thermal and how it would behave in reacting systems. The gas temperatures of the microplasma had been reported in only three configurations. Block[46] measured a temperature of 1700K in atmospheric pressure air at 4mA, Kurunczi[47] measured a temperature of 400K in 400 Torr Neon at 1 mA, and Penache[48] measured a temperature of 1100 K in 300 Torr Argon at 0.5 mA. These initial measurements show

---

3 The submission of these reviews predates by several days the first publication of work as part of this dissertation and so gives good reference of the prior state of the art.

gas temperatures range from values close to room temperature to approximately 2000K and though some dependencies were observed (lower for noble gases, higher for molecular gases, and increasing with pressure) other factors affecting the heat balance and non-equilibrium temperatures were unexplored.

2.3. Introduction to Plasma Processing and Thin Film Deposition

There are many important applications of non-thermal plasmas to the manufacturing of materials. Most notable is the processing of semiconductors for the manufacturing of microelectronics and integrated circuits. As much as 30% of all steps in the manufacturing of integrated circuits involve plasmas and purchases of plasma processing equipment account for about 5% of the 260 billion dollar semiconductor industry.[4, 5] Other areas in which plasma processing is important include automotive, textile processing, and biomedical applications.[6] Plasma processing techniques include: removal of material through etching, additional of material through plasma enhanced chemical vapor deposition, and without significant addition or removal of material the modification of surface chemical bonds and functionality.[7]

2.3.1. Plasma Enhanced Chemical Vapor Deposition

Plasma enhanced chemical vapor deposition (PECVD) is a type of plasma processing in which material is deposited onto surfaces in the form of thin films. It is a variant of thermal CVD in that a plasma rather than temperature is used to activate the

chemical processes. In the plasma the precursors (species from which the deposition products are forms) are partially dissociated or otherwise chemically activated. The precursor undergoes a chemical change at a solid surface, leaving a solid layer typically an amorphous or crystalline homogeneous and uniform film. Almost all industrial applications of this processing occurs in low-temperature non-thermal plasma systems.[6] This is because the necessary plasma conditions are easier to maintain at pressures of 10's of millitorr to a few torr. This dissertation investigates atmospheric pressure plasma enhanced chemical vapor deposition (AP-PECVD) which has several advantages and challenges in comparison to traditional PECVD.

Plasma-enhanced chemical vapor deposition (PECVD) is widely used to coat thin films onto materials using plasmas in gas mixtures. These films serve many purposes.[8] For example, silicon dioxide and silicon nitride layers are essential components of integrated circuits. Diamond-like coatings increase the wear and corrosion resistance of metal parts. Nanocoatings of glass onto plastic sheeting prevent oxygen and moisture penetration. Thicker coatings may be used for scratch protection on structural plastics. Polymer coatings are used as dielectrics or temporary masks in integrated circuits.

Most thin film PECVD processes[4] take place in vacuum-based plasma reactors. Performing PECVD at atmospheric pressure has several advantages: firstly, microfabrication is less expensive as there is no need for expensive vacuum pumps; secondly, the process uses less energy and is more environmentally-friendly because operating at ambient pressure and temperature satisfies "Green Chemistry"[9] principles; thirdly, free from the constraints of a vacuum chamber, the processing takes place in continuous rather batch mode and can treat any size shape or object. Similarly, non-

vacuum compatible substrates can be treated by operating at an atmospheric pressure. Lastly, due to the higher operating gas densities, the deposition rate is likely be higher allowing for more rapid processing.

While the benefits of atmospheric pressure plasma processing are well documented, significant challenges still exist. The requirements for thin film deposition by PECVD are that the plasma be 1) uniform, 2) stable, and 3) non-thermal. Using traditional technologies, such plasma can only be generated in low-pressure systems. This is because, at atmospheric pressure caused by the increased collisionality and decreased stabilizing effect of the reactor walls, instabilities arise that prevent a uniform and non-thermal discharge to be maintained. Depending on the type of discharge, these instabilities include 1) glow-to-arc transition (GAT), 2) ionization overheating thermal instability, 3) α-mode to γ-mode transition, and 4) streamer formation. The first three of these types eventually lead to thermalization of the plasma discharge, and the last type leads to spatial non-uniformities.

2.3.2. Thin Film & Thick Film Deposition

Film deposition can occur using many varieties of precursors. In this research though amorphous carbon (a-C) was chosen as a test material for several reasons. First is the relative safety of the precursors, second is the potential variety of materials from diamond like carbon (DLC) to polymers which may be deposited and third, the possible sooting of the precursors presents a relevant challenge. Such material, for example DLC,

also has many desirable material properties and if the cost of production could be reduced by these atmospheric pressure techniques, their application can be extended beyond existing niches. In typical PECVD of a-C and DLC, hydrogen with trace amounts (~1%) of methane is fed into a low pressure plasma discharge chamber and hydrogenated amorphous carbon (a-C:H) is deposited. The general mechanism of deposition[7, 49] is that a flux of carbon containing reactive molecules (CH_3, CH_2) and ions from the plasma deposits carbon in both sp^2 and sp^3 phase onto the substrate. Atomic hydrogen created by the plasma chemically etches hydrogen from C-H sp^3 allowing the formation of C-C sp^3 bonds. Energetic ions and hydrogen from the plasma also preferentially etch sp^2 phase carbon from the deposited layer enriching the sp^3 content. Energetic ions also provide energy to form sp3 phases through stitching processes.[50] At atmospheric pressure the deposition mechanisms are expected to be generally similar, as shown in figure 2.17. In the plasma discharge the chemically active species such as CH_3 and CH_2 are generated and may deposit on the surface in a thin film as in the case of low pressure systems. However, at atmospheric pressure due to the increased density and collisionality there is also an increased propensity to nucleate particles within the discharge which may deposit forming a non-uniform, particle comprised, rough thick film. Pyrolysis of acetylene is at the root of the particle formation mechanism. Such particle formation can usually be suppressed if the temperature is kept sufficiently low, typically $<400^oC$. In addition to non-uniformities due to particle growth non-uniformities in the film can also occur if the plasma in non-uniform.

Figure 2.17: Illustration indicating thick film and thin film mechanisms of film

deposition.

In summary for various precursors thick films are formed by large particles from

the volume which deposit onto the surface. Thin films in contrast are formed by

individual molecules or very small nano-particles which bind to the surface. Thin films

are characteristically smooth and uniform with no noticeable boundaries. In thick films

individual particles may be seen and surface roughness is given by the particles size. The

requirement of how smooth a film is smooth enough is given by application but in

general if the roughness is >100nm and sufficient to generate microscopic non-

uniformities it is considered a thick film.

2.3.3. *Atmospheric pressure deposition*

Atmospheric pressure plasma discharges[10] are of growing interest in plasma

materials processing and micro-manufacturing techniques for several reasons. These

include: lower facility costs for a variety of techniques and methods currently performed

in vacuum conditions[51], continuous rather than batch processes for inline manufacturing, and higher deposition rate due to the higher processing densities.[52, 53] At atmospheric pressure there are also opportunities to work with materials and devices which previously have not been considered. For example, deposition onto non-vacuum compatible substrates or large devices. Also considering the microplasma discharges addressed here, the localized nature and atmospheric pressure operation allow for them to be used on components of already assembled devices which may not fit in a vacuum system or be vacuum compatible.

A requirement for many of these vacuum processing techniques is the creation of a non-thermal plasma (also called cold plasmas)[2]. In non-thermal plasmas, excitation and ionization of particles occurs mainly through electron impact, leading to a non-equilibrium distribution of energy. In plasma materials processing the non-equilibrium nature allows for the creation of active species to interact with the substrate without generating excessive heat which could destroy the substrate.[3] The creation of non-thermal plasmas of the same type as used in vacuum processing (called glow discharges) at atmospheric pressure is a challenge[10] due to several problems which arises due to the inherent decrease in collision lengths and increase in power density of glow discharges with pressure. First, this can lead to instabilities, an overheating of the discharge, transition to a thermal discharge and transition from the glow mode to an arc discharge.[1] The arc discharge with temperatures ~ 10000 K is unsuitable for most materials processing even if the arc is only transient. Traditional non-thermal atmospheric pressure plasmas such as coronas and dielectric barrier discharges solve the overheating problems by operating at low currents or limiting the current density through the use of dielectric

barriers respectively. But some limitations with these discharges occuring due to their spatial and temporal non-uniformities lead to another problem of deposition non-uniformity. The last problem, due to the increased collisionality at atmospheric pressures, is the increased formation of particles. At higher number densities, n, volumetric processes ($\sim n^2$) which lead to particle formation may overwhelm surface deposition events which are dependent on surface fluxes ($\sim n$). These problems can be summarized as 1) the creation of stable non-thermal plasma discharges 2) discharge uniformity and size, and 3) particle formation.

2.3.4. *Literature Review on Atmospheric pressure deposition*

There are several different approaches currently being researched to remedy these problems mainly relying on novel plasma discharges and deposition systems and comparisons of low pressure and atmospheric pressure deposited films indicate many similarities.[54] Atmospheric pressure plasma enhanced chemical vapor deposition (AP-PECVD) of thin films has been attempted for various materials including for example (but not limited to): silicon oxides and various glasses[55-57], titanium oxides,[58, 59] silicon,[60, 61] alumina,[62] hydrocarbons[12, 13, 63, 64], and fluorocarbons.[33] These various films have been deposited in turn by several different types of discharges including 1) helium glow DBDs,[12, 33, 55, 62, 63] 2) non-helium continuous wave DBDs,[56] 3) short (μs) pulsed DBDs,[60] 4) helium RF (13-27 MHz) afterglows (so called APPJs and cold torches),[57, 59] 5) helium RF (13.6MHz) CCPs,[58] 6) helium VHF (150MHz) CCPs,[61]

and 7) DC microplasmas.[13, 64] In most of these systems the deposition of uniform thin films without patterns, granules, particles, globules or significant (> 50nm) surface roughness requires significant use of helium buffer gas to maintain discharge uniformity and stability. For the helium based systems typically precursor concentrations are around 0.1% with typical deposition rates in the 0.2 to 2 nm/s range for the lower frequency DBD systems and as high as 15 nm/s for the RF and VHF CCPs and jets (it should be noted that the RF and VHF systems typically have significantly higher gas flow rates to help with discharge cooling). Among the non-helium based discharges reviewed clear evidence of the deposition of uniform thin films is not shown. Though nanosecond duration pulses seem effective for generating uniform DBDs[34, 65] in complex gases. It is not clear if the µs pulses of Matsumoto[60] are sufficient to ensure no discharge filamentation during deposition and some non-uniformity and surface roughness appears apparent from the images presented. Likewise sinusoidal DBDs generate film non-uniformities when the precursor concentration is too high (~>0.1%).[55, 56] For DC microplasma AP-PECVD of Ito et al[13] though precursor concentrations as high as 75% were tested and material was deposited, no evidence of the nature, uniformity or thin film quality of the deposits is presented. In addition device fouling and electrode destruction was noted during atmospheric pressure operation and it required operation at reduced pressures to attain more stable deposition. Another DC microplasma is shown by Sankaran[44] in which diamond particles are deposition at 100-500 Torr operation. Guo[45] also using a microplasma and shows deposition of amorphous carbon thin films but the system is actually a microsclae uniform DBD using helium gas and RF microplasmas at atmospheric pressure.

In summary the only successful application of PECVD at atmospheric pressure have required extensive used of helium >97% in the process gas to stabilized the discharge. The films produced with helium appear similar to those from low pressure systems and atmospheric pressure processing seems promising. It remains to be seen if the increased cost of helium use will outweigh the benefits of atmospheric pressure operation. Without the use of helium discharge operation appears too unstable to deposit thin films though the particle deposition observed may have interesting applications.

2.3.5. *Classification of Amorphous Carbon Films*

The hydrogen and methane precursors used in this study result in the deposition of various types of hydrogenated amorphous carbon (a-C:H. In the limits these might include sp^2 bonded graphitic material, sp^3 bonded carbon in the form of diamond, and various sp^3 bonded carbon hydrogen mixtures such as polymers), see figure 2.18. The deposited material is often heterogeneous and can contain mixtures of nano/micro crystalline diamond, graphite, amorphous sp^2 carbon, amorphous sp^3 carbon and polymeric (hydrogen containing) carbon. Depending on the relative concentrations of these components terms such as graphite like carbon hydrogenated (GLCH), diamond like carbon hydrogenated (DLCH), hydrogen containing polymer like carbon (PLCH) and tetrahedral amorphous carbon (taC) are used (although the nomenclature does vary somewhat in the literature)[66]. Typically if the H content is sufficiently low (<20%), the H is dropped from the name of the material.[67]
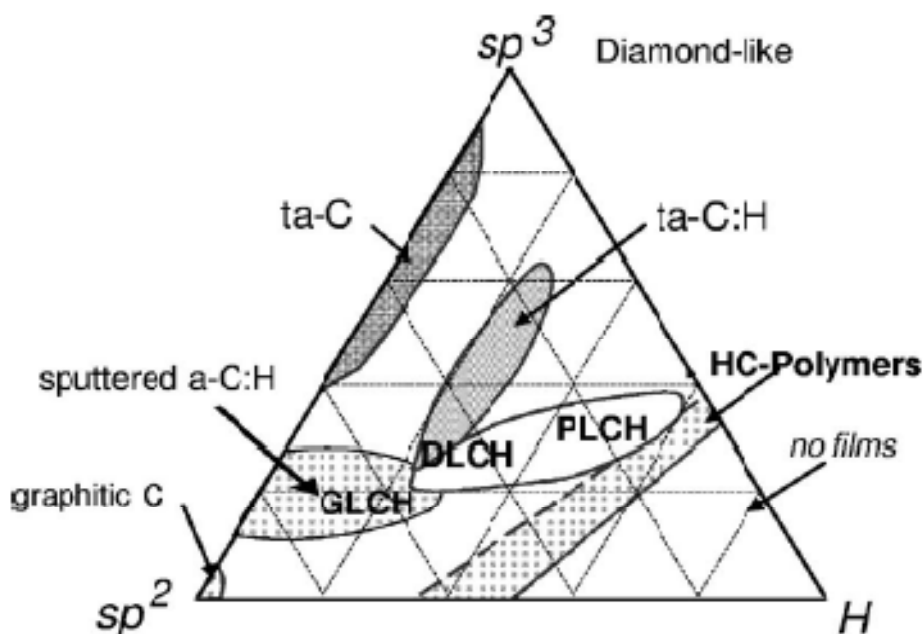
Figure 2.18: Classification schemes of amorphous carbon film dependant on carbon sp^2 or sp^3 content and hydrogen content.[49]

Typical PECVD using glow discharges result in materials which lie along the GLCH. DLCH, PLCH line. Films of ta-C:H and other materials are also can be formed using plasmas but with more tailored properties such as electron cyclotron wave resonance plasma sources and filtered cathodic vacuum arc and are beyond the scope of this discussion. In general in the low pressure PECVD of a-C:H[49] the energy of the ions controls the type of deposit. High energy ions generated by DC plasmas and RF CCPs with significant bias are used to generate GLCH. Without energetic ions PLCH are formed. DLCH are formed by moderate energy ions. The general theory is that the ions etch away hydrogen and provide energy to stitch together the sp3 bond forming a more uniform sp^3 bonded carbon. Too much ion energy though will remove all the hydrogen which helps to form the initial sp^3 structures.

3. Initial Characterization of a DC Atmospheric Pressure Normal Glow Discharge

3.1. Context

"*Characterization of a dc atmospheric pressure normal glow discharge.*" In the context of this dissertation, it was the first work to clearly demonstrate the DC microplasma as a type of normal glow discharge operating at atmospheric pressure. As a "normal glow," the characteristics of the micro-scale, plasma discharge could be understood by using scaling parameters from the well-known, low pressure, normal glow discharge. Some of the peculiar differences from low pressure glow discharges were also noted, but the general characterization as a normal glow discharge gave a framework for understanding these discharges. Toward the goal of AP-PECVD applications, this first step in understanding what type of discharge we were working with was necessary to determine what could be done with the system. This paper was widely accepted in the plasma research community due to its fundamental research into atmospheric pressure plasmas, and the use of optical emission spectroscopy temperature measurements. Since its publication, it has been cited more than 21 times.

3.2. Summary

Atmospheric pressure DC glow discharges were generated between a thin cylindrical anode and a flat cathode. Voltage-current characteristics, visualization of the discharge, and estimations of current density indicate that the discharge is operating in

the normal glow regime. Emission spectroscopy and gas temperature measurements using the 2nd positive band of N_2 indicate that the discharge forms a non-equilibirum plasma. Rotational temperatures are 700 K and 1550 K and vibrational temperatures are 5000 K and 4500 K for a 0.4 mA and 10 mA discharge respectively. The discharge was studied for inter-electrode gap spacing in the range of 20 μm to 1.5 cm. It is possible to distinguish a negative glow, Faraday dark space and positive column regions of the discharge. The radius of the primary column is about 50 μm and is relatively constant with changes in electrode spacing and discharge current. Estimations show that this radial size is important in balancing heat generation and diffusion and in preventing thermal instabilities and the transition to an arc.

3.3. Introduction

One of the most studied non-equilibrium plasma discharges is the low pressure normal glow discharge and its positive column and descriptions of such discharges can be found in many introductory plasma texts.[1] On the voltage vs. current diagram, the glow discharge corresponds to the region between the Townsend discharge and the arc discharge, where the discharge voltage remains essentially constant for varying plasma current. Glow discharges at higher pressures are hardly attainable due to instabilities which lead to a glow-to-arc transition (GAT) [10]. As the pressure is increased the current density increases until reaching the threshold for the development of instabilities leading to a transition to the arc phase. GAT is thus the transition from a non-thermal to a thermal discharge. There are generally two steps resulting in GAT: a) contraction and

thermalization of the discharge resulting from heating of the neutrals (Thermal or Ionization-Overheating instability[2]), and b) heating of the cathode resulting in transition from secondary electron emission to thermionic emission of electrons at the cathode. Generally the thermal instability is suppressed in low pressure discharges by cooling by the walls.

Methods to create DC glow discharges at up to atmospheric pressures have been reported. Fan [38] used water cooling of the electrodes and stable discharges were achievable in hydrogen and nitrogen at up to 2A. In air, though appearing as a stable glow, even at the lowest currents tested (~100mA) high frequency transitions between glow and arc were noted. Gambling and Edels [39], created glow discharges in air for currents between 10mA and 0.5A noting a stable arc above 0.5A. In a similar discharge in hydrogen [40] a transition from glow to arc was noted to occur at around 1.5 A. Several methods have been tried to stabilize the glow discharge and prevent glow to arc transition (GAT). Generally the thermal instability can be prevented if the gas residence time in the discharge is small compared to the heating time. Thus DBDs and pulsed coronas exist in non-equilibrium conditions when the discharge duration is shorter than the heating time. In DC coronas the heating time is long due to the small specific energy input. At high pressures discharges in atomic gases and lighter elements are typically more stable [38] probably due to faster diffusions times and slower energy transfer from electronic to translational energy modes.[2] In DC glow discharges at atmospheric pressure, high speed gas flows have been used to provide sufficient cooling of discharges at high pressures [69]. DC microhollow cathode discharges (MHCD) have been reported by Sankaran et al.[44, 70-72] and Stark and Schoenbach [73-75]. The MHCD of Sankaran is flow stabilized and

operates at up to 20 mA. Stark and Schoenbach operated the MHCD in atmospheric pressure air for current up to 22 mA. Stark and Schoenbach report the discharge being stabilized because the microhollow cathode supplies electrons to the positive column of the discharge rather than the instability prone cathode region as in a traditional glow discharge. RF discharges at atmospheric pressure have also been stabilized in MHCD again typically using gas flows and atomic or light species [76]. Akishev et al [77] have created diffuse atmospheric pressure discharges in the regime between the corona and spark discharges. The discharges are unique higher current corona discharges that fill the discharge gap and operate in a gas flow.

In this chapter, we report recent investigations showing the operation of glow discharges in atmospheric pressure air at lower currents than reported by Gambling and Edels [39]. At lower currents no fluctuating glow-to-arc transitions are seen and a glow discharge is observable without any surrounding diffuse glow as seen by Gambling and Edels [39]. At these currents the discharge is shown to be stable with diameters of about 100 μm. High pressure discharges stabilized by operating with small characteristic dimension have been termed microplasmas.[43] Current-voltage measurements, temperature measurements, visualization and parametric studies of the discharge show it to be a normal glow discharge.

3.4. Experimental Setup

The main characteristics of a plasma discharge such as the breakdown voltage, the voltage current characteristic, and structure of the discharge depend on the geometry of

the electrodes and the container, the gas used, the pressure in the chamber, the electrode material and the external circuit. Typical voltage current characteristic of DC discharges are highly nonlinear.[29] The circuit used to generate the glow discharge is similar to that used in low pressure glow discharges. Figure 3.1 is a schematic of the setup used for creating and analyzing the discharge. A DC power supply is connected in series to a ballast resistor, a shunt resistor, and the discharge. Various values of shunt resistor, ballast resistor, power supply polarity, and applied voltage were used depending on the regime of study. For studies in the normal glow discharge regime in air the shunt resistance was 1 kΩ and the ballast was 100 kΩ. The shunt resistor is connected to a voltmeter or an oscilloscope for DC or time dependant current measurements respectively. When necessary an operational amplifier was placed between the current shunt and voltage measurement device to provide high input impedance – low output impedance buffering or isolation from high voltages. For time dependant current measurements the current shunt was place between one electrode of the discharge and ground so the signal would not be affected by the inherent impedance of the ballast resistor or the frequency response of the operational amplifier. A high impedance (>10 MΩ) voltage probe or voltage divider was occasionally used to directly measure the discharge voltage and/or power supply voltage though typically the power supply voltage was set and the discharge voltage was calculated from the measured current and known resistance values.
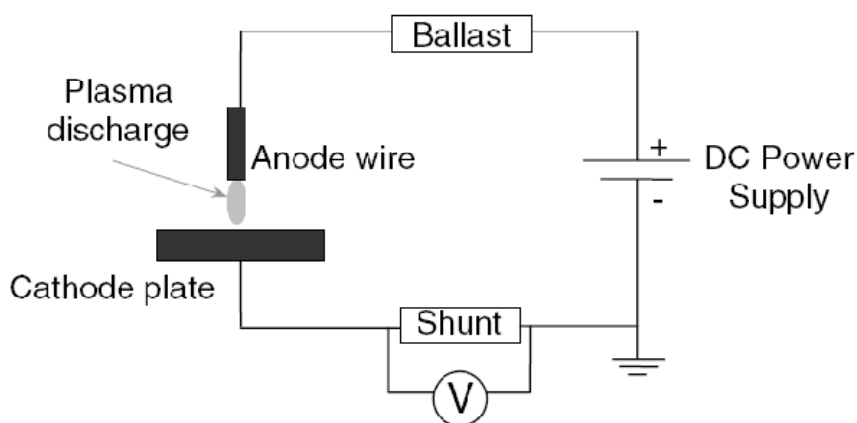
Figure 3.1: Electric circuit used to generate and analyze the glow discharge.

Figure 3.2 is a photograph of the experimental apparatus used. The discharge chamber is a 1" square x 2" quartz tube sealed with end caps and o-rings on top and bottom. On the top there are holes for the gas inlet, gas outlet and the wire electrode. The lower electrode is isolated from ground and made from stainless steel though other electrode materials can be affixed to cover the lower electrode. The upper electrode is a wire mounted to a three axis positioning stage. The vertical axis of the stage controls the spacing between the wire tip and the lower electrode and is adjusted by a motorized micrometer capable of 5 μm resolution. Various materials including iron, stainless steel, copper, brass, gold, graphite, and tungsten were used as wire materials. The gas inlet was connected to mass flow controllers and supplies of hydrogen, helium, or argon. For discharges in air the upper end cap could be removed.
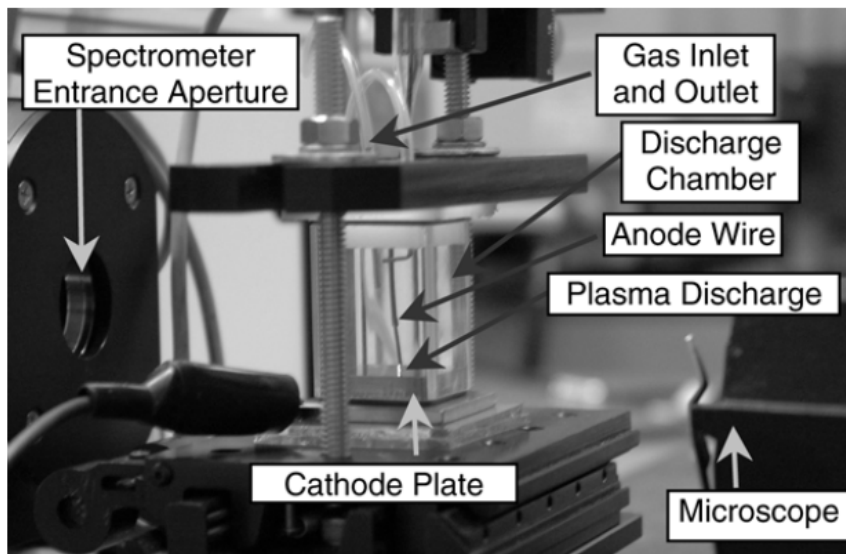
Figure 3.2: Photograph of the experimental setup

For visualizing the discharge a 640x480 resolution Sony CCD-iris color video camera was mounted to a microscope focused on the discharge. The microscope-camera setup provided a variable magnification allowing between a 2 mm x 1.5 mm and a 20 mm x 15 mm fields of view. The corresponding minimum pixel size at maximum magnification was thus about 3 μm. Still images from the CCD camera were captured digitally by a PC.

For spectroscopy an Acton Research SpectraPro 500i scanning monochromator was used. The entrance slit to the monochromator was placed near the quartz tube ~1" from the discharge facing the discharge. Optical emission spectra (OES) of the discharge were taken in a range of 200-450 nm averaging emission from the entire discharge. A Roper Scientific model 7430 CCD camera was mounted to the exit slit to digitally acquire the spectra at approximately 0.6 nm resolutions. Typical acquisition times for the

CCD images were 1-5 seconds. Background images with the discharge off were subtracted and a low pressure mercury lamp was used to determine the slit (apparatus) function and calibrate the spectrometer.

3.5. Experimental Results and Discussion

3.5.1. Discharge Visualization

Figure 3.3 shows a series of images of the glow discharge in air at increasing electrode spacing. The anode is the wire coming from the top of the image and the cathode is the surface along the bottom edge of the image. Breakdown voltages begin at around 500V for 50 μm spacing and increase with increased electrode spacing. For electrode spacings of 0.1, 0.5, 1 and 3 mm the voltages across the plasma required to sustain the discharge were 385, 430, 505, and 780 Volts respectively. Images (a), (b) and (c) were taken at the same magnification; image (d) was taken at a decreased magnification. Clearly visible in these images are the familiar bright and dark regions of a low pressure glow discharge. Beginning near the cathode we see the 'Negative Glow' region which maintains approximately the same length as the electrode spacing is increased. Moving up from the 'negative glow' we have the 'Faraday dark space' followed by the 'positive column'. The length of the 'positive column' increases with increasing electrode spacing. Of note is that the discharge does not completely cover the electrodes or fill the discharge volume. For the same discharge current and same gap spacing with differing electrode sizes the shape and size of the discharge are identical. Also the width of the 'negative glow' and 'positive column' increases to different degrees

with increasing discharge current (this result is quantified later). These general visualizations of our glow discharge match those of a low pressure normal glow. For a low pressure glow discharge in the region between the 'negative glow' and the cathode, termed the cathode sheath, there are typically several other bright and dark regions. From these images at atmospheric pressure the cathode sheath is unresolved and less than 10 μm in thickness. The occurrence of luminous and non-luminous regions is one of the major indications that the discharge is a non-thermal discharge. These images are similar to those of Gambling and Edels [39] except that at these low current no diffuse glow surrounding the primary column is seen.
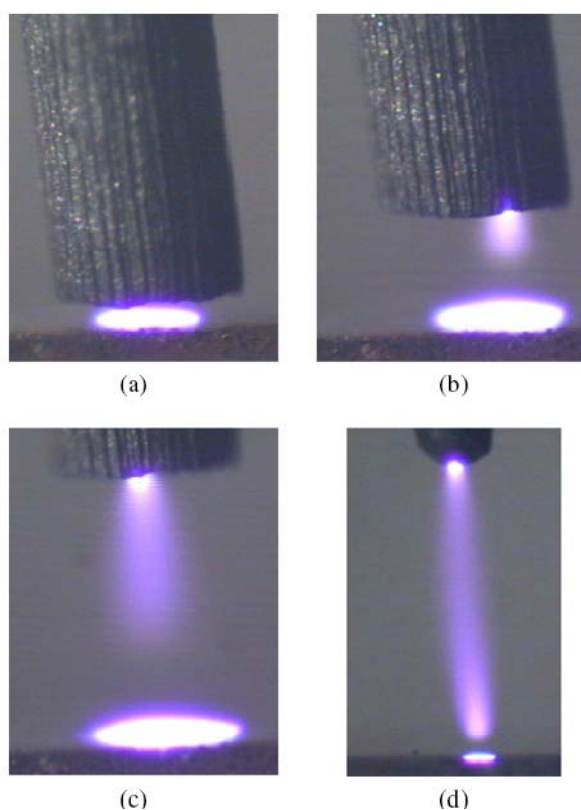
Figure 3.3: Images of glow discharge in atmospheric pressure air at (*a*) 0.1 mm, (*b*) 0.5 mm, (*c*) 1mm and (*d*) 3mm electrode spacings.

3.5.2. Current-Voltage Characteristics

Figure 3.4 is a plot of discharge voltage vs. discharge current for electrode spacings between 20 µm and 3 mm. Errors in the electrode spacing of ± 5 µm are due to thermal expansion of the wire and shortening of the gap at higher currents. Errors in current are ±20 µA and errors in voltage are less than 5 V. These plots are for a stainless steel anode and cathode, and with the upper wire electrode 0.8 mm in diameter as anode. The current was varied by changing the DC power supply voltage with a constant ballast resistor. Oscilloscope traces and Fourier power spectrums of the discharge current showed the current to be constant with no significant AC components other than a <1% 60Hz noise (probably from building) and a <0.1% ~50 kHz signal. Over the range of currents shown all of the discharges were similar in structure to those of Figure 3.3.
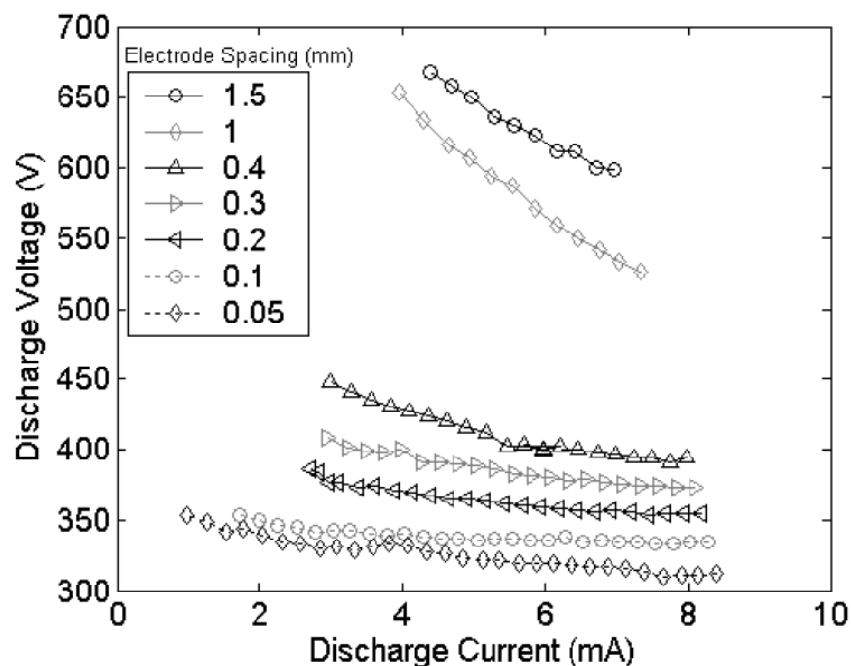
Figure 3.4: Voltage current characteristics for plasma discharge in air at several electrode spacings.

Generally there was no significant change of the I-V characteristics or discharge for different electrode materials or polarity. There are several notable exceptions to this for certain configurations: a) For thin (<100 μm) upper electrode wires and high discharge currents the upper electrode would melt. This only occurred when the wire was the cathode indicating that the heating occurred due to energetic ions from the cathode sheath and not resistive heating. b) For medium sized (~200 μm) wires as cathode, as the current is increased the width of the 'negative glow' increases until it covers the entire lower surface of the wire. If the current is further increased the 'negative glow' "spills over" the edge of the wire and begins to cover the sides of the wire. This affect is analogous to the transition from a normal glow to abnormal glow in low pressure glow discharges; however, there is not an increase in current density since the cathode area is not limited.

For sufficiently large electrodes wires this affect did not occur. c) In air discharges with oxidizable materials as the cathode the 'Negative Glow' moves around on the cathode electrode leaving behind a trail of oxide coating until no clean surface is within reach of the discharge and the discharge extinguishes.

Shown in Figure 3.4 are characteristics of the discharges corresponding to powers between 50 mW to 5 W. For the small spacing of electrodes the *V-I* characteristic is relatively 'flat'. This is consistent with the idea of this being a normal glow discharge and with past measurement in atmospheric pressure glows [38, 39]and MHCD operating in normal glow mode [74]. For a normal glow discharge in air the normal cathode sheath potential drop is around 270V,[2] the discharge voltage above that occurs mostly in the positive column. For the larger electrode spacing the *V-I* characteristics has a negative *dV/dI* and a negative resistance. This may be due to neutral gas temperature gradients along the positive column and will be explored further when considering discharges at higher current.

3.5.3. *Breakdown Characteristics*

The breakdown voltage to initiate the glow discharge followed the general trends of a Paschen curve. The *pd* (pressure x electrode spacing) at minimum breakdown voltage in air is about 0.5 cm-Torr. At atmospheric pressure this corresponds to an electrode spacing of about 7 μm. Due to dust, vibrations, and positioner inaccuracy the smallest spacing reliably achievable was 20μm. At higher *pd* than the minimum on the Paschen curve the

breakdown voltage is expected to be a logarithmic function of electrode spacing (for constant pressure = 760 Torr). The equation, $V_{br} = 940ln(d)+5750$, where d is the electrode spacing in cm and V_{br} is the breakdown voltage in Volts, fit our data to within 2% for d between 40μm and 1.5 mm.

The characteristics of the breakdown and the formation of the discharge were sensitive to the ballast resistor, the power supply polarity, and the electrode spacing. On the *V-I* characteristic curve at lower currents than the normal glow discharge, we typically have the Townsend discharge region, corona, and subnormal glow. *V-I* characteristics could be obtained for the Townsend regime and the corona regime when the wire electrode was negative. Figure 3.5a is a plot of the discharge current vs. time as breakdown occurs. For larger gaps and ballast resistors of 100 kΩ a high current spark initiates the discharge then the current decreases and a normal glow discharge is formed. Figure 3.5a is an image of the spark breakdown and glow discharge forming around it. The relaxation time is a function of the capacitance in the circuit. The peak current of the spark increases with larger gap distances. For small gaps the peak current is on the order of the glow discharge current and a spark breakdown is not visible. For large gaps the duration of the spark may be as long as 0.02 seconds and a single spark can be imaged. If a large ballast resistor is used insufficient current will be available and the discharge will breakdown, extinguish and then repeat. The rate of repetition is increases with decreased electrode spacing, decreased ballast resistance, and increased power supply voltage. This high current breakdown and repetition are similar to the 'streamer-like' pulsating seen in MHCD.[15] When the rate of repetition is on the order of 50 kHz the discharge does not completely extinguish and low amplitude current oscillations are observable. The

discharge in this mode appears as a less intense glow than shown in Figure 3.3. In vacuum glow discharges this mode is referred to as subnormal oscillations [78].
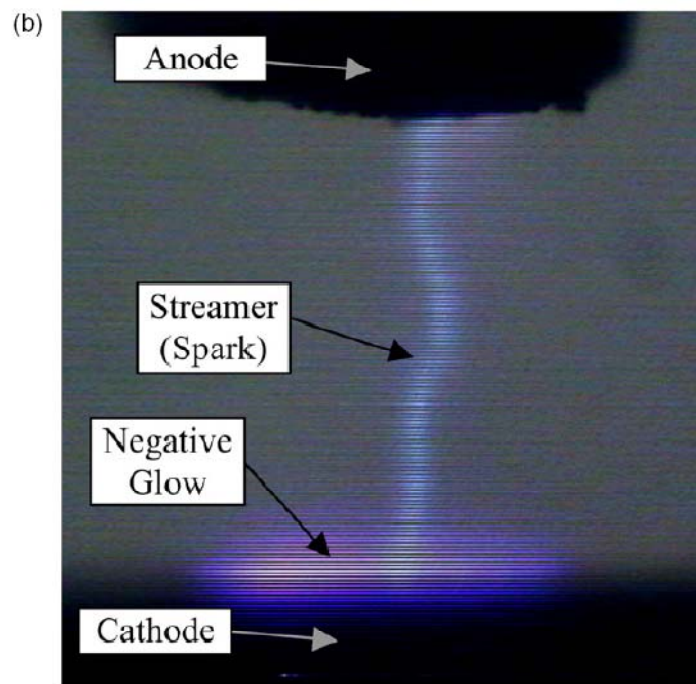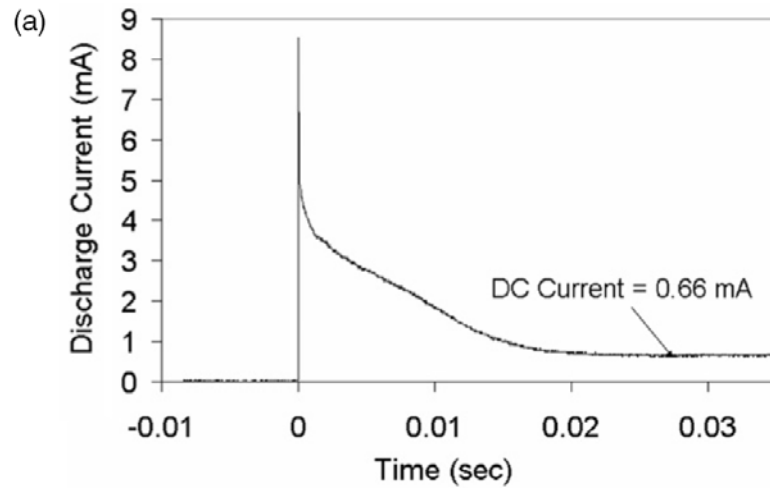
Figure 3.5: (*a*) Discharge current and (*b*) image during initial breakdown and formation of glow discharge.

Discharges with large d (>1.5mm) as shown in Figures 3d and 6 could be created in two ways. If a power supply with sufficient high voltage capability was used the discharge could be directly initiated. An alternative method was to initiate the discharge at smaller d and then extend the discharge by moving the upper electrode. Since the required breakdown voltage was not available in these cases the discharge was only marginally stable. A large disturbance, for example a significant gas flow, could extinguish the discharge. Larger discharge currents were more stable than smaller discharge current. There appeared to be a minimum current for a stable discharge which increased with d roughly following the trend as shown by the minimum currents in Figure 4.

3.5.4. Glow to arc transition

Figures 3.3 and 3.4 represent the discharge when operating in normal glow discharge mode. At larger electrode spacing and larger currents the discharge deviates from this normal behavior. Figure 3.6 is a series of images with increasing discharge current at an electrode spacing of 8.3 mm. The currents for images (a), (b), (c) and (d) are 6, 12, 25, and 33 mA respectively. These images correspond to points on the *V-I* characteristic in Figure 3.7. At larger electrode spacing the cathode spot begins to meander and the discharge bends similar to the non-stationary filamentary mode of Akishev.[77] As the discharge current is increased there begins to be a diffuse glow surrounding the positive column and spreading into the Faraday dark space which is whitish in color. This diffuse surrounding glow is probably identical to that seen by

Gambling and Edels [38, 39]. Image 3.6c is similar in form to that obtained for the MHCD with a third electrode extending the discharge [73]. At even higher currentssome orange color appears to emanate into the diffuse glow from the electrodes as the electrodes overheat.
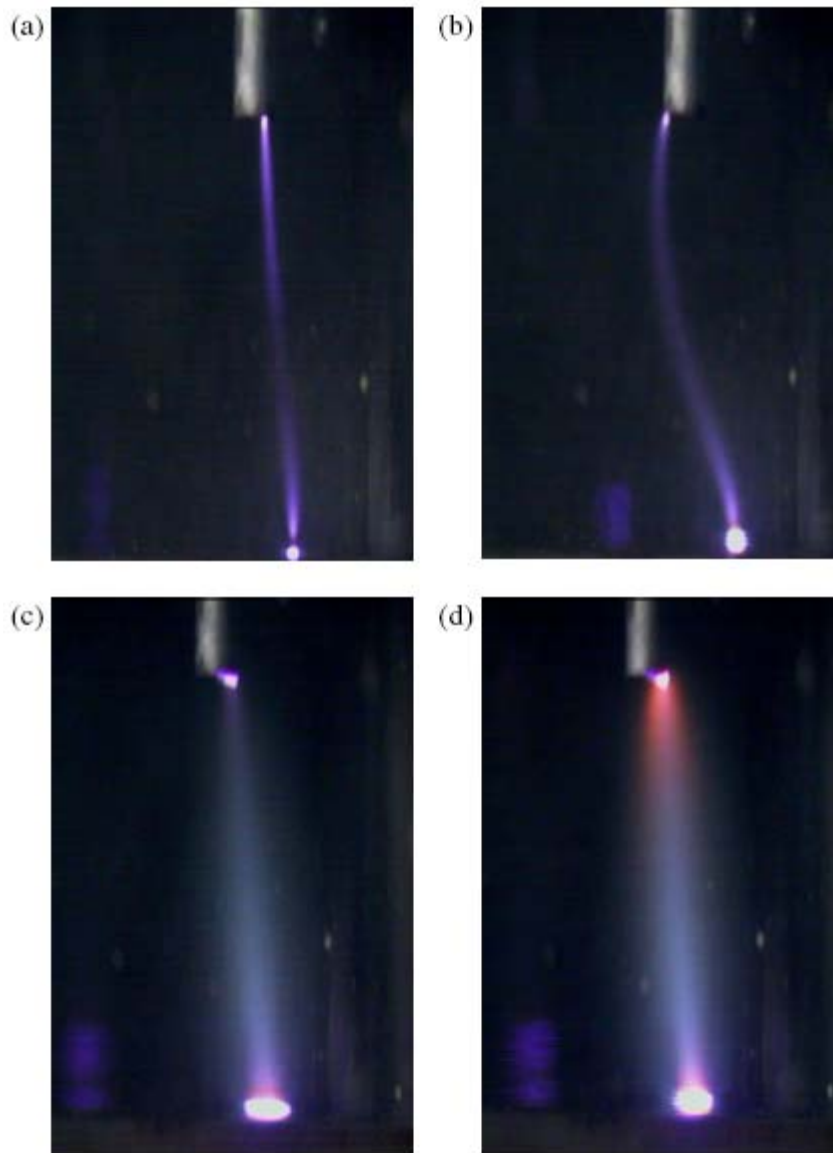
Figure 3.6: Transition from normal glow discharge to transitional discharge with increasing current (*a*)→(*d*). Images (*a*), (*b*), (*c*), (*d*) are 6 mA, 12 mA, 25 mA, and 33mA

discharge currents, respectively. Images correspond with points on the $V-I$ characteristic at 8.3mm electrode spacing in figure 7.

Figure 3.7 is a *V-I* characteristic encompassing the corona, normal glow, and high current glow transition regions for several gap spacings. The characteristic to the left of the normal glow region is similar to that achieved in vacuum DC discharges. The corona is only achievable when the polarity was reversed (thin wire as cathode) and when the gap spacing and breakdown voltage are large. Between the Townsend regime and the normal glow the discharge breakdown is unsteady as described above, data points on the figure are rms currents. The two separate curves at the same gap spacing correspond with a hysterisis between the breakdown conditions and sustaining conditions for the discharge. Continued operation in these regimes requires a ballast resistance of about 10 MΩ due to the significant negative resistance, *dV/dI*.
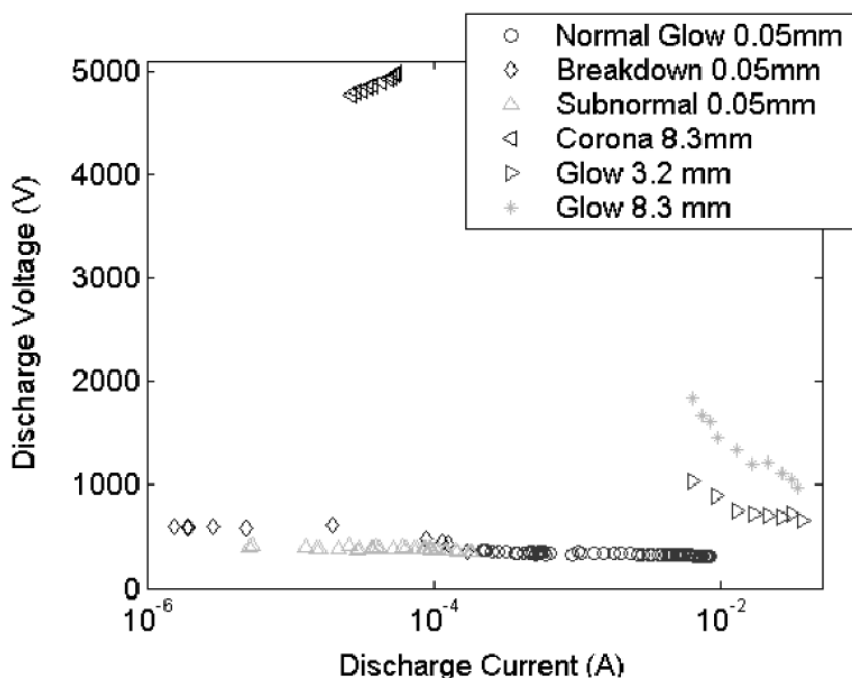
Figure 3.7: Voltage–current characteristic for discharge in air at atmospheric pressure encompassing corona, breakdown, subnormal, normal glow and initial GAT regimes.

The normal glow to arc transition region is different than on the traditional vacuum *V-I* characteristics. No abnormal glow region is noted because the cathode area is not limited. For the currents shown here a contraction of the discharge and transition to an arc is still not visible. There are two key properties that are different in arc and DC glow: the mechanism of ionization inside the discharge column and the mechanism of cathode electron emission. Transition between two regimes of ionization – from direct electron impact to thermal ionization – is smooth, and it can be determined by studying electric field-current dependence of the discharge column: the electric field is independent on current for direct electron impact ionization (glow discharge), and the electric field drops with current growth, negative *dV/dI*, for thermal ionization (arc

discharge). Transition from secondary electron emission to thermionic emission on the cathode is accompanied by relatively sharp drop on the dependence of discharge voltage on current. Previous works [38, 39] indicate this sharp drop does not begin until around 100mA.

Shown in Figures 3.4 and 3.7 are some regions of negative resistance. This is especially apparent at larger electrode spacing and smaller currents. This coincides with some canting and bending of the discharge visible in Figure 3.6. This is especially apparent at larger electrode spacing and smaller currents. Also visible in Figure 3.6a is a slightly darker region about midway in the positive column. Bending of the discharge would correspond with a lengthening of the primary column and a slight increase in the discharge voltage. The precise reasoning and physics for this is under investigation and may be related to thermal effects such as buoyancy, temperature gradients along the length of the positive column. The negative resistance regions seen in Figures 3.4 and 3.7 thus may not be GAT but rather other effects.

3.5.5. *Spectral Characteristics and Temperature Measurement*

Figure 3.8 is the Optical Emission Spectrum (OES) from the glow discharge in air between 200 and 450 nm. Conditions were: 3.8 mA discharge in air with 150 μm electrode spacing. Table 3.1 summarizes the lines registering with intensities greater than 1% of the maximum value and the corresponding identified transition. The identified transitions were calculated based upon vibrational constants [79]. The brightest lines between 300 and 450 nm are due to the nitrogen 2nd positive electronic transition N_2

($C^3\Pi_u$-$B^3\Pi_g$) and its family of vibrational and rotational level subtransitions. In the ultra violet region between 200 and 300 nm there are weaker NO lines from the NO ($A^2\Sigma^+$, v'-X, v") electronic transition. No OH line which exceeded the height of the tail of the N_2 2nd positive transitions was visible at 308 nm. Some significant N_2+ first negative, N_2^+ ($B_2\Sigma^+_u$-$X^2\Sigma^+_g$), transitions were also visible in the violet range. Additional spectra and transitions from air at higher wavelengths in the visible range could not be attained due to the tunable range of the 3600 grooves/mm, UV optimized, holographic grating used. The appearance of transitions with high (~4) initial vibrational quantum number in Table 3.1 is telling of a high vibrational temperature.
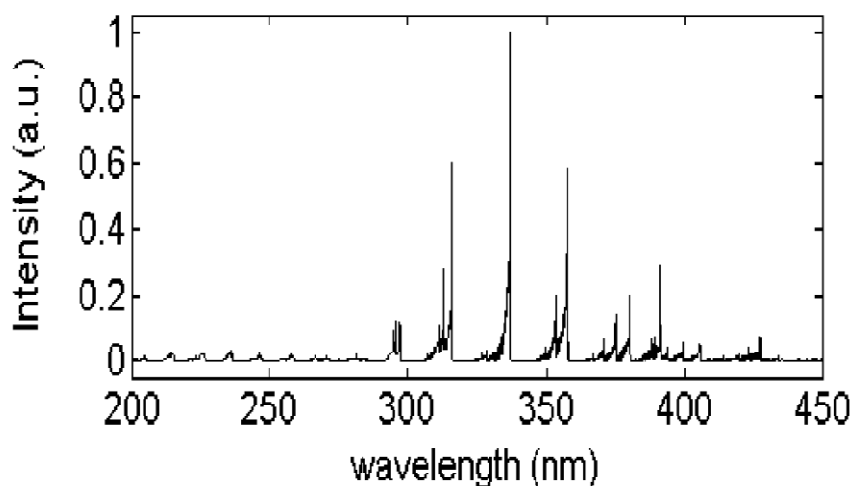
Figure 3.8: Spectra from the microglow discharge between 200 and 450 nm. Conditions are 3.8mA discharge in air with 150μmelectrode spacing.

Table 3.1: Significant spectral lines in atmospheric pressure air glow discharge.

Excited species	Wavelength (nm)	Electronic transition	Vibrational transition	Peak (%)
NO	204.7	$NO(A\,^2\Sigma^+, v'-X, v'')$	2–0	1.2
NO	214.9	$NO(A\,^2\Sigma^+, v'-X, v'')$	1–0	2.6
NO	226.2	$NO(A\,^2\Sigma^+, v'-X, v'')$	0–0	2.5
NO	236.3	$NO(A\,^2\Sigma^+, v'-X, v'')$	0–1	3.3
NO	247.1	$NO(A\,^2\Sigma^+, v'-X, v'')$	0–2	2.4
NO	258.7	$NO(A\,^2\Sigma^+, v'-X, v'')$	0–3	2.0
NO	271.3	$NO(A\,^2\Sigma^+, v'-X, v'')$	0–5	1.4
N_2	295.2	$N_2(C\,^3\Pi_u-B\,^3\Pi_g)$	4–2	9.7
N_2	296.1	$N_2(C\,^3\Pi_u\ B\,^3\Pi_g)$	3 1	12.7
N_2	297.5	$N_2(C\,^3\Pi_u-B\,^3\Pi_g)$	2–0	11.9
N_2	311.5	$N_2(C\,^3\Pi_u-B\,^3\Pi_g)$	3–2	10.3
N_2	313.4	$N_2(C\,^3\Pi_u-B\,^3\Pi_g)$	2–1	28.5
N_2	315.6	$N_2(C\,^3\Pi_u-B\,^3\Pi_g)$	1–0	60.1
N_2	326.6	$N_2(C\,^3\Pi_u-B\,^3\Pi_g)$	4–4	2.5
N_2	328.3	$N_2(C\,^3\Pi_u-B\,^3\Pi_g)$	3–3	3.1
N_2	330.8	$N_2(C\,^3\Pi_u-B\,^3\Pi_g)$	2–2	2.7
N_2	333.7	$N_2(C\,^3\Pi_u-B\,^3\Pi_g)$	1–1	7.6
N_2	337.0	$N_2(C\,^3\Pi_u-B\,^3\Pi_g)$	0–0	100
N_2	349.9	$N_2(C\,^3\Pi_u-B\,^3\Pi_g)$	2–3	4.1
N_2	353.6	$N_2(C\,^3\Pi_u-B\,^3\Pi_g)$	1–2	20
N_2^+	356.1	$N_2^+(B\,^2\Sigma_u^+-X\,^2\Sigma_g^+)$	2–1	14.6
N_2	357.6	$N_2(C\,^3\Pi_u-B\,^3\Pi_g)$	0–1	58.5
N_2	358.0	$N_2^+(B\,^2\Sigma_u^+-X\,^2\Sigma_g^+)$	1–0	5.4
N_2	367.0	$N_2(C\,^3\Pi_u\ B\,^3\Pi_g)$	3 5	2
N_2	370.9	$N_2(C\,^3\Pi_u-B\,^3\Pi_g)$	2–4	6.5
N_2	375.4	$N_2(C\,^3\Pi_u-B\,^3\Pi_g)$	1–3	14.0
N_2	380.4	$N_2(C\,^3\Pi_u-B\,^3\Pi_g)$	0–2	19.5
N_2^+	388.2	$N_2^+(B\,^2\Sigma_u^+-X\,^2\Sigma_g^+)$	1–1	6.6
N_2	389.3	$N_2(C\,^3\Pi_u-B\,^3\Pi_g)$	3–6	7.3
N_2^+	391.1	$N_2^+(B\,^2\Sigma_u^+-X\,^2\Sigma_g^+)$	0–0	29.13
N_2	394.1	$N_2(C\,^3\Pi_u-B\,^3\Pi_g)$	2–5	3.6
N_2	399.7	$N_2(C\,^3\Pi_u-B\,^3\Pi_g)$	1–4	5.5
N_2	405.8	$N_2(C\,^3\Pi_u-B\,^3\Pi_g)$	0–3	5.1
N_2	414.0	$N_2(C\,^3\Pi_u-B\,^3\Pi_g)$	3–7	12.7
N_2^+	419.7	$N_2^+(B\,^2\Sigma_u^+-X\,^2\Sigma_g^+)$	2–3	2.3
N_2^+	423.4	$N_2^+(B\,^2\Sigma_u^+-X\,^2\Sigma_g^+)$	1–2	3.6
N_2^+	427.5	$N_2^+(B\,^2\Sigma_u^+\ X\,^2\Sigma_g^+)$	0 1	7.7
N_2	434.3	$N_2(C\,^3\Pi_u-B\,^3\Pi_g)$	0–4	1.4

Figure 3.9 is the measured spectra and a curvefit using SPECAIR software [80, 81] at 10 mA discharge current. The strongest line is the N_2 2nd+ (0-0) at 337 nm and it overlaps with other lines in the 330 to 337 nm range as listed on the figure. The comb like peaks to the left of 337 nm corresponds to the rotational sublevels of the transition. The relative intensities of these rotational transitions are related to the distribution among

rotational energies of the nitrogen molecules. A Boltzmann distribution is assumed with a rotational temperature, T_{rot}. The rotational and translational temperatures, T_{tran}, were assumed equal. This should be valid considering the short times of rotational to translational energy transfer. The relative intensities of transitions with different initial vibrational energies are related to the distribution among vibrational energies. Again a Boltzmann distribution is assumed with a vibrational temperature T_{vib}. SPECAIR [80, 81], a spectroscopic modeling code developed by Stanford University was used to model the spectra from these transitions. A least squares curvefit between the modeled spectra and the experimental spectra was obtained using T_{rot} and T_{vib} as fitting parameters. The determined temperatures were 1550K and 4500K for rotation and vibration respectively. These temperatures indicate the non-equilibrium nature of the discharge and are close to the 1700 K – 2000 K rotational temperatures measured in a MHCD.[46]
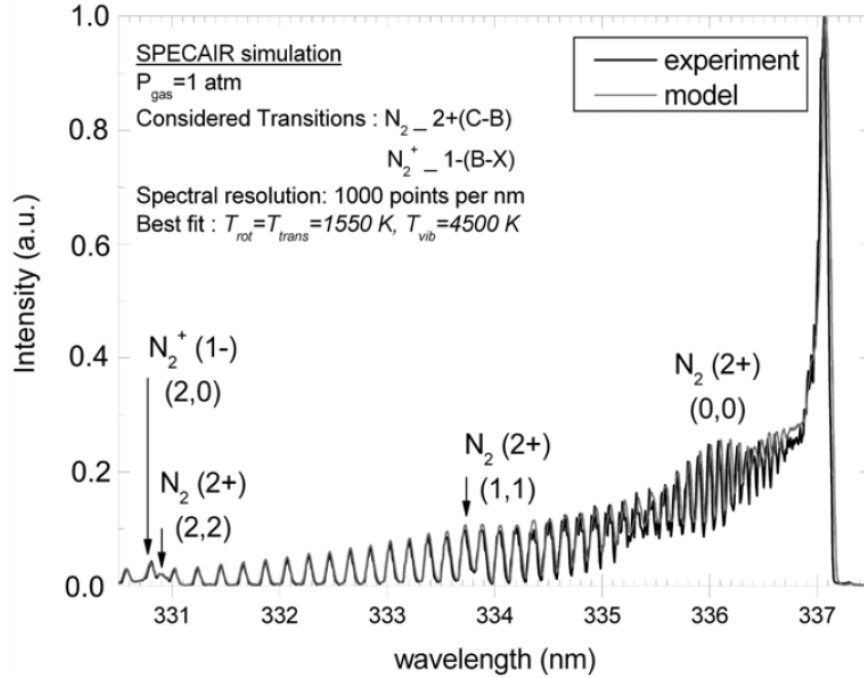
Figure 3.9: Measured OES and curve fit using SPECAIR for 10mA glow discharge in atmospheric pressure air.

Figure 3.10 is a plot of the measured and curvefit spectra for a 0.4 mA discharge in air. For this condition the inter electrode spacing was 50 μm. The temperatures determined by SPECAIR were T_{rot} =700 K and T_{vib} = 5000K. This discharge was very small in size and only the negative glow was visible. The lower temperature at a lower discharge current is to be expected since there is a corresponding decrease in discharge power and heating. The lower current operation is also more non-equilibrium T_{vib}/T_{tran} = 7.1 at 0.4 mA whereas T_{vib}/T_{tran} = 3 for the 10mA discharge current. This may also be expected since the rate of vibrational to translational energy transfer k_{VT} increases exponentially with T_{tran}: $k_{VT} = Bexp(-A'T_{tran}^{-1/3})$ [20].
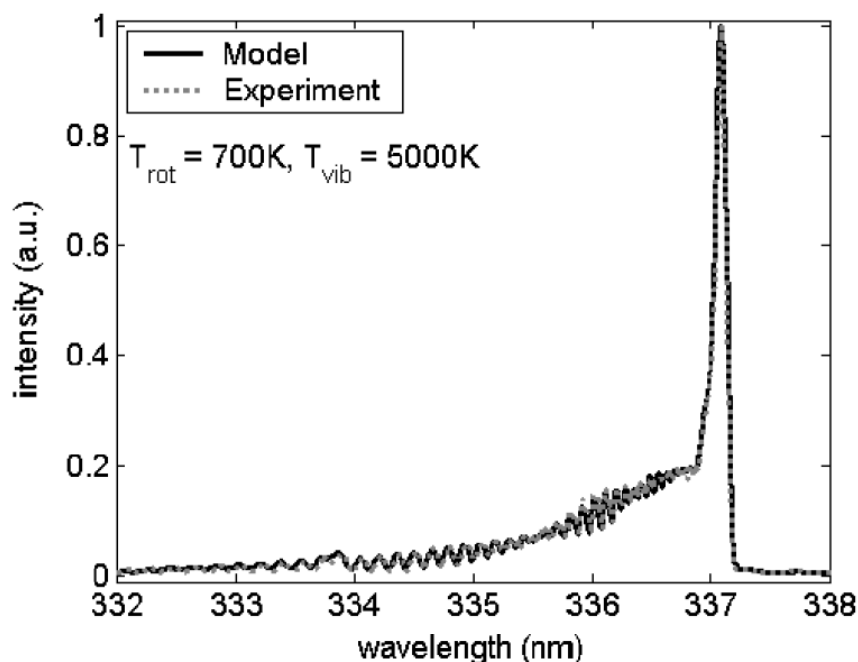
Figure 3.10: Measured OES and curve fit using SPECAIR for 0.4mA glow discharge in atmospheric pressure air.

The accuracy of the rotational temperature measurement is higher than the vibrational since many transitions were considered. The error in rotational temperature is less than 100K. Since only 3 vibrational transitions were considered for the vibrational temperature the errors are larger. Technically this temperature corresponds to the temperature of nitrogen in the initial electronic state of the transitions N_2 ($C^3\Pi_u$) and not to the majority of nitrogen which is in the ground electronic state. The ground state and excited state probably have similar rotational temperatures considering the high density however the vibrational temperature is not necessarily the same. The temperature measurements are also spatially averaged, and there may be variations within the negative glow and primary column. Also the temperature drops off rapidly outside the

discharge. A thermocouple placed 5 mm from the discharge measured an increase from room temperature of about 100K. This indicates temperature gradients greater than 2300K/cm.

3.5.6. *Current Density Measurements*

Images such as those shown in Figure 3 were used to estimate the dimensions of the positive column, and negative glow. For several different electrode spacing and discharge currents multiple images were taken. Background images were subtracted to isolate the glowing region of the discharge, and the microscope and camera were aligned to minimize reflections of the discharge on the cathode plate. In each image first the Faraday dark space was identified then the image was divided into negative glow and positive column regions. In each region the width was defined at the widest point by the number of pixels over which the grayscale intensity was 50% of the maximum intensity in that region. The cross sectional area of the discharge was then calculated assuming that the negative glow and positive column were cylindrical in shape. For multiple images at a single discharge current and gap spacing the widths were averaged. Using the measured area and discharge current the current density in the negative glow and positive column regions was calculated. This assumes that the region of electron current corresponds with the region of emitted light and probably slightly over estimates the current density.

Figure 3.11 is a plot of the width of the positive column and negative glow as a function of current for several different electrode spacings. Figure 3.12 is a plot of the current density in the positive column and negative glow as a function of current for

several different electrode spacings. As can be seen from Figure 3.12 the current density in the negative glow region is nearly constant at a value of about 6 A/cm^2 for currents between 2 mA and 8 mA. The occurrence of a constant or normal current density in the cathode region is another hallmark indicating that the discharge is a normal glow discharge. The positive column has increasing current density with increasing current and a slowly increasing size compared to the negative glow. In a low pressure glow discharge typically the positive column has the same current density as the negative glow or fills the entire discharge volume. The departure from the behavior of a low pressure glow discharge indicates that other effects are important in determining the size of the positive column and will be discussed in the analysis section.
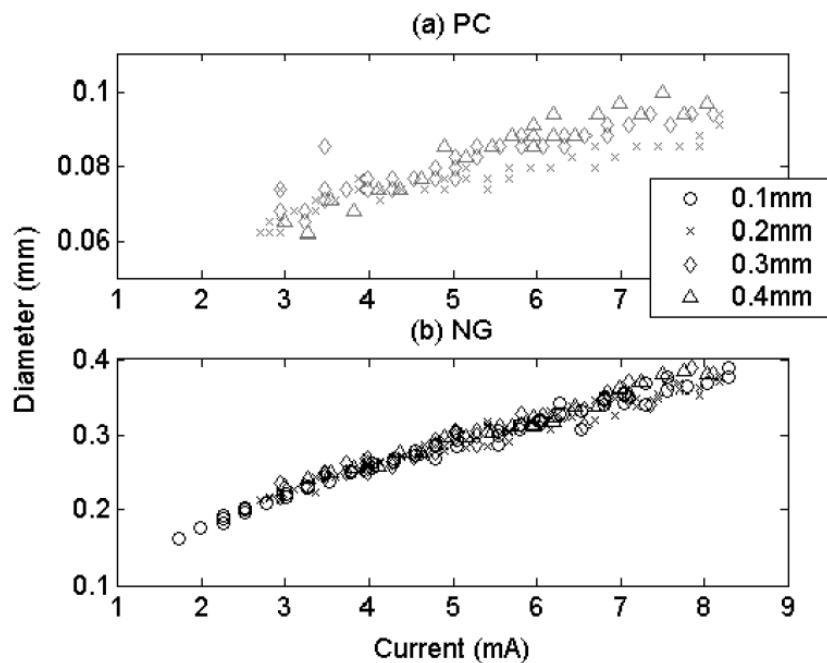
Figure 3.11: Plot of diameter of the positive column (PC) (*a*) and (*b*) negative glow (NG) regions of the microglow discharge as a function of discharge current for electrode spacing between 0.1 and 0.4 mm. At 0.1mm gap spacing the positive column was not visible. Discharge is in air and conditions correspond to those in figure 3.4.
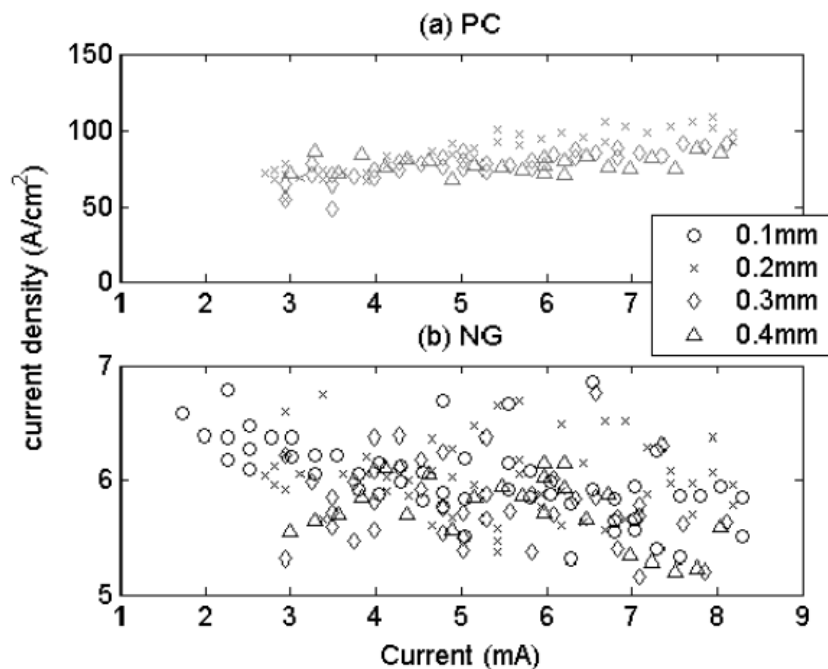
Figure 3.12: Plot of current density of the (*a*) positive column (PC) and (*b*) negative

glow (NG) regions of the APG discharge as a function of discharge current for electrode

spacing between 0.1 and 0.4 mm. At 0.1mm the positive column was not visible.

Discharge is in air and conditions correspond to those in figure 3.4.

3.5.7. Electric Field Measurements

From Figure 3.3 we see that at increasing electrode spacing the length of the

negative glow remains constant while the length of the positive column changes. This is

consistent with the discharge being a glow discharge and the electric field in the primary

column can be attained by measuring the change in discharge voltage as a function of

electrode spacing while maintaining the discharge current constant. Figure 3.13 is a plot

of the discharge voltage as a function of electrode spacing for three different discharge

currents. These curves are approximately straight lines indicating that the electric field is nearly constant. Some deviation from this straight line behavior was apparent at large electrode spacing due to canting of the discharge. Electric fields between 1 and 5 kV/cm were found and the electric field decreased with increased discharge current.
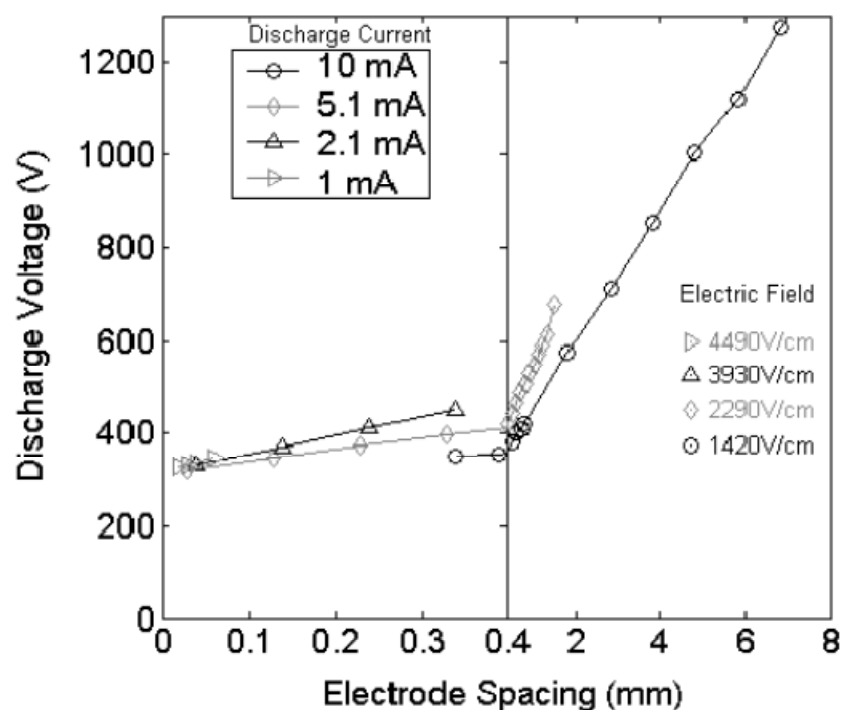
Figure 3.13: Discharge voltage as a function of electrode spacing for three different discharge currents. Also shown is the electric field in the positive column which corresponds to the best fit line. Note the change in *x*-scale at 0.4 mm.

3.5.8. *Discharges in helium, hydrogen and argon*

Glow discharges were also generated in Helium, Hydrogen and Argon at atmospheric pressure. Optical emission spectroscopy was used to take spectra of the

gases to ensure no trace amounts of air were visible for all the discharges and no significant N_2 lines were visible. Some significant OH lines at 308 nm were visible for the Helium and Hydrogen discharges, probably due to water absorbed on surfaces, however these could be lessen if care was taken to evacuate and purge the discharge vessel. Operation of the discharges in these gases was generally similar to the glow discharge in air. Some notable exceptions were: a) each gas has distinct discharge colors and spectral lines corresponding to the species b) in Helium and Hydrogen the scale of the discharge in every dimension was larger than that for a similar current discharge in air. c) In Helium the maximum electrode spacing achieved was 75 mm. d) in Hydrogen the primary column has standing striations for some conditions, probably of the same variety as seen in low pressure discharges. Figure 3.14 is an image of the standing striations in the hydrogen discharge at atmospheric pressure. e) In Hydrogen and Helium higher discharge currents could be achieved without transition to an arc or overheating the electrodes f) The Argon discharge was narrower and was prone to transition to an arc at lower currents than an air discharge.
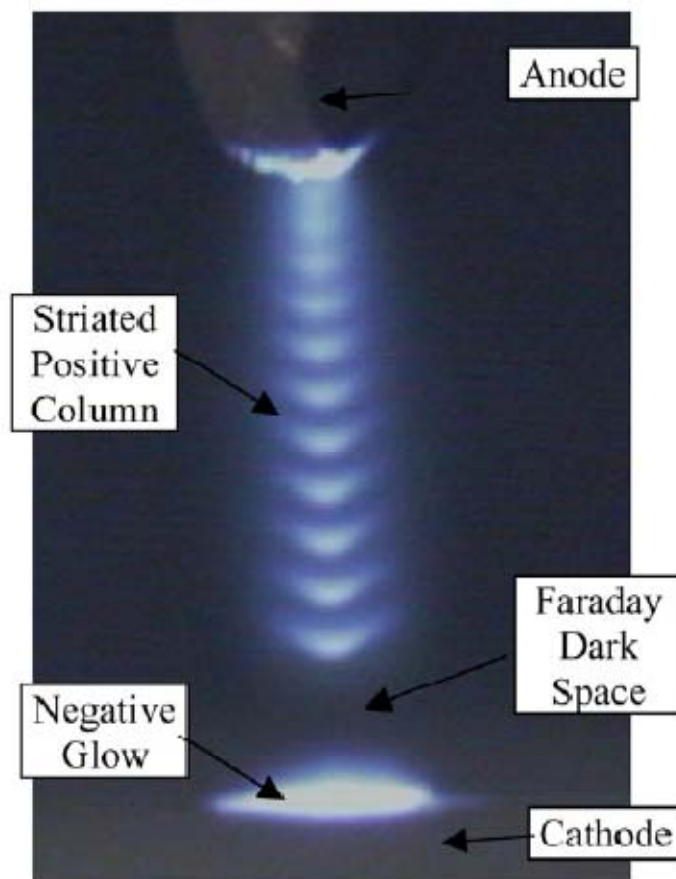
Figure 3.14: Image of the glow discharge in atmospheric pressure hydrogen. Positive column and negative glow are visible. In addition standing striations are visible in the positive column.

3.6. Analysis

3.6.1. *Normal Glow Discharge*

Based upon the various measurements detailed above, the discharge may be considered as a normal glow discharge. Significant analytical and heuristic formulations are available to describe the parameters of a low pressure normal glow discharge [3,4,

27]. In this section some of those formulations are compared to our experimental results. One caveat is that many of these formulations assume a room temperature gas 293K which is typical of low pressure glow discharges. Many of the heuristic invariants used in these formulations are listed as dependant on pressure p when in fact they are functions of gas density. At constant temperature this is not important however for variable temperatures as high as 1500K in the glow discharge this effect needs to be taken into account. The scaling with density instead of pressure and the variation with gas temperature was checked and taken into account when modifying these well known formulations for our atmospheric pressure glow discharge. The replacement of p in the relations by an effective pressure, $p_{eff} = pT_n / T$, was sufficient correction in most cases, where p is the pressure in Torr, T_n is the normal gas temperature (293K) and T is the actual gas temperature.

For example, consider the current density. The low pressure normal glow current density for Air and an iron electrode at room temperature from the literature[2] is approximately 300 $\mu A/cm^2$-Torr^2. The current density is given as proportional to the pressure squared. Taking into account the gas temperature and density dependence, the formula for the current density is modified to be: $j=j_np^2(T_n/T)^2$, where j_n is the normal current density at room temperature (300 $\mu A/cm^2$-Torr^2). For a discharge current of 10 mA, $p = 760$ Torr and $T = 1550$ K the calculated normal glow current density in the cathode regions is 6.52 A/cm^2. This is within the error bars on the measured temperature to the experimentally measured current density at that current of 5.8 A/cm^2. For our condition at 0.4 mA discharge current, and $T = 700$K, the current density was measured to be 33 A/cm^2. The analytically calculated normal current density is 31 A/cm^2. The non-

constant current density is still the normal current density because of changes in temperature. The correspondence between the experimentally measured current density and the normal glow current density is further evidence that the discharge is a normal glow discharge at atmospheric pressure. The normal cathode layer thickness and normal cathode potential drop are also consistent with our experimental results as discussed earlier.

Another parameter for comparison is the electric field, *E*. *E/p* for low pressure glow discharges is typically in the range of 10 to 30 V/cm-Torr.[2] Again using an effective pressure, electric fields at 760 Torr and 1500K should be in the range of 1.5 to 4.5 kV/cm. These values are consistent with those shown in Figure 3.4 for higher discharge currents. At lower discharge currents and lower gas temperatures the electric field would be expected to increase. *E/n* can also be determined from the discharge regime. If the electron density in the discharge is controlled by electron attachment, the frequencies of ionization and electron attachment which are both function of *E/n* will be equal. In air this occurs at $E/n = 13 \times 10^{-16}$ V/cm^{-2}.[2] At 1550K this corresponds to an electric field of 6.1 kV/cm, about a factor 4 higher than the measured value at 10 mA. If the electron density in the discharge is controlled by particle diffusion out of the discharge, the Engel-Steenbeck relation holds.[2] Taking into account the gas temperature of 1550K and discharge diameter of 50μm the electron temperature should be around 1.4 eV which corresponds with an E/n of 6×10^{-16} V/cm^{-2} and an electric field of 2.8 kV/cm considerably closer to the experimental value. This means that electron density in our 10 mA discharge is probably controlled by particle diffusion out of the discharge.

3.6.2. *Discharge Thermal Balance*

These estimations further indicate that the discharge is a normal glow discharge where charge losses are controlled be particles diffusion. Building on these estimations we explain the stability of the discharge. We can show that the discharge is stable due to its small size; neutral molecules are able to leave the volume of the discharge before they get too 'hot'. To estimate this, consider the diffusion time of a neutral out of a cylindrical volume and the heating time of a neutral in that volume. Calculations here correspond to the primary column of the discharge at 10mA with 500 µm electrode spacing. The time for a neutral to diffuse out of the discharge is the cooling time, τ_c, and is related to the diffusion coefficient, D, and the radius of the cylindrical volume, R: $\tau_{cooling} = R^2/(4D)$. D is proportional to the mean free path and the molecular speed and thus has a $T^{3/2}/p$ dependence. D is 0.147 cm^2/sec for N_2 in room temperature atmospheric pressure air [82].

The heating time for a single neutral is the inverse of the electron-neutral heating collision frequency, ν_{en}, which in turn is the electron density n_e times the rate constant for vibrational excitation of the neutral, k_{en}: $\tau_{heating} = 1/(n_e k_{en})$.For molecular gases like air the vibrational excitation of the molecule is the fastest mode of energy transfer between the electrons and the neutrals. For nitrogen and 1.2 eV electrons k_{en} is 5×10^{-9} cm^3/s. In the primary column of a glow discharge the current is mainly carried by the electrons and the electron density, n_e, can be estimated from the current density, j, and the electron drift velocity v_d: $n_e = j/(e v_d)$. The drift velocity is typically expressed as a function of, E/p, the reduced electric field, or if taking into account the effective pressure, ET/pT_n. Our, experimentally measured ET/pT_n in about 10 V/cm-Torr, and corresponding v_d is 5×10^6 cm/s. The current density, j, calculated before was for the negative glow. In the positive

column the current density may be controlled by other mechanisms, and the measured current density of about 100 A/cm^2 corresponds to a n_e of 1×10^{14}cm^{-3}. The heating time for the discharge is thus calculated to be 1.5 µs. Equating the heating and cooling time gives an estimate for the radius of a stable discharge at 35µm: $R^2 = 4Dev_d/(k_{en}j)$. The calculated radius of a stable discharge (35µm) and the experimentally measured discharge radius (55µm) are close. This indicates that the discharge is thermally stable probably due to its size.

3.6.3. Non-Equilibrium Discharge

These estimations can also be used to show why the discharge can sustain a non-equilibrium regime ($T_{vib}>T_{tran}$). In order for the discharge to be non-equilibrium, the energy gained in vibrational excitation should be greater than the energy lost by vibrational to translational (V-T) relaxation. Taking into account that at our conditions the fraction of atomic oxygen is small [32], for preliminary estimations N_2-O relaxation can be neglected and N_2-N_2 relaxation is the major mechanism. From a simple energy balance [2] the condition for operation in a non-equilibrium regime is that the ionization fraction, n_e/n, is greater than k_{VT}/k_{ev}. The rate of vibrational excitation is a function of the electron temperature and varies only slightly over the investigated discharge regime, $k_{ev} = 0.5 - 1.1$ x10^{-8} cm^3/s. As discussed earlier V-T relaxation is a strong function of gas temperature [20]. For the 10mA discharge k_{VT} is 10^{-16} cm^3/s and the ionization degree (10^{-6}) is several orders of magnitude greater than k_{VT}/k_{ev}. For the 0.4 mA discharge, although the ionization degree is lower, the translational temperature is also lower and thus the

relaxation rate is significantly lower and a higher degree of non-equilibrium can be maintained. The non-equilibrium relationship shows that the experimentally measured vibrational-translational non-equilibrium is provided by a high degree of ionization.

3.6.4. *Summary of measured and estimate discharge parameters*

Using the experimentally measured parameters of current density, temperature, and electric field, discharge parameters such as the electron density, reduced electric field, electron temperature, and ionization degree were calculated. T_e as a function of E/n, v_d, as a function of E/p_{eff}, k_{en} as a function of T_e and other relations were taken from [2] using data for air when possible and for N_2 otherwise. Electron density n_e was calculated from the current density as above. Table 3.2 summarizes these parameters for the discharges corresponding to the two conditions at which temperature measurements were made, 0.4 mA and 10 mA. As discussed these calculations show three things which agree well with our experimental results. The atmospheric pressure discharge: a) is a normal glow discharge, b) is thermally stabilized by it size and c) can maintain a high degree of vibrational – translational non-equilibrium. Thus, the discharge is an atmospheric pressure micro-size stabilized normal glow discharge with strong V-T non-equilibrium ('micro-glow').

Table 3.2: Measured and estimated discharge parameters in the APG discharge in air at

0.4 and 10mA discharge currents.

	Discharge current (mA)	
	0.4	10
Electrode spacing (mm)	0.05	0.5
Discharge voltage (V)	340	380
Discharge power (W)	0.136	3.8
Negative glow diameter (μm)	39	470
Positive column diameter (μm)	—	110
Electric field in positive column (kV cm^{-1})	5.0	1.4
Translational temperature (K)	700	1550
Vibrational temperature (K)	5000	4500
Negative glow current density (A cm^{-2})	33.48	5.8
Positive column current density (A cm^{-2})	—	105
E/n (V cm^{-2})	4.8×10^{-16}	3×10^{-16}
T_e (eV)	1.4	1.2
n_e in negative glow (1 cm^{-3})	3×10^{13}	7.2×10^{12}
n_e in positive column (1 cm^{-3})	—	1.3×10^{14}
Ionization degree negative glow	3×10^{-6}	15×10^{-7}
Ionization degree positive column	—	3×10^{-5}
Critical ionization degree k_{VT}/k_{en}	1×10^{-11}	3×10^{-8}

3.7. Chapter Conclusions

We have generated atmospheric pressure microplasma discharges in our laboratories. Several experimentally observed facts lead us to believe this is an atmospheric pressure normal glow discharge: a) Visualization of the discharge show distinct bright and dark regions corresponding to the 'negative glow', 'Faraday dark space' and 'positive column' of a glow discharge. b) Voltage-current characteristics of these discharges are relatively 'flat' and correspond to the regime of a normal glow

discharge. c) Current density measurements indicate a constant current density with increasing discharge current in the 'negative glow' region. Additionally, low pressure normal glow discharge analysis accurately matches our atmospheric pressure discharge. Correspondence is seen with experimentally measured values of the current density and electric field. The accurate application of normal glow discharge physics further indicates that the atmospheric pressure discharge is a normal glow discharge. Spectroscopic temperature measurements indicate that the discharge is a non-thermal, non-equilibrium discharge, with T_{trans} = 700K and 1550 K and T_{vib} = 5000K and 4500K respectively for the 0.4 mA and 10 mA discharges in air. Low pressure normal glow discharges are also non-thermal; however, gas temperatures are lower and typically near room temperature. For our discharge, calculations show that the non-equilibrium regime is maintained. Estimations also show that the non-thermal atmospheric pressure glow discharge is thermally stable because of its size. For ~ 100 μm diameter discharges the time for diffusion out of the discharge volume is on the order of the heating time within the volume.

A series of analyses which agreed well with experimental observations help us in understanding the discharge characteristics. For low currents and small gap length the discharge behaves as a normal glow discharge. The breakdown characteristics are also similar to low pressure discharges. However, explorations at high current (greater than approximately 20mA) and large electrode spacing (greater than approximately 1 mm) indicate that the discharge can appear less like a normal glow discharge without transitioning to an arc. At large electrode spacing the primary column begins to bend and

is only sustained with higher discharge voltages. At larger current the primary column appears as a diffuse glow.

4. Global Temperature Characteristics, Thermal Balance, and Temperature Measurement Techniques

4.1. Context

The non-thermal nature of these discharges is the most important characteristic for determining their usefulness in AP-PECVD. From the results of Chapter 3, we know these discharges to be non-thermal but warm. Temperatures are typically in the 700K-1500K range for air. Lower temperatures are required so as not to damage the substrates, and also to avoid the thermal mechanism of particle formation, thus ensuring a high quality film deposition. Given this, a significant effort was put into discovering what determines the temperature of these discharges. This chapter focuses on understanding the discharge temperatures through optical emission spectroscopy. Though, the work, also, has had an impact with respect to the diagnostic techniques developed. These results closely follow a paper published on this matter, "Spectroscopic Studies and Rotational and Vibrational Temperature Measurements of Atmospheric Pressure Normal Glow Plasma Discharges in Air."[83] This document focused on temperature measurement techniques, measuring global temperatures, the changes in temperature with discharge conditions, and how these relate to the overall heat balance for the system.

4.2. Summary

DC normal glow discharges were created in atmospheric pressure air for a pin to plate type geometry. The rotational and vibrational temperatures of the discharge were measured by comparing modeled optical emission spectra with spectroscopic

measurements from the discharge. The temperatures were measured as a function of discharge current, ranging from 50 μA to 30 mA, and discharge length ranging from 50 μm to 1 mm. Rotational temperatures from 400 K to 2000 K were measured over this range. Vibrational temperatures vary from 2000 K to as high as 5000 K indicating a non-equilibrium plasma discharge. Spectroscopic measurements were compared using several different vibrational bands of the 2nd positive system of N_2, the 1st negative system of N_2^+, and the UV transitions of NO. NO and N_2^+ transitions were also used to determine the electronic temperature and N_2^+ density. The discharge temperature appears to be controlled by two cooling mechanisms; 1) radial conductive cooling which results in an increase in temperature with increasing discharge current and 2) axial cooling to the electrodes which results in a temperature saturation with increase in discharge current. The measured discharge temperature initially increases rapidly with discharge current then becomes nearly constant at higher discharge current. Thus radial cooling appears to dominate at lower discharge currents and the axial cooling at higher discharge currents. The vibrational temperature decreases with increasing rotational temperature due to increase vibrational to translation relaxation but the discharge remains non-thermal and stable over the range studied. The discharge appears to have a maximum vibrational temperature at the low current limit of the normal glow regime.

4.3. Introduction

Atmospheric pressure plasmas have recently been developed which lie between the corona and arc regimes[77] [68, 84]. Due to *'pd'* and 'normal current density' scaling

these discharges are typically sub-millimeter in size. These 'microplasmas' [36] are non-equilibrium, but still warm, with characteristic gas temperatures measured between 1000 K and 2000 K [68, 77, 80]. We have shown [68] that many of these DC microplasmas are pressure and temperature scaled versions of the normal glow (NG) discharges observed in vacuum.

The exception to the similarity between low pressure normal glow (LPNG) and atmospheric pressure normal glow (APNG) discharges is that at atmospheric pressure the discharge that is not confined by side walls, and the gas temperature can no longer be considered constant and near room temperature. These thermal effects can significantly affect the physics of the discharges, the non-equilibrium nature, and their applicability for use in micro-fabrication and other processes [2]. For example, at constant pressure an increase in the gas temperature and corresponding decrease in density, n, and thus changes the reduced electric field, E/n, assuming constant electric field E. The reduced electric field in turn determines T_e and the rates of electron-initiated chemical reactions and ionization rates. Also an increase in the gas temperature exponentially increases the rate of energy transfer between vibrational and translational modes, thus decreasing the non-equilibrium nature of the discharge and promoting unstable transition to an arc. For some applications an excessive increase in gas temperature can be undesirable due to overheating of the substrate and increased molecular dissociation. In the complex reacting systems for materials deposition excessively high temperatures can also thermally initiate undesirable chemical reactions leading to particle formation, excessive dissociate of precursors or similar deleterious effects.

Detailed parametric temperature measurements are reported here for atmospheric pressure glow discharges in air. The goals were to find useful operating regimes, compile results for comparison to future modeling, and understand the nature of the temperature dependencies. Normal glow discharges in non-flowing air between effectively parallel electrodes was studied. This geometry may not be ideal for attaining low temperatures but was studied because of its fundamental nature and simplicity. More sophisticated electrode geometries and added gas flows [74] [77]can probably be viewed as variant of the DC normal glow discharge studied here. Air was studied because it is readily attainable, used in practical applications, and because air represents a working gas in which a stable and low temperature discharge is difficult to attain due to the presence of oxygen. The temperatures were measured using optical emission spectroscopy because the technique is non-intrusive, accurate over a wide range of conditions, and can differentiate between the temperatures of different internal energy modes.

4.4. Experimental Setup

Figure 4.1 is a photo of the experimental setup used. This experimental setup is similar to that used in our previous studies [68] although several improvements have been made. A thin wire anode is suspended over a planar cathode. Although this may traditionally be considered a pin to plate configuration the electrodes may actually be considered to be two planar electrodes for several reasons: the diameter of the discharge is several times smaller than the diameter of the anode electrode; an increase in the diameter of the anode wire does not change the characteristics of the discharge; the end

of the wire is flat, and the edges of the wire are rounded. The cathode plate was 25 mm square and 9.4 mm thick. The anode was 0.5 mm in diameter attached to a 12 mm diameter stainless steel anode holder which acts as a heatsink. The anode is fixed in place, and the cathode can be moved through a flexible bellows using a micrometer to change the inter-electrode spacing. The discharge chamber is a 10 cm cube with two quartz windows for spectroscopy and visualizing the discharge. The chamber is sealable and there are gas inlets and outlets for testing in a variety of pressures and discharge gases. In the studies for atmospheric pressure air no gas flow was used and the chamber was unsealed as shown in Figure 4.1.
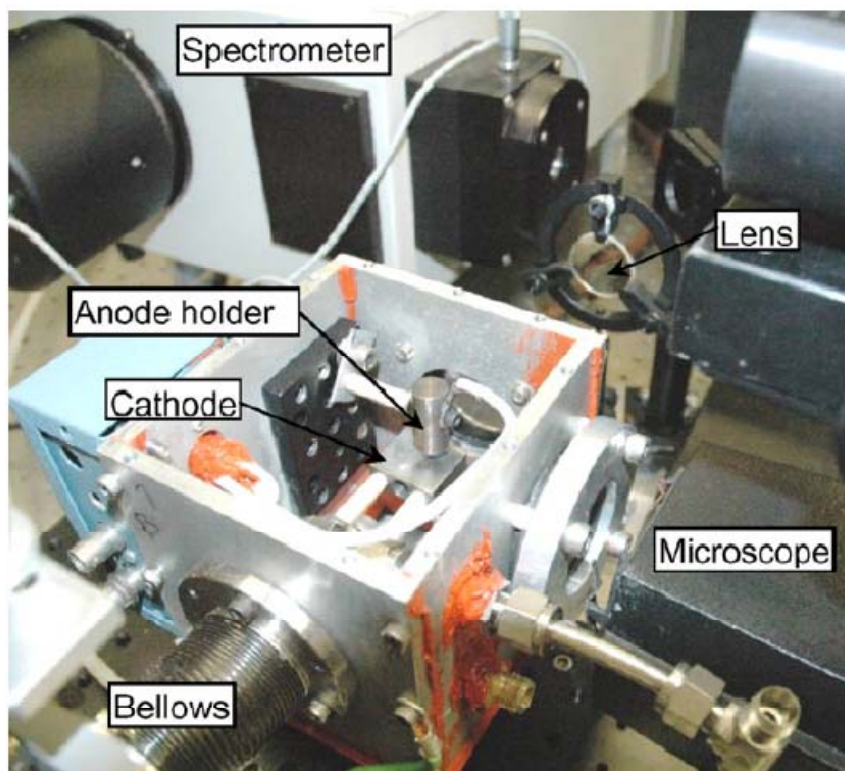
Figure 4.1: Photo of the experimental setup which shows the spectrometer, microscope, and discharge chamber.

The circuit used to generate the glow discharge is similar to that used before [68] and that used in low pressure glow discharges[1]. Figure 4.2 is a schematic of the circuit used for creating and analyzing the discharge. A dc power supply is connected in series to a ballast resistor, a shunt resistor and the discharge. Various values of shunt resistor, ballast resistor, power supply polarity and applied voltage were used depending on the regime of study. For studies in the normal glow discharge regime in air the shunt resistance was 100 Ω and the ballast was 200 kΩ. The ballast resistor acts to electrically stabilize the discharge circuit ensuring that the discharge current increases monotonically with an increase in power supply voltage. This is necessary since a DC electric discharge has a nonlinear voltage vs. current characteristic. The ballast resistor is placed physically close to the discharge in order to reduce the stray capacitance of the circuit and to improve the stability of the discharge. The shunt resistor is connected to an oscilloscope and is used to measure DC and low frequency current. A Pearsons model 2877 current transformer probe was connected inline to measure high frequency current oscillations up to 50 MHz. A BK-precision high impedance, 1000:1, high voltage (HV) probe connected to an oscilloscope is used to measure the discharge voltage and oscillations up to 1 MHz.
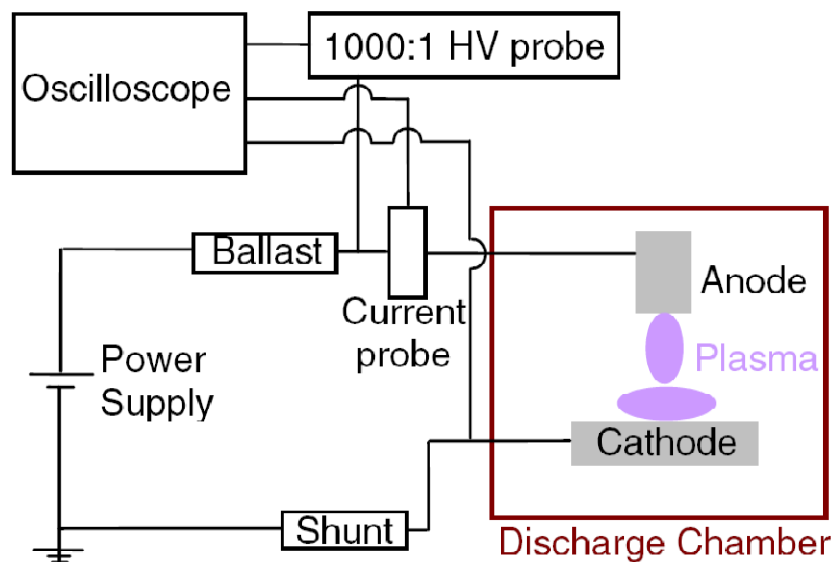
Figure 4.2: Schematic of circuit to generate and analyze the glow discharge

For visualizing the discharge a 640×480 resolution DIGITAL color CCD video camera was mounted on a microscope focused on the discharge. The microscope–camera setup provided a variable magnification allowing between a 2 mm $\times$ 1.5 mm and a 20 mm $\times$ 15 mm field of view. The corresponding minimum pixel size at maximum magnification was thus about 3 μm. Still images from the CCD camera were captured digitally by a PC.

For spectroscopy an Acton Research SpectraPro 500i scanning monochromator was used. Light from the discharge was focused onto the entrance slit of the spectrometer using a UV-lens and mirror as shown in Figure 4.1. Optical emission spectra (OES) of the discharge were taken in a range of 200–450 nm averaging emission from the entire discharge. A Roper Scientific model 7430 CCD camera was mounted onto the exit slit to digitally acquire the spectra at approximately 0.01 nm resolutions. Background images

with the discharge off were subtracted and a low pressure mercury lamp was used to determine the 'slit (apparatus) function' and to calibrate the spectrometer.

4.5. Spectroscopic Model and Best Fit Temperatures

SPECAIR [80, 85, 86] was used to model optical emission spectra (OES) and for the determination of the temperature by comparisons between the model and experimental spectra . SPECAIR is a FORTRAN program which can simulate the emission spectra of air in the ultra-violet (UV), visible, and near infrared (NIR) ranges. The emission spectra are functions of the temperature of the air and the relative population of different atomic/molecular species within the air mixture. SPECAIR is able to simulate air in non-equilibrium conditions. This is done by allowing the temperatures of translational, rotational, vibrational, and electronically excited states (T_{trans}, T_{rot}, T_{vib}, T_{elex}) to be arbitrarily specified. T_{elex} is the electronic excitation temperature which corresponds to the Boltzmann distribution among excited electronic states and may differ from T_e, the electron temperature which is the translational temperature of free electrons. SPECAIR can also simulate various air component mixtures since the relative population of the different species within air can also be arbitrarily specified. SPECAIR was originally used and validated in determining temperatures for thermal equilibrium and chemically non-equilibrium discharges in excess of 2000K. However the approach and the code have been used for thermally non-equilibrium discharges with temperatures approaching room temperature.[87-91]

SPECAIR calculates the OES by determining the population of the upper state of the transitions as determined by a Boltzmann distribution and the specified temperature of the internal energy mode. A collisional-radiative model is not used to determine the upper state populations from the ground state populations. The modeled transition probabilities are calculated based upon tabulated data for a given set of transitions. In the present calculations the following transitions were used: N_2 2nd positive system (N_2 $C^3\Pi_u \rightarrow B^3\Pi_g$), N_2^+ 1st negative system (N_2^+ $B^2\Sigma_u^+ \rightarrow X^2\Sigma_g^+$), and the NO β, γ, δ, and ε systems (NO $B^2\Pi \rightarrow X^2\Pi$, $A^2\Sigma^+ \rightarrow X^2\Pi$, $C^2\Pi \rightarrow X^2\Pi$, and $D^2\Sigma^+ \rightarrow X^2\Pi$, transitions respectively). From the calculated probability and population, the light emission intensity is calculated at the wavelength of the transition. A line shape is determined from the natural line width, thermal Doppler broadening and collisional broadening. The intensities from all calculated transitions and species are combined at each wavelength in a specified wavelength range. This 'narrow line' spectra is then convolved with the spectrometer 'slit function' to model the observed spectra.

In thermally non-equilibrium plasmas, because of their very nature, there are at least five temperatures T_{trans}, T_{rot}, T_{vib}, T_{elex}, T_e. These temperatures cannot be assumed to be equal nor can they be assumed the same from species to species. Even the often assumed conditions such as $T_{vib} = T_{elex} = T_e$ should not be assumed and in some cases have been directly shown to be incorrect [86]. The modeled spectra are sensitive to T_{rot}, T_{vib}, T_{elex} because the upper states of the emission transition have different electronic excitation energies, vibrational energy, and/or rotational energies. The population of the upper states is given by equation 3.1 [86] which assumes the internal energy levels follow Boltzmann distributions at T_{elex}, T_{vib}, and T_{rot} respectively. n is the population of the upper

state (denoted by ') with a given electronic excitation (*e*), vibrational (*v*) and rotational (*J*) quantum level. g_e and (*2J+1*) are the degeneracy (or statistical weighting) of the electronic excitation and rotational internal energy levels respectively, the vibrational level degeneracy is one. *L* is a line alteration factors due to nuclear spin and σ is 2 for homo-nuclear molecules and 1 for hetero-nuclear molecules. ε is the energy of the respective level. The summation in the denominator represents the combined rotational, vibrational and electronic excitation partition function.

$$n_{e'v'J'} = n_{total}\frac{L}{\sigma}\frac{g_e(2J+1)\exp\left[-\dfrac{\varepsilon_{e'}}{T_{elex}}-\dfrac{\varepsilon_{v'}}{T_{vib}}-\dfrac{\varepsilon_{J'}}{T_{rot}}\right]}{\displaystyle\sum_{e,v,J}g_e(2J+1)\exp\left[-\dfrac{\varepsilon_e}{T_{elex}}-\dfrac{\varepsilon_V}{T_{vib}}-\dfrac{\varepsilon_J}{T_{rot}}\right]} \quad \text{(eq 3.1)}$$

The term exp(-ε/T) in equation 1 represent the Boltzmann distribution. However, it is not always correct to assume that within a given internal energy mode the energy distribution function is Boltzmann. For rotational energy the assumption of a Boltzmann distribution with T_{rot} is accurate because the energy levels are closely spaced, and the characteristic temperature of the rotational energy mode is significantly less than the typical rotational temperature. For most species it can be assumed that the T_{rot} is close to T_{trans} and is effectively considered T_{gas} of the mixture because rotational-to-translational relaxation is fast at atmospheric pressure [86].

For vibrational and electronically excited states the temperature of the mode is on the order of the characteristic energy of the mode and assumption of a Boltzmann distribution can be inaccurate since the quantization of the states becomes important and the rates of specific paths of energy transfer from state-to-state need to be considered. The deviation from Boltzmann can occur in several ways. For example in certain vibrational systems Treanor distributions have been measured [2] due to preferential energy transfer to the higher vibrational states. A deviation from Boltzmann can also be due to the fact that OES only probes the states of electronically excited species. It is possible that the distribution functions are altered by the electronic excitation. For T_{rot} it has been shown the rotational distribution of the upper state is sufficiently similar to that of the lower state to have equal temperatures even with small changes due to the excitation [88]. For the T_{vib} and T_{elex} collisional-radiative models attempt to take into account such processes but were not used in our modeling. Another complication is that in atmospheric pressure plasma the de-excitation time of the electronically excited states is non-negligible in comparison to the time between collisions. For N_2 C-B transitions the de-excitation time is a few tens of nanoseconds and at atmospheric pressure the time between collisions is about one ns. For these reason it is only possible to speak of an apparent T_{vib} and T_{elex}. Although in practice when comparing the experimental rotational and vibrational line structure with Boltzmann computed distributions of the upper state there is fairly good superposition as shown later in Figure 4.4. In those cases the good superposition indicates that the Boltzmann assumption may be valid.

In summary these "temperatures" describe the relative population of different vibrational and rotational levels of C^3 state of molecular nitrogen. Rotational distribution

of C^3 state reflects the rotational population of ground state and gives information on the translational temperature of the gas. Vibrational spectra of second positive system cannot be directly associated with vibrational or translational temperatures of molecules. This distribution reflects interplay between the population by electon impact from different lower states and depopulation due to collisional quenching and radiative processes. Thus the vibrational distribution is a qualitative indicator for electron's temperature in the discharge region.

In the present study, the temperature measurements were made by comparing the modeled spectra with the experimental spectra. The accuracy of the fit was determined by the root mean square error (RMSE). The best fit corresponds to the RMSE closest to zero. The conditions of the discharge were determined to be those parameters which result in the best fit. The model fitting parameters were T_{trans}, T_{rot}, T_{vib}, T_{elex} and species concentrations. Depending on the spectral range the best fit might only be sensitive to a subset of these parameters.

Additional parameters which change the spectra are due to the experimental setup. Some of them are 1) wavelength offset due to spectrometer resolution and calibration, 2) wavelength dispersion due to spectrometer optics, 3) intensity offset due to background signal and noise, 4) changes in camera sensitivity and light transmission with wavelength, and 5) apparatus line broadening due to the dimensions of the slit entrance aperture. Items 1 to 4 can be taken into account by correcting the experimental measured wavelength, λ, and intensity, I. Assuming linear variations we have, $\lambda_{corrected} = \lambda + C1 + C2*(\lambda - \lambda_0)$, and $I_{corrected} = I + C3 + C4*(\lambda - \lambda_0)$, where $C1$ to $C4$ correspond respectively to the parameters described and listed as 1) to 4) above and λ_0 is

some reference wavelength (in our case the middle wavelength of the range). The scanning monochromator used can acquire the spectrum over an approximately 10 nm range in a single camera image. Over such short wavelength ranges assuming $C1$, $C2$, and $C3$ constant, and assuming $C4 = 0$ is reasonable. Longer wavelength ranges can be acquired by turning the grating and stitching together the images from different wavelength sub-ranges. For longer wavelength ranges $C1$, $C2$, $C3$, $C4$ are piecewise non-constant and can complicate correcting the experimental spectra. For simplicity and accuracy in most cases only normalized spectra were compared corresponding to a single camera image. The apparatus line broadening is taken into account by convolving the modeled natural (narrow-line) spectra with the slit function. The slit function was measured and then approximated using a pseudo-Voight function of the same characteristic full width at half maximum (FWHM). The range of uncertainty in these experimental parameters was reduced by using a mercury lamp to calibrate the spectrometer and measure the slit function. However, better fits to experimental data could be achieved by using C1, C2, C3 and the FWHM of the slit function as fitting parameters. This is because the slit function cannot be measure for all wavelengths and the calibration cannot be accurate over all wavelength ranges. The search for the best fit conditions was automated using a MATLAB routine based on the simplex search method [92]. This allowed for the rapid analysis of a large number of experimental spectra. The matlab program which was used to interface with the SPECAIR program and perform these automates analysis is detailed in appendix A.

4.6. Experimental Results and Discussion

Figure 4.3 is an image of the APNG in air for a current of 3.0 mA and an electrode spacing of 400 μm and is similar to those reported earlier [68]. The anode wire is visible in the top of the image and the cathode plane is visible at the bottom. Distinct features which characterize this as a normal glow discharge are: the bright region near the cathode, the negative glow; above that, the Farady dark space; and lastly the luminous positive column continuing to the anode. Due to *'pd'* and normal current density scaling, the characteristic sizes of the normal glow discharge are hundreds of microns when operating at atmospheric pressure. We see from this figure that although the geometry is pin-to-plate because of the small size of the discharge as described earlier it is effectively plate-to-plate.
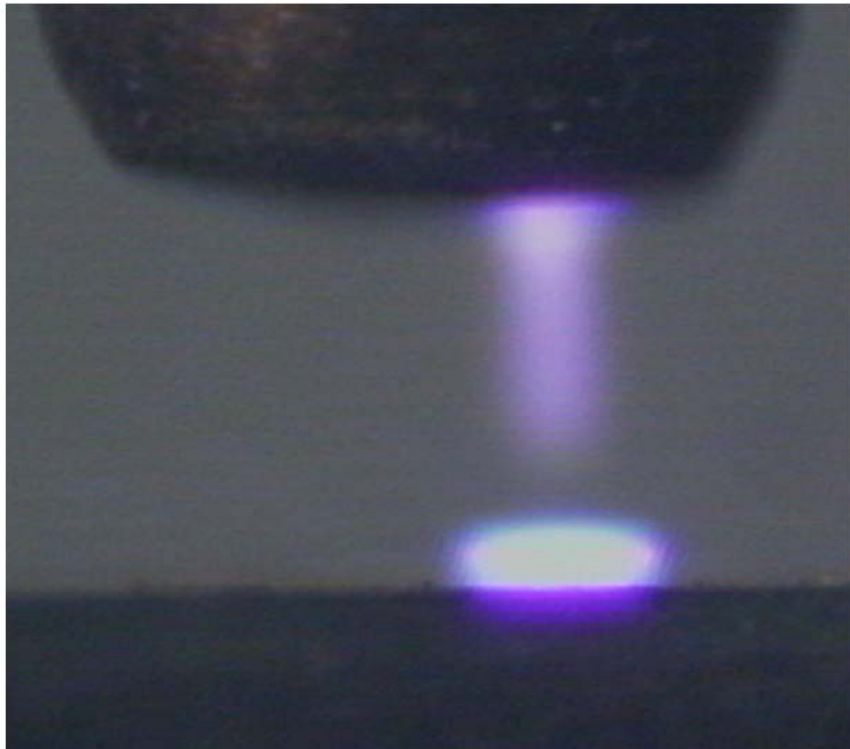
Figure 4.3: APNG in Air at 3.0 mA current and 400 μm electrode spacing.

These experimental results are reported in three sections. Section 1 focuses on calculating the error bars associated with the spectroscopic measurements and determining the best transitions to use for measuring T_{rot} and T_{vib}. Section 2 focuses on the use of the NO and N_2^+ transitions for determining T_{elec} and the relative N_2^+ density. Section 3 reports the results of a parametric study. T_{rot} and T_{vib} are measured as function of the discharge current and the electrode spacing. A discussion and explanation of the observed trends is also included in section 3.

4.6.1. *Spectral Sensitivity of Results*

Figure 4.4 shows the measured spectra and corresponding best fit modeled spectra for a 2 mA discharge and 300 μm electrode spacing for spectra centered at (a) 296 nm, (b) 313 nm, (c) 334 nm and (d) 375 nm respectively. These transitions correspond to different vibrational bands of the N_2 (C-B) transitions. These transitions were chosen because they represent regions of the spectra where the N_2 (C-B) transitions can be seen independent of transitions for different species and electronic states. These spectra are thus independent of species fractions and T_{elec}. The relative heights of two band heads with different initial vibrational quantum number are sensitive to T_{vib}. The vibrational band heads are labeled in the graphs. The band tails is due to sub-transitions between

different rotational quantum numbers and are the small frequent overlapped peaks decaying to left of band head in Figure 4.4. The relative height of the band head to the tail is sensitive to T_{rot}.
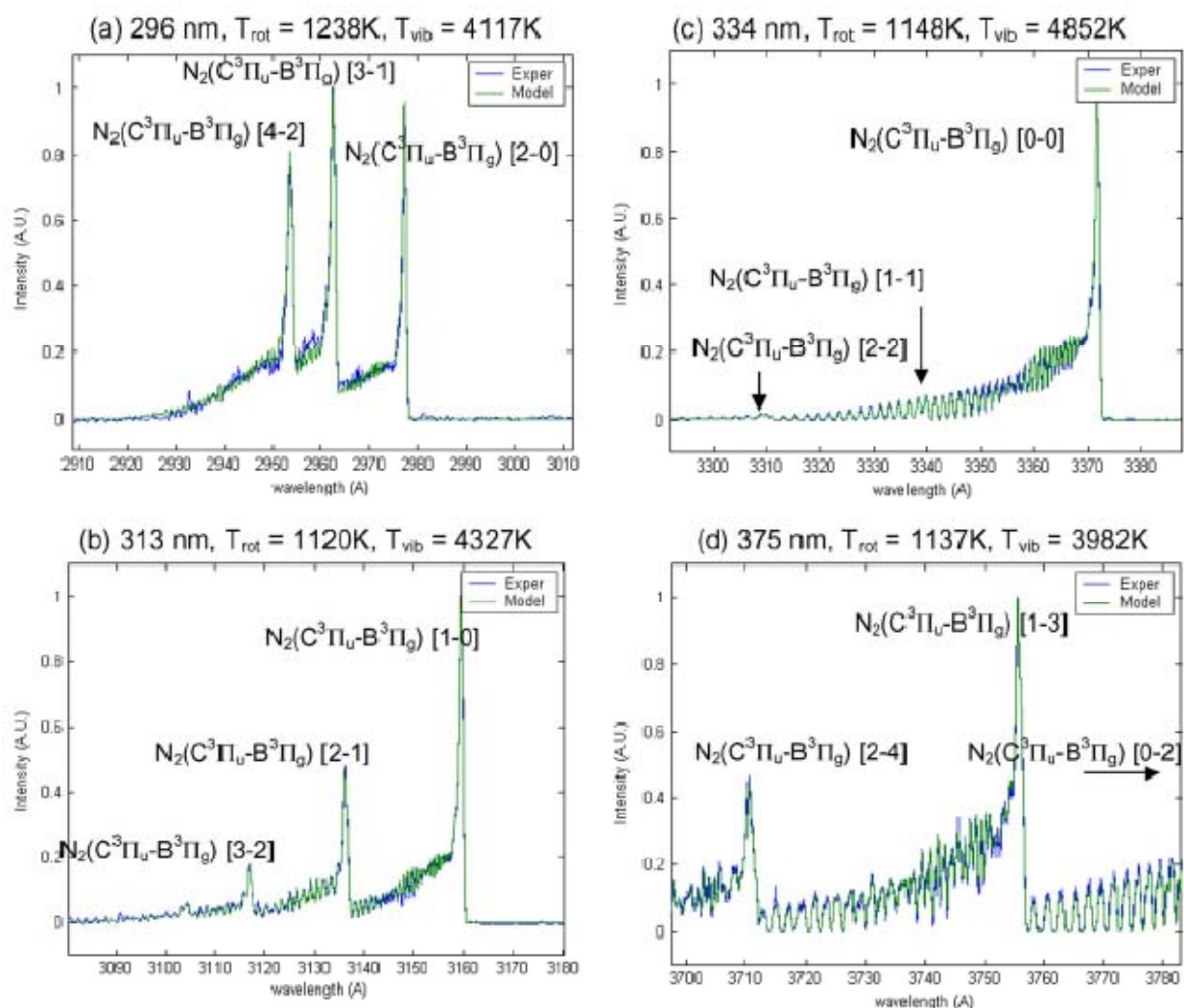
Figure 4.4: Measured spectra and corresponding best fit modeled spectra for a 2 mA discharge for spectra centered at (a) 296 nm, (b) 313 nm, (c) 334 nm and (d) 375 nm

The sensitivity of the fitting procedure and the precision to which the fitting parameters can be determined can be illustrated by plotting the RMSE value as a function of the fitting parameters. Figure 5 is a contour plot of the RMSE as a function of T_{vib} and T_{rot} for (a) the 334 nm and (b) 375 nm spectra. The best fit temperatures correspond to the minimum value of the RMSE, $RMSE_{bestfit}$. Comparisons of the fitting error, RMSE, to the statistical error, STD, where STD is the standard deviation of multiple experimental spectra, can be used to determine the sensitivity and precision of the spectral model with regards to the fitting parameters. In Figure 5 the contour plots of RMSE as functions of modeled T_{rot} and T_{vib} are shown. The contour corresponding to a value of $RMSE_{bestfit}$ + STD is the blue filled contour in the center and represents the conditions where the change in error between experiment and model is on the order of the statistical error in the data. Any T_{vib}, T_{rot} pair within this contour is within the errors of the measurements. Thus the width and high of the $RMSE_{bestfit}$ + STD contour can be used to determine an error bar for T_{rot} and T_{vib} respectively. We calculate that at 334 nm the T_{vib} cannot be precisely determined (worse than +4000K/-2000 K) and T_{rot} can be determined to within ± 39 K. For the 375 nm spectra the precision in determining the temperatures were ± 130 K and ± 37 K for T_{vib} and T_{rot} respectively. The developers of SPECAIR use an accuracy of ± 50 K [80] for rotational and vibrational temperature. The total error is due to both inaccuracies of the model and imprecision of the experiments. For measurements using the 375 nm spectra the error bars for vibrational temperature determined are less than ± 180 K; the error bars for rotational temperature are ± 87 K. Another matter illustrated by figure 5b is the 'line of approach' to the best fit rotational and vibrational temperatures (as shown by the dashed lines and represent either the best fit T_{rot} for a

given T_{vib} or the best fit T_{vib} for a given T_{rot}); when parallel to axes this indicates that the best fit T_{rot} and T_{vib} are decoupled. The search routine to find the best fit temperatures is expedited by taking this into account.
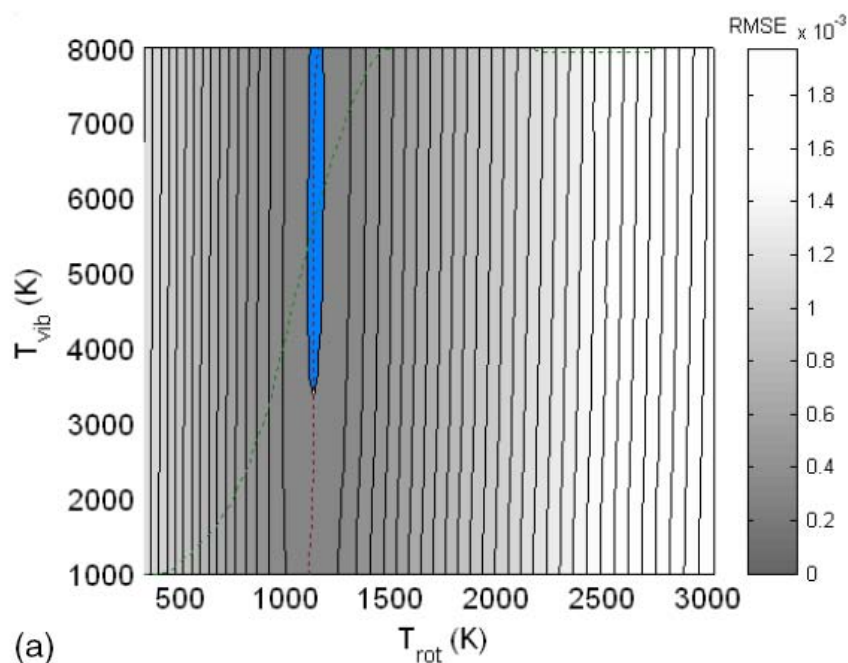
(a)
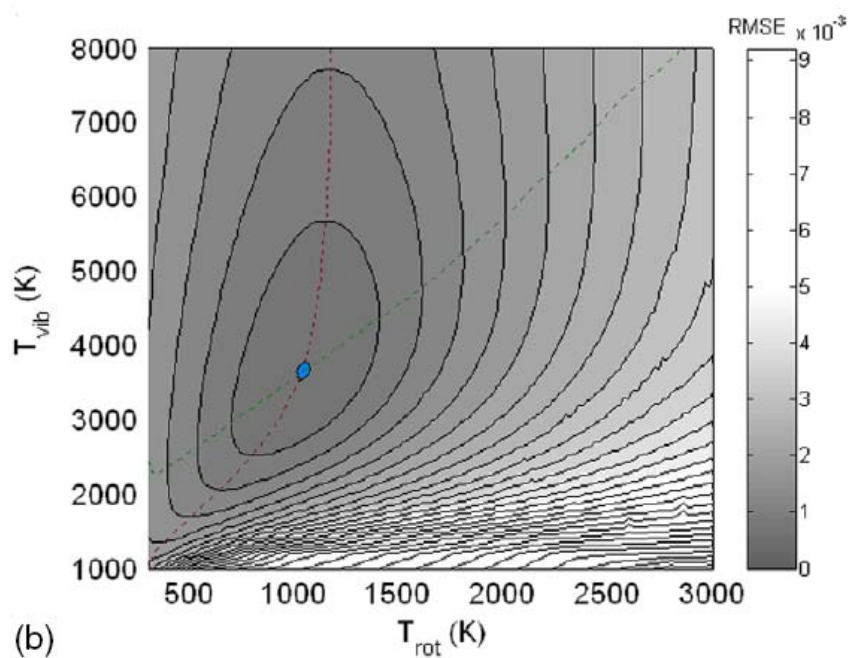
(b)

Figure 4.5: Contour plots of RMSE as a function of modeled T_{rot} and T_{vib} for spectra around (a) 334 nm and (b) 375 nm attained from a 2 mA discharge and 300 μm electrode spacing.

Figures 4.6 and 4.7 are plots of the rotational and vibrational temperature as a function of discharge current comparing measurements using the four spectra ranges shown in Figure 4.4. The error bars were calculated for each spectra range as described above. As can be seen the measured temperatures are within the error bars of measurements using other transitions. For the majority of the temperature measurements made later in this paper the transitions around 375 nm were used because they could most precisely determine both T_{rot} and T_{vib}. Compared to the transition at 334 nm, the transition at 375 nm provides a significantly more precise T_{vib} since several strong vibrational transitions are compared. Compared to the transitions at 296 nm and 313 nm, the transition at 375 nm is more intense and the spectrometer has higher resolution resulting in slightly better determination of both T_{vib} and T_{rot}. From these measurements we see that the discharge is non-equilibrium $T_{vib} > T_{gas}$ over a range of discharge currents.
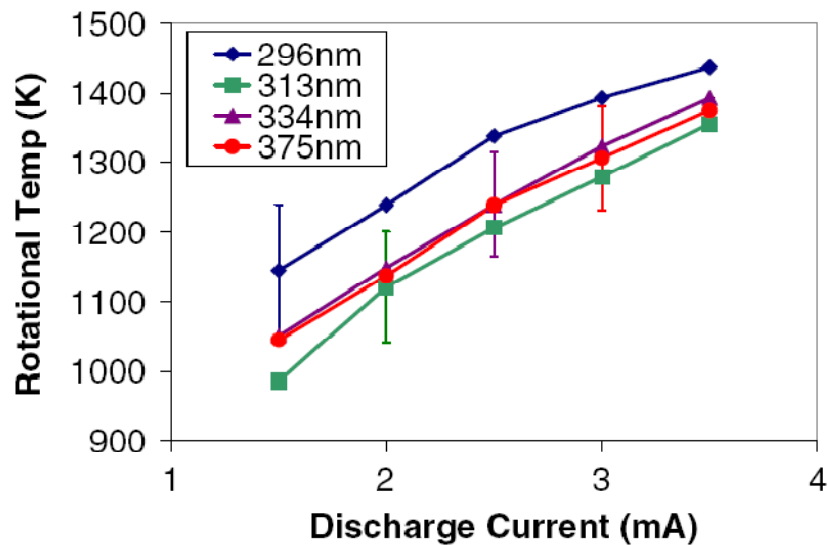
Figure 4.6. Plot of Trot versus discharge current comparing results using different vibrational transitions of the N2 2nd positive system.
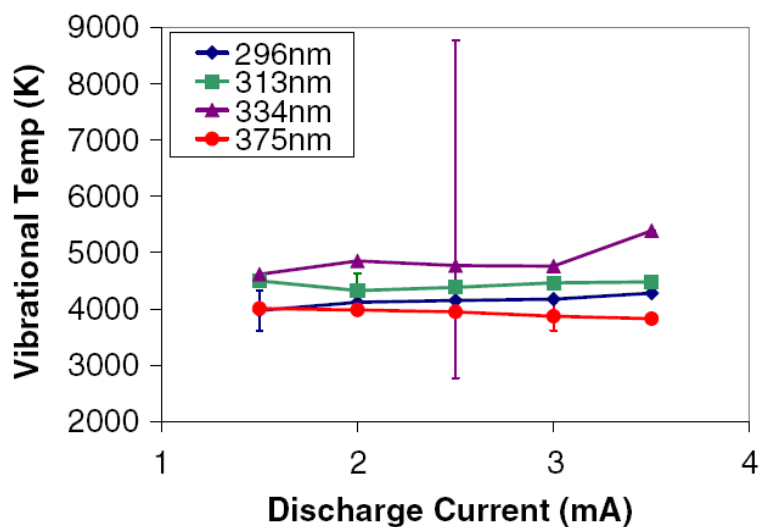
Figure 7. Plot of Tvib versus discharge current comparing results using different vibrational transitions of the N2 2nd positive system. Error bars given for one point are indicative of the entire curve.

4.6.2. Measurements of electron temperature and ion density

NO transitions in the range from 218 to 228 nm were use to determine the vibrational, electronic, and rotational temperatures. The strongest lines in this range is due to the γ transitions, also weaker but significant are the β, δ and ε transitions. Each of these transitions has a different initial electronic state and so the OES is sensitive to T_{elex}. Within the γ transitions there are different vibrational levels and rotational levels and thus the spectra are sensitive to T_{rot} and T_{vib}. Figure 4.8 is a plot of the modeled and experimental spectra for a 3.8 mA discharge in air with electrode spacing of 300 μm. The best fit temperatures were $T_{\text{rot}} = 2200$ K, $T_{\text{vib}} = 4077$ K, and $T_{\text{elex}} = 4074$ K. The rotational temperatures measured are higher than for the same discharge using the N_2 lines around 375nm. This may be due to the fact that NO is produced as a result of chemical reactions and residual chemical energy may manifest itself as elevated temperatures[93]. That T_{elex} and T_{vib} are measured to be equal is a very interesting. It should be restated that this T_{elex} corresponds to the distribution of electronic energy among the excited states (A, B, C, D) and not the electronic temperature relative to the ground (X) state. One might expect that $T_e = T_{elex}$ since the electronically excited states are attained by collision with electrons and should mirror the electron energy distribution function. However, in atmospheric pressure plasmas lower excitation temperatures as in our case with T_{exec} near T_{vib} are measured [91, 94]. Such non-equilibrium systems may be classified as ionizing systems [95] where excitation and ionization exceed recombination and radiative decay. Excitation and ionization is balanced by particle diffusing from the plasma region. There is thus a net upward flow in excitation space and results in an over population of the ground state and low-level electronic states relative to the equilibrium population. This over population would be perceived as a lower T_{elex}. A lower bound on T_{elex} of T_{vib} might occur due to

collisions and vibrational–excitation energy transfer; however, such complexities in molecular systems such as air are poorly understood.
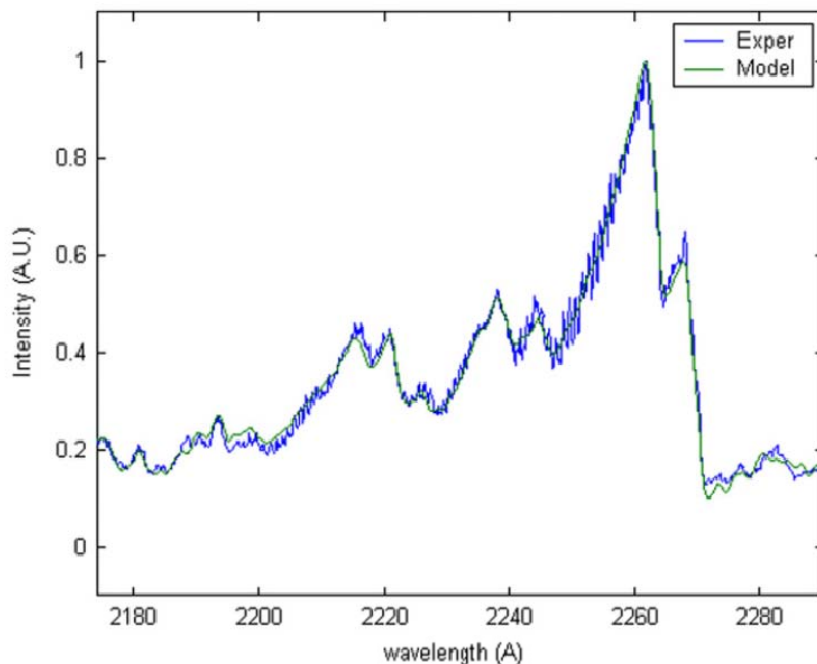
Figure 4.8. Experimental and modeled NO spectra used to determine T_{rot} = 2200 ± 100 K, T_{vib} = 4077 ± 250 K, T_{elex} = 4074 ± 400 K, for a 3.8mA glow discharge in air and 300μm electrode spacing.

Spectra in the range from 351 nm to 359 nm can be used to determine the relative densities of N_2^+ and N_2. The SPECAIR modeled OES from this range are due to both N_2 and N_2^+ transitions. The relative concentration of nitrogen ions N_2^+/N_2 can thus be determined and used to approximate a lower bound on the ionization fraction and plasma density in the discharge. N_2^+ is not the only ion present in the air plasma however it is

typically the most prevalent ion. Figure 4.9 shows a spectrum attained around 355 nm for a 3.8 mA discharge at an electrode spacing of 300 μm. The two larger band heads at 357.5 nm and 353.3 nm are due to the 1-0 and 2-1 vibrational transition of the N_2 2nd positive system, the smaller peak at 358.3 nm is due to the N_2^+ 1st negative system. The N_2 transitions can be used to determine both T_{rot} and T_{vib}. The relative intensity of the two systems is due to both species concentration and T_{elex} as shown in the inset equation of Figure 4.9; where, I is the intensity of the line, n is the density of the species, and ε is the energy of the excited state. An increase in the height of the N_2^+ line could be due to either a increase in the ion density or an decrease in T_{elex} since the energy of the N_2^+ excited state is less than the energy of the N_2 excited state ($\varepsilon_{N2+} < \varepsilon_{N2}$). T_{elex} and N_2^+/N_2 thus cannot be determined independently. The multiple bestfit result solutions can be expressed by the equation $N_2^+/N_2 = 1.383 * exp(- 90500/T_{elex})$ which is approximated the best solutions within a factor of 2. One estimate of N_2^+/N_2 can be implemented by assuming $T_{elex} = T_{vib}$. This assumption is somewhat justified by the measurements using the NO spectra where $T_{vib} = T_{elex}$ was found. Progressing from measurement of $T_{vib}(NO)$ = $T_{elex}(NO)$ to the assumption of $T_{vib}(N_2) = T_{elex}(N_2) = T_{elex}(N_2^+)$, however, is not entirely justified but was implemented non-the-less to determine N_2^+/N_2. Using the spectra in Figure 9 we determined T_{rot} = 1282 K, T_{vib} = 5015 K and $N_2^+/N_2 = 1.25 \times 10^{-8}$. This corresponds to a nitrogen ion density of about 5.5×10^{10} cm^{-3}. Similar values of the ion density have been estimated for other atmospheric pressure discharges in air [96]; however, measurements and estimates of electron densities have a somewhat higher value of about 10^{13} cm^{-3}[68, 97]. A possible explanation for the low nitrogen ion density is that N_4^+ [98] or another ion is the dominant ions in the air plasma. Another possible assumption

for interpreting the spectra is to assume $T_{elex} = T_e$. T_e was estimated from the measured electric field and density to be about 1.2-1.4 eV. Using this assumption we determine $N_2^+/N_2 = 2 \times 10^{-3}$ and nitrogen ion density of 9×10^{15} cm^{-3}, which is at the upper limit of what might be expected for a glow discharge[36]. The appropriate T_{elex} to use in this situation is unclear.
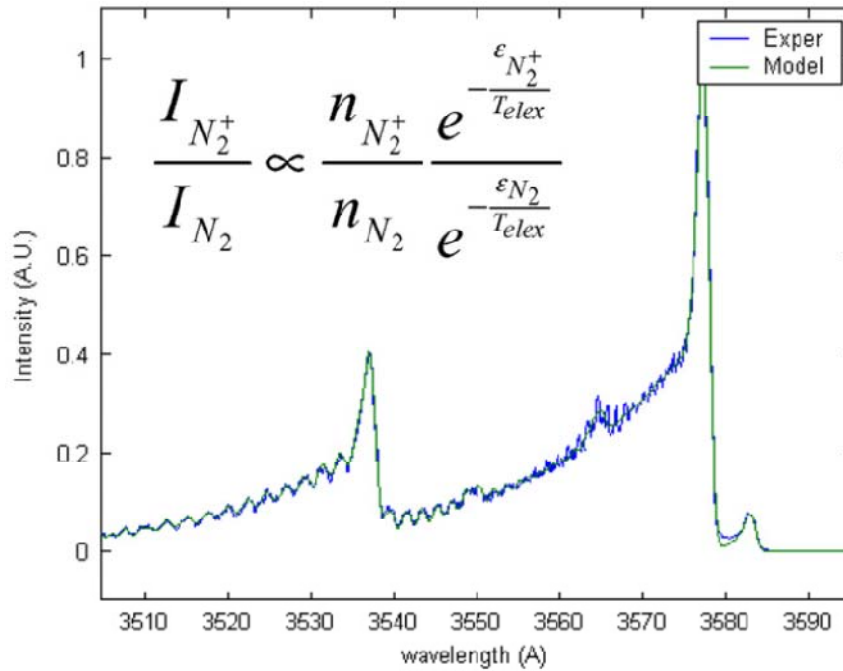
Figure 4.9: Experimental and modeled N2 and N+2 spectra used to determine Trot = 1282 ± 100 K, Tvib = 5015 ± 250K and$N_2^+/$N2 = 1.25 × 10−8 assuming Tvib = Telex for a 3.8mA glow discharge in atmospheric pressure air and 300μm electrode spacing.

4.6.3. Temperature Characteristic and Heat Balance

Results of measurements of the discharge temperature as a function of discharge current over a range from 10μA to 40 mA are shown in Figure 4.10. The low current conditions are for an electrode spacing of approximately 70 μm; the higher currents are at a spacing of 300 μm. Two different electrode spacings were used because the smaller currents could only be attained with the smaller electrode spacing. The temperature increases rapidly at low currents then appears to asymptotically approaching a constant temperature for larger discharge currents. The voltage-current characteristic corresponding to this temperature-current characteristic is shown in Figure 4.11. The discharge voltage is relatively constant over most of the range of discharge currents indicating normal glow operation. The sharp, approximately 600V, increase in the discharge voltage at currents below 300 μA corresponds with operation in the sub-normal mode and was noted by high frequency oscillations in current and voltage. Above 300 μA all the discharges had no oscillation in either voltage or current and were in the so called normal glow mode. The approximately 50 V decrease in discharge voltage in going from currents of 1 mA to 35 mA can be shown to correspond with the observed increase in temperature. As the temperature increases there is a corresponding decrease in density (at constant pressure = 1 atm). The decrease in density corresponds with a decrease in electric field (at constant E/n and T_e) and thus a decrease in discharge voltage (for constant electrode spacing) at higher currents.
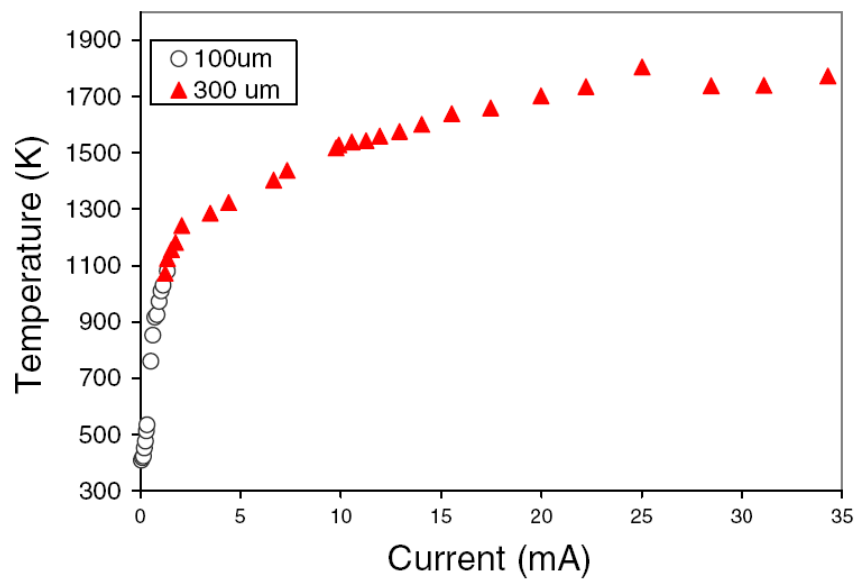
Figure 4.10. Variation of rotational temperature with discharge current for a glow

discharge in atmospheric pressure air at 100 and 300μm electrode spacing.
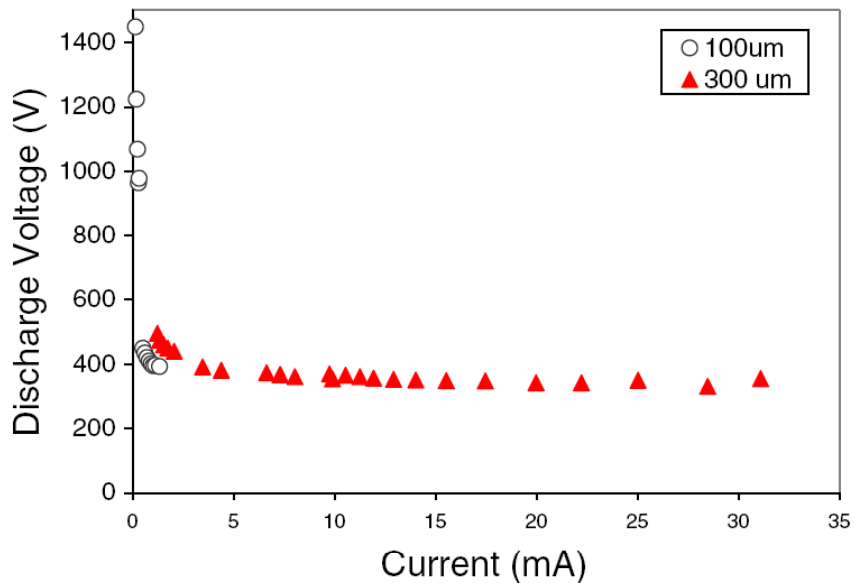
Figure 4.11. Discharge voltage variation with discharge current for a glow discharge in

atmospheric pressure air at 100 and 300μm electrode spacing.

Figure 4.12 shows the change in measured vibrational temperature with discharge current for the same conditions as shown in Figures 4.10 and 4.11. Going from subnormal to normal discharge there is an increase in the vibrational temperature. In the normal glow discharge regime there is a decrease in the vibrational temperature with increasing current which corresponds to an increase in the rotational temperature. Figure 4.13 shows the variation of discharge temperature with electrode spacing for a 3.5 mA discharge. There is a measured increase in rotational temperature with electrode spacing. The vibrational temperature is seen to have a peak at around 400 μm. It would appear from figures 4.12 and 4.13 that there is an optimal current and electrode spacing for achieving high vibrational temperatures.
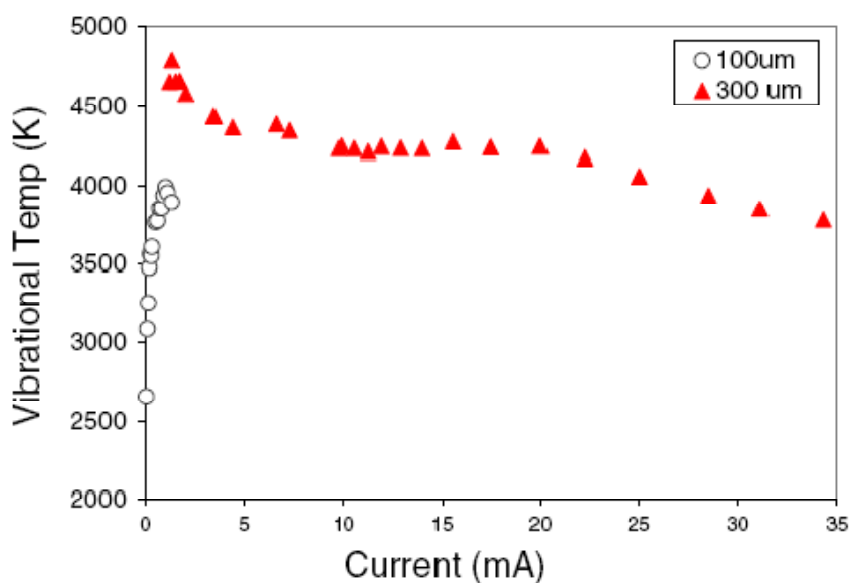
Figure 4.12. Variation of vibrational temperature with discharge current for a glow discharge in atmospheric pressure air at 100 and 300μm electrode spacing.
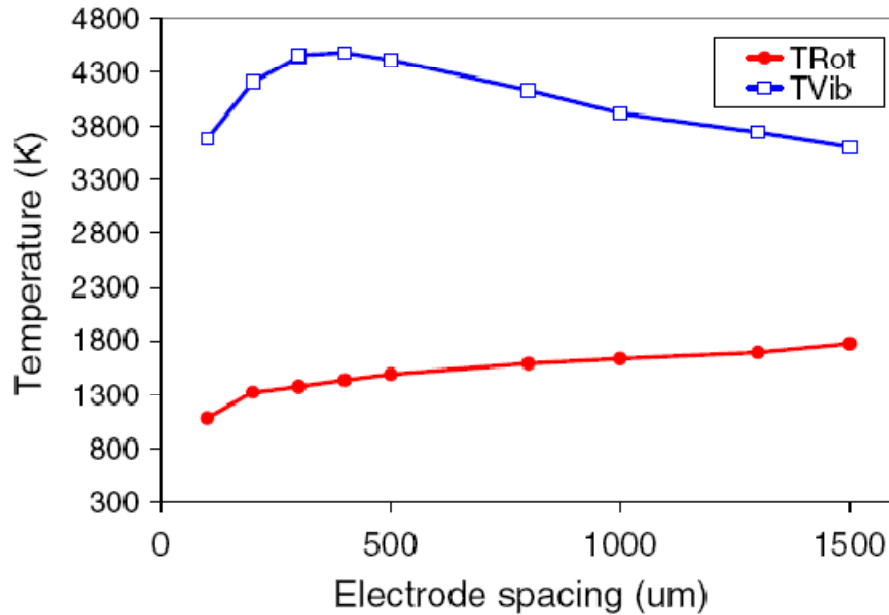
Figure 4.13. Rotational and vibrational temperature versus electrode spacing (in μm) for a 3.5mA discharge using the transitions around 375 nm.

The dependence of the gas temperature on discharge current as shown by the shape of the curve in Figure 10 can be explained by considering the two major mechanism of cooling the discharge during steady state. Consider the plasma as a cylindrical heat source of radius R and length, d. The power generated can be expressed as $w_p = I(V_n + Ed) = (\pi R^2)j(V_n + Ed)$ where I is the discharge current, V_n is the voltage drop in the cathode region, and E is the electric field in the positive column. Some of the parameters and an illustration of this simplified heat balance in given in figure 4.14. Since we are operating in a normal glow discharge mode, the diameter of the discharge is related to the current by the normal current density j and $I=\pi R^2 j$. This equation roughly takes into account that a longer discharge does not create a proportionally large power

due to the lower power density in the positive column compared to the cathode region. The first mode of cooling is radial cooling through the gas. The effective cooling area is the surface area of the plasma $2\pi Rd$ and the radial heat transfer can be expressed as $q_1 = (2\pi Rd)h_1 \Delta T$ where ΔT is the difference in temperature between the plasma and surroundings and h_1 is the effective heat transfer coefficient. h_1 is determined by the diffusion of gas out of the discharge and will decrease with an increase in the radius of the discharge. Treating the surrounding gas as a cooling shell, $h_1 = k/(R\ln(R_\infty / R))$ [99], where k is the conductivity of the gas and R_∞ is an effective outer boundary where the temperature is that of the surroundings. The logarithm varies slowly and can be approximated by a constant of order unity. If radial cooling were the only method of cooling then $\Delta T \approx I(V_n + Ed)/dk$ and an increase in temperature with discharge current is predicted. The second mode is axial cooling to the electrodes and $q_1 = (\pi R^2)h_2 \Delta T$, where h_2 is the effective heat transfer coefficient to the electrodes. Assuming highly conducting electrodes, h_2 is constant and is independent of the size of the discharge. If axial cooling were the only method of cooling then $\Delta T \approx j(V_n + Ed)/h_2$ and the discharge temperature would be independent of the discharge current because j = const. The ratio of the radial to axial cooling is $Rd:R^2$ and axial cooling becomes more important for larger diameter, higher current discharges. Thus, at low discharge currents an increase in temperature with discharge current is expected and, at higher discharge currents a near constant temperature. This is consistent with the experimental results shown in Figures 10 and 13. The gas temperature increases with discharge current and then levels off. Also for smaller electrode spacing the electrodes provide a larger proportion of the cooling and the temperature decreases with electrode spacing. This

simplified analysis neglects some important effects such as: non-uniform heating and cooling along the discharge, property variations with temperature, buoyancy induced convection, and instabilities such as ionization overheating. But, it is sufficient to explain the major experimentally observed trends in the normal glow discharge operating regime.

$$q_1 = (2\pi R d)h_1 \Delta T$$
$$h_1 \propto \frac{D}{R^2}$$
$$q_2 = (\pi R^2)h_2 \Delta T$$
$$w_p = (\pi R^2)j(V_n + Ed)$$
$$w_p = q_1 + q_2$$
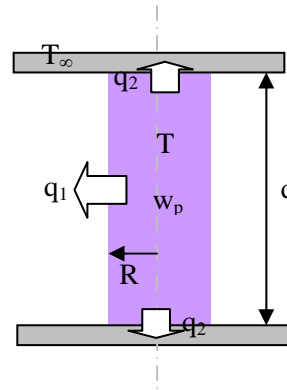
Figure 4.14: Equations and geometry for simplified heat balance of glow discharge.

The vibrational temperature is determined by the balance of vibrational excitation, and vibrational de-excitation or relaxation. By considering the excitation rate due to collision with electrons, the rate of vibrational to translational (V-T) relaxation and the rate of collisions with the electrode, the observed experimental trends for T_{vib} can be explained. At very low currents there is a decrease in the vibrational temperature with current. This is because in the sub-normal regime the electron density and rate of excitation decreases and the vibrational temperature can be expected to be lower. In the normal glow regime the current density is relatively constant and no significant change in the excitation rate is expected. The variations of the T_{vib} with discharge current while operating in the normal glow regime can be understood by taking into account the exponential increase in the rate of V-T relaxation with gas temperature [20]. The

vibrational temperature decreases at higher currents because of the increase in gas temperature and corresponding increase in the rate of V-T relaxation. Thus the decrease in T_{vib} correlates with an increase in T_{rot}. For a given electrode spacing T_{vib} thus experiences a maximum as a function of discharge current as shown in Figure 12. Typically this occurs slightly above the low current limit of the normal glow regime. This low current limit is determined approximately by where the radius and length of the negative glow region are equal [2]. Below that current the discharge extinguishes or has oscillations in the subnormal mode. There is also a decrease in T_{vib} when the electrode spacing is decreased due to increased relaxation at the electrodes. There is also a decrease in T_{vib} with larger gap spacing due to the increase in gas temperature. For a given current T_{vib} thus also experiences a maximum as a function of electrode spacing as shown in figure 13. The gap length corresponding to the maximum varies with discharge current.

4.7. Chapter Conclusions

Non-thermal glow discharges of the normal glow type were created in atmospheric pressure air. Optical emission spectroscopy provided measurements of the vibrational and rotational temperature over a range of discharge conditions within the normal glow regime. The method of determining the temperatures was to fit modeled optical emission spectra with spectroscopic measurements from the discharge. An analysis of the sensitivity of the RMSE to the fit parameters determined error bars on the temperature measurements. Different transitions within the 2nd positive column measured similar rotational and vibrational temperatures. The transitions around 375 nm appeared best suited for measurements of both vibrational and rotational temperatures because of

the higher spectrometry sensitivity and stronger emission strength of the line. The most intense of the transitions at 334 nm were inaccurate at determining the vibrational temperature because only one strong vibrational transition occurred in the range. Spectra of the UV NO transitions around 224 nm showed that for NO T_{elex} and T_{vib} are equal. Measurements using the overlapped spectra of N_2^+ and N_2 were used to estimate an ion number density, assuming $T_{elex}=T_{vib,}$ and gave results for nitrogen ion density of about 5.5×10^{10} cm^{-3}. The gas temperature measured in the normal glow regime show an increase in rotational temperature with discharge current and electrode spacing. The observed variations can be explained by a simplified heat balance analysis. Radial cooling appears dominant for smaller diameter discharges and the axial cooling for larger diameter discharges. The vibrational temperature decreases with increasing rotational temperature and also decreases at low discharge currents and smaller electrode spacing. This results in an optimal regime for creating vibrationally excited species. Overall the atmospheric pressure normal glow discharge in air was shown to be non-equilibrium. Depending on the application, regimes can be chosen for maximum vibrational temperature or low gas temperature and moderate vibrational excitation.

5. Spatially Resolved Temperature and Spectroscopic Measurements

5.1. Context

Continuing from the last chapter which described the global thermal characteristics of the micro-glow discharge, this section describes the spatially resolved, microscopic variations in temperature along the axis of the discharge. The measurement technique is a modification of low pressure techniques for spatially-resolved, optical emission spectroscopy. Modifying it to work at atmospheric pressure presented some challenges related to the micro-scale of the discharge under investigation. In addition to developing a measurement technique, this study furthered the understanding of microplasmas by revealing relationships between the structure of the discharges and their measured properties. Specific interactions among the plasma sheaths, measured temperatures, and oxidation of electrode materials at the anode and cathode were also noted. These differences in the anode and cathode sheath behaviors were important in controlling the position of the discharge during deposition. This chapter closely follows that of a published paper, "Spatially Resolved Temperature Measurements of Atmospheric Pressure Normal Glow Microplasmas in Air."[100]

5.2. Summary

The rotational and vibrational temperatures of DC normal glow air discharges were measured by comparing modeled optical emission spectra of the N_2 2nd positive system with spectroscopic measurements from the discharges. Using an imaging

spectrometer and optical assembly the temperature measurements were spatially resolved to about 6 μm. Results are presented for a 3.8 mA discharge at an electrode spacing of 400 μm. Rotational temperatures are highest in the near-cathode region around 1500 K and decrease towards the anode to about 1100 K. Throughout the discharge higher rotational temperatures correspond with lower vibrational temperatures. The maximum vibrational temperature measured is around 5000 K. Emission from the N_2^+ 1st negative system was also measured and is only intense in the negative glow region. The temperature near the anode is sensitive to the anode material. Gold, stainless steel, and tungsten electrodes were studied. Oxidizing anode materials can create a bright and hot anode spot several hundred degrees (K) warmer than for non-reacting anode materials. Also comparisons between spatially resolved and previously studied emission averaged temperatures indicate that the emission-averaged temperatures correspond to those of the negative glow regions.

5.3. Introduction

Atmospheric pressure plasmas have recently been studied which lie between the corona and arc regimes [68, 77, 84]. Due to '*pd*' (pressure x electrode spacing) and normal current density scaling these discharges are typically sub-millimeter in size. These 'microplasmas' [36] are non-equilibrium, but still warm, with characteristic gas temperatures measured around 2000 K [68, 77, 80]. We have shown experimentally [68] and Kushner[37] has shown through simulations that some of these DC microplasmas are density-scaled versions of the normal glow discharges observed in low pressure.

The main exception to the similarity between low pressure normal glows and atmospheric pressure normal glows is that at atmospheric pressure the gas temperature ($T_{gas} = T_{rot} = T_{trans}$) can no longer be considered constant and to be near room temperature. Based upon the mechanisms of the heat balance, the temperatures in these discharges vary from about 600 K to above 2000 K over the discharge currents and discharges sizes corresponding to the normal glow operating regime [83]. The temperatures may also vary significantly within the volume of the discharge, as is studied herein. These thermal effects can significantly affect the physics of the discharge, the non-equilibrium nature, and their applicability for use in micro-fabrication and other processes [2].

Previously used optical emission spectroscopy techniques using the 2nd positive system of N_2 [80, 83, 86] were employed here for temperature measurements. Techniques for attaining spatially resolved temperatures are well known from studies of low pressure plasma systems and can be applied to microplasma systems [101]. An obstacle in studying atmospheric pressure microplasmas is the inherently small size of the discharges. To facilitate future research in microplasmas the experimental scheme and procedures taken to attain the spectra are presented in this paper. Detailed spatially resolved spectra and temperature measurements are also reported for comparison to computationally modeled temperature profiles [102] and emission-averaged temperature measurements [83]. In performing these studies a significant anode material effect on the temperature distribution was noted which could not be revealed from the earlier emission-averaged temperature measurements.

5.4. Experimental Setup and Procedure

The circuit and electrode configurations used to generate the plasma discharges are similar to that used in our previous studies [68, 83] and are shown in Figure 5.1. A DC power supply is connected in series to a ballast resistor and the anode of the discharge. For these studies in the normal glow discharge regime in air the ballast resistor was 200 kΩ. The anode is a thin wire suspended over the planar cathode. Tungsten, gold, and stainless steel anode wire materials were used with diameters of 1 mm. The spacing between the electrodes is controlled by a micropositioner and for the temperature measurement experiments was set to 400 ± 5 μm. The cathode of the discharge is a grounded gold wire approximately 1 mm in diameter. The power supply voltage and discharge current are measured using the voltmeter and ammeter internal to the power supply. The plasma discharge voltage is derived from the known resistance. A Pearsons model 2877 current transformer probe was also connected inline to measure high frequency current oscillations and ensure DC operation of the discharge.
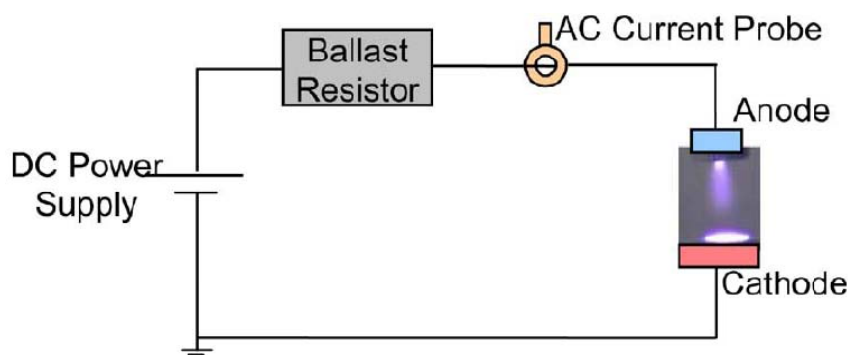
Figure 5.1: Electrical circuit for generating microplasma discharge

For visualizing the discharge during operation a 640×480 resolution Digital color CCD video camera was mounted on a microscope focused on the discharge. The microscope–camera setup provided a variable magnification allowing between a 2.0 mm $\times$ 1.5 mm and a 20.0 mm $\times$ 15.0 mm field of view. The corresponding minimum pixel size at maximum magnification was thus about 3 μm. Still images from the CCD camera were captured digitally by a PC.

For spectroscopy an Acton Research SpectraPro 500i scanning imaging monochromator was used. This type of spectrometer uses a CCD camera (Roper Scientific model 7430CCD 1024 pixel by 256 pixel by 16 bit) mounted onto the exit to digitally acquire the light. The camera and mirrors within the spectrometer are configured such that the horizontal axis (1024 pixels) indicates wavelength due to the dispersive grating but the vertical axis (256 pixels) maintains an image of the entrance slit to the spectrometer. Spectra in the range of 370 nm to 380 nm were imaged at approximately 0.01 nm resolutions. Background images with the discharge off were subtracted and a low pressure mercury lamp was used to determine the slit (apparatus) function and to calibrate the spectrometer.

External to the spectrometer an image of the discharge was created on the entrance slit of the spectrometer using a concave UV mirror as schematically shown in Figure 5.2. The discharge and mirror are placed such that an approximately 10 times magnified image of the discharge is created on the entrance slit to the spectrometer. Within the spectrometer the vertical axis maintains the image of the discharge while the

horizontal axis is wavelength dispersed due to the grating. The image magnification of the discharge was necessary to attain high spatial resolution along the axis of the microplasmas. Across the discharge the attained spectra are line of sight averaged. The pixels on the CCD camera are 26 μm in size; depending on the magnification we were able to attain approximately 2 μm per pixel. The mirror and discharge setup were mounted on micro-positioning stages to be able to accurately adjust and direct the light into the spectrometer.
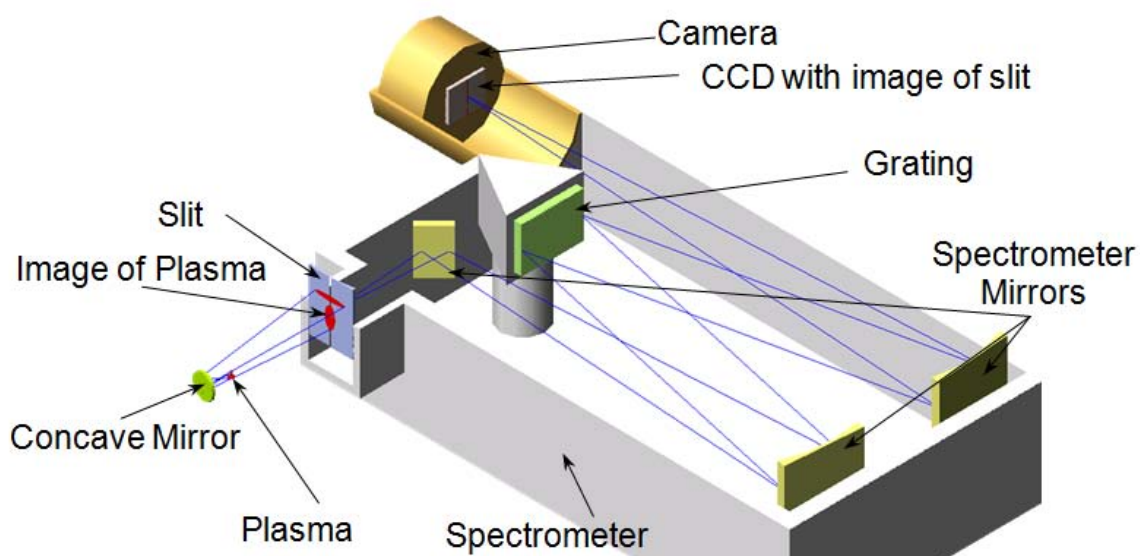
Figure 5.2: Schematic of optical setup showing raytrace (blue lines), magnification of discharge onto the spectrometer entrance slit, and imaging of the slit by the camera.

The use of a mirror rather than a lens was an important step in creating this experimental setup. The main disadvantage with using lens is chromatic aberrations, or changes in the index of refraction of the lens material with the wavelength of the transmitted light. When performing imaging spectroscopy, these aberrations cause the

discharge to be in focus and at a certain magnification for one wavelength, and out of focus and with a different magnification for other wavelengths. Over the approximately 10 nm wavelength range around 375 nm used in our spectroscopic studies the focus shifts by approximately 300 μm [103] (see Figure 5.3) which is unacceptable for studying microplasmas, which are only 200 μm in diameter. The solution used was a concave mirror with a 50 mm focal length. This primary surface of the mirror is reflective ensuring no chromatic effects. The only additional concern in using a mirror is that the light path needs to pass near the object. In our case the angle was $< 5^o$ to ensure little spherical aberrations and was easily achieved due to the small size of the discharge setup. The use of achromatic lens and optical fibers were also unacceptable due respectively to limited operation in the UV and poor spatial resolution.
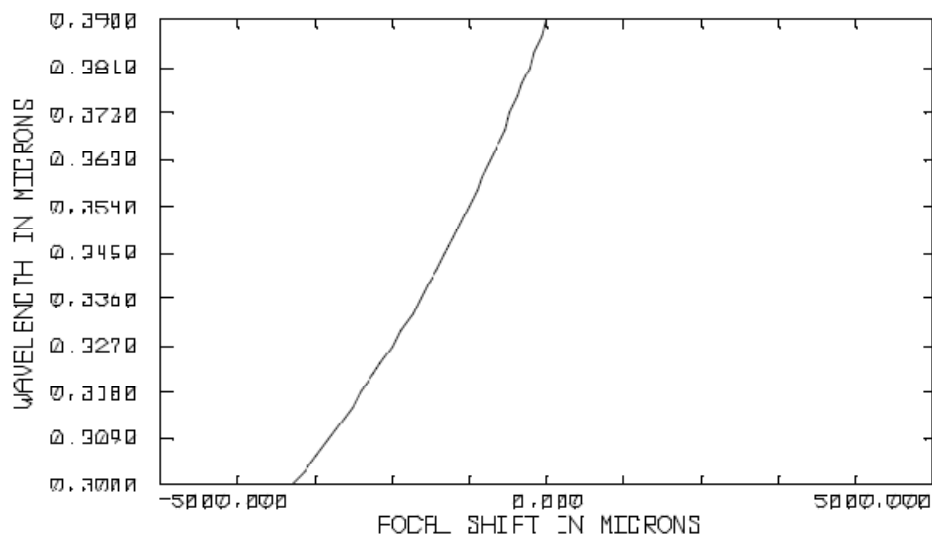
Figure 5.3: Relationship between wavelength of light and focal length of lens.

The spectral images were taken in the following way. First the spectrometer grating was turned to 0 degrees or 0 nm, in which case the grating transmits the 0th order mode and is non-dispersive. Thus both the horizontal and vertical axes image the entrance slit to the spectrometer. The spectrometer camera was then adjusted such that it was focused onto and aligned with the entrance slit. Alignment of the camera by hand with the spectrometer slit could not be achieved to an accuracy of better than 0.5^{o} and additional improved alignment was done by post processing of the image. The entrance slit was then opened and the discharge was imaged through the slit as shown in Figure 5.4. The grey scale image intensity attained is shown here in pseudo-color to better reveal features. The position of the discharge and the mirror were adjusted to create a properly magnified and focused image of the discharge. The discharge was also shifted so that when the slit was narrowed for spectroscopic imaging it would image the centerline of the discharge. In Figure 5.4 we clearly see the positive column, negative glow, and Faraday dark space of the normal glow discharge. The location of the anode and cathode denoted on Figure 5.4 are determined by the decrease in the light intensity near the anode and a measurement of the gap length by moving the anode wire until it touches the cathode.
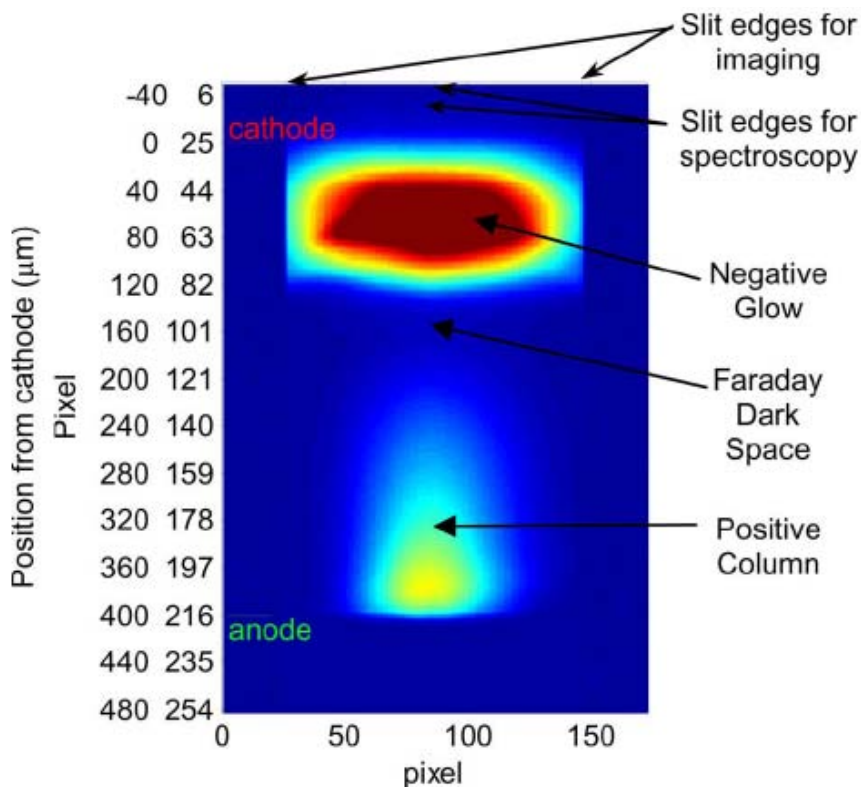
Figure 5.4: Pseudo-color intensity image of microplasma discharge through the open spectrometer slit for 3.8 mA discharge with gold anode.

After focusing, the slit was closed to approximately 100 μm and the grating was tuned to 375 nm. Figure 5.5 is the image attained. The vertical axes is Figures 5.4 and 5.5 are the same; these corresponding to spatial distance from anode to cathode. In Figure 5.5, the horizontal axis is wavelength. The contrast in this image has been increased to emphasize some of the dimmer features. That the vertical axis maintains focus can be seen by the dark areas corresponding to the cathode and anode edges along with the bright negative glow and positive column. In the horizontal axis we see the alternating bright and dark bands corresponding to the rotational and vibrational transition of the N_2

2nd positive transitions in this wavelength range. The alignment of the camera was checked by tracking the maxima and minima in the image (the negative glow, the Faraday dark space, and the near anode glow) across the horizontal wavelength axis as shown in Figure 5.6. The camera alignment cannot be perfect but is aligned to within approximately +/- 1 pixel (6 μm) across the 1024 pixel wavelength range or about 0.1 degrees.
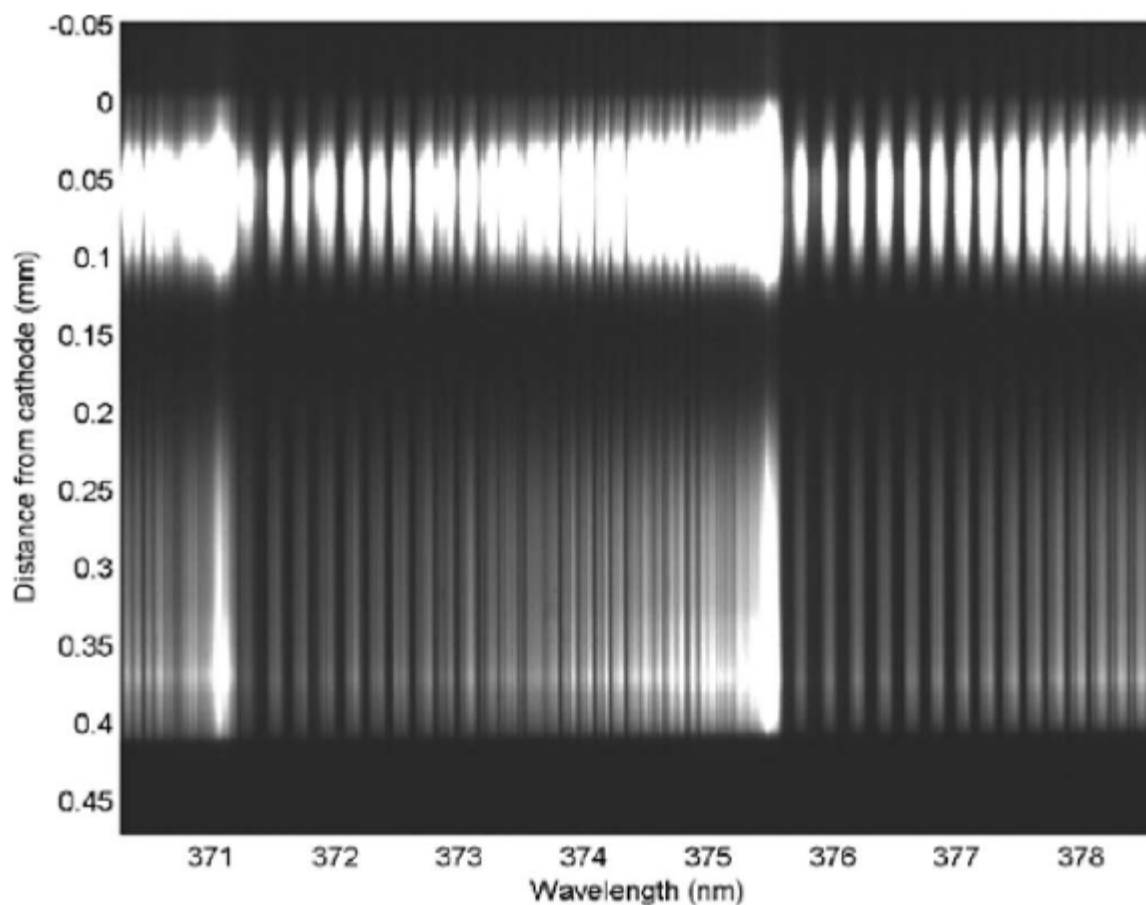
Figure 5.5: Spectral image of microplasma along discharge axis and around 375 nm. Discharge conditions were 3.8 mA, 400 μm discharge, and with gold anode.
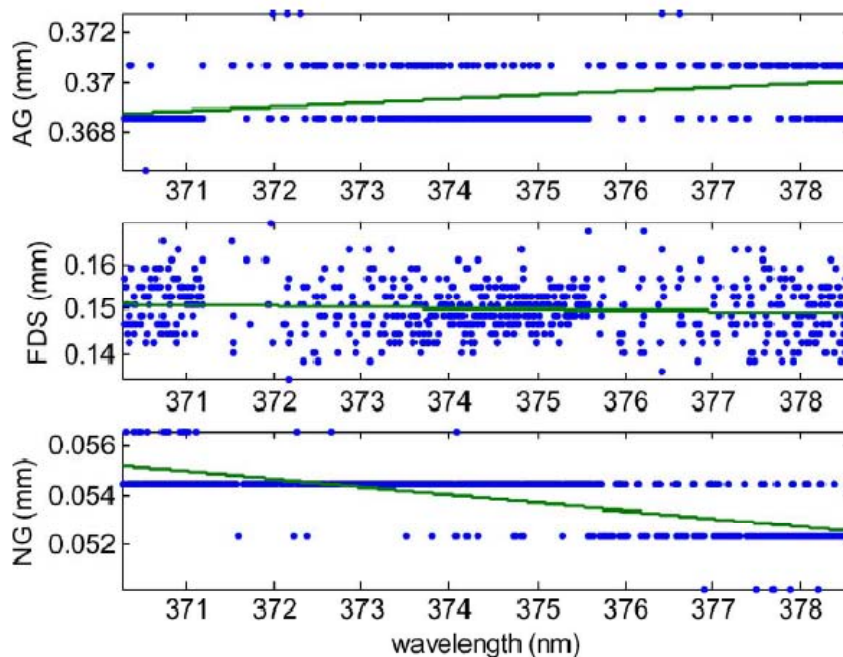
Figure 5.6: Location from the cathode of the negative glow (NG), Faraday dark space (FDS) and anode glow (AG) along the wavelength axis; used to determine the angular alignment of the camera. Data points at a given wavelength are indicated along with a best fit line.

In total there are about 200 spectra attained along the axis of the discharge each corresponding to a horizontal pixel row in Figure 5.5. As discussed earlier, the optics and camera cannot be perfectly aligned or corrected for and the actual resolution is slightly worse than a single pixel. In our analysis we created the spectra using a running average over 3 pixels. The spectra were analyzed by fitting spectra modeled using SPECAIR [80, 83, 86] to the experimentally attained spectra in a manner identical to that present in our previous papers [83]. The relevant fitting parameters were the T_{vib} and T_{rot}.

5.5. Results and Discussion

5.5.1. *Spectral Analysis*

Measured, spatially resolved temperatures are presented for a 3.8 mA discharge at an electrode spacing of 400 μm. The spectra were attained using the methods described above. Figure 5.7(a) shows the normalized spectra attained at three different regions in the discharge – at the brightest spot in the positive column (PC), at the brightest spot in the negative glow (NG), and at the dimmest spot in the Faraday dark space (FDS) for a 3.8mA, 400μm discharge with gold anode. In the center of the spectra at 375.5 nm we see the brightest peak N_2 $(C^3\Pi_u-B^3\Pi_g)$ [1-3] where C-B refers to the electronic transition and [1-3] refers to the vibrational transition. To the left of the peak we see the tail of the transition which corresponds to the higher energy rotational sub-transitions. The second most intense peak at 371 nm is the N_2 $(C^3\Pi_u-B^3\Pi_g)$ [2-4] transition. At the right of the spectra we see the tail of the N_2 $(C^3\Pi_u-B^3\Pi_g)$ [0-2] transition. The transitions that have different initial vibrational energy are used to determine the vibrational temperature. Without a full analysis of these spectra we can see some general trends. The [2-4] peak is higher relative to the [1-3] peak in the positive column region relative to the negative glow region as seen in Figure 5.7(b) and this corresponds to a higher vibrational temperature. Also since the tail of the [1-3] peak is higher in the negative glow spectra we known that near cathode region has higher rotational temperature indicating it is warmer than the positive column. The absolute measured intensities of the spectra are given in the legend of the figure. In the dark region the signal level is much lower and the

rotational temperature is difficult to determine due to the noise. That so little light is attained from the Faraday dark space indicated that the system is properly focused.
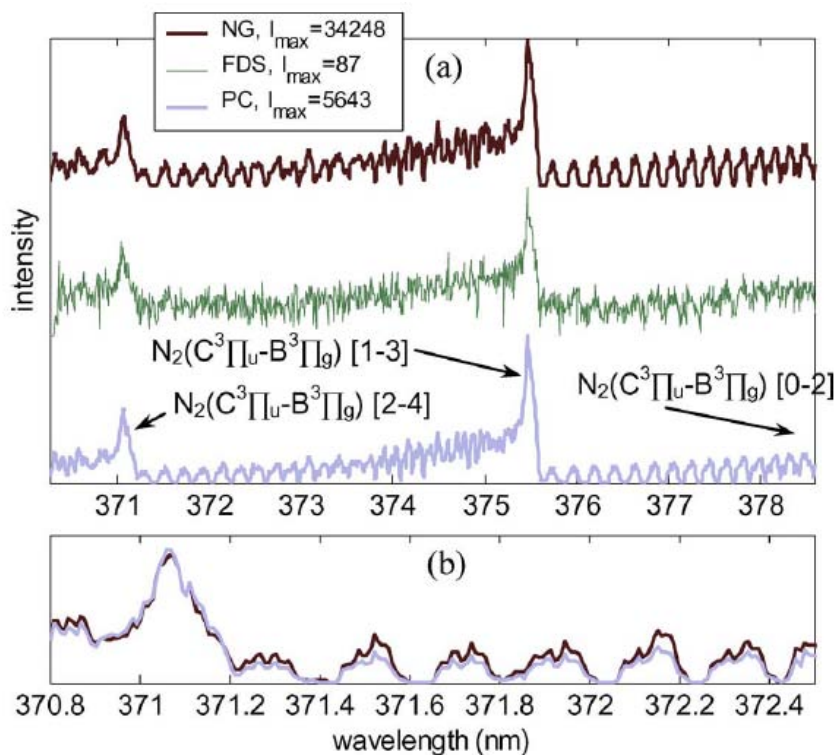
Figure 5.7: (a) Comparison of experimental spectra in the near cathode (NG), Faraday Dark Space (FDS), and positive column (PC) regions for the 3.8mA, 400μm discharge with gold anode. (b) Zoomed comparison of the spectra for the NG and PC zones.

Figure 5.8 shows the experimental and modeled spectra for the negative glow region. The modeled and experimental spectra are in very close agreement indicating the high accuracy of the spectral model. Also the discharge is non-thermal with $T_{vib} > T_{rot}$, but warm, with the gas temperature significantly greater than the ambient temperature.
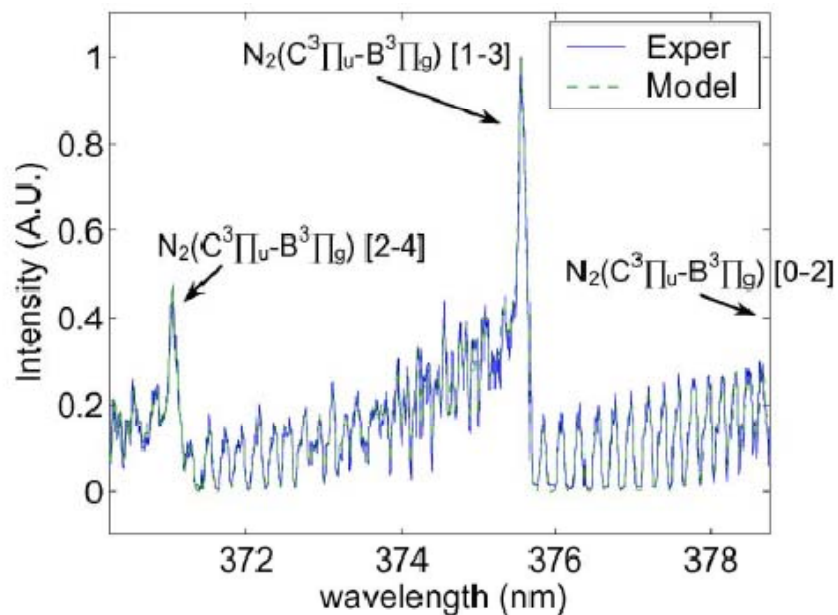
Figure 5.8: Experimental spectra and best fit modeled spectra (T_{rot} = 1446 K, T_{vib} = 4124 K) in the negative glow region for the 3.8 mA, 400 μm discharge with gold anode.

5.5.2. Axial Temperature Distribution

In total several hundred spectra were analyzed using an automated procedure to determine the temperature from Figure 5.5. Figure 5.9 shows the measured best-fit rotational and vibrational temperatures as a function of the position from the cathode. In general the errors in measured rotational temperature are less than ±100 K, and for vibrational temperatures less than ±10%. Figure 5.9(a) shows the maximum signal level normalized by the background intensity (labeled signal to noise ratio SNR). When the SNR is less than two (indicated by the grayed-out portions of the plot), the spectral signal is very weak and the fit temperatures maybe incorrect. The signal level is high in the negative glow, drops through the Faraday dark space, and increases again through the

positive column. A decrease in light intensity at the electrodes is also observed. Figure 5.9(b) shows the root mean square error (RMSE) of the modeled spectra to the normalized experimentally measured spectra. The RMSE is higher when the signal level is low, as expected.
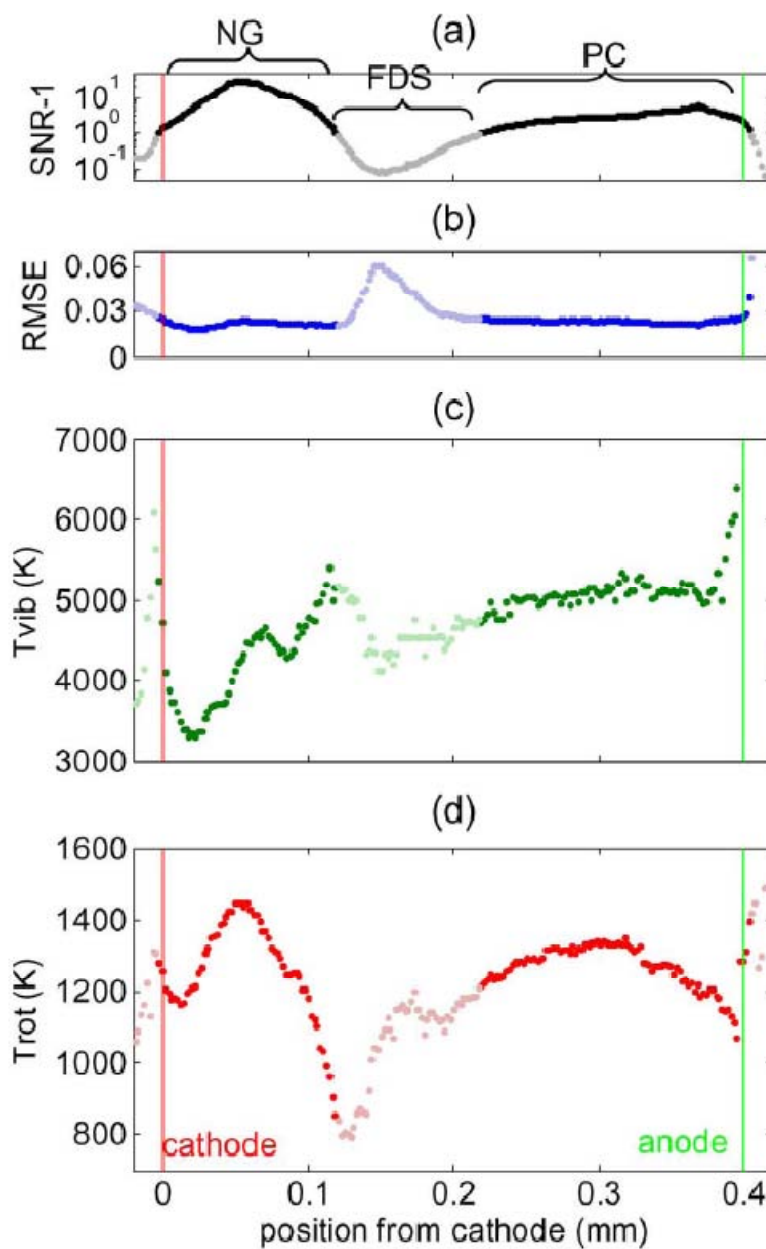
Figure 5.9: (a) The intensity of the N_2 ($C^3\Pi_u$-$B^3\Pi_g$) [1-3] peak normalized by the background intensity and indications of the negative glow (NG), Faraday dark space (FDS) and positive column (PC) regions. (b) The root mean square error (RMSE) of the spectral model fitting. Corresponding plots of (c) vibrational temperature and (d) rotational temperature along the discharge gap for the 3.8mA, 400μm discharge with gold anode. Light-colored points correspond to regions where the signal level was low.

The discharge is hottest in the negative glow region with a maximum temperature of 1450 K. Approaching the Faraday dark space there is a decrease in temperature. Within the Faraday dark space the fit temperatures are questionable due to the low signal level; but, none-the-less they show reasonable results and an increase in temperature to that of the positive column. The temperature in the positive column is about 1300K and decreases towards the anode where the temperature is about 1100 K. The peaks and valleys in the rotational temperature are consistent with heating of the gas by energetic electrons and cooling to the electrodes. The temperature peak in the negative glow corresponds with the high electric field due to the presence of the cathode sheath and expected high plasma density. In the Faraday dark space the electric field is low and the electrons are less energetic, leading to a decrease in gas temperature to about 800K. The apparent temperature gradient approaching the Faraday dark space is quite high, approximately 8500 K/mm. In the positive column the electric field should be approximately constant and higher than in the Faraday dark space, though less than in the cathode region, the temperatures are similarly in a mid-range and slowly varying. Approaching the electrodes on either side there is a decrease in temperature. The measured temperatures from very near the electrode surfaces (~ 10 μm) may not be accurate due to difficulties in accurately imaging the electrodes. The actual bulk temperatures of the electrodes have been measured using thermocouples and are less than 400 K. The vibrational temperature measurements show that the entire discharge is non-thermal. There is also a general correspondence between higher vibrational temperatures and lower rotational temperatures similar to that seen in our previous experiments with

changes in discharge current [83]. This is probably due to the increased V-T relaxation rates at higher gas temperatures.[20]

The measured rotational temperature profile (Figure 5.9(d)) is similar in shape to those obtained using computational modeling for argon [102] although the temperatures here are much higher as might be expected for an air discharge. The maximum rotational temperature occurs in the cathode region and decreases towards the electrodes. In the modeling [102] there was also a steep decrease in temperature between the negative glow and Faraday dark space. One qualitative difference is that in the modeling there was no temperature minimum near the Faraday dark space as seen in the experimental results. The precise reason for this is unclear though it may be due to insufficient modeling of non-local electron effects. The energy distribution of the electrons entering the FDS from the NG may have a depleted high energy tail due to the excessive ionization in the NG. Also in [102] isothermal (room temperature) boundary conditions were used. This is idealized since there is probably a temperature gradient within the electrode material. Experimentally the electrodes are cooled only by conduction through the lead wires and natural convection.

A comparison between the spatially resolved temperatures presented here and the emission-averaged temperatures presented in our other works [68, 83] suggests that the emission-averaged temperature corresponds with that of the negative glow region. In reference [83] for a 3.8 mA discharge at 400 μm spacing we measured a temperature of 1435 K. This corresponds most closely to the negative glow region and not the spatially averaged temperature. This is because in the emission-averaged spectra the light gathered is the total emission over the entire volume of emitted light and not an average over the

anode to cathode distance. The negative glow region is significantly brighter and larger in diameter than the positive column region of the discharge. The light emitted from the negative glow region thus overwhelms all other sources of light and the spectral shape would correspond to that of the negative glow. The emission-averaged temperatures measured are thus not the spatially averaged temperature but more closely the temperature of the negative glow.

5.5.3. *Emission from Nitrogen Ions*

Spatially resolved spectra were also attained for the discharge at wavelengths in the range of 350 nm to 359 nm as shown in Figure 5.10. In this range the observed spectra are due both to nitrogen molecules, N_2, and nitrogen molecular ions, N_2^+, as labeled in Figure 5.10. Using the N_2 spectra around 354 nm the T_{rot} and T_{vib} measured were within the prescribed error bars for the temperatures measured around 375nm, shown in Figure 5.9. Figure 5.11 shows a plot of the N_2 peak and N_2^+ peak normalized by the background signal and with the background subtracted (SNR – 1). Significant emissions from the ions are only present in the negative glow region of the plasma. The intensity of the emission from the ions cannot be used to measure the ion density as the relative intensity is a coupled function of the electronic excitation temperature, T_{elex}, and the ionization fraction [83]. The decrease in emission from the ions in the positive column can be due to either a decrease in ion density or an increase in the electron temperature.
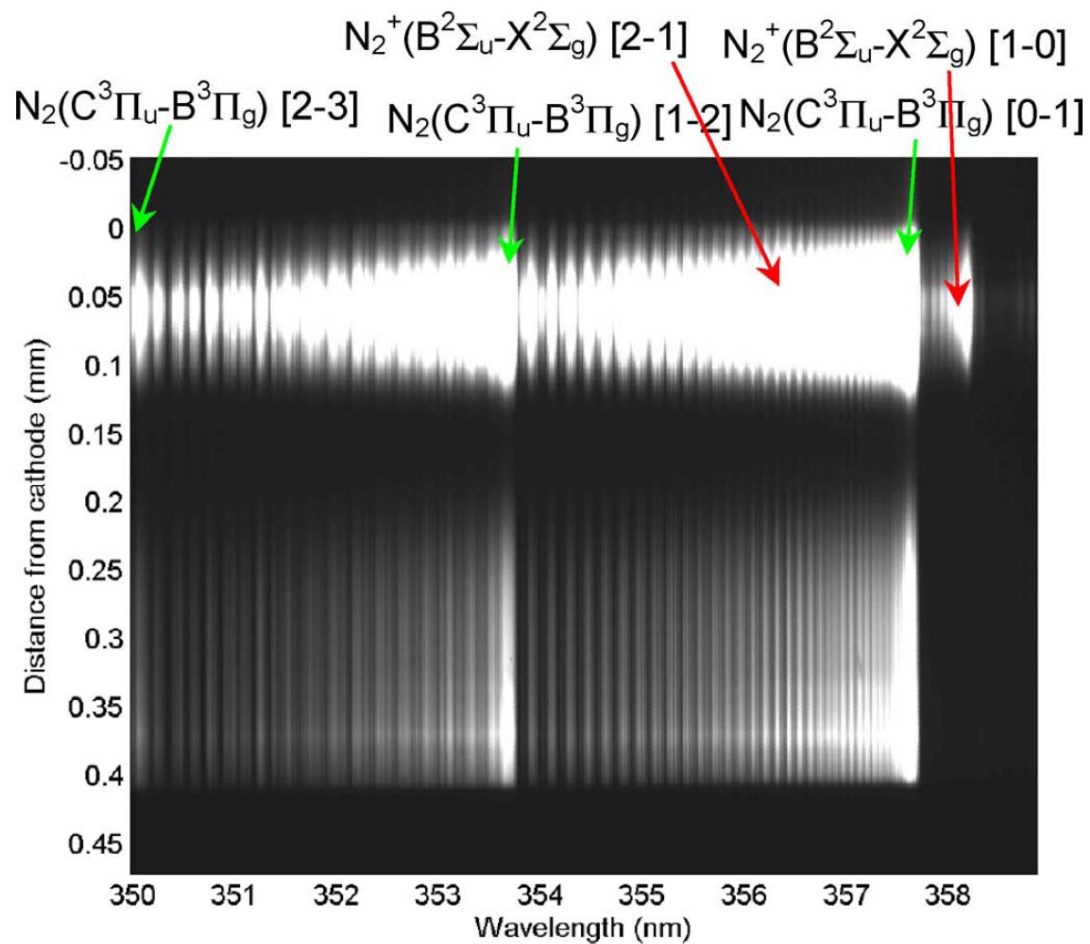
Figure 5.9: Spectral image of microplasma along discharge axis and around 354 nm.

Arrows indicate the band head location of transition for N_2 2nd positive system and N_2^+ 1st

negative system. Discharge conditions were 3.8 mA, 400 μm discharge, and with gold
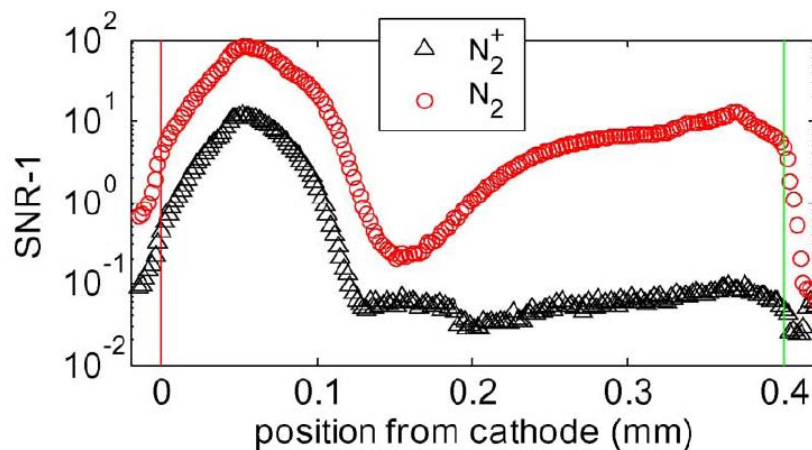
anode.

Figure 5.11: Intensities of the $N_2^+(B^2\Sigma_u$-$X^2\Sigma_g)$ [1-0] peak and the $N_2(C^3\Pi_u$-$B^3\Pi_g)$ [0-1]

peak along the discharge axis.

5.5.4. *Anode Material Effect*

A significant anode material effect was noted in performing these experiments. Namely depending on the anode material an increase in the near anode temperature could be observed. Figure 5.12 is a plot of the rotational temperature profile between the anode (stainless steel) and the cathode. The cathode material, discharge current, and electrode spacing are the same as for Figure 5.9(d). In general the temperature profiles are quite similar with maximum temperatures near the cathode of about 1450 K a decreasing toward the Faraday dark space and an increase in temperature into the positive column. In both cases the positive column has a temperature of about 1300 K. In the case of the stainless steel anode, however, there is an approximately 200 K increase in the gas temperature near the anode that was not observed in the case of a gold anode. This material effect was not observed in the emission-averaged temperatures because in both cases the near cathode temperature is the same.
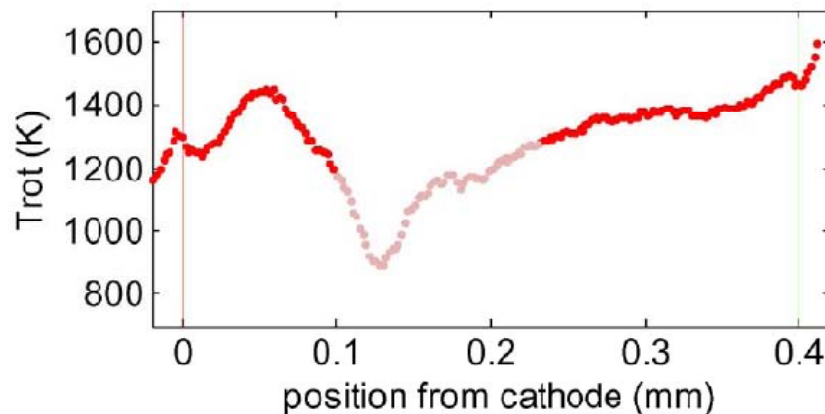
Figure 5.12: Plot of rotational temperature along the discharge gap for the 3.8mA, 400µm discharge with stainless steel anode.

The increase in temperature for the stainless steel anode corresponds with the appearance of a bright anode spot observable in images of the discharge. Figure 5.13 shows images of the discharges for tungsten, gold, and stainless steel anodes taken through the spectrometer slit similar to that shown in Figure 5.4. These images were taken with the CCD camera attached to the spectrometer and we can see absolute intensity images (though they are un-calibrated). In order to compare the images the discharge conditions and exposure time were kept constant. The image intensities are all shown with the same color scale as indicated by the labeled color bar. The tungsten anode creates a bright anode spot, Figure 5.13(a), the stainless steel anode a dimmer spot, Figure 5.13(c), and a gold anode the dimmest anode region, Figure 5.13(b). Close inspection of the images reveals that the bright spot corresponds with a reduction in the radius of the positive column in the region of the anode. A narrowing of the discharge would correspond with an increase in current density, electron density and local gas heating. Thus a narrowing would result in the observed increase in temperature near the anode. The narrowing appears to be an effect of the anode material. We believe the effect

occurs due to the formation of thin dielectric oxide layers on the anode. Tungsten which readily forms an oxide scale layer in air plasmas and at elevated temperatures [104] has the brightest anode spot. Temperature measurement could not be attained for the Tungsten anode because of the presence of emission from metallic ions (likely tungsten) in the attained spectra. These ions are likely due to the high temperatures and evaporation of tungsten at the anode and possibly due to the volatile oxidation of tungsten. Gold is the most stable element known to man and though oxides can form in oxygen plasmas they forms very slowly in the best of conditions (~ 0.1 nm/min) and they are unstable in air and at elevated temperatures [105]. The gold electrode is not likely to form a dielectric layer and has the largest and coolest anode spot. The oxidation of the stainless steel at elevated temperature (known as scaling or heat tinting) is moderately fast (~300 nm/min) [106] and the stainless steel has a moderately bright and hot anode spot.
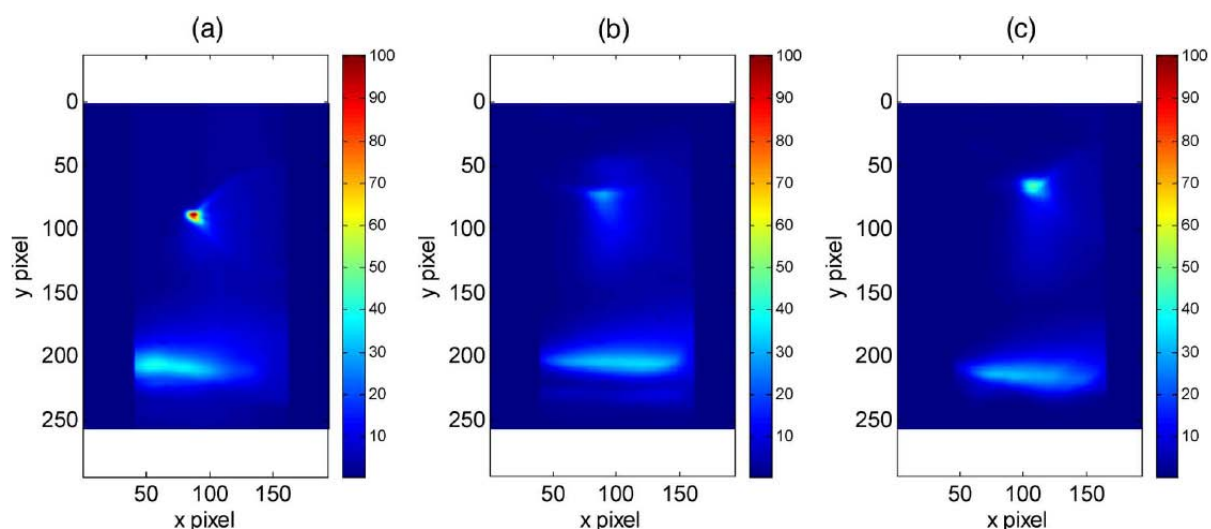
Figure 5.13: Image intensity of microplasma discharges taken through the spectrometer slit for (a) tungsten anode, (b) gold anode and (c) stainless steel anode. Images were taken for the same exposure time and intensity of the light collected is present on the

same scale for all pictures. Discharge current was 3.8mA in all cases and the electrode

spacings were approximately 550μm.

The dielectric coating limits the effective size of the anode electrode and causes the discharge to be focused on a spot. The final spot size would be determined by the balance of oxide growth and ablation rates. Easier to oxidize materials will thus have smaller/hotter anode spots. Such a discharge contraction would electrically have to be accompanied by an increase in the anode sheath voltage which causes the plasma to constrict [107, 108]. The change required though is only several volts (based upon a 1 eV electron temperature) and could be easily attributed to errors in the discharge length of less than 5 μm ($E \sim 3$ kV/cm) and thus could not be accurately measured. The changes in the anode region though significant in temperature may thus have little effect on the voltage-current characteristics and general operation of the discharge. The discharge also still operates in the normal glow mode since the cathode current density is unaffected by the change in anode material.

5.6. Chapter Conclusions

Optical emission spectroscopy was used to characterize a normal glow DC microplasma in air. Measurements with high spatial resolution were obtained by using an imaging spectrometer and UV compatible mirrors rather than lenses as optics. N_2 2nd positive system rotational and vibrational spectroscopy was used to determine the gas temperature and vibrational temperature of the discharge. The measured gas temperature

was between 800 K and 1450 K peaking near the cathode. The vibrational temperature confirms the non-thermal nature of the discharge. Comparisons between spatially resolved and previously studied emission-averaged temperatures indicate that emission-averaged temperatures correspond to that of the negative glow region. The temperature near the anode is sensitive to the anode material and increases corresponding to a contraction of the discharge. The discharge contraction may be due to anode oxidation. The measured material effects and temperature distributions should contribute to the understanding and application of atmospheric pressure microplasmas.

Characterization and Stabilization of Atmospheric Pressure DC Microplasmas and their Application to Thin Film Deposition

Volume 2

A Thesis

Submitted to the Faculty

of

Drexel University

by

David Alexander Staack

in partial fulfillment of the

requirements for the degree

of

Doctor of Philosophy

December 2008

6. Comparison of Microplasma Discharges in Atomic and Molecular Gases

6.1. Context

In the preceding chapters, the fundamental experiments on atmospheric pressure normal glow discharges were, for the most part, confined to discussions of discharges in ambient air. This chapter expands that research, and looks at discharge operation in nitrogen, hydrogen, argon, and helium. Measurements are made of general characteristics, but special attention is paid to the mechanism of energy transfer and heat balance. As discussed in Chapter 2, the avenues of energy transfer are quite different e→V→T for molecular gases and e→T for atomic. These factors are important to PECVD processes as they will determine if energy can go into vibrational modes and enhance chemistry, without causing excessive gas heating. These gases span a range of thermal conductivity and degrees of freedom as shown in table 6.1. As such, they provide a more comprehensive insight into the plasma physics and thermodynamics of these systems. The results are used to estimate the plasma conditions and control gas temperatures in other discharges. This chapter is based on the publication, "DC Normal Glow Discharges in Atmospheric Pressure Atomic and Molecular Gases."[109]

Table 6.1: Set of thermal conductivities and energy transfer routes explored in characterization of microplasma discharges in multiple gases.

	e$\rightarrow$T	e$\rightarrow$V$\rightarrow$T
Lower Conductivity	Argon	N_2, Air (also electronegative)
Higher Conductivity	Helium	Hydrogen

6.2. Summary

DC glow discharges were experimentally investigated in atmospheric pressure helium, argon, hydrogen, nitrogen and air. The discharges were characterized by visualization of the discharges and voltage and current measurements for current of up to several mA. Significant differences are seen in the gas temperature, however all of the discharges appear to operate as temperature and pressure scaled versions of low pressure discharges. In the normal glow discharges, features such as negative glow, Faraday dark space, and positive column regions are clearly observable. In hydrogen and to a lesser degree in helium and argon standing striations of the positive column were visible in the normal glow regime. Normal glow characteristic such as normal current density at the cathode and constant electric field in the positive column are observed although there are some unexplained effects. The emission spectra for each of the discharges were studied. Also the rotational and vibrational temperature of the discharges were measured by adding trace amounts of N_2 to the discharge gas and comparing modeled optical emission spectra of the N_2 2nd positive system with spectroscopic measurements from the discharge. The

gas temperatures for a 3.5 mA normal glow discharge were around 420 K, 680 K, 750 K, 890 K, and 1320 K in helium, argon, hydrogen, nitrogen, and air respectively. Measured vibrational and excitation temperatures indicate non-thermal discharge operation. Mixtures of gases achieved intermediate temperatures.

6.3. Introduction

Atmospheric pressure plasma discharges are of great interest because of the lower costs and simplified operation in comparison with low pressure plasma processing, and also because of the possibility of applications to non-vacuum compatible materials and processes [10]. A requirement for many of these applications is a non-thermal plasma. Non-thermal plasmas (also called cold plasmas) are characterized by a non-equilibrium distribution of energy between different degrees of freedom, different excited states and different particles. Usually the situation can be simplified a little assuming that energy distribution can be described by several temperatures such as the electron temperature (T_e), electronic excitation temperature (T_{elex}), vibrational temperature (T_{vib}), rotational temperature (T_{rot}) and translational temperature (T_{trans}). In non-thermal plasmas created by externally applied electric fields typically $T_e > T_{elex} > T_{vib} > T_{rot} = T_{trans}$. The non-equilibrium nature allows for the creation of active species without generating excessive heat which may damage substrates or cause excessive dissociation. Also the chemical processes which occur in the non-equilibrium plasma are beyond those which are accessible by the addition of only thermal energy.

The most well known low pressure non-thermal discharge is the normal glow discharge [2, 29]. The normal glow discharge exists typically in the discharge gap between parallel electrodes at currents higher than the threshold for Townsend breakdown and while ion induced secondary electron emission from the cathode sustains the discharge. The behavior of the plasma in this regime is very well known and studied. Relationships for scaling of the electric field, current density, and voltage drop can be used to predict and accurately estimate the discharge parameters. At atmospheric pressure the scaled version of a normal glow discharge has characteristic dimensions of 10s – 100s of microns and has been termed by some as microplasma.[36] Such microplasmas in air are non-thermal plasmas with temperatures ranging from several hundred to over one thousand Kelvin [83], but are often limited in applications by their small size. Due to the elevated temperature and possible transition to an arc, the regimes of stable operation for microplasma are often limited to lower powers and less complex gas mixtures than their low pressure counterparts. The elevated gas temperature thus can pose problems for the application of such discharges to processes.

The gas temperature is largely determined by the rate of energy transfer from the electrons to the neutral gas although a notable amount of heating also occurs due to the Joule heating of the ions in the cathode sheath [110]. In general the energy transfer from the electrons can be quite inefficient due to the significant difference in characteristic energy and different masses of the interacting particles. The mechanism for a system to be maintained as a non-equilibrium one can be described as follows: the electric field heats the electrons to high energy, the electrons slowly give their energy to the neutral gas, and the neutral gas has time to remain cool by leaving the discharge area or

transferring heat to the electrodes or discharge tube walls [2]. Scaling a discharge with pressure; the power of the discharge remains constant but the surface area through which cooling occurs scales as $1/p^2$.[37] Thus at atmospheric pressure the required cooling rates are very high and heating can overcome cooling. For this reason maintaining stable cold plasmas at atmospheric pressure becomes difficult.

A significant difference is observed in the energy transfer between the electrons and neutral atoms and electrons and neutral molecules. In atomic gases the gas temperature increase results by mainly translational energy transfer from collisions between electrons to atoms, so called e-T (electron-translational) energy transfer. In molecular gases electrons can transfer energy to additional intermediate internal energy modes of the molecule such as vibrational and rotational energy. Since the typical characteristic vibrational energy (0.2-0.5 eV) is comparable with typical electron temperatures (~1eV) the majority of the electron energy can be transferred to vibrational modes, e-V, and then to gas temperature through mechanisms of V-T relaxation. Since the rate of e-V and V-T energy transfer are significantly faster than e-T, molecular gases typically have higher heating rates and are more susceptible to thermalization [2].

In this paper we study atmospheric pressure non-thermal discharges operating in the normal glow mode for a variety of gases. Although the DC normal glow discharge is only one of many types of atmospheric pressure discharges we believe this to be the most basic form of non-thermal atmospheric pressure discharge and many of the insights gained may be applicable to other forms of discharges. The paper consists of topics as follows. First is a presentation of the experimental setup and diagnostic equipment and techniques. Second is a presentation of the experimental results. Normal glow discharges

are studied in air, nitrogen, hydrogen, argon, and helium. The discharges are studied through visualization, voltage and current measurements, current density estimations, optical emission spectroscopy and temperature measurements. The thermal and electrical effects of creating helium-air mixtures as well as the discharge scaling with pressure are also investigated. Air was studied due to its widespread use and availability. Nitrogen was studied due to its molecular similarities with air other than the presence of oxygen. Helium was studied because it is atomic (and thus lacks vibrational and rotational internal energy modes), has a high thermal conductivity and low breakdown voltage which make it useful in creating lower temperature and more stable plasma discharges. Argon was studied because like helium it is a noble gas but due to its high weight has a lower thermal conductivity. Hydrogen was studied because similar to helium it has a high thermal conductivity, although it is molecular. We are also studying the use of hydrogen in processes for thin film deposition of amorphous carbon using atmospheric pressure methane, hydrogen mixtures [111]. This study of normal glow discharges in various gases provides a framework for understanding the thermal effects apparent at atmospheric pressure and further describes the relationship between low pressure and atmospheric pressure normal glow discharges.

6.4. Experimental Setup

Figure 6.1 is a photograph of the experimental setup used. This experimental setup is similar to that used in our previous studies [68]. A wire anode is suspended over a planar electrode. The stainless steel cathode plate was 2.5 cm square and 1 cm thick. The anode wire was about 0.1-0.5 mm in diameter and was interchangeable and attached to a

stainless steel block which acts as a heat sink. For most of these experiments a 0.2 mm

gold wire was used, other materials such as stainless steel and silver were also used with

no significant changes in the global characteristics of the discharge through subtle changes

in the anode sheath have been observed for different anode materials[100]. The anode is

fixed in place, and the cathode can be moved through a flexible bellows using a

micrometer to change the inter-electrode spacing. The discharge chamber is a 10 cm cube

with two quartz windows for spectroscopy and visualization of the discharge. The

chamber is sealable and there are gas inlets and outlets for testing in a variety of pressures

and discharge gases.
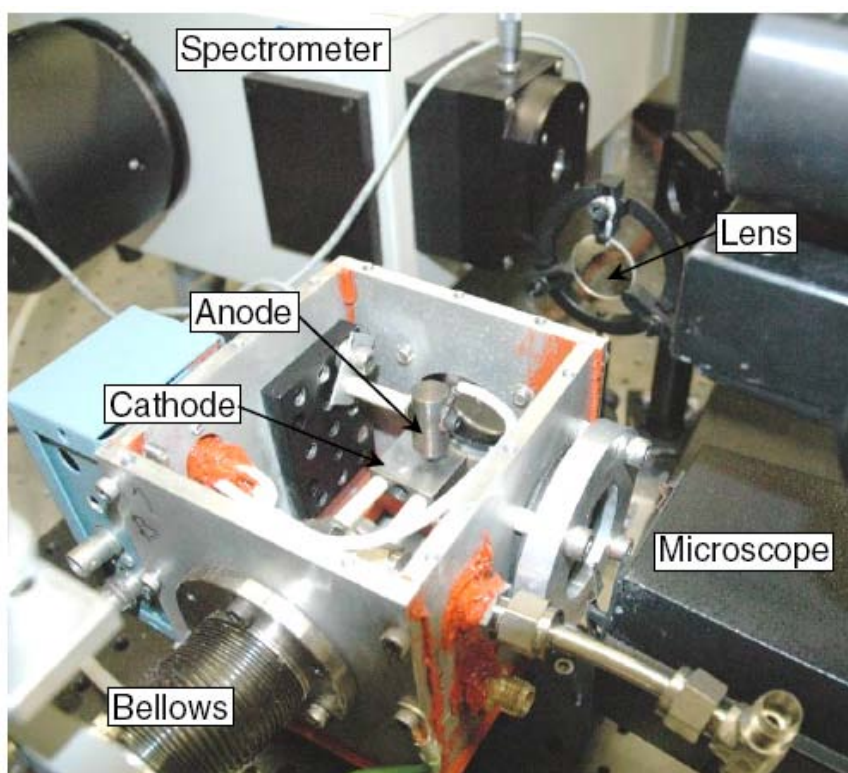
Figure 6.1: Photograph of the experimental setup which shows the spectrometer,

microscope, and discharge chamber.

The circuit used to generate the glow discharge is similar to that used before [68] and that used in low pressure glow discharges.[1] Figure 6.2 is a schematic of the circuit used for creating and analyzing the discharge. A dc power supply (Bertran 205B) is connected in series to a ballast resistor, and to the discharge. Various values of ballast resistor, power supply polarity and applied voltage (0-5000 V) were used depending on the regime of study. The current through the discharge was varied by changing the power supply voltage with a constant ballast resistor. For studies in the normal glow discharge regime typically the ballast resistant was between 250 kΩ and 1 MΩ. Additionally the ballast resistor must be placed physically close to the discharge in order to reduce the stray capacitance of the circuit and to improve the stability of the discharge. A Pearsons model 2877 current transformer probe was connected inline to measure high frequency current oscillations up to 50 MHz. A BK-precision high impedance 1000:1 voltage probe connected to an oscilloscope is used to measure the discharge voltage and oscillations up to 1 MHz. These high frequency probes were always placed directly adjacent to the anode to measure the stable DC operation of the discharge. Power supply voltage and current reading were also built into the high voltage power supply.
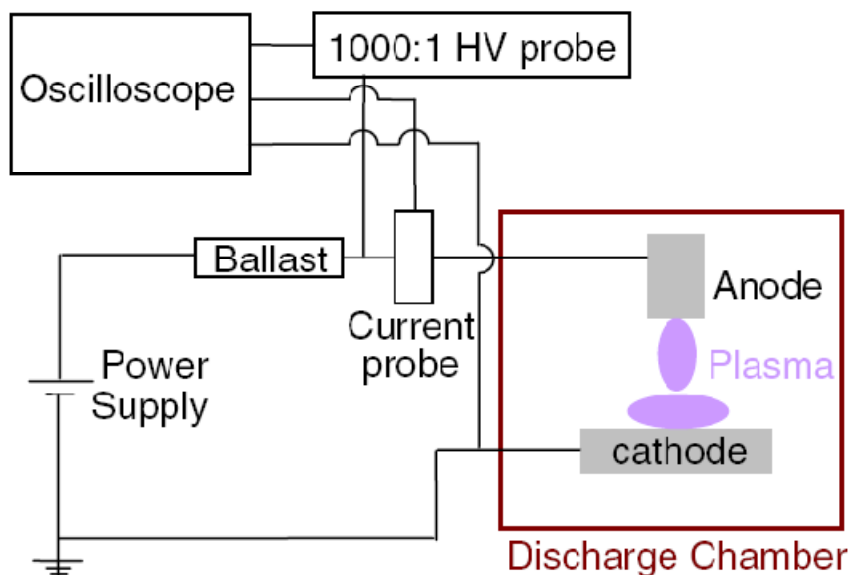
Figure 6.2: Schematic of the circuit for the generation of the glow discharge

For visualizing the discharge a 640×480 resolution DIGITAL color CCD video camera was mounted on a microscope focused on the discharge. The microscope–camera setup provided a variable magnification allowing between a 2mm $\times$ 1.5mm and a 20mm$\times$ 15mm field of view. The corresponding minimum pixel size at maximum magnification was thus about 3μm. Still images from the CCD camera were captured digitally by a PC. These images were used to verify stable operation of the discharge. Also the sizes of the features of the discharges were attained from these images. Together with the current and voltage measurements these were used to estimate the current densities and electric fields.

For spectroscopy an Acton Research SpectraPro 500i scanning monochromator was used. Light from the discharge was focused onto the entrance slit of the spectrometer using a lens as shown in Figure 1. Optical emission spectra (OES) of the discharge were

taken in a range of 200–1100 nm averaging emission from the entire discharge. This spectral range was measured using 3 different gratings: a 3600 g/mm UV optimized grating for the 200-450 nm range, a 2400 g/mm visible optimized grating for the 400 nm to 700 nm range and a 600 g/mm IR grating from the 600 nm to 1000 nm range (the upper spectral range was limited by the CCD camera). Filters at 418 nm and 580 nm were placed in the light path to ensure that the signals from the 2nd order mode from the gratings did not overlap the 1st order mode signals at higher wavelengths. A Roper Scientific model 7430CCD camera was mounted onto the exit of the spectrometer to digitally acquire the spectra. Background images with the discharge off were subtracted and a low pressure mercury lamp was used to determine the slit (apparatus) function and calibrate the wavelength of the spectrometer. Corrections for the efficiencies of the gratings, camera and other components of the optical setup were not made. For comparisons over short ranges (<10 nm) this error is <1% in intensity; over larger wavelength ranges (100's nm) the errors can be as large as a factor of four.[112] The spectra were analyzed and temperature measurements were made using the rotational and vibrational transitions of the N_2 2nd positive system. The analysis entailed fitting modeled spectra to the measured spectra with T_{vib} and T_{rot} as fitting parameters. Details of the method are in available in references [80, 83]. Additional spectral measurements were also made to measure the excitation temperature and are described later.

Operation in pure gases and gas mixtures were attained by using a pair of mass flow controllers, Omega FMA 2600. For studies in pure gases the purity was ensured in the following way. First the discharge chamber was evacuated to approximately 100 Torr. Then the chamber was filled with the test gas and a flow rate of 500 sccm was

maintained. The exhaust valve on the chamber was partially closed so that the pressure in the discharge chamber was 5-10 Torr above ambient and the system was allowed to run for approximately 15-20 minutes. This time frame was determined through a series of experiments where light emission from the N_2 2nd positive transition at 337 nm and the voltage were monitored during the purging process. For constant current and discharge gap the discharge voltage would typically change as the gas is changed within the first ten minutes and reach a steady state within 15 minutes.

6.5. Experimental Results

Figure 6.3 shows images of the discharges attained while operating in helium, argon, hydrogen, nitrogen, and air. For all images the discharge current was 3.0 mA and the inter-electrode spacing was 400 μm. The cathode is a plate along the bottom of the image and the anode is a wire coming from the top of the image. All of these discharges in general have a similar appearance and are similar in structure to that of low pressure normal glow discharges. Visible are negative glow, Faraday dark space, positive column, and anode glow regions. Obvious differences are in the apparent color of the discharges, and variations in the relative dimensions and brightness of the regions. The negative glow is the largest in helium and smallest in hydrogen indicating lower and higher current densities respectively. The length of the Faraday dark space varies from gas to gas, is hard to discern in the helium image, and is longest in the hydrogen discharge. The positive columns for most of the discharges are similar in diameter with the exception of helium whose positive column is noticeably broader and less intense. Striation of the positive

column in these images are visible hydrogen and to a lesser degree in argon. An anode glow region is clearly visible in helium and hydrogen but is not easy to distinguish in argon, nitrogen, and air.
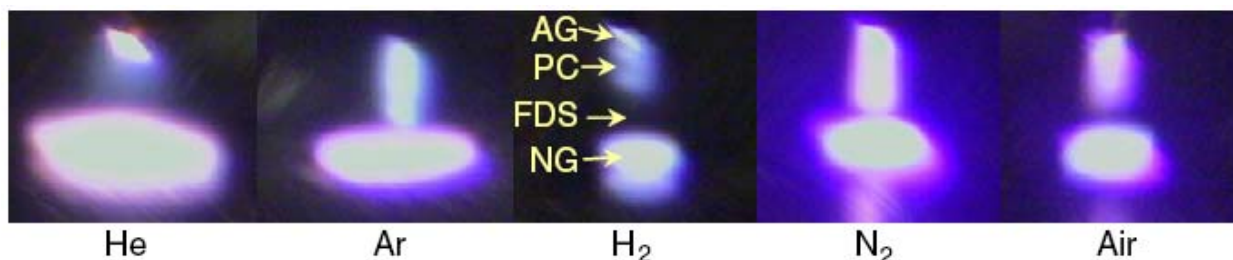
Figure 6.3: Image of normal glow discharge in Helium, Argon, Hydrogen, Nitrogen, and Air for an electrode spacing of 400 μm and a current of 3.0 mA. Negative glow (NG), Faraday dark space (FDS), positive column, (PC) and anode glow (AG) regions are labeled for the hydrogen discharge and are visible to varying degrees in each of the discharges.

More specific measurements and comparisons of the various discharges are made in the following sections. First spectroscopic studies of the pure gases are described including a) overall optical emission spectra and species identification, b) temperature measurements including rotational, vibrational and excitation temperatures. Second the electrical characteristics are presented including a) voltage-current characteristics, and estimations of b) electric field, and c) current-density. Lastly, results for gas mixtures and scaling with pressure are presented.

6.5.1. *Spectroscopy and Temperature Measurements*

6.5.1.1.   *Spectra and Line Identification*

The various colors apparent in the images of the discharges (Fig. 6.3) are due to the presence of electronic transitions within the visible spectrum for each different discharge gas. Figure 6.4 is a plot of the emission spectra in the range of 200 nm - 1100 nm. Each gas has different characteristic electronic excitation energies and emission wavelengths. The lines were identified by comparison with a variety of resources [18, 86, 113-115]. All of the lines could be unambiguously identified. In air and nitrogen the dominant lines are due to the N_2 2nd positive system (300 nm - 420 nm) and the N_2 1st positive system (600 nm - 900 nm). This violet and red mixture likely gives the characteristic pink color. Also visible in both nitrogen and air are transitions from N_2^+ 1st negative system. Visible in the air discharge but not in nitrogen are atomic oxygen lines at around 777 nm due to the dissociation of the O_2 in air. The dominant lines in the hydrogen spectra are from atomic hydrogen due to the Balmer series are visible at 656 nm and 486 nm. The molecular spectrum of hydrogen has few characteristic features as the rotational structure is so open that there are no heads or close groups to form the usual band structure. The Fucher-α (d-a) transitions are visible at around 600 nm and the lines in the range of 250 nm - 950 nm are due to a variety of unspecified transitions. The spectra for Hydrogen occur over a large range because the band head systems in H_2 overlap and are not easily distinguished due to the large energy spacing between vibrational and rotational levels. In helium the strongest lines are due to atomic emission of He at 587.6 nm, 667.8 nm, 706.5 nm; however noticeable emissions is also observed due to typical trace impurities of water vapor and nitrogen in the high purity Helium

(99.99%) used as the discharge gas. The strongest impurity lines are due to H and O probably from the dissociation of H_2O. Also visible are N_2^+ at 391.4 nm (peak height 0.0067), and OH at 308 nm (peak height 0.0013). The very high electronic excitation energy of Helium causes even very low levels of impurities < 0.01% to cause noticeable light emission. In Argon all of the strong lines are due to atomic Ar. Impurities in Ar of OH at 308 nm and H at 656 nm are visible at peak heights of 0.004 and 0.003 respectively. Tabulation of the spectral survey is presented in table 6.2.
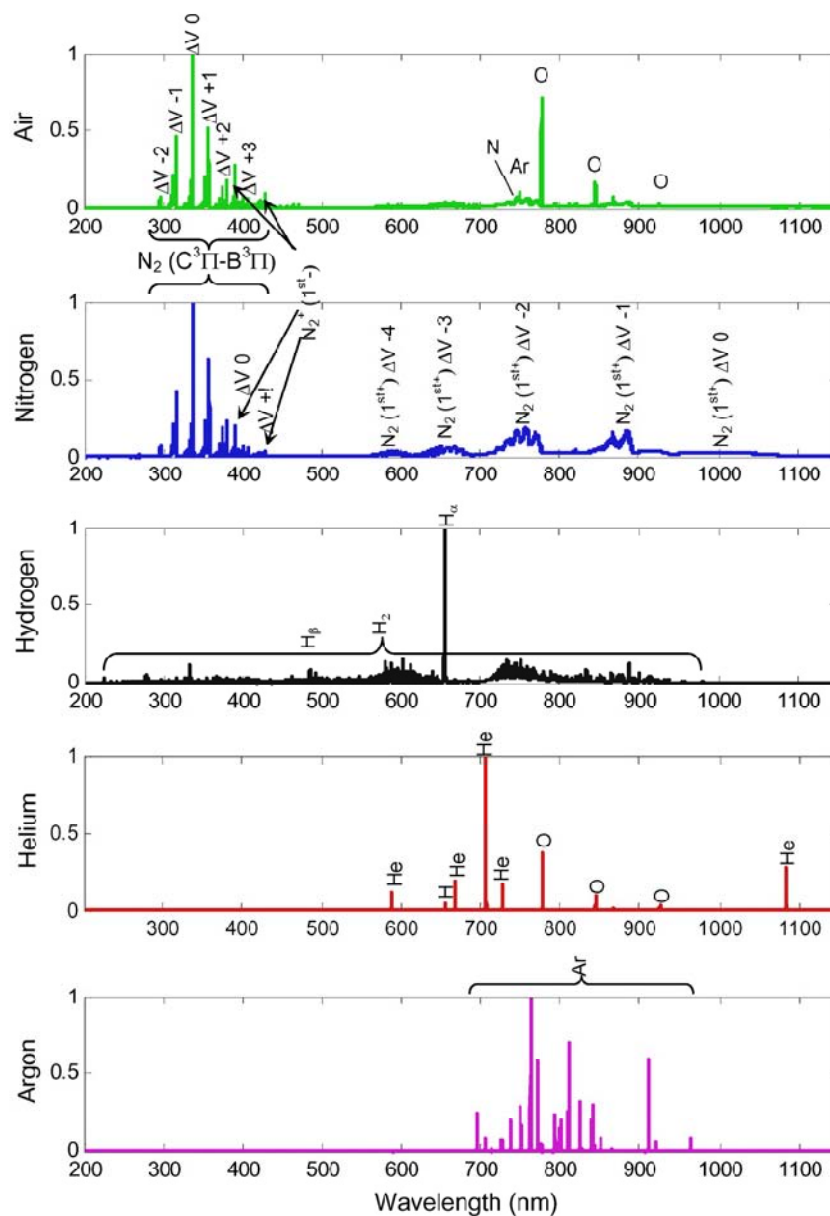
Figure 6.4: Optical emission spectra for 3.5 mA, 0.5 mm glow discharges at atmospheric

pressure in room air, and high purity (>99.99%) nitrogen, hydrogen, helium, and argon.

Intensities are normalized by the maximum peak height.

Table 6.2. Transition identification and intensity for air (a), argon (b), helium (c), hydrogen (d) and nitrogen (e) normal glow discharges.

Species	Wavelength (nm)	Transition	
(a) Air			
OH	309	$A\,^2\Sigma^+ - X\,^2\Pi\,\Delta\mathrm{Vib}\,0$	4.85
O	777.4	$2s2.2p3.(4S^*).3s - 2s2.2p3.(4S^*).3p$	70
O	844.6	$2s2.2p3.(4S^*).3s - 2s2.2p3.(4S^*).3p$	16.5
O	926.3	$2s2.2p3.(4S^*).3p - 2s2.2p3.(4S^*).3d$	3.78
NO	271.5	$\gamma\,\Delta\mathrm{Vib}\,+4(A\,^2S^+ - X\,^2\Pi)$	0.35
N_2^+	358	1st negative $\Delta\mathrm{Vib}\,-1\,(B\,^2\Sigma_u^+ - X\,^2\Sigma_g^+)$	4.48
N_2^+	391.1	1st negative $\Delta\mathrm{Vib}\,0\,(B\,^2\Sigma_u^+ - X\,^2\Sigma_g^+)$	27.9
N_2^+	427.8	1st negative $\Delta\mathrm{Vib}\,+1\,(B\,^2\Sigma_u^+ - X\,^2\Sigma_g^+)$	9.3
N_2^+	470.9	1st negative $\Delta\mathrm{Vib}\,+2\,(B\,^2\Sigma_u^+ - X\,^2\Sigma_g^+)$	2.8
N_2^+	514.9	1st negative $\Delta\mathrm{Vib}\,+3\,(B\,^2\Sigma_u^+ - X\,^2\Sigma_g^+)$	1
N_2	297.6	2nd positive $\Delta\mathrm{Vib}\,-2\,(C\,^3\Pi - B\,^3\Pi)$	6.6
N_2	315.6	2nd positive $\Delta\mathrm{Vib}\,-1\,(C\,^3\Pi - B\,^3\Pi)$	46.5
N_2	337	2nd positive $\Delta\mathrm{Vib}\,0\,(C\,^3\Pi - B\,^3\Pi)$	100
N_2	357.6	2nd positive $\Delta\mathrm{Vib}\,+1\,(C\,^3\Pi - B\,^3\Pi)$	51.3
N_2	380.4	2nd positive $\Delta\mathrm{Vib}\,+2\,(C\,^3\Pi - B\,^3\Pi)$	17.7
N_2	405.8	2nd positive $\Delta\mathrm{Vib}\,+3\,(C\,^3\Pi - B\,^3\Pi)$	6.6
N_2	434.3	2nd positive $\Delta\mathrm{Vib}\,+4\,(C\,^3\Pi - B\,^3\Pi)$	2.1
N_2	598.8	1st positive $\Delta\mathrm{Vib}\,-4\,(B\,^3\Pi_u - A\,^3\Pi_g)$	1.6
N_2	669.4	1st positive $\Delta\mathrm{Vib}\,-3\,(B\,^3\Pi_u - A\,^3\Pi_g)$	3.6
N_2	758.6	1st positive $\Delta\mathrm{Vib}\,-2\,(B\,^3\Pi_u - A\,^3\Pi_g)$	6.5
N_2	884	1st positive $\Delta\mathrm{Vib}\,-1\,(B\,^3\Pi_u - A\,^3\Pi_g)$	4.4
N_2	1033	1st positive $\Delta\mathrm{Vib}\,0\,(B\,^3\Pi_u - A\,^3\Pi_g)$	1.2
N	744.2	$2s2.2p2.(3P).3s - 2s2.2p2.(3P).3p$	6.3
N	746.8	$2s2.2p2.(3P).3s - 2s2.2p2.(3P).3p$	7.7
N	818.8	$2s2.2p2.(3P).3s - 2s2.2p2.(3P).3p$	2.6
N	821.6	$2s2.2p2.(3P).3s - 2s2.2p2.(3P).3p$	2.8
N	824.2	$2s2.2p2.(3P).3s - 2s2.2p2.(3P).3p$	2.1
N	862.9	$2s2.2p2.(3P).3s - 2s2.2p2.(3P).3p$	4
N	868.3	$2s2.2p2.(3P).3s - 2s2.2p2.(3P).3p$	7.2
N	939.3	$2s2.2p2.(3P).3s - 2s2.2p2.(3P).3p$	1.7
N	1010.9	$2s2.2p2.(3P).3p - 2s2.2p2.(3P).3d$	1.6
H	656.2	Balmer α, 3d-2p	4.9
Ar	696.5	$3s2.3p5.(2P^*\langle 3/2\rangle).4s - 3s2.3p5.(2P^*\langle 1/2\rangle).4p$	2.1
Ar	738.4	$3s2.3p5.(2P^*\langle 3/2\rangle).4s - 3s2.3p5.(2P^*\langle 1/2\rangle).4p$	4.8
Ar	750.4	$3s2.3p5.(2P^*\langle 1/2\rangle).4s - 3s2.3p5.(2P^*\langle 1/2\rangle).4p$	10.6
Ar	763.5	$3s2.3p5.(2P^*\langle 3/2\rangle).4s - 3s2.3p5.(2P^*\langle 3/2\rangle).4p$	5.6
Ar	794.8	$3s2.3p5.(2P^*\langle 1/2\rangle).4s - 3s2.3p5.(2P^*\langle 1/2\rangle).4p$	3.4
Ar	801.5	$3s2.3p5.(2P^*\langle 3/2\rangle).4s - 3s2.3p5.(2P^*\langle 3/2\rangle).4p$	2
Ar	811.5	$3s2.3p5.(2P^*\langle 3/2\rangle).4s - 3s2.3p5.(2P^*\langle 3/2\rangle).4p$	3.5
Ar	826.4	$3s2.3p5.(2P^*\langle 1/2\rangle).4s - 3s2.3p5.(2P^*\langle 1/2\rangle).4p$	1.7
Ar	842.5	$3s2.3p5.(2P^*\langle 3/2\rangle).4s - 3s2.3p5.(2P^*\langle 3/2\rangle).4p$	2.6
Ar	912.3	$3s2.3p5.(2P^*\langle 3/2\rangle).4s - 3s2.3p5.(2P^*\langle 3/2\rangle).4p$	1.8
(b) Ar			
OH	309	$A\,^2\Sigma^+ - X\,^2\Pi$	0.4
H	656.27	Balmer α, 3d-2p	0.27
Ar	696.5431	$3s2.3p5.(2P^*\langle 3/2\rangle).4s - 3s2.3p5.(2P^*\langle 1/2\rangle).4p$	24.7
Ar	738.398	$3s2.3p5.(2P^*\langle 3/2\rangle).4s - 3s2.3p5.(2P^*\langle 1/2\rangle).4p$	20.2
Ar	750.3869	$3s2.3p5.(2P^*\langle 1/2\rangle).4s - 3s2.3p5.(2P^*\langle 1/2\rangle).4p$	28.8
Ar	751.4652	$3s2.3p5.(2P^*\langle 3/2\rangle).4s - 3s2.3p5.(2P^*\langle 3/2\rangle).4p$	17
Ar	763.5106	$3s2.3p5.(2P^*\langle 3/2\rangle).4s - 3s2.3p5.(2P^*\langle 3/2\rangle).4p$	100
Ar	772.4	$3s2.3p5.(2P^*\langle 3/2\rangle).4s - 3s2.3p5.(2P^*\langle 3/2\rangle).4p$	58.4
Ar	794.82	$3s2.3p5.(2P^*\langle 1/2\rangle).4s - 3s2.3p5.(2P^*\langle 1/2\rangle).4p$	24.4
Ar	800.6157	$3s2.3p5.(2P^*\langle 3/2\rangle).4s - 3s2.3p5.(2P^*\langle 3/2\rangle).4p$	14.6
Ar	801.4786	$3s2.3p5.(2P^*\langle 3/2\rangle).4s - 3s2.3p5.(2P^*\langle 3/2\rangle).4p$	19.5
Ar	810.3693	$3s2.3p5.(2P^*\langle 3/2\rangle).4s - 3s2.3p5.(2P^*\langle 3/2\rangle).4p$	26.4
Ar	811.5311	$3s2.3p5.(2P^*\langle 3/2\rangle).4s - 3s2.3p5.(2P^*\langle 3/2\rangle).4p$	69.9
Ar	826.4522	$3s2.3p5.(2P^*\langle 1/2\rangle).4s - 3s2.3p5.(2P^*\langle 1/2\rangle).4p$	32
Ar	840.821	$3s2.3p5.(2P^*\langle 1/2\rangle).4s - 3s2.3p5.(2P^*\langle 1/2\rangle).4p$	20
Ar	842.4648	$3s2.3p5.(2P^*\langle 3/2\rangle).4s - 3s2.3p5.(2P^*\langle 3/2\rangle).4p$	29.9
Ar	912.2967	$3s2.3p5.(2P^*\langle 3/2\rangle).4s - 3s2.3p5.(2P^*\langle 3/2\rangle).4p$	60

Table 6.2: Continued

Species	Wavelength (nm)	Transition	
(c) He			
OH	282.8	$A\,^2\Sigma^+\!-\!X\,^2\Pi\,\Delta$Vib -1	0.06
OH	309.0	$A\,^2\Sigma^+\!-\!X\,^2\Pi\,\Delta$Vib 0	1.13
O	777.4	2s2.2p3.(4S*).3s $-$ 2s2.2p3.(4S*).3p	37.5
O	844.6	2s2.2p3.(4S*).3s $-$ 2s2.2p3.(4S*).3p	9.27
O	926.3	2s2.2p3.(4S*).3p $-$ 2s2.2p3.(4S*).3d	3.6
NH	335.9	$A\,^3\Pi\!-\!X\,^3\Sigma\,\Delta$Vib 0	0.24
N_2^+	391.1	1st negative ΔVib 0 ($B\,^2\Sigma_u^+\!-\!X\,^2\Sigma_g^+$)	0.67
N_2^+	427.8	1st negative ΔVib $+1$ ($B\,^2\Sigma_u^+\!-\!X\,^2\Sigma_g^+$)	0.26
N_2	337.0	2nd positive ΔVib 0 ($C\,^3\Pi\!-\!B\,^3\Pi$)	0.45
N_2	357.6	2nd positive ΔVib $+1$ ($C\,^3\Pi\!-\!B\,^3\Pi$)	0.32
N_2	380.4	2nd positive ΔVib $+2$ ($C\,^3\Pi\!-\!B\,^3\Pi$)	0.15
N	744.2	2s2.2p2.(3P).3s $-$ 2s2.2p2.(3P).3p	0.33
N	746.8	2s2.2p2.(3P).3s $-$ 2s2.2p2.(3P).3p	0.48
N	862.9	2s2.2p2.(3P).3s $-$ 2s2.2p2.(3P).3p	0.32
N	868.3	2s2.2p2.(3P).3s $-$ 2s2.2p2.(3P).3p	1.1
He	388.9	1s.2s $-$ 1s.3p	0.87
He	447.1	1s.2p $-$ 1s.4d	0.14
He	501.6	1s.2s $-$ 1s.3p	1.78
He	587.6	1s.2p $-$ 1s.3d	11.45
He	667.8	1s.2p $-$ 1s.3d	18.8
He	706.5	1s.2p $-$ 1s.3s	100
He	728.1	1s.2p $-$ 1s.3s	16.46
He	1083.0	1s.2s $-$ 1s.2p	28.1
H	486.1	4d-2p, Hb	0.13
H	656.3	3d-2p, Ha	4.62
(d) H_2			
H	434.04	Balmer γ, 5d-2p	0.6
H	486.13	Balmer β, 4d-2p	4
H	656.27	Balmer α, 3d-2p	100
H_2	462.6	G-B (0,0) R branch	2.18
H_2	596.4	R branch - Fulcher-a	4.7
H_2	602.3	Q branch - Fulcher-a	7.2
H_2	751	Various	14
H_2	889	Various	11.8
(e) N_2			
N_2^+	358.0	1st negative ΔVib -1 ($B\,^2\Sigma_u^+\!-\!X\,^2\Sigma_g^+$)	3.95
N_2^+	391.1	1st negative ΔVib 0 ($B\,^2\Sigma_u^+\!-\!X\,^2\Sigma_g^+$)	19.4
N_2^+	427.8	1st negative ΔVib $+1$ ($B\,^2\Sigma_u^+\!-\!X\,^2\Sigma_g^+$)	3.28
N_2^+	470.9	1st negative ΔVib $+2$ ($B\,^2\Sigma_u^+\!-\!X\,^2\Sigma_g^+$)	0.87
N_2	297.6	2nd positive ΔVib -2 ($C\,^3\Pi\!-\!B\,^3\Pi$)	6.75
N_2	315.6	2nd positive ΔVib -1 ($C\,^3\Pi\!-\!B\,^3\Pi$)	42.5
N_2	337.0	2nd positive ΔVib 0 ($C\,^3\Pi\!-\!B\,^3\Pi$)	100
N_2	357.6	2nd positive ΔVib $+1$ ($C\,^3\Pi\!-\!B\,^3\Pi$)	62.6
N_2	380.4	2nd positive ΔVib $+2$ ($C\,^3\Pi\!-\!B\,^3\Pi$)	23.3
N_2	405.8	2nd positive ΔVib $+3$ ($C\,^3\Pi\!-\!B\,^3\Pi$)	6.01
N_2	434.3	2nd positive ΔVib $+4$ ($C\,^3\Pi\!-\!B\,^3\Pi$)	1.24
N_2	598.8	1st positive ΔVib -4 ($B\,^3\Pi_u\!-\!A\,^3\Pi_g$)	3.6
N_2	669.4	1st positive ΔVib -3 ($B\,^3\Pi_u\!-\!A\,^3\Pi_g$)	6.1
N_2	758.6	1st positive ΔVib -2 ($B\,^3\Pi_u\!-\!A\,^3\Pi_g$)	18.2
N_2	884.0	1st positive ΔVib -1 ($B\,^3\Pi_u\!-\!A\,^3\Pi_g$)	17.1
N_2	1033.0	1st positive ΔVib 0 ($B\,^3\Pi_u\!-\!A\,^3\Pi_g$)	2.82
N	818.8	2s2.2p2.(3P).3s $-$ 2s2.2p2.(3P).3p	3.4
N	821.6	2s2.2p2.(3P).3s $-$ 2s2.2p2.(3P).3p	4.51
N	824.2	2s2.2p2.(3P).3s $-$ 2s2.2p2.(3P).3p	3.14

6.5.1.2.   *Rotational temperature measurements*

The spectral emissions were used to make several temperature measurements. Figure 6.5 is a plot of the temperature measured using the Δvib $+2$ transitions of the N_2 2nd positive system for the various discharge gases as a function of discharge current. For these measurements if the gas did not naturally contain nitrogen (helium, argon, hydrogen) a flow rate of 0.5 sccm of nitrogen gas was mixed in with the 500 sccm flow of the test gas. This trace amount of nitrogen allows for measurable light emission from the N_2 2nd positive system and so facilitates measurement of the rotational temperature which is approximately equal to the neutral gas temperature. This trace amount however was not enough to significantly alter the V-I and other electrical characteristics of the discharge. An exception to this occurred when mixing the N_2 into H_2; the 0.1% addition of nitrogen was insufficient to cause significant radiation from the N_2 2nd positive system and a nitrogen content of approximately 3% needed to be used. This is may be due to the competition between N_2 and H_2 for electronic excitation and thus higher concentrations of N_2 are need to observe the same intensity of emission.
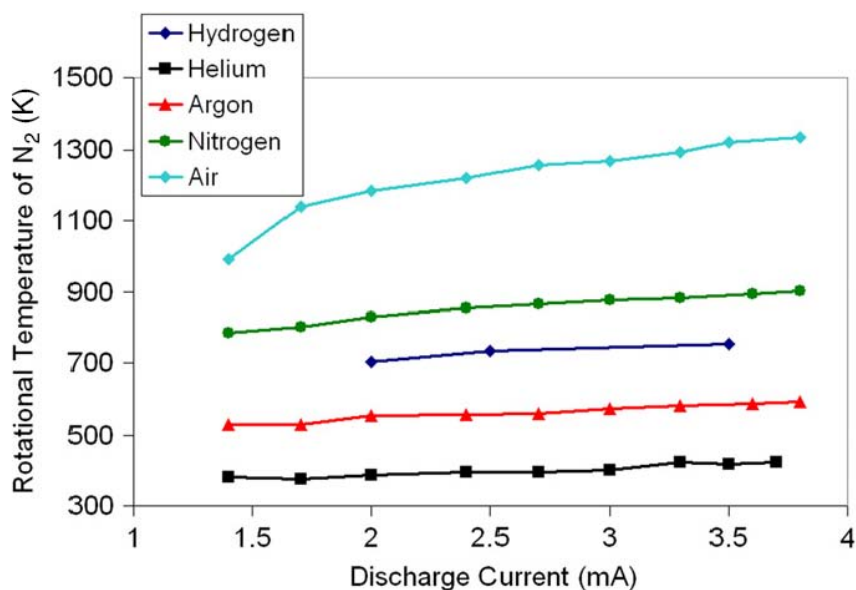
Figure 6.5: Gas temperature measurement using addition of trace N_2 in normal glow at 0.3 mm electrode spacing for hydrogen, helium, argon, nitrogen, and air.

The measured temperatures are highly dependent on the discharge gas as might be expected based upon the discussion of method of energy transfer in the introduction. The molecular gases are significantly warmer than the atomic gases. This is due to the increase in energy transfer from electrons to neutrals by *e-V* and *V-T* energy transfer. In atomic gases where only *e-T* energy transfer is available, the gas temperature is lower. Within the types of gases there is also a trend in lower temperatures for high conductivity gases. Helium and argon are both atomic but the temperature of helium is significantly lower due to its higher thermal conductivity; similarly hydrogen is cooler than nitrogen. For hydrogen the high thermal conductivity is insufficient to offset the increase in energy transfer due to molecular modes and the hydrogen is warmer than the Argon. The temperature of air is several hundred Kelvin warmer than nitrogen, this is probably due to

the oxygen, carbon dioxide and water vapor which further facilitate energy transfer to the neutrals and increase the gas temperature.

6.5.1.3.   Vibrational and Excitation Temperature

Vibrational temperatures could also be measured from the N_2 Δvib +2 spectra and the results are shown in Figure 6.6. For the atomic gases, the vibrational temperature shown is that of the molecular nitrogen added to the discharge gas. The vibrational temperatures for the molecular gases and helium are in the 4000K – 5000K range and are indicative of the non-equilibrium nature of the discharges. For the atomic Argon slightly lower vibrational temperatures of approximately 1800K are measured. This interesting trend is not yet explained but may be related to specific interactions between the argon and nitrogen [116].
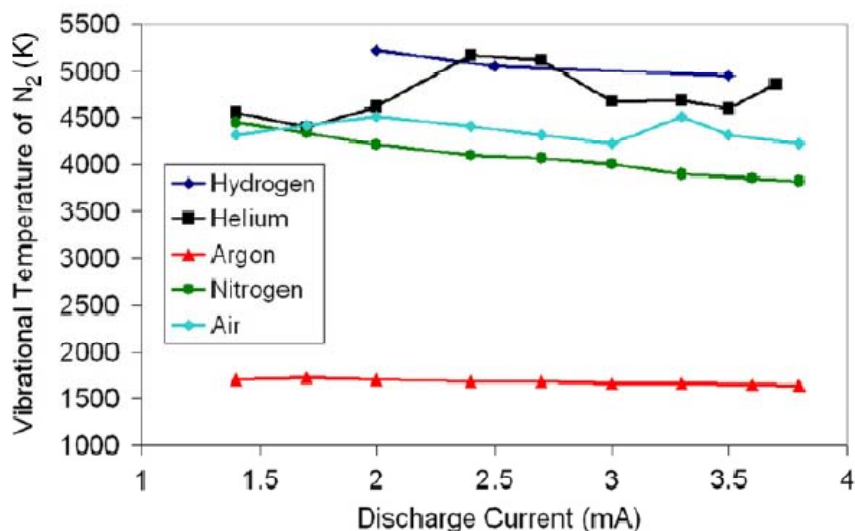
Figure 6.6: Vibrational temperature measurements using addition of trace N_2 in normal glow at 0.3 mm electrode spacing regime for helium, argon, air, nitrogen, and hydrogen.

In helium and hydrogen the atomic transitions were used to determine the electronic excitation temperature T_{elex} by comparing line intensities for different upper-state energies on the familiar Boltzmann plots [117, 118]. The relationship relates the line intensity weighted by a constant for that transition to the distribution of energies,

$\dfrac{I\lambda}{g_2 A_{21}} \approx e^{-E_2/T_{elex}}$, where I is the measured line intensity, λ is the wavelength of the line, g_2 is the degeneracy of the upper state of the transition, A_{21} is the emission coefficient, and E_2 is the upper state energy. Such constants are readily available in online NIST databases and other resources.[115] Figure 6.7 shows the Boltzmann plot for the atomic hydrogen lines observed in Figure 4. Fitting an exponential to the measured intensities of the α, β, and γ transitions of the hydrogen Balmer series results in a T_{elex} of 4193 K. The excitation temperature is quite near the measured vibrational temperature and this results in $T_{elex} \approx T_{vib}$ which is similar to what was measured using NO spectra in Air plasmas [83]. If such relationship consistently held true it would greatly facilitate the estimation of species densities from optical emission spectra. The excitation temperature is likely not equal to the electron temperature, $T_{elex} \neq T_e$ and this is often observed [118]. From the Boltzmann relation it might be expected that $T_{elex} = T_e$ since it is free electrons which cause the excitation and their energies should be described by a Boltzmann distribution at a given temperature. However, the discrepancy can arise in that this Boltzmann plot only fits to high energy electrons in a small range ~12 eV to 13 eV. The bulk electrons have significantly lower energy ~ 1eV and the electron energy distribution function is typically highly non-Maxwellian [119]. Also the electron density and residence

time of the excited molecules in ionizing plasmas, such as shown here, may not be sufficient for the electron distribution to reach equilibrium with the electronic excitation distribution [95]. Figure 6.8 shows the measurement of T_{elex} in the Helium discharge using a set of identified helium atomic lines. In the Helium discharge T_{elex} is measured to be 1766 K. This is less than the measured T_{vib} shown in Figure 6.6. Regretfully in this case $T_{elex}(He) \neq T_{vib}(N_2$ in He$)$. A complete study of when and if $T_{elex} \approx T_{vib}$, is likely difficult to predict and beyond the scope of this paper, but is worthy of future study. This excitation temperature of Helium is comparatively quite low but again it should be noted that here we are measuring only the high energy tail of the electron distribution function (in this case ~22.5 eV) and equilibrium is likely not achieved.
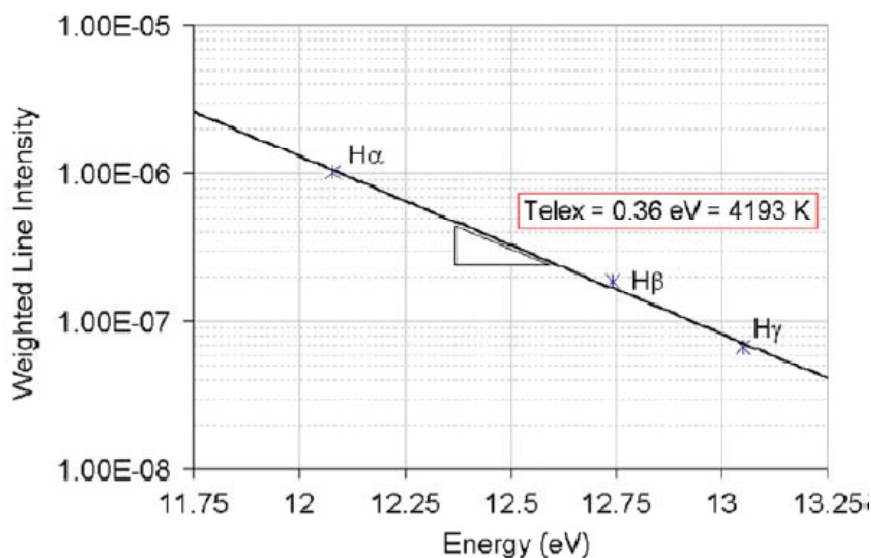
Figure 6.7: Boltzmann plot of the atomic hydrogen Balmer lines used to measure T_{elex} in a 3.5 mA H_2 glow discharge.
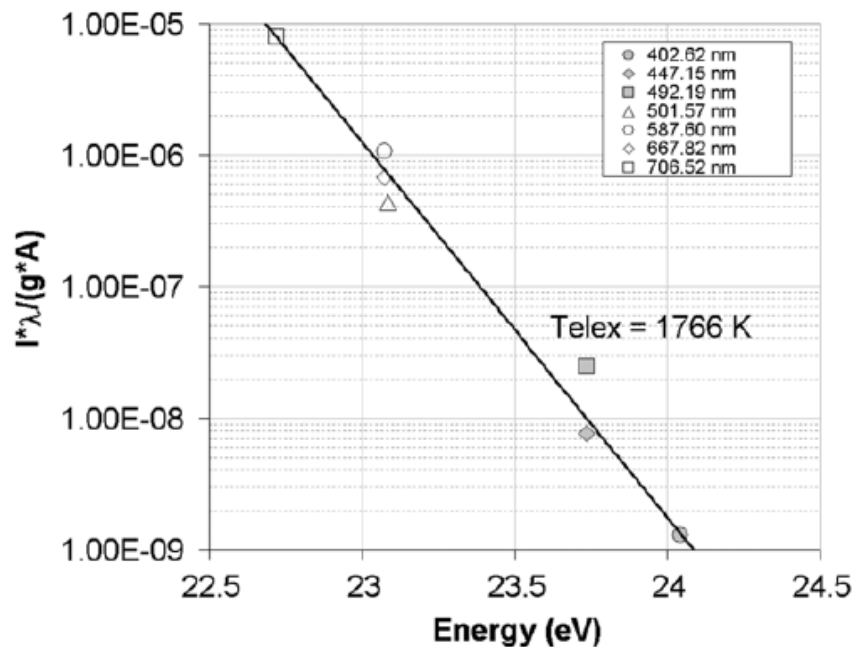
Figure 6.8: Boltzmann plot of atomic helium lines used to measure T_{elex} in a 3.5mA, He glow discharge.

6.5.2. *Electrical Characterization*

Figure 6.9 shows the voltage-current characteristics for the microplasmas in various gases while operating in the normal glow regime at an electrode spacing of 400 µm. The maximum current, 3.8 mA, was determined by limitations of the power supply used. The V-I characteristic are generally flat as is to be expected in the normal glow regime. In the air, hydrogen, and nitrogen discharges there is a slight negative slope to the characteristic, -25 V/mA, -25 V/mA and -14 V/mA respectively. In helium and argon the slope are noticeably flatter, less than 4 V/mA. Some of these changes are likely due to changes in the electric field with current and also slight decrease in the length of the positive column with an increase in current as will be discussed further later. The

voltages required for sustaining the discharges in helium, argon, nitrogen, air, and hydrogen are 177, 187, 286, 394, 389 Volts at 3 mA. These ranking of these values are generally consistent with observations from low pressure glow discharges as is evident by the normal cathode voltage drop listed in the literature as 150, 165, 215, 269, 250, for each gas respectively.[2] The voltage required to sustain the discharge is greater than the normal cathode voltage drop as is to be expected since additional voltage is required to sustain the length of positive column and the total voltage depends on the electric field in the positive column and the discharge length.
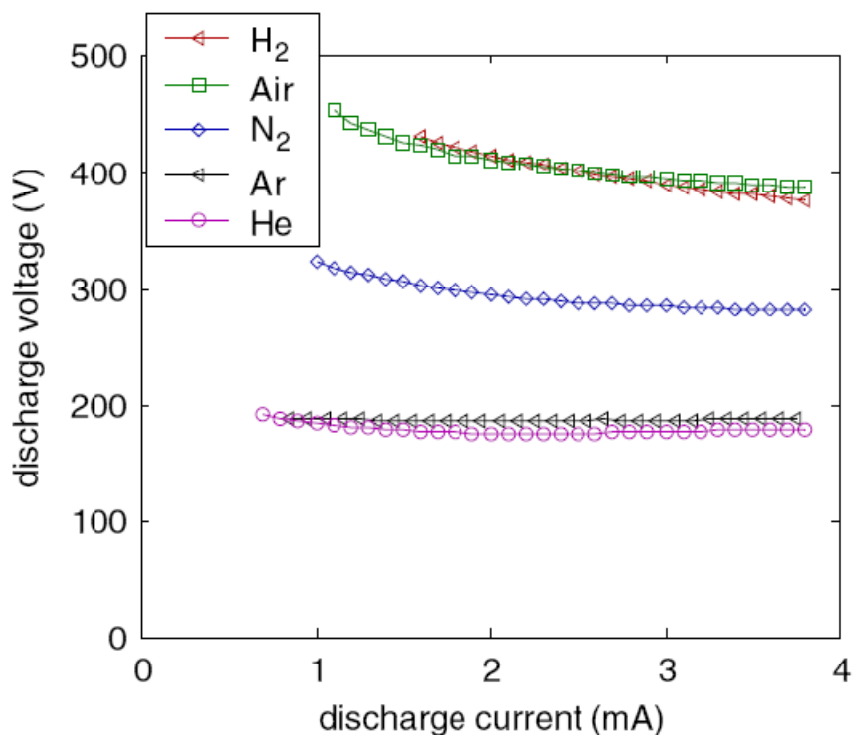
Figure 6.9: Voltage vs. Current for DC glows in hydrogen, air, nitrogen, argon and helium.

Some insight into the voltage drop in the positive column can be gained by comparing voltage-current characteristic taken at different electrode spacings. Figure 6.10 shows the V-I characteristics for glow discharge in hydrogen at electrode spacings of 0.2, 0.4, and 0.6 mm. Visually the main change in the discharge while extending its length is that positive column gets longer while the other features remain the same. This is expected of normal glow discharge operation and was observed in all of the gases. Figure 6.11 is a set of images each at 1.2 mA current in hydrogen for the discharge lengths of 0.2, 0.4 and 0.6 mm. We see as the discharge gets longer the positive column fill the gap. Thus the change in voltage with electrode spacing observed in Figure 6.10 is thus mainly the increase in voltage in the positive column. This assumes a constant voltage drop in the cathode sheath, negative glow, Faraday dark space and anode sheath regions. The change in discharge voltage, V_d, corresponding to a change in electrode spacing, d, is approximately the electric field in the positive column, $E_{PC} = \Delta V_d / \Delta d$. From the data shown in Figure 6.10 the electric field in the positive column can be calculated.
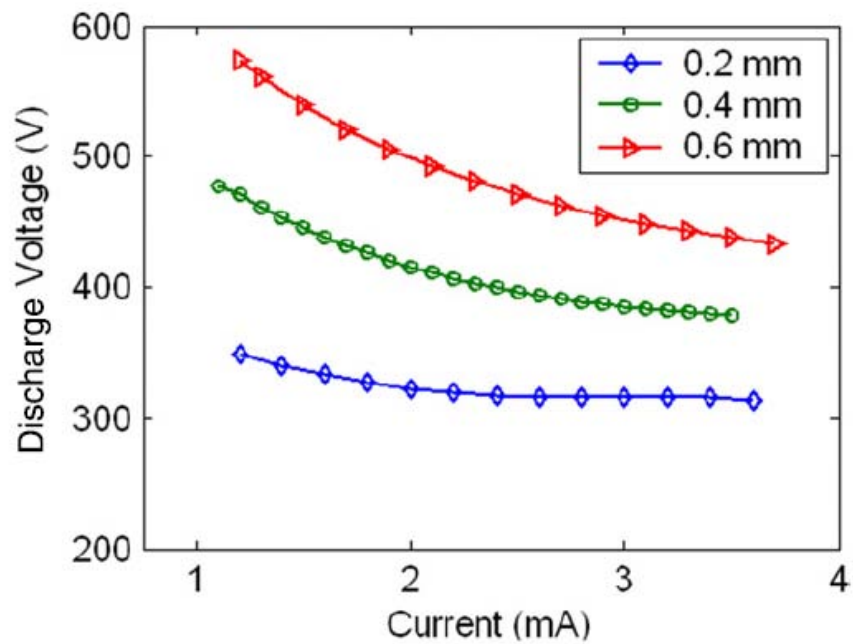
Figure 6.10: Hydrogen discharge V-I characteristic at different electrode spacing.
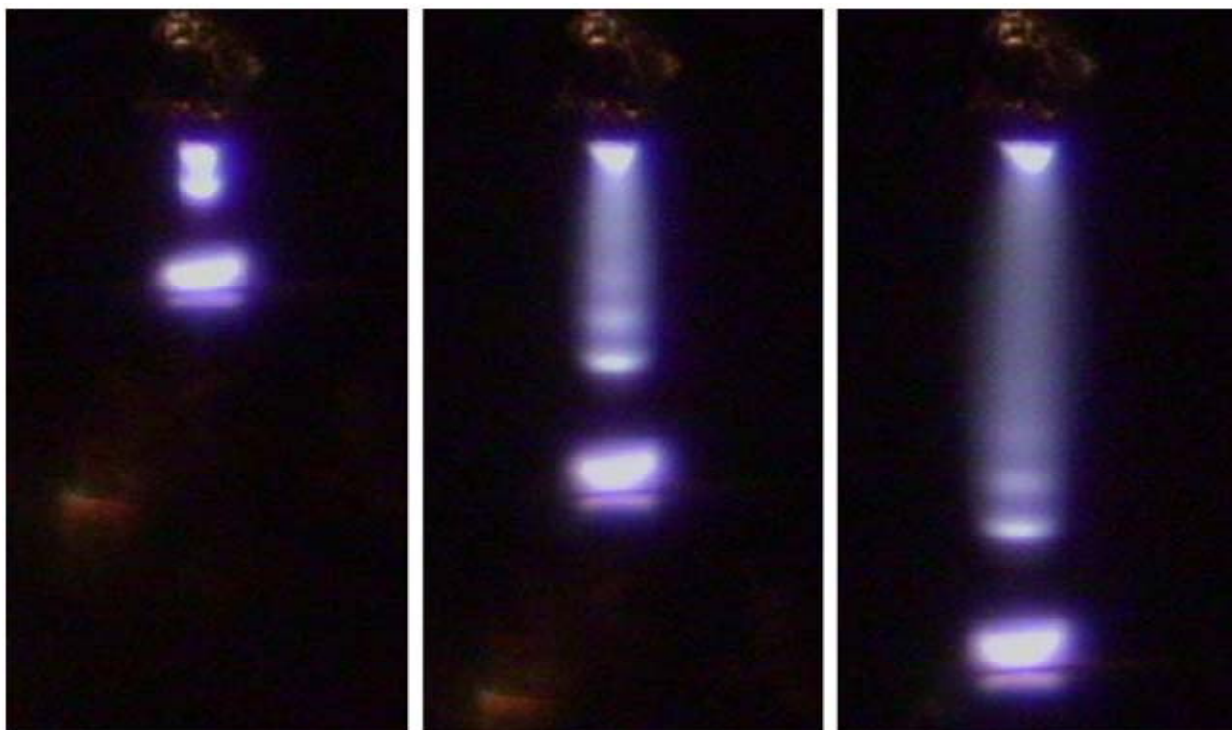
Figure 6.11: Change in discharge with increase in discharge length for 1.2 mA

discharges in hydrogen.

Figure 6.12 is a plot of the electric field in the positive column using this method

as a function of the discharge current for the various gases. Generally the electric fields

are in the range of 1 to 4 kV/cm or taking into account the pressure and temperature gives

reduced electric fields, E/p_{eff}, of about 1 to 15 V/cm·Torr which is in the expected range

for normal glow discharges[1]. $p_{eff} = p*300/T$, is the effective pressure and takes into

account that the similarity parameter E/p actually has a dependence E/n.[2]   In the

following discussions all similarity parameters will assume a pressure given by p_{eff}.

Helium and argon have lower electric fields than the molecular gases as a result of the

fact that the amount of energy required to maintain a sufficiently high electron

temperatures and densities to have ionization rates balance loses is easier in atomic gases

since there is no electron energy loss to molecular internal energy modes. For the

molecular gases there is a noticeable decrease in the electric field in the positive column

with an increase in the discharge current. In comparison to low pressure normal glow

discharges the electric field in the positive column is determined by the Engel-Steenbeck

relation and should be constant if we have a constant diameter discharge and are in a

diffusion controlled regime.[2] Our measured negative slope on the figure 12 however

does not necessarily indicate deviation from the normal glow operation due to several

reasons as follows. 1) The decrease in electric field corresponds to an increase in the gas

temperature with current. The reduced electric field thus does not change as significantly.

The temperature increases less than 25% so this is only a partial explanation for the

approximately 50% decrease in electric field observed. 2) The positive column increases slightly in diameter (~35%) with increasing current (see figure 15 for example). *E/p* decreases for increasing diameter as given by Raizer[1] and available in Fridman [2]. The similarity parameter *pR* (*p* is pressure and *R* is radius of the discharge) ranges from about 6 to 9 Torr·cm in our discharges. Over this range *E/p* in argon and helium is relatively constant; however, in air hydrogen, and nitrogen *E/p* decreases by as much as 30%. Together these two effects explain the difference between the expected flat characteristics and those measured. Thus our conjecture that the atmospheric pressure discharges operate in the normal glow diffusion controlled regime is maintained. The slope, dE/dI, is negative because of the increase in gas temperature and increase in discharge diameter.
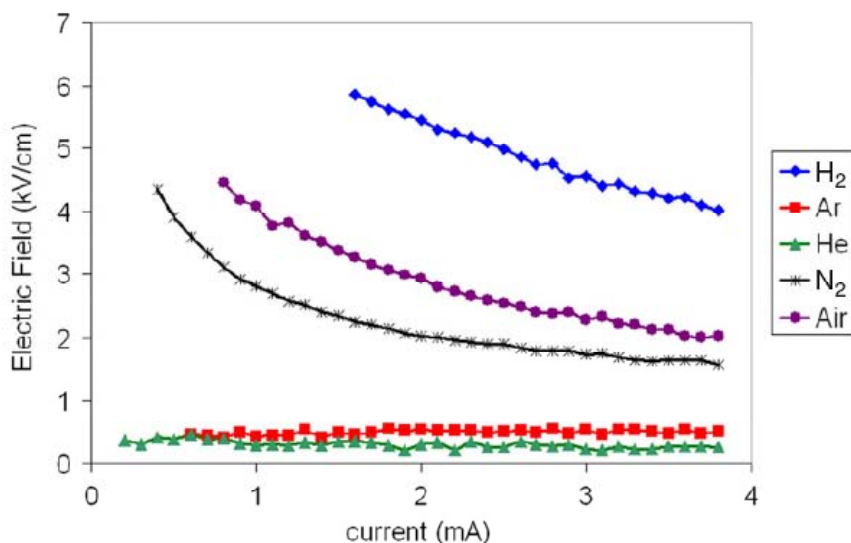
Figure 6.12: Electric field in the positive column for various discharge gases as a function of the discharge current.

The very low electric field in Helium, ~300 V/cm, leads to the possibility of creating discharges as long as 5 cm in length using only the 5kV power supply. Figure 13 is an image of such a discharge. The cathode is the lower metal plate, and the anode is the wire. This discharge was created in a square glass tube. The majority of the discharge is positive column. These are created by initiating the discharge at a shorter length (where the power supply can generate the breakdown voltage) then extending the discharge gap. The inset image in Figure 6.13 shows a zoom in of the cathode region for similar conditions. Visible in the positive column are several (2-3) striations. These striations are visible in helium similar to hydrogen and they die out into the positive column. The bending of the discharge observed here in helium occurs for longer discharge lengths in the other gases as well. For shorter discharge lengths the near electrode electric field, which is perpendicular to the surface, likely maintains a vertical discharge. For longer length the electrodes have little influence and the shape is likely determined by the balance of weaker effects such as; temperature variations, gas composition changes due to the plasma chemistry, thermal or electrically driven flows, and surface charging effects.
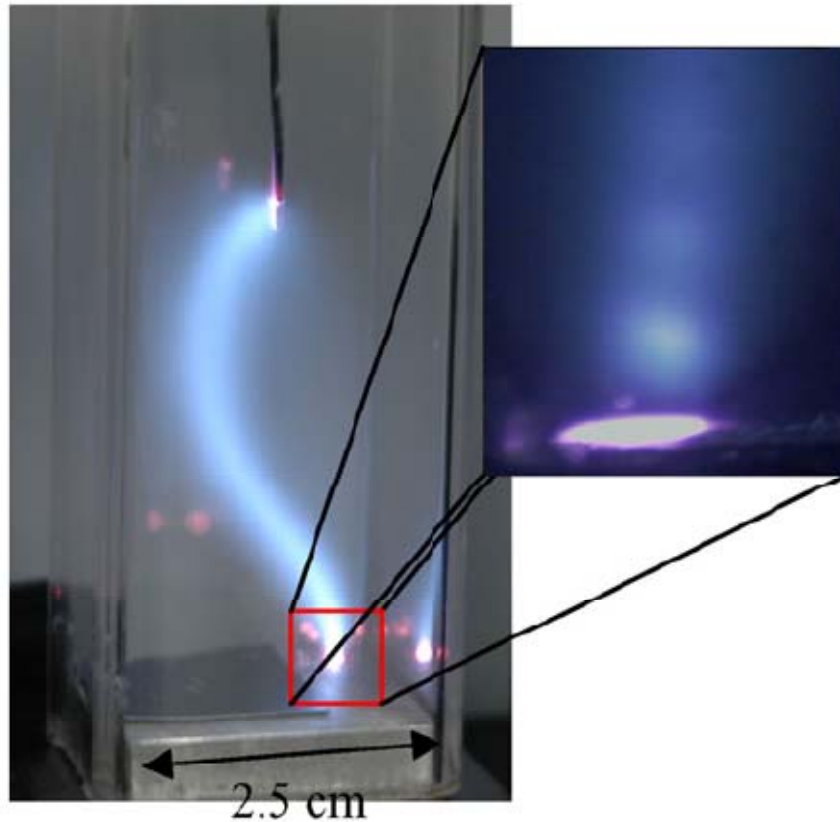
Figure 6.13: Approximately 5 cm long glow discharge in helium at atmospheric

pressure.

6.5.2.1.   Image Analysis

Together with the voltage and current measurements images of the discharges were taken. These images were used to calculate the dimensions of the discharge features and to calculate the current density and similar parameters. Figure 6.14 shows a series of images taken for the discharges in hydrogen between currents of 1.1 mA and 3.4 mA. Images were taken over the range of current up to 3.8 mA and for all of the gases but results are only detailed here for hydrogen due to the interesting observation of the

striations. The dimensions of various features in the discharge are shown in Figure 6.15. These dimensions are calculated using an algorithm applied to the gray scaled images; for example the width and length of the negative glow is defined by the rectangular region near the cathode where the intensity is 85% of the peak intensity in that region. The thresholds and dimension are somewhat subjective and thus errors of several pixels and as much as 10 μm might be expected but the analysis was applied uniformly to all the images and the trends are correct. The negative glow is seen to grow in diameter with increasing current. Also the Faraday dark space grows in length, reducing the length of the positive column with increasing current.
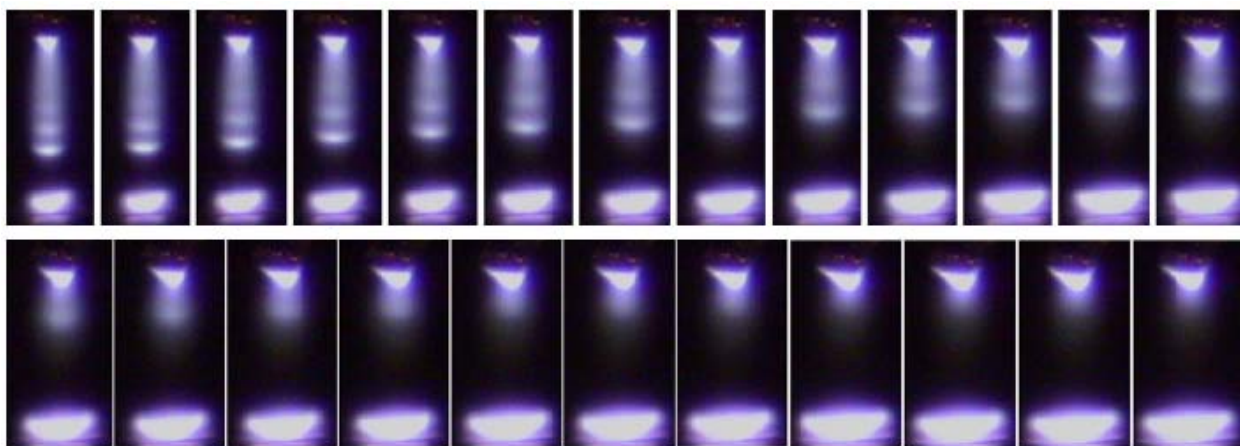
Figure 6.14: Striated discharges in hydrogen for 400 μm electrode spacing 1.1mA to 2.3 mA (top row) and 2.4 mA to 3.4 mA (bottom row) at 0.1 mA increments
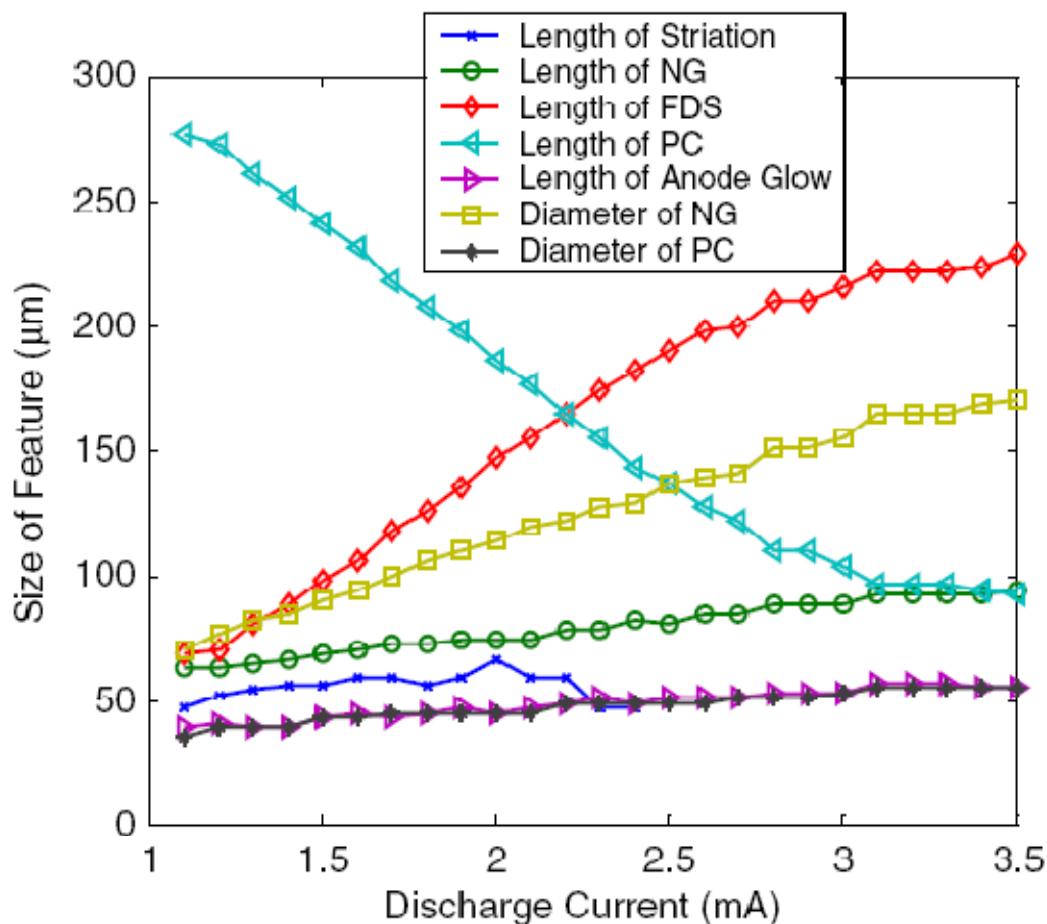
Figure 6.15: Dimension of various regions of the discharge and a function of the

discharge current for 400μm discharges in hydrogen.

The standing striations observed are visually appealing though apparently their

effects on the plasma properties are minor.[1] From a physics point of view they are likely

due to ionization waves.[120] The striations are stationary due to the nearby presence of

the strong fixed gradients of the cathode layer. Farther from the cathode where its

influence is weaker the striations die out as is apparent in figure 6.11, 6.13 and 6.14. In

our visualization of Hydrogen discharges the number of striations visible in the positive

column reduces from about 3 to zero as the positive column reduces in length with

increased current, but the distance between peaks or length of the striation is relatively constant at about 50-60 μm.

The change in length of the Faraday dark space is an interesting observation and is most notable in hydrogen but occurs to a noticeable degree in air as well and very slightly in nitrogen. Figure 6.16 is a set of images similar to Figure 6.14 but for the other discharge gases and with larger steps in current. With increasing current in the air discharge we see and increase in the length of the Faraday dark space. In Argon and Helium no such effect is observed. The increase in length of the Faraday dark space is present only for discharges in which the voltage current characteristics (Figure 6.9) have a negative slope. This is a consistent observation, the Faraday dark space is a region of relatively low electric field compared to the positive column. As the Farday dark space displaces the positive column at higher currents a decrease in voltage would be expected.

It is interesting to note that the Faraday dark space increase in length with increasing current. From a physical point of view the purpose of the Faraday dark space is to transition from the sheath-like conditions in the negative glow to the plasma-like conditions in the positive column[7]. The electron density in the negative glow is determined by the level high enough to sustain the necessary ion current through the cathode sheath (i.e. Towsend breakdown in the sheath). The electron density in the positive column is determined by the level sufficient to sustain the plasma (source/sink balance) and is typically lower than in the negative glow region. The Farady dark space is the region over which the electron density decreases (sinks > sources). The length of the Faraday dark space is determined in part by the rate at which the electron density decreases and the change in electron density from the negative glow to the positive

column. For hydrogen, figure 6.15, and air, figure 6.16, the change in length of the faraday dark space correspond to the change in the difference in radius of the negative glow and positive column. However, for argon where the radius of the negative glow is much larger than the radius of the positive column and no significant change in the length of the Faraday dark space is noted. As such the reason for the change in length of the Faraday dark space remains unexplained.
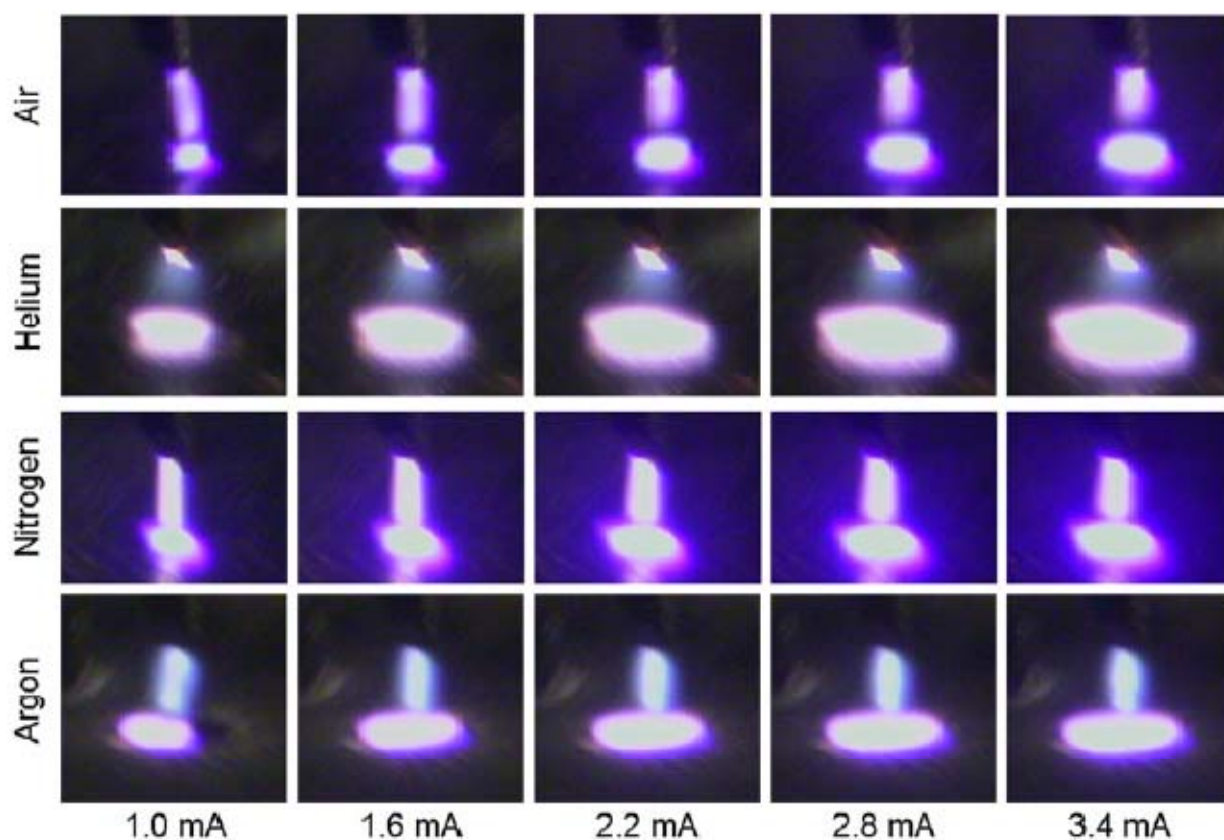
Figure 6.16: Image of the discharges in the various gases as a function of discharge current for 0.4 mm electrode spacing.

6.5.2.2.   Current Density

The measured dimensions and currents in Figure 6.16 and similar data can be used to estimate the current density in the various discharges. Figure 6.17 is a plot of the measured current densities as a function of the discharge current. The major sources of uncertainty in these calculations are in the resolution of the discharge image and in the determination of the edges of the regions which may be in error of about 3 pixels. For the smaller Hydrogen discharges this corresponds to about +/- 2 A/cm^2. Within the uncertainties the current density is relatively constant with increasing current. This is another clear indication that these discharges are operating in the normal glow regime. The theoretical basis of the normal current density is based on the classical theory of cathode layer developed in the first half of 20th century by von Engel and Steenbeck[107] and indicates that the normalized current density should only be a function of the discharge gas and gas density. Scaling our measured current densities by the pressure and measured temperatures we get normalized normal current densities, $j_n = j \times (T/300)^2 \times (1/p^2)$ of 135, 53, 150, 3.3, and 5.8 μA/cm^2/Torr^2 for the H_2, N_2, Air, He, and Ar respectively. This can be compared with ranges of normalized current densities values from the literature [2, 121] of 64-110, 380-400, 280, 2.2-5, and 20-160 μA/cm^2/Torr^2. The values for air, He and H_2 are reasonably close; however, our observations are almost an order of magnitude lower for the nitrogen and argon discharges. For the helium discharge we can also compare to atmospheric pressure studies of higher current DC glow discharges [122, 123] where the measured current density was 1.8 A/cm^2, near our measured value of 1.4 A/cm^2. The normal current density is determined by the balance of charge production and loses in the negative glow volume and cathode sheath. At higher pressures, though much

of the scaling of production and diffusion rates is taken into account by the normalized current density, a factor which is not taken into account in the change in the actual species present. For example in argon the dominant ion changes from Ar^+ to Ar_2^+ with increasing pressure. The measured current density of the Argon discharge is 0.83 A/cm^2 close to the value of 1.0 A/cm^2 predicted by atmospheric pressure plasmas modeling [102] which takes into account these chemical changes. In nitrogen even at 10 Torr other researchers have measured normalized current densities of 400 µA/cm^2/Torr^2 [124]. The significant difference in current density cannot be explained by an error in either the temperature measurement (a temperature of > 2000K would be required) or in discharge diameter (an error of almost 40 pixels would be required).
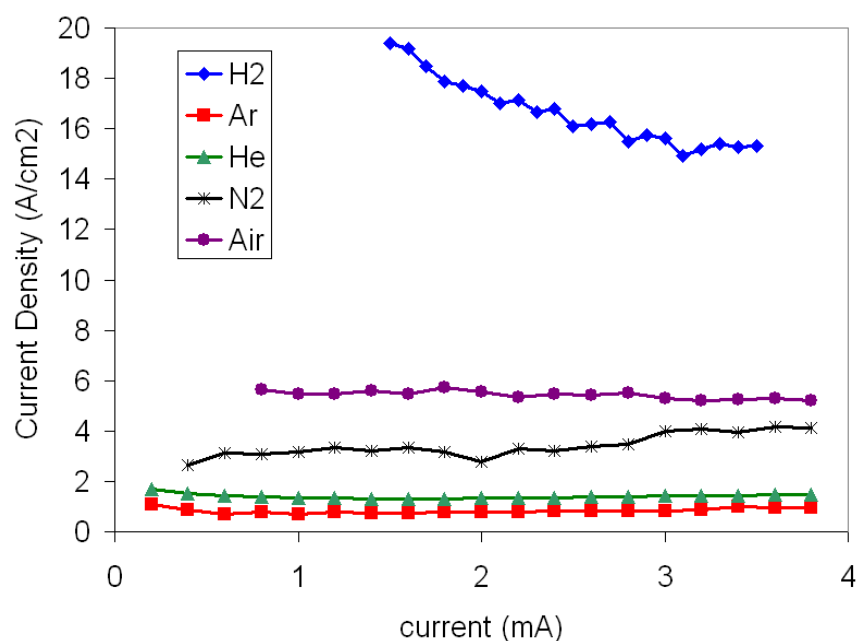
Figure 6.17: Current densities measured in the negative glow of the glow discharge for the various gases at an electrode spacing of 0.4 mm.

6.5.3. Pressure Variation

The significant gas temperature effects shown in Figure 6.6 are apparent in atmospheric pressure glow discharge but not in low pressure discharges. Figure 6.18 is a plot of the temperature as a function of pressure for a DC normal glow discharge in air showing both the measured rotational and vibrational temperatures of Nitrogen. The pressure was controlled using a roughing vacuum pump and air bleed valve from 120 to 760 Torr. In this plot the discharge current and discharge voltage was the same for each pressure, 3.5mA and 400V respectively. This was done by increasing the discharge gap, *d*, as the pressure, *p*, was decreased effectively maintaining the same '*pd*' and discharge power. We see from this plot that the gas temperature, which is equal to the rotational temperature, increases with pressure from 650 K to 1300 K. The vibrational temperature also increases slightly from about 3300 K to 3900 K. Over this pressure range we do not see a complete cooling of the discharge to room temperature conditions which should occur around several Torr. In Figure 6.19 we see the current density in the discharge as a function of the pressure. The current density in the negative glow decreases with pressure as expected from the von Engel and Steenbeck normalized current density.[107] A trend of $j \sim p^2$, typically observed for low pressure (< 1 Torr)[29] is not observed due to the combined temperature and pressure effects. The temperature decreases with pressure and a lower temperature would cause a higher current density. The combined decrease in temperature (causing higher *j*) and decrease in pressure (causing lower *j*) result in a net decrease in the current density with decreasing pressure. In the positive column a similar combination of effects results in an almost constant diameter of the positive column discussed further below.
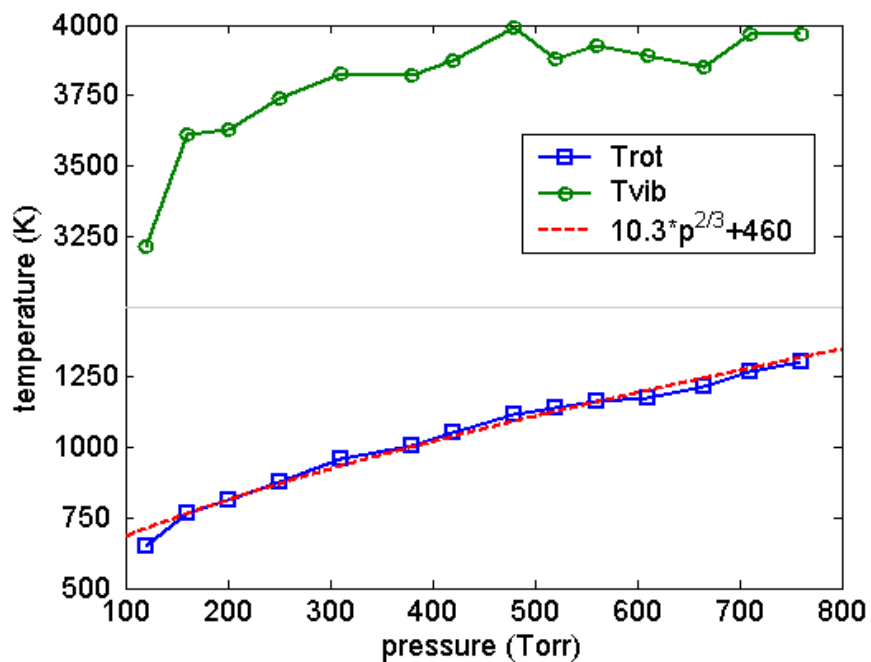
Fig 6.18: Variation of gas temperature with pressure in DC glow normal discharge in air,

3.5mA and 400V.
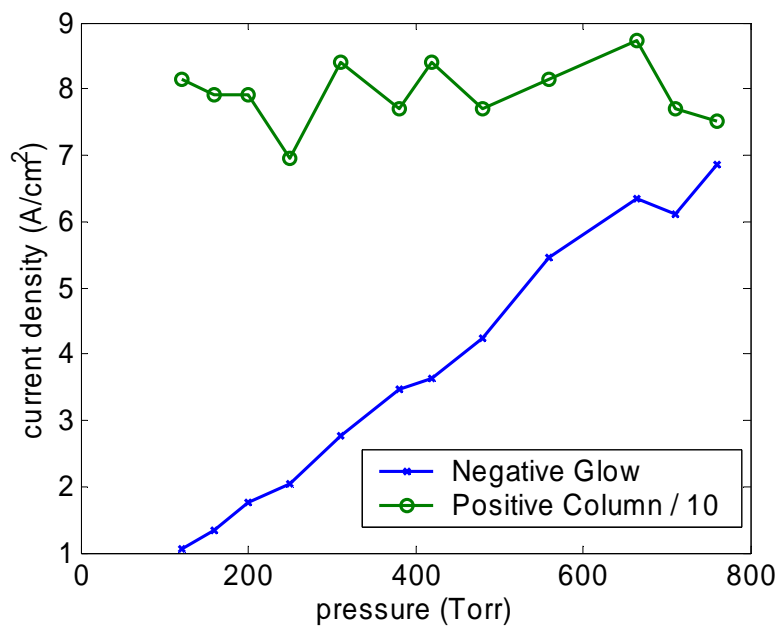
Figure 6.19: Current density in the positive column and negative glow as a function of the air pressure.

6.5.3.1.   Radius of the Positive Column

A distinct difference in the operation of atmospheric pressure normal glow discharges and low pressure normal glow discharges is in the factors determining the radius of the discharge. For the negative glow region the von Engel and Steenbeck normalized current density taking into account both temperature and pressure seems to accurately predict the discharge diameter at both high and low pressures. For the positive column typically in low pressure systems the discharge fills the tube in which it is generated. For moderate pressures, ~ few Torr, the positive column can abruptly transition to only the axis of the tube with an increase in electron density. Such discharges mode are typically called constricted mode [125, 126]. Physically the contraction is thought to occur because the gas temperature is locally higher on the axis of the discharge. The high temperature corresponds with a lower density (at constant pressure) and thus an increase of *E/n* and exponential increase in ionization. Ionization decreases with radius and at some radius recombination will exceed ionization and the plasma will be bounded. The diameter of the contracted discharge is thus highly dependent on the radial non-uniformity of the discharge temperature and the size of the higher temperature zone.

As originally introduced in ref. [68] the radius of the warm region and thus positive column can be roughly estimated by determining the radius where diffusion cooling and electron impact heating of the gas balance. The time for a neutral to diffuse out of the

discharge is the cooling time, τ_c, and is related to the diffusion coefficient, D, and the radius of the cylindrical volume, R: $\tau_{cooling} = R^2/(4D)$. The heating time for a single neutral is the inverse of the electron-neutral heating collision frequency, ν_{en}, which in turn is the electron density n_e times the rate constant for electron neutral energy transfer collisions, k_{en}: $\tau_{heating} = 1/(n_e k_{en})$. For molecular gases like air, hydrogen, and nitrogen, the e-V energy transfer is the fastest mode. For atomic gases e-T energy transfer determines k_{en}. k_{en} is thus different for each species and also varies with T_e. The diffusion coefficient D can be determined from the species, pressure and temperature, $D \sim T^{3/2}/p$. The radius is thus approximately, $R^2 = \left(4D_{nom}\left(\frac{T}{T_{nom}}\right)^{3/2}\right)\Big/\left(n_e k_{en}\left(\frac{p}{p_{nom}}\right)\right)$, where the subscript *nom* denotes nominal condition at room temperature and pressure. The gas specific properties are thus D_{nom} and k_{en}. T and n_e also vary with gas and pressure as they are dependent on the discharge conditions.

A simple check of this relationship can be made considering the air discharge pressure, temperature and radius variation. R was observed to be approximately constant (Fig. 6.19 constant current density), for rough approximation k_{en} is approximately constant (assuming constant T_e), and we can neglecting changes in n_e. These assumption and constant R in the heating-time-cooling-time balance relationship would require that $T \sim p^{2/3}$ in figure 6.18. The dashed line on figure 6.18 shows that this relationship fits the observed data well. The model with the positive column radius corresponding to the radius of the high temperature zone is thus suitably accurate and predicts some observed trends for the positive column radius in Air. Consideration of n_e changes (not measured) and more precise estimation of energy transfer rates would be needed to make comparisons for the positive column radius in different gases. We might consider that

Helium is large diameter due to high diffusivity and poor energy transfer (small k_{en}).
Argon though it has poor energy transfer is small diameter due to higher atomic mass and
smaller diffusivity. Nitrogen and air are similar to each other with nitrogen small due to
slightly lower temperature. Lastly hydrogen, similar to He, has high D but it also has
highest energy transfer and so is small in diameter. As mention though detailed modeling
would be necessary to further verify the source of these trends.

6.5.4.   Gas Mixtures

Varying the gas pressure and discharge current ate two methods to control the
discharge gas temperature. The variation with pressure may not be a viable alternative in
all applications. The variation with discharge current is not that significant except for at
very low currents [83]. Another method is to mix molecular (warm) gases with atomic
(cool) gases to achieve discharges at intermediate temperatures. Mixtures with helium are
the obvious choice to reduce the gas temperature since helium operates at the lowest
temperatures. Argon is not a good candidate because its low thermal conductivity causes
it to operate when pure at approximately 700K. Neon possibly could be another low
temperature gas additive but it was not tested. Figure 20 is a plot of the discharge gas
temperature for helium-air mixtures. As we see the effect of helium addition is nearly
linear with respect to the percentage of helium added. The total flow into the vessel was
1.0 SLPM (standard-liters-per-minute) and the flow rates at 40% were 0.4 SLPM He and
0.6 SLPM Air. The discharge gas temperature decrease almost linearly proportional to
the amount of helium added. This effect is likely due to the increased thermal
conductivity of the gas. At high concentration of helium >95% there is a sudden drop in

the temperature. This is likely due to reduced cathode sheath potential and ion joule heating which only occurs at very high helium concentration. This drastic drop is also seen in the voltage required to sustain the discharge. The discharge voltage only reduce to something similar to that achieved in helium when >95% of the Air has been replaced by helium. Similar effects showing significant change in V-I characteristics for small nitrogen addition to helium was observed by other researchers as well [122].
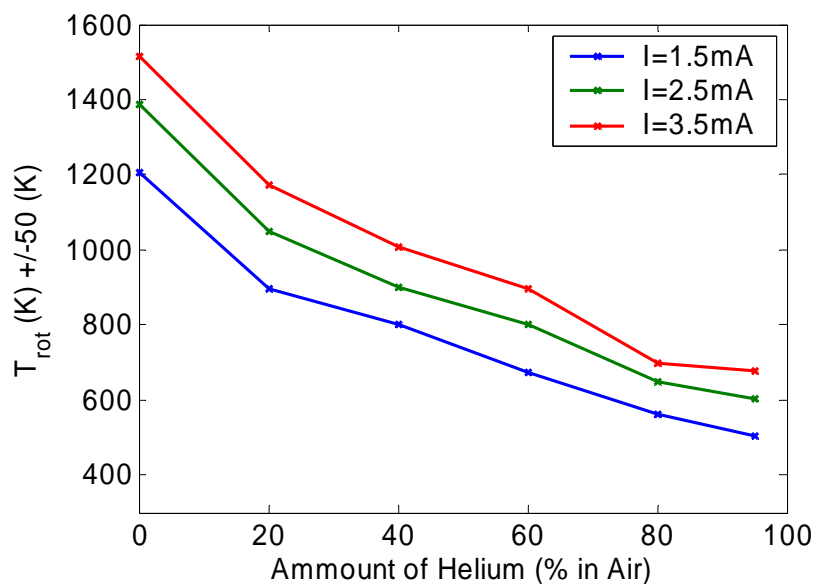
Figure 6.20: Effect of helium addition on the discharge gas temperature of helium-air mixtures.
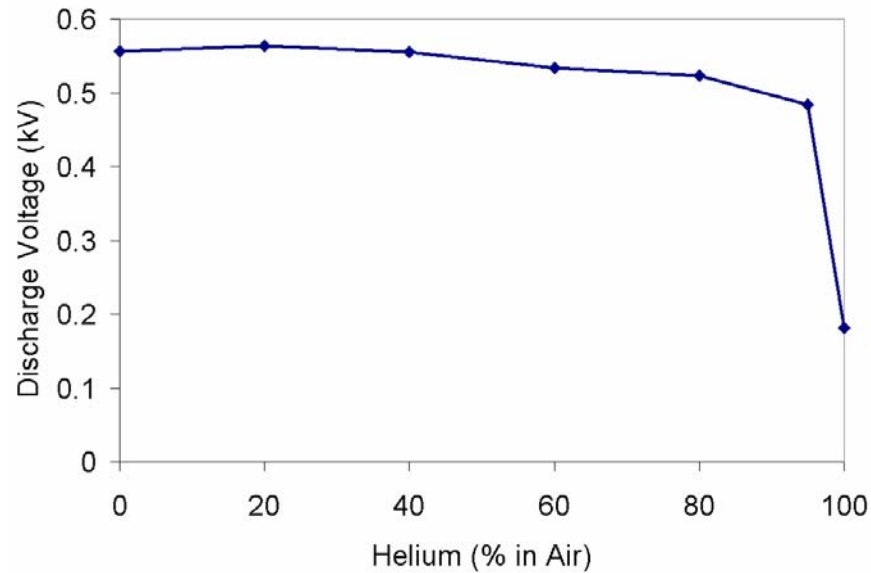
Figure 6.21: Effect of helium addition on the discharge voltage for 2.5 mA discharge.

6.6. Chapter Conclusions

DC normal glow discharges were experimentally investigated in atmospheric pressure Helium, Argon, Hydrogen, Nitrogen and Air. The discharges were characterized by visualization of the discharges and voltage and current measurements for current of several mA, a summary of the measured parameters discussed within this paper is given in Table 6.3. In the normal glow discharges features such as negative glow, Faraday dark space, and positive column regions are clearly observable. In hydrogen and to a lesser extent in argon and helium standing striations of the positive column were visible in the normal glow regime. Normal glow characteristic such as normal current density at the cathode and constant electric field in the positive column are observed and compare well with non-dimensional values from low pressure discharges and Engel-Steenbeck relations.

The rotational and vibrational temperature of the discharges were measured by adding trace amounts of N_2 to the discharge gas and comparing modeled optical emission spectra of the N_2 2nd positive system with spectroscopic measurements from the discharge. The gas temperatures for a 2 mA normal glow discharge were around 350 K, 600 K, 650 K, 900 K, and 1200 K in helium, argon, hydrogen, nitrogen, and air respectively. Gas temperature increase as expected with the number and accessibility of internal energy modes, and decrease with increased thermal conductivity. Vibrational temperatures of N_2 were around 4000K and indicate non-thermal discharge operation. Helium is the only gas able to operate near room temperature over a variety of currents. Mixtures of helium with air achieved intermediate temperatures however the electrical characteristics typically still match that of the air.

Table 6.3: Summary of discharge properties for atmospheric pressure DC normal glow discharges at 0.4 mm electrode spacing and current of 3.5 mA in Air, Nitrogen, Hydrogen, Argon, and Helium.

	Air	N_2	H_2	Ar	He
Discharge length (mm)	0.4	0.4	0.4	0.4	0.4
Discharge voltage (V)	388	283	380	187	178
Discharge current (mA)	3.5	3.5	3.5	3.5	3.5
Discharge power (W)	1.36	0.99	1.33	0.65	0.62
Negative glow diameter (μm)	291	330	171	678	554
Electric field in the positive column (kV cm^{-1})	2.13	1.65	4.20	0.48	0.27
Rotational temperature (K)	1320	887	754	632	417
Vibrational temperature (K)	5906	3870	4956	1667	4598
Electronic excitation temperature (K)	—	—	4193	—	1766
Negative glow current density (A cm^{-2})	5.25	4.09	15.3	0.97	1.45
p_{eff} (Torr)	173	257	302	361	547
E/p_{eff} in positive column (V cm^{-1} Torr^{-1})	12.3	6.4	13.9	1.32	0.49

7. Suppression of Instabilities

7.1. Context

This chapter brings to the forefront a subtlety in the operation of these microplasmas which was previously observed but not understood. Namely, although these systems could be stable they were not always so. Two modes exist; the stable discharge form as presented in the previous chapters and an unstable one which could occur for very similar operating conditions. For the discharge operation in air, it was noted in Chapter 4 that, in the circuit setup, "the stray capacitance was reduced in order to improve the stability of the discharge."[4] This necessary condition was experimentally known but not understood. In later experiments with hydrogen plasmas and hydrogen-methane mixtures for AP-PECVD, the same mode change occurred but was not as easily remedied. In the hydrogen discharges, instability suppression required a deeper understanding of why the fluctuations arose. The understanding and solution of this instability problem is the most essential piece of the puzzle in discovering how to attain thin film AP-PECVD with microplasmas. Initially, the method to suppress the instabilities was noted experimentally; however, the mathematical analysis of the fluctuation allowed for the instability suppression technique to be pushed to its limit. A stable discharge in hydrogen and hydrogen-methane mixtures would not have been possible without the mathematical analysis. This chapter represents a study of the instabilities and their suppression from both an experimental and analytical point of view.

---

[4] The stable operation of these microplasma discharges presented in the earlier results of chapter 3 was the result of the unconscious manifestation of experimental aptitude often labeled as luck.

The contents of this chapter correspond to a paper currently under review for publication, "Stabilization of the Ionization Overheating Thermal Instability in Atmospheric Pressure Microplasmas." [127]

7.2. Summary

Stable DC atmospheric pressure plasmas can regularly be generated in air using microplasma systems, and rapid cooling due to the small size is typically suggested as the thermally stabilizing mechanism. However, temperatures of the stable discharges are significantly higher than ambient and stable operation is not easily achieved in all gases at similar sizes. Revisiting a traditional analysis of the thermal instability we find that the inclusion of the simple ballasted external circuit in the analysis leads to additional stabilizing mechanisms. This stabilization occurs in microplasmas due to the characteristic times of the external circuit and the instability being comparable which allows the electric field to change during the time frame of the instability. Experimentally this is implemented by reducing the stray capacitance of the external circuit. This stabilizing mechanism is verified in several gases and its application in a plasma enhanced chemical vapor deposition system leads to more uniform film deposition.

7.3. Introduction

A challenge with maintaining non-thermal plasmas at atmospheric pressure is preventing thermalization of the discharge and thus maintaining a stable non-thermal discharge. This thermalization typically arises due to inherent instabilities in the plasma, such as the thermal instability also referred to as the ionization overheating instability[1, 27]

(IOI), which, result in a rapid increase in the gas discharge temperature if they are not suppressed. At atmospheric pressure these types of instabilities are more prevalent due to the increased collisionality of the systems. In this chapter we address the onset of the ionization overheating instability with regards to atmospheric pressure DC normal glow discharges[127] which are a basic type of atmospheric pressure microplasma dicharges.[36] These discharges are non-equilibrium but warm with gas temperatures significantly in excess of the ambient temperature.[83] By many considerations - due to having a gas temperature several times greater than the ambient temperature, these discharges should be unstable or thermal;[2] however, experimentally they can be stable and non-thermal. Unstable discharge regimes though exist as well especially for certain discharge gases and electrical configurations. In this paper, the instabilities in a microdischarge (see Figure 7.1 below) are addressed both from an analytical and experimental perspective. We show that through modification of the external circuit we can increase the range of stable operation. The schematic of the discharge circuit used in our analysis and experiments is shown in Figure 1. A voltage supply, V_1, is connected in series with a ballast resistor, $R_b \sim 500$ kΩ, and the microplasma discharge which has an effective resistance, R_p, dependant on the discharge conditions. A parasitic or stray capacitance, C_1, due to the wiring and geometry exists, regardless, in parallel to the discharge. The capacitance is variable depending on wire length and type and typical values are ~100 pF. The stray capacitance can significantly affect the discharge stability, by acting to control the rate at which the voltage applied to the plasma, V_p, and electric field, E, change across the discharge gap.
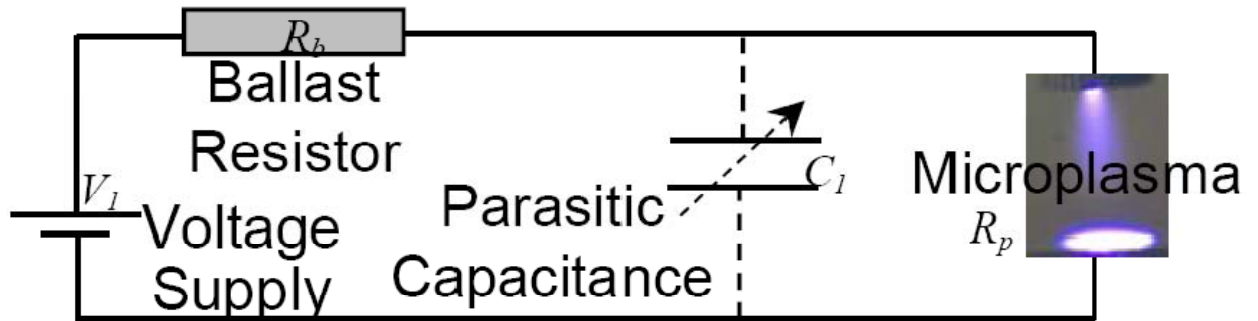
Figure 7.1: Schematic of electric circuit used to generate the microplasmas and for stability analysis.

7.4. Analysis of the Ionization Overheating Instability

Creating stable non-thermal plasmas requires the prevention of thermalization of the discharge as energy is added. Energy given to the electrons from electric field is transferred through inelastic collisions to internal energy modes and translational energy of the gas. In non-equilibrium systems an energy sink maintains this energy flow as one way. Sinks can include electrode surfaces, chamber walls, gas flows and any 'off' time between pulses of the applied voltage. An energy sink is necessary to maintain low gas temperatures but is not the only consideration for stability. In atmospheric pressure systems a common instability which arises and results in thermalization of the discharge is referred to as the ionization overheating instability or thermal instability[1, 2, 27]. This instability is indicated in the causal chain shown in expression (7.A) and can be initiated at any step. An incremental increase, δ, in the electron density n_e leads through collision to an increase in gas temperature, T_o. The T_o increase corresponds with a decrease in neutral density, n_o, by the equation of state at constant pressure. The decrease in density

corresponds to an increase in the reduced electric field, E/n, assuming a constant electric field, E. The electron temperature, T_e is largely determined by E/n and an increase in E/n causes an increase in T_e. At slightly higher T_e the ionization rate, k_i, increases dramatically and causes a further increase in n_e. The chain thus is closed and provides positive feedback.

$$\uparrow \delta n_e \Rightarrow \uparrow \delta T_o \Rightarrow \downarrow \delta n_o \Rightarrow \uparrow \delta \frac{E}{n} \Rightarrow \uparrow \delta T_e \Rightarrow \uparrow \delta k_i \Rightarrow \uparrow \delta n_e \qquad \text{(7.A)}$$

This mechanism is known to be one of the major mechanisms by which non-thermal discharges becomes thermal discharges. In the literature often the transition to a thermal discharge is termed as a glow to arc transition. For clarification we address the relationship between the IOI and the glow to arc transition (GAT).[10] Here GAT corresponds to the transition from secondary electron emission (SEE) to thermionic electron emission (TEE) at the cathode. Glow discharges are sustained by SEE whereas arc discharges are sustained by TEE. This transition to TEE results in an increase in current density, j, and n_e which can often lead to IOI and thermalization of the discharge though in many types of low pressure hot cathode glow discharges this is not the case.[128] Conversely discharges sustained by SEE may become thermal discharges through the IOI addressed here. In that case the contraction and increased heating due to IOI causes TEE and GAT. Thus often in atmospheric pressure discharges GAT and IOI are synonymous though in practice significant limitations on GAT are often imposed by the power supply and the electrode materials.

7.4.1. *Discharge instability without external circuit*

General plasma instabilities including the IOI have analytically been described in detail in many sources.[1, 2, 21-28] Here we consider a simple case wherein just the IOI can be described by the perturbation analysis of a system of two equations (7.1), (7.2) for n_e and T_o.

$$\frac{\partial}{\partial t} n_e = n_e n_o k_i - n_e \frac{D_a}{4\Lambda^2} \tag{7.1}$$

$$\frac{\partial}{\partial t} T_o = \frac{\gamma-1}{\gamma} \frac{jE}{n_o k} - (T_o - T_\infty) \frac{D}{4\Lambda^2} \tag{7.2}$$

Here D_a, is ambipolar electron diffusion coefficient, Λ denotes characteristic discharge size, j is current density, k is the Boltzmann constant, γ is the ratio of specific heats, T_∞ is ambient temperature, , and , D gas diffusion coefficient. The increases in T_o and n_e can be expressed as perturbation from a stable case with exponential growth factor, Ω, in time, t, for example as $T_o=T_o{}^{(0)}+\delta T_o \exp(\Omega t)$ *and* $n_e=n_e{}^{(0)}+\delta n_e \exp(\Omega t)$. Here, as in past studies, for simplification we have considered only inhomogeneities with wave vector perpendicular to the applied electric field which will lead to catastrophic instabilities and discharge contraction. Variations with respect to the electron energy (steps 4,5, and 6 in expression (7.A)) are assumed to be fast and represented by algebraic equations. Similarly sound modes or pressure equilibration time (step 3 in expression

(7.A)) for small magnitude, bounded wavelength perturbations is negligible. Traditionally *E* is taken as a constant; though we readdress this later. Substitution of the perturbed solutions into the linearized equations yields a system of homogeneous algebraic equations for the amplitude of the perturbed values. The values of Ω are the eigen-values of the system. It is stable if the growth factor, Ω, is less than zero, has oscillatory components if imaginary, and is unstable otherwise. Several additional simplifying assumptions can be made including 1) that the rate of ionization ($v_i = n_o k_i$) is greater than the instability growth rate and 2) the sensitivity of the ionization rate to changes in temperature is greater than the sensitivity of gas and electron diffusion to such changes. These assumptions are valid and essentially mean that the gas temperature increase (step 2 in (7.A)) is the rate limiting step in the IOI. Taking these simplifications into account an expression for growth rate, Ω, can be attained as is shown in (7.3).

$$\Omega = \left(\frac{\gamma-1}{\gamma} \frac{jE}{n_o k T_o} \right) \left(\frac{d \ln k_i}{d \ln T_e} \right) - \frac{D}{4\Lambda^2} \tag{7.3}$$

The first part of the first term in (3) is the inverse of the characteristic time of doubling the gas temperature noted as the heating frequency, v_h. The second part of the first term is the logarithmic sensitivity of the ionization rate to a change in electron temperature ($d\ln k_i/d\ln T_e$), and in the following equations and discussions is abbreviated as $\hat{k}_i$. This term arises from properly accounting for the exponential dependence of the ionization rate on electron temperature in the linearization of the system. The second term in equation (7.3) is the gas cooling frequency, v_c. To illustrate how the IOI becomes more prevalent at atmospheric pressures equations (7.4a, 7.4b) depict these frequencies with pressure invariant discharge scaling parameters for normal glow discharges[2] grouped in

brackets. The destabilizing heating term with pressure squared dependence will become more prevalent at higher pressures and the cooling term will be insufficient to stabilize the discharge even taking into account its smaller size.

$$v_h = \left[\left(\tfrac{\gamma-1}{\gamma} \right) \hat{k}_i \left(\frac{j}{p^2} \right) \left(\frac{E}{p} \right) \right] p^2, \qquad v_c = \left[\frac{(Dp/T^{\frac{3}{2}})}{4(p\Lambda)^2} \right] pT^{\frac{3}{2}} \qquad (7.4a, 7.4b)$$

Numerical values for the instability growth rate can be estimated from measured discharge parameters in atmospheric pressure microplasmas[109] and are summarized in Table 7.1 for a variety of gases at nominal conditions. Here E, j, T_o, and Λ are from measured experimental parameters for the positive column of the microplasma which are taken from reference 20. D_{300K} is the gas specific diffusion coefficient at room temperature. Since $k_i \sim exp(I/T_e)$, $\hat{k}_i$ is approximately I/T_e , where I is the ionization energy, and for these simple estimations we assume $T_e = 1$ eV. v_h and v_c are calculated from these parameters by equations (7.4a) and (7.4b). Ω is calculated by equation (7.3). R_p and C_{1max} are related to when the external circuit is included in the analysis and are discussed later. From these estimations v_h and v_c are comparable in value. This is to be expected since for these discharges (with the possible exception of helium which has the lowest gas temperature) the size of the discharge and steady state heat balance are correlated.[109] Since the additional $\hat{k}_i$ factor is included in the calculation of Ω, all of these systems are calculated to be unstable. The numerical value of Ω is on the order of MHz which is significantly higher than for low pressure systems. For molecular gases this calculation of Ω is slightly inaccurate due to the dominant mechanism of gas heating

through intermediate vibrational modes; that is the first two step in (7.A) should be expanded to be three steps: $\uparrow n_e \rightarrow \uparrow T_{vib} \rightarrow \uparrow T_o$, where T_{vib} is the vibrational temperature.[2, 26] The total energy transferred from electrons to the gas is still accurately depicted by the joule heating term, jE, and the additional energy transfer is properly accounted for by the experimentally measured higher E in molecular gases as compared to atomic gases. However the rate limiting step is no longer simply ν_h, but also includes the rates of electron to vibrational (e-V) and vibrational to translational (V-T) energy transfer (ν_{eV} and ν_{VT}). Accounting for this, the first term in equation (7.4) is increased by a factor of 1-5 depending on the relative rates of electron to vibrational (e-V) and vibrational to translational (V-T) energy transfer. A factor of 1 is used in the table and thus gives a slight underestimate of Ω and overestimate of C_{1max}. This additional factor increases with increasing gas temperature and can be large due to the non-linear dependence of V-T energy transfer on the gas temperature.[20]

Table 7.1: Discharge parameters, estimations of instability growth rates, and related parametersfor a 3.5 mA, 400 µm discharge gap in various gases.

Gas	E (kV/cm)	j (A/cm^2)	T_o (K)	Λ (µm)	D_{300K} (cm^2/s)	$\hat{k}_1$	ν_h (kHz)	ν_e (kHz)	Ω (MHz)	R_p (kΩ)	C_{1max} (pF)
Ar	0.48	22	630	29	0.115	15.8	42	42	0.6	53	478
He	0.27	16	417	33	1.103	24.6	17	161	0.3	51	1847
Air	2.13	23	1320	28	0.147	15.6	138	169	2.0	111	71
N$_2$	1.65	20	887	30	0.144	15.6	93	80	1.4	81	141
H$_2$	4.2	38	754	23	1.007	15.4	436	786	5.9	109	24

7.4.2. Inclusion of the External Circuit

These calculated values, shown in Table 7.1, indicate instability, $\Omega > 0$, and that can often be the case. But, in our reported experiments in air[68], we observed that by placing the ballast resistor in the external circuit electrically close to the discharge it would be stabilized. To fully understand the role of the external circuit in stabilizing the microplasma discharges we repeated the traditional IOI perturbation analysis taking into account the parasitic capacitance in the external circuit (shown earlier in Figure 7.1). The external circuit is now formally included in the stability analysis by the addition of a third equation as shown in equation (7.5).[110]

$$\frac{\partial}{\partial t} V_p = \frac{V_1 - V_p}{R_b C_1} - \frac{V_p}{R_p C_1}$$

(7.5)

The same analytical method as before is used to evaluate the possible role of the external circuit. The results (now third order) are in the form of complicated expressions. If we additionally assume that the gas cooling is relatively insignificant ($\nu_c < \Omega$, see the numerical estimations in table I), and a ballast resistor, R_b, is comparable with R_p we attain a simplified expression for the rate of the instability growth as shown in equation (7.6) (coefficients of order unity have been neglected for simplicity).

$$\Omega = \left(\frac{\gamma - 1}{\gamma} \frac{jE}{n_o k T_o} \right) \left(\frac{d \ln k_i}{d \ln T_e} \right) - \left(\frac{1}{R_p C_1} \right) \left(\frac{d \ln k_i}{d \ln T_e} \right)$$

(7.6)

The new term contains a factor $1/R_p C_1$ which is the capacitor's characteristic discharging frequency through the plasma, ν_{RC}, and since the applied electric field is directly associated with ionization, it has a logarithmic sensitivity factor as well. In terms

of the causal chain for the instability growth indicated in expression (7.A), the traditional low pressure analysis provides stability by preventing step 2 (the increase in gas temperature) by effective cooling. With the fast response of the external circuit considered here, we prevent step 4 (the increase in reduced electric field). In response to the perturbation and increase in n_e, the plasma resistance, $R_p \sim 1/n_e T_o$, will decrease and more current will flow into the discharge. This discharges the capacitor and for small capacitance the voltage on the capacitor and the electric field across the discharge gap will quickly reduce such that there is no significant change in E/n_o. A useful expression taking into account both the destabilizing and stabilizing mechanism is shown in (7.8). The 1st term is responsible for the IOI and scales as p^2, the 2nd term corresponds to wall cooling stabilization at low pressures, and the 3rd term represents the passive external circuit stabilization. From this analysis we see that in order to stabilize the discharge, υ_{RC} should be the same magnitude as υ_h. The external circuit stray capacitance, C_1, thus has a maximal value above which the discharge will be unstable. Estimates of this value, C_{1max}, are included in table 7.1 and for air are about 71 pF. In terms of typical high voltage coaxial cabling at ~100pF/m this corresponds to less than 71cm of cable. Hydrogen is the most difficult to stabilize and helium is the easiest.

$$\Omega = \hat{k}_i v_h - v_c - \hat{k}_i v_{RC} \qquad (7.7)$$

7.4.3. Discussion of Analytical Results

The general approach in this analysis is identical to many previous analyses; however, with the relaxation of the assumption that the electric field is constant. The

external circuit is included to determine the changes in the electric field. Such inclusion of the external circuit is generally not found in the existing literature on the ionization overheating instability. This is due in part to the different system considered. The majority and most detailed analysis of the IOI were applications to high power gas discharge lasers where the discharge was indirectly sustained.[1, 27] The original study on the thermal instability[129] however was conducted for a glow discharge controlled by the diffusion of charges to the tube walls, similar to our microplasma which is controlled by diffusion of charges out of the warm discharge zone. In this paper Ecker et. al did include an external circuit into their analysis; however, only by a simple algebraic equation $E = (V_I-IR_b)/L$, where L is the discharge gap length and I is the discharge current. Effectively they neglected any stray capacitance, $C_I=0$. In their solution the discharge was always stable at low currents, similar to our solution with ν_{RC} approaching infinity. Instability was only achieved in their solution at high currents above some critical value. Our work in this way is an extension of Ecker et. al. at low currents although approached from the perspective of more recent works. We show that the low current glow discharges can also be unstable if the response time of the external circuit is too slow, i.e. the parasitic capacitance is too large.

Though over simplified in some respects these results are the first which show that the time dependant effects in the external circuit are especially important to the stability of atmospheric pressure plasma. There are physical reasons why the time response of the external circuit plays a crucial role in atmospheric pressure microplasmas whereas previously it has been ignored. The characteristic frequencies of the instability scale with discharge pressure as shown in equation 7.4a. Thus at lower pressures the

times for the instabilities to develop are much slower. The parameters of the external circuit *(R_b, V_1, C_1)* and the global electrical characteristics of the discharge (V_p, R_p); however, do not scale with pressure. They are thus the same for atmospheric pressure microplasma and low pressure normal glow discharges. For low pressures the circuit is much faster than the instability and its response can be assumed instantaneous as was done by Ecker et. al. At atmospheric pressure the characteristic time of the instability and the external circuit are comparable and our analytical approach is necessary to capture their interaction. In comparison to studies which assume a constant electric field this is not the case for microplasma discharges. The electric circuit can play a role because the changes in plasma parameters can be conveyed to the boundary electrodes of the discharge which connect to the external circuit. This can happen within the time frame of IOI in high pressure discharges as the characteristic times of space charge relaxation and electron transit to the electrode (<0.1ns and ~50ns) are shorter than the characteristic instability time $1/\Omega \sim 1$ µs. In systems using external sources to support the plasma this may not be the case.

7.5. Experimental Results

7.5.1. *Application of discharge stabilization to a DC microplasma*

Experimentally the stabilization mechanism of reducing the stray capacitance was readily achievable in most discharge situations and we were able to verify our hypothesized mechanisms. When the instability arose it was not observed in the voltage and current measurements of the power supply because supply's built in probes measure RMS currents, and the instability arises as a high frequency cyclic behavior. Figure 7.2

shows measured RMS voltage and currents as it is observed for a 400 µm long microplasma in atmospheric pressure hydrogen. The instabilities onsets at lower currents and departs at higher currents with a hysteresis loop as shown. The unstable discharges appear different from the stable discharges as shown in the insets on figure 7.2. The unstable discharge has a more conical shape, is absent of striations, has a less clearly defined Faraday dark space, has a broader cathode spot, and makes a faint buzzing noise. The instability is prevalent at lower current because though υ_h is approximately the same magnitude due to normal current density, υ_{RC} is smaller since $R_p=V_p/I$. Of gases tested (Air, N_2, Ar, He, H_2)[109] as predicted in table 7.1, hydrogen was the most difficult in which to attain stable discharges due to the higher j, E, and thus υ_h in hydrogen. These V-I characteristics in hydrogen were acquired with a 250kΩ ballast resistor placed 2 cm from the anode and an addition 250kΩ resistor on the cathode side 3cm from the cathode. Only with this careful placement of the resistors to minimize wire lengths and reduce the stray capacitance could stable discharges be attained. From estimates of $\Omega = 6$ MHz, for H_2, a $C_l<24$pF is required corresponding to a wire length of less than 25cm in practice stable discharges could only be achieved with stray capacitances less than 3 pF.
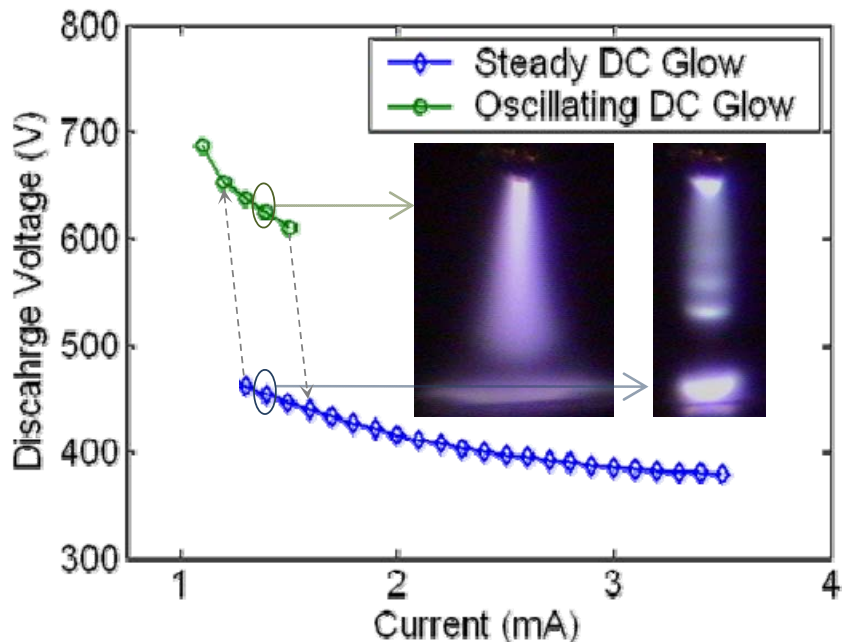
Figure 7.2: RMS Voltage-current characteristic for 400µm DC microplasma glow discharge is atmospheric pressure hydrogen showing transition from unstable/oscillating to stable modes and corresponding change in the appearance of the discharge (insets). For the discharge images shown the anode is a wire at the top of the image and cathode is a plate at the bottom.

Figure 7.3 shows the measured current for an unstable discharge in air at RMS current 3.8 mA, 300µm gap, and 30 cm cable length (C_1 measured with capacitance meter as ~45pF). These waveforms were attained by placing a current transformer (Pearsons 2887, 50MHz bandwidth) on the anode lead wire. Similar voltage measurement could not be made because high frequency voltage dividers utilize capacitive dividers that modify the circuit adding a capacitance and causing stronger instabilities. As is seen the instability presents itself as a sharp increase in the discharge

current consistent with a runaway increase in n_e. The parasitic capacitance eventually discharges and the power supply imposes a current limitation preventing IOI from fully transitioning to a stable arc resulting in pulsing discharges appearing as a sharp increase in current, then turning off and repeating when the circuit recovers (frequency ~ 50kHz). Increasing the power supply voltage and current results in an increase in the frequency of the pulsing, with an eventual sharp transition to a stable discharge at higher currents and lower R_p as shown in Fig. 7.2. To further verify that the instability is also due to stray capacitance, C_1, a high voltage variable capacitor (7 pF -1000 pF) was placed in parallel with a microplasma in helium (the most stable and low temperature discharge tested). Stable to unstable transition was visually observed at a capacitance of about 600 pF for a 2.9mA, 290V discharge as shown in A and B of figure 7.4. The change in discharge appearance is similar to that observed in hydrogen with here the positive column being notably contracted due to the instability. The required capacitance is of the order of that predicted by our analysis. The onset of the instability occurs with no changes in the power supply voltage, ballast resistance, or load line indicating that the instability can be controlled solely by the stray capacitance. The complete cycle of the instability is not predictable by our analysis which is limited to small perturbations and only the initial onset of the instability. To our knowledge instabilities of this type have not been numerically modeled. Though sufficient mechanism probably exist in available models such unstable numerical simulations are often only presented after careful consideration.
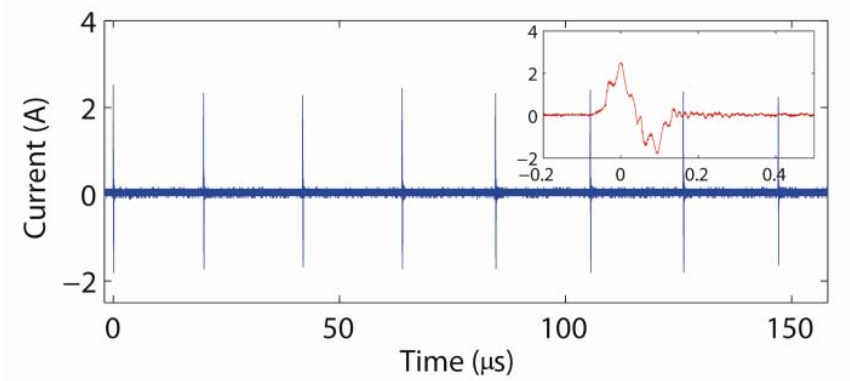
Figure 7.3: Current waveform during unstable operation of a DC glow discharge in atmospheric pressure air. Inset shows higher temporal resolution measurement.
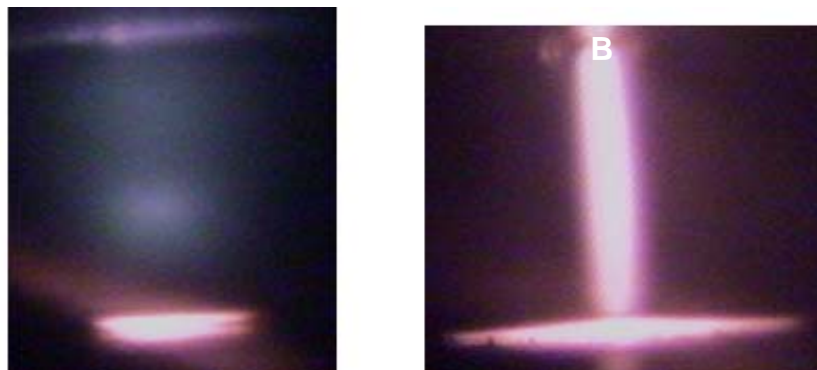
Figure 7.4: Images of atmospheric pressure microplasmas in Helium (A) stable with only nominal (~50 pF) parasitic capacitance and (B) unstable with ~ 600pF capacitor in parallel with discharge. RMS current was 2.9 mA for both discharges.

7.5.2. *Application of Discharge Stabilization to PECVD*

In application we are using this stabilization method to produce more film like plasma enhanced chemical vapor deposition (PECVD) as shown in Figure 7.5. In this

experiment deposition was performed by generating the discharge in a CH_4/H_2 mixture (1%/99%) using the same discharge system with a silicon wafer as cathode operating at 2.5mA discharge current and with a 400 µm discharge gap. Visually the discharges appear similar to the pure H_2 discharge shown in figure 7.2 and the small amount of methane addition does not significantly alter the discharge. Deposition of amorphous hydrogenated carbon (with varying structure and H to C ratios) occurs in the vicinity of the negative glow. The unstable discharge (Fig. 7.5A) which has a stray capacitance of approximately 20 pF, mainly produces many carbonaceous spots each likely corresponding to the contracted discharge which develops during the IOI. These spots are visible in figure 7.5A. Though some not completely understood film like deposits are also seen in Fig. 7.5A at the outer edge, they deposit likely from the initial non-thermal regime of the discharge. The stabilized discharge, $C_1 < 5pF$, (Fig. 5B) produces a more uniform film under the negative glow. Detailed study of these deposition processes as affected by gas discharge parameters will be available in Chapter 8. The larger diameter of the deposition region for the unstabilized case likely corresponds to the observed larger size of the negative glow region in the unstable case (Figure 7.2). The most striking result, towards the goal of depositing uniform thin films, is the significant improvement in uniformity of the film achieved by stabilizing the plasma discharge.
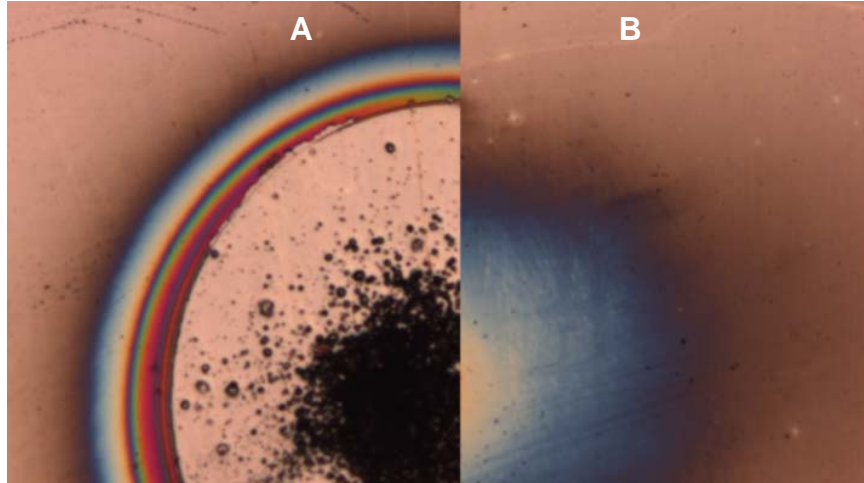
Figure 7.5: Micrographs of deposited amorphous carbon (aC:H) from atmospheric pressure CH$_4$/H2 mixture (1%/99%) in case of (A) unstabilized and (B) external circuit stabilized microplasmas. Magnification in both images is the same.

7.6. Chapter Conclusions

Stable atmospheric pressure microplasmas have been created by reducing the discharge size to millimeters or less. These discharges are non-thermal but warm, $T_e >$ $T_{gas} > T_{ambient}$. Traditional considerations indicate that such atmospheric pressure discharges should be susceptible to the ionization overheating instabilities, due to the scaling of the frequency of the instability increment with pressure and operation at temperatures significantly above ambient; however they are stable. Suggestions have been that, at these small sizes, rapid cooling to the electrodes stabilizes the microplasmas. In this paper we revisit the perturbation analyses leading to the ionization overheating instability and apply them to atmospheric pressure microplasmas systems. Wall cooling, while having a stabilizing influence, appears inadequate to prevent the instabilities.

Through experimentation we noted that stable and unstable modes could be attained and their appearance was very sensitive to the configuration of the external circuit, most notably the parasitic capacitances due to wiring and electrode geometry. Addition of the external circuit into the perturbation analysis revealed a significant stabilizing factor inversely proportional to the parasitic capacitance. Instabilities can be suppressed if the external circuit responds to changes in the plasma at frequencies on the order of the characteristic gas heating rate.

Both by analytical methods and experiment we have shown that atmospheric pressure normal glow microplasmas are susceptible to instabilities which can be suppressed by careful modification of the external circuit of the discharge. This directly leads to the ability to operate stable DC microplasma at lower discharge currents and in a wider variety of gases. This circuit stabilization mechanism described here is simple requiring no active elements and is relatively easy to implement. However, there are practical limits as to the minimum achievable capacitance in the external circuit and thus to the overall applicability of this method. For example, it is difficult to reduce stray capacitance for a discharge system with rather large area of electrodes. Circuit wiring schemes with parasitic capacitance less the several pF are also not easily achieved.

Though shown here for DC microplasma the concept of using a fast response time external circuit to stabilize the ionization overheating instability may be more generally applied to understanding other types of atmospheric pressure discharge non-uniformities and instabilities. The mechanisms of the instability shown in equation 1 are generally applicable to most any self sustained atmospheric pressure non-thermal discharge system. The rate of the instability growth can be quite fast on the order of 1 MHz depending

mostly on the local current density in the discharge system. Systems which have sufficiently high current density such that the ionization overheating instability cannot be stabilized by simple diffusive gas cooling including the streamers in DBD discharges, and all gamma mode discharges (whether DC, AC or RF). Such systems may benefit from a fast response time of the external circuit or alternatively higher frequency pulsing or excitation.

8.   Realization of Thin Film Deposition

8.1. Context

This chapter represents the use of the general knowledge gained by the previous studies to a specific application. Here, thin film, atmospheric pressure, plasma-enhanced chemical vapor deposition (AP-PECVD), using the DC microplasmas studied, is demonstrated. This has never been done before. The chapter, though similar to the previous ones, focuses on the fundamentals, and addresses the customary problems associated with thin film deposition at atmospheric pressure, namely: 1) discharge stability, 2) particle formation, and 3) deposition uniformity. The solutions given to these problems rely heavily on the control of instabilities and temperature, as well as the determination of discharge size, structure, and behavior as presented in the earlier chapters/papers. This section corresponds to a paper currently in preparation for publication "Realization of Thin Film Deposition Using Atmospheric Pressure DC Microplasmas."[130] This chapter addresses each of the customary problems, in turn, and offers step-by-step improvement of the thin film quality of the deposition. Along with the demonstration of thin film deposition materials, characterization of the deposited samples is included to show that a range of amorphous, carbon thin films can be deposited, comparable to those of other techniques.

8.2. Summary

Atmospheric pressure DC microplasma discharges in methane-hydrogen mixtures were used to created amorphous carbon coatings on silicon substrates. Several major concerns exist in attempting to use atmospheric pressure plasmas for plasma enhanced chemical vapor deposition (PECVD), which determines the characterization of the deposition as "thick film" or "thin film" and its usefulness in applications. These include: 1) Plasma stabilization, 2) discharge uniformity and size, and 3) particle formation. Here we address these concerns and through modification of the plasma discharge conditions including external circuit parameters, substrate temperature, gas temperature, and gas mixture and are able to control the uniformity and particle generation within the plasma resulting in the deposition of thin films. Transparent hydrogenated amorphous carbon thin films can be deposited at atmospheric pressure using the high energy density glow discharge at a rate of about 10 nm/s. Though uniform, the deposition is localized to the small region of the discharge and this may be used to advantage in maskless micropatterning. The quality of the thin films is mainly characterized by optical micrographs and profilometry though some properties of the deposited films are also characterized by Raman spectroscopy, and indentation analyses.

8.3. Introduction

Atmospheric pressure plasma discharges[10] are of growing interest in plasma materials processing and micro-manufacturing techniques for several reasons. These include: lower facility costs for a variety of techniques and methods currently performed in vacuum conditions[51], continuous rather than batch processes for inline manufacturing,

and higher deposition rate due to the higher processing densities.[52, 53] At atmospheric pressure there are also opportunities to work with materials and devices which previously have not been considered. For example, deposition onto non-vacuum compatible substrates or large devices. Also considering the microplasma discharges addressed here, the localized nature and atmospheric pressure operation allow for them to be used on components of already assembled devices which may not fit in a vacuum system or be vacuum compatible.

A requirement for many of these vacuum processing techniques is the creation of a non-thermal plasma (also called cold plasmas).[2] In non-thermal plasmas, excitation and ionization of particles occurs mainly through electron impact, leading to a non-equilibrium distribution of energy. In plasma materials processing the non-equilibrium nature allows for the creation of active species to interact with the substrate without generating excessive heat which could destroy the substrate.[3] The creation of non-thermal plasmas of the same type as used in vacuum processing (called glow discharges) at atmospheric pressure is a challenge[10] due to several problems which arises due to the inherent decrease in collision lengths and increase in power density of glow discharges with pressure. First, this can lead to instabilities, an overheating of the discharge, transition to a thermal discharge and transition from the glow mode to an arc discharge.[1] The arc discharge with temperatures ~ 10000 K is unsuitable for most materials processing even if the arc is only transient. Traditional non-thermal atmospheric pressure plasmas such as coronas and dielectric barrier discharges solve the overheating problems by operating at low currents or limiting the current density through the use of dielectric barriers respectively. But some limitations with these discharges occuring due to their

spatial and temporal non-uniformities lead to another problem of deposition non-uniformity. The last problem, due to the increased collisionality at atmospheric pressures, is the increased formation of particles. At higher gas densities, n, volumetric processes ($\sim n^2$) which lead to particle formation may overwhelm surface deposition events which are dependent on surface fluxes ($\sim n$). These problems can be summarized as 1) the creation of stable non-thermal plasma discharges 2) discharge uniformity and size, and 3) particle formation.

There are several different approaches currently being researched to remedy these problems mainly relying on novel plasma discharges and deposition systems and comparisons of low pressure and atmospheric pressure deposited films indicate many similarities.[54] Atmospheric pressure plasma enhanced chemical vapor deposition (AP-PECVD) of thin films has been attempted for various materials including for example (but not limited to): silicon oxides and various glasses[55-57], titanium oxides,[58, 59] silicon,[60, 61] alumina,[62] hydrocarbons[12, 13, 63, 64], and fluorocarbons.[33] These various films have been deposited in turn by several different types of discharges including 1) helium glow DBDs,[12, 33, 55, 62, 63] 2) non-helium sinusoidal DBDs,[56] 3) short (μs) pulsed DBDs,[60] 4) helium RF (13-27 MHz) afterglows (so called APPJs and cold torches),[57, 59] 5) helium RF (13.6MHz) CCPs,[58] 6) helium VHF (150MHz) CCPs,[61] and 7) DC microplasmas.[13, 64] In most of these systems the deposition of uniform thin films without patterns, granules, particles, globules or significant (> 50nm) surface roughness requires significant use of helium buffer gas to maintain discharge uniformity and stability. For the helium based systems typically precursor concentrations are around 0.1% with typical deposition rates in the 0.2 to 2 nm/s range for the lower frequency DBD systems and as high as 15

nm/s for the RF and VHF CCPs and jets (it should be noted that the RF and VHF systems typically have significantly higher gas flow rates to help with discharge cooling). Among the non-helium based discharges reviewed clear evidence of the deposition of uniform thin films is not shown. Though nanosecond duration pulses seem effective for generating uniform DBDs[34, 65] in complex gases. It is not clear if the µs pulses of Matsumoto[60] are sufficient to ensure no discharge filamentation during deposition and some non-uniformity and surface roughness appears apparent from the images presented. Likewise sinusoidal DBDs generate film non-uniformities when the precursor concentration is too high (~>0.1%).[55, 56] For DC microplasma AP-PECVD of Ito et al[13] though precursor concentrations as high as 75% were tested and material was deposited, no evidence of the nature, uniformity or thin film quality of the deposits is presented. In addition device fouling and electrode destruction was noted during atmospheric pressure operation and it required operation at reduced pressures to attain more stable deposition.

In this chapter we address the following issues: discharge stability, deposition uniformity, and particle formation in the AP-PECVD of uniform thin films with reference to the use of DC microplasmas.[36] Specifically we use DC normal glow microplasmas.[68] Recent investigations of these atmospheric pressure micro-glow discharges have shown them to be non-equilibrium, uniform plasma discharges, similar to those normal glow discharge used in vacuum materials processing.[37] [68]A major difference from low-pressure systems is that the gas temperature can be significantly higher than the ambient; though some mechanisms to control the temperature exist including noble gas admixtures[109] and minimizing discharge power.[83] In comparison to helium glow DBDs, microplasmas have typically 2-3 orders of magnitude higher power densities. This higher

power density is more challenging in terms of maintaining low discharge temperatures and preventing particle formation. However, the DC glow is more stable and does not have temporal or spatial non-uniformities. As a proof of the concept that such plasmas can indeed perform processing similar to some vacuum techniques, amorphous carbon (a-C) film deposition was attempted using plasma enhanced chemical vapor deposition (PECVD) methods. A severe disadvantage in depositing large area films is presented by the small size of the discharge. However, we show in preliminary work that by rastering the discharge, this small size may be used to advantage by allowing maskless micropatterning with feature sizes of about 25 um.

Amorphous carbon (a-C) was chosen as a test material for several reasons. First is the relative safety of the precursors, second is the potential variety of materials from diamond like carbon (DLC) to polymers which may be deposited and third, the possible sooting of the precursors presents a relevant challenge. Such material also has many desirable material properties and if the cost of production could be reduced by these atmospheric pressure techniques, their application can be extended beyond existing niches. In typical PECVD of a-C and DLC, hydrogen with trace amounts (~1%) of methane is fed into a low pressure plasma discharge chamber and hydrogenated amorphous carbon (a-C:H) is deposited. The general mechanism of deposition[7, 49] is that a flux of carbon containing reactive molecules (CH_3, CH_2) and ions from the plasma deposits carbon in both sp^2 and sp^3 phase onto the substrate. Atomic hydrogen created by the plasma chemically etches hydrogen from C-H sp^3 allowing the formation of C-C sp^3 bonds. Energetic ions and hydrogen from the plasma also preferentially etch sp^2 phase carbon from the deposited layer enriching the sp^3 content. Energetic ions also provide

energy to form sp3 phases through stitching processes.[50] At atmospheric pressure the deposition mechanisms are expected to be generally similar, as shown in figure 8.1. In the plasma discharge the chemically active species such as CH_3 and CH_2 are generated and may deposit on the surface in a thin film as in the case of low pressure systems. However, at atmospheric pressure due to the increased density and collisionality there is also an increased propensity to nucleate particles within the discharge which may deposit forming a non-uniform, particle comprised, rough thick film. Pyrolysis of acetylene is at the root of the particle formation mechanism. Such particle formation can usually be suppressed if the temperature is kept sufficiently low, typically <400°C. In addition to non-uniformities due to particle growth non-uniformities in the film can also occur if the plasma in non-uniform.
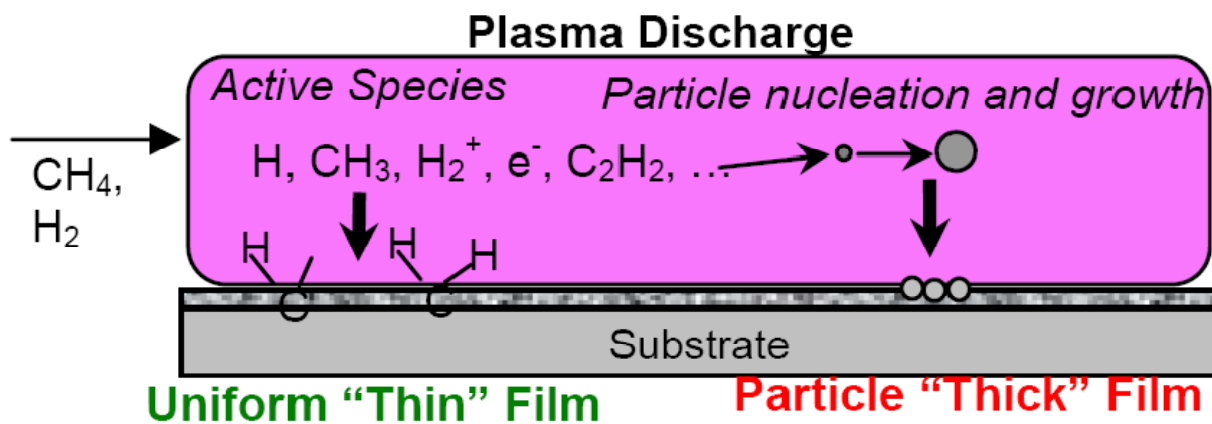
Figure 8.1: Schematic representation of particle and thin film mechanisms of deposition.

The hydrogen and methane precursors used in this study result in the deposition of various types of hydrogenated amorphous carbon (a-C:H). In the limits these might

include sp^2 bonded graphitic material, sp^3 bonded carbon in the form of diamond, and various sp^3 bonded carbon hydrogen mixtures such as polymers. Raman spectroscopy is a fast and non-destructive method for the analysis of carbon materials. a-C:H deposited using PECVD can contain widely varying sp^3 content and hydrogen content. The deposited material is often heterogeneous and can contain mixtures of nano/micro crystalline diamond, graphite, amorphous sp^2 carbon, amorphous sp^3 carbon and polymeric (hydrogen containing) carbon. Depending on the relative concentrations of these components terms such as graphite like carbon hydrogenated (GLCH), diamond like carbon hydrogenated (DLCH), hydrogen containing polymer like carbon (PLCH) and tetrahedral amorphous carbon (taC) are used (although the nomenclature does vary somewhat in the literature)[66]. Typically if the H content is sufficiently low (<20%), the H is dropped from the name of the material.[67]

8.4. Experimental Setup and Methods

8.4.1. Reactor Chamber

The PECVD reactor used in these experiments is identical to that used in our previous studies[109] and is shown in Figure 8.2. The microplasma discharge is generated between an anode electrode wire 0.5 mm in diameter suspended above a conductive silicon wafer substrate which is cathode biased. The electrode polarity can be reversed. The substrate holder can be heated from room temperature to about 300°C and is movable using computer controlled stepper motors and a 3 axis micropositioner. The gas mixture inside of the chamber is maintained by a set of mass flow controls. The gas inlet is

baffled such that species influx into the discharge zone is largely diffusive. The power supply is connect in series to two ballast resistors placed inside of the chamber near the discharge which minimizes stray capacitances in the circuit.
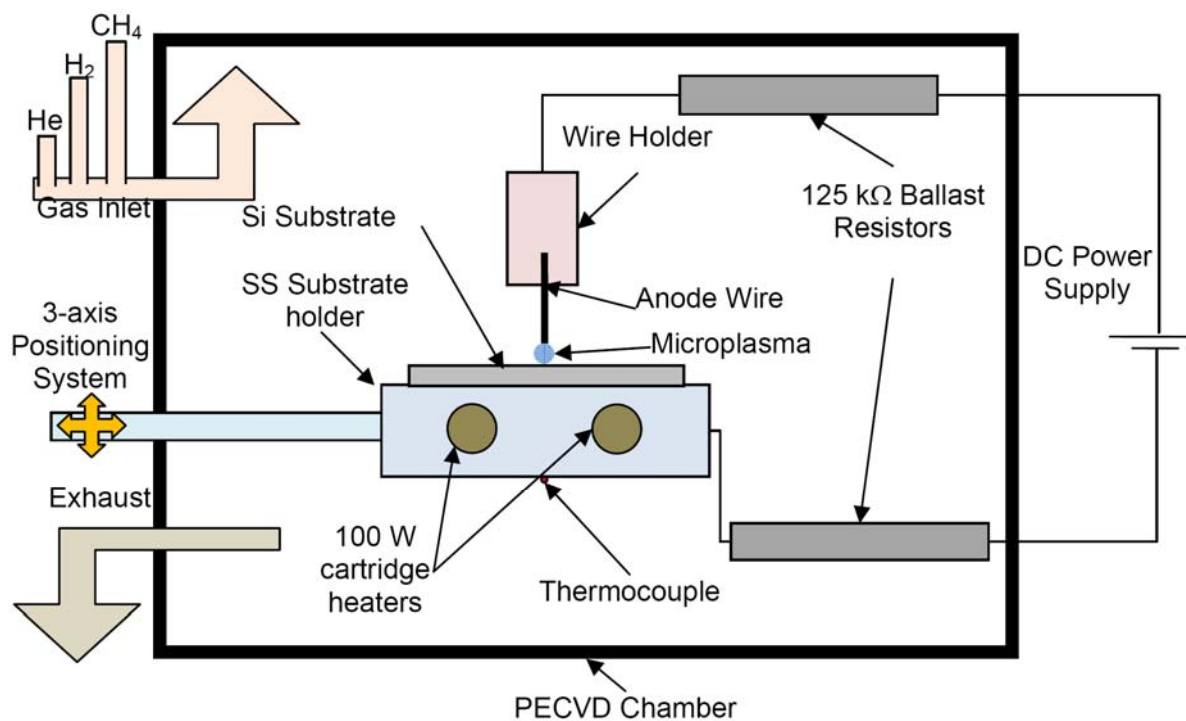
Figure 8.2: Schematic of AP-PECVD reactor

8.4.2. *Discharge Setup*

Figure 8.3 shows an image of this discharge for 2 mA discharge current, cathode biasing of the substrate, and 1% CH_4. A 100 μm wire anode is visible coming from the top of the image. The silicon substrate has a mirror quality and a reflection of the discharge and wire is visible in the bottom half of the image. The planar silicon substrate/cathode is at the mirror-symmetry line in the center of the image. The image of

the micro-plasma was taken through a microscope, the gap between the anode and cathode is about 400 μm. Discharge conditions such as methane fraction, and discharge current were varied to see the effects upon the deposited material. Also helium was added to the hydrogen-methane mixture in order to reduce the discharge temperature.
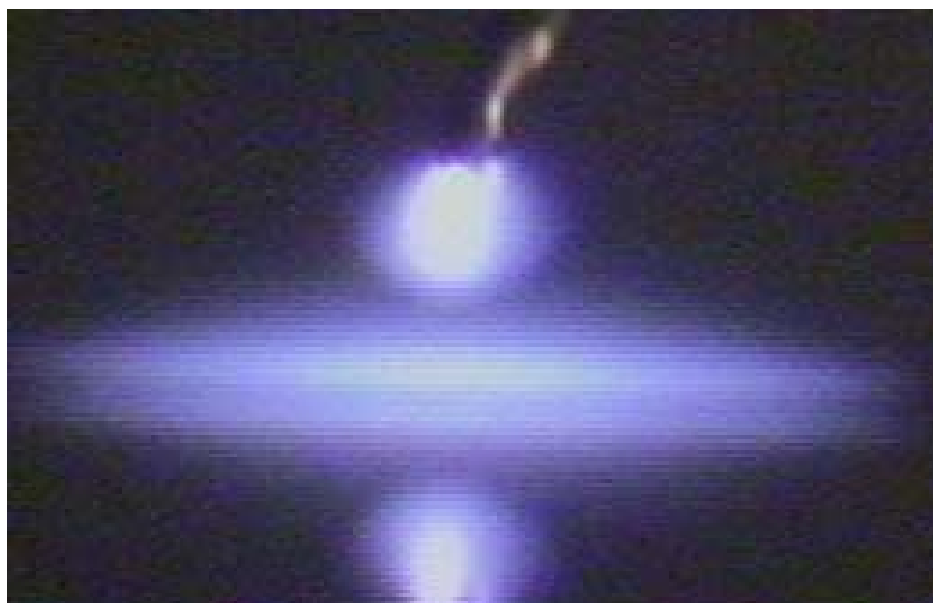
Figure 8.3: 2mA DC microplasma with an unstabilized circuit in atmospheric pressure H_2/CH_4 (99%/1%) mixture.

8.4.3. *Sample Treatment*

Samples were treated as follows. A 25 mm square piece was cut from a <100> silicon wafer and then cleaned by washing with alcohol and then water. Drying was done with a lint free wipe. The silicon was then placed onto the substrate holder in the AP-PECVD chamber. The chamber was sealed then evacuated and filled with the H_2/CH_4 gas

mixture. About 500 sccm of process gas was flowed into the chamber and let out through an exhaust valve; the gas mixture and flow rate was maintained by two mass flow controllers. The pressure in the chamber was maintained at around 770 Torr. The anode wire was positioned over the center of the substrate at a gap of about 0.5 mm. If desired the substrate heater was turned on and a thermocouple was used to monitor the substrate temperature. After steady state was achieved the plasma discharge was turned on for different time intervals varying from several seconds to several minutes. In certain situations the substrate was moved and a deposition pattern was written onto the substrate. After deposition, the discharge was turned off, the chamber unsealed, and the substrate removed. Due to the localized nature of the deposition a circular deposition region corresponding to the area of the discharge is typically seen. Regions adjacent to the discharge but not under the discharge could occasionally develop a sooty residue which was easily removed. This was more likely to occur at higher discharge current and higher methane concentration. Within the circular region a hard deposit is formed which is difficult to remove. Prior to the Raman spectroscopy and other analyses the samples were cleaned as mentioned above.

8.4.4. Raman Analysis

Two Renishaw RM1000 Raman Micro-spectrometers were used to image and analyze the deposited samples. One was configured for use in the visible and infrared at 514 nm, 633nm or 780 nm, and the other for use in the ultraviolet at 325 nm. Ultraviolet excitation at 244 nm is also often deemed necessary for more conclusive analysis of

DLC[67] however was not available for use. The Raman microscope was used to analyze regions of several microns in size. No laser heating effects were noted by changing the sampling duration or laser power probably due to the high thermal conductivity of the silicon substrate. Raman spectra were acquired at various times and accumulations depending on the signal levels from the sample.

The Raman spectra of hydrogenated carbon compounds generally show the presence of several peaks including; the graphitic (G), disorder (D), sp^3 vibrational density of states (T), diamond peaks, and peaks due to polymers.[49, 67, 131-134] The G peak is due to carbon stretching in all sp^2 bonds; in crystalline graphite it is a sharp peak around 1580 cm^{-1}, and in amorphous carbons it becomes significantly broader and may shift in position. The D peak is due to the breathing modes of sp^2 atoms in carbon rings and occurs around 1360 cm^{-1}. The T peak is due to the carbon stretching in sp^3 bonds having a vibrational density of states distribution around 1060 cm^{-1}. Crystalline diamond has a sharp peak at 1332 cm^{-1}. Polymers in general provide a significant fluorescence background signal in the visible part of the spectrum. Also specific polymers may be present such as polyacetylene with bands at 1150^{-1} and 1450 cm^{-1}.[135] Broad C-H polymer bands may also be present at 2940 cm^{-1}.

Interpretation of the Raman spectra follows some of the methods described by the University of Cambridge research group.[131, 136, 137] The spectra are fit by a G-peak, a D-peak , and a linear background signal. In the 514 nm spectra, parameters such as the G peak location, pos(G), the relative intensity of the D and G peak heights, I(D)/I(G), and normalized slope of the background line, m/I(G), are used to estimate the hydrogen content, crystal size, and sp^3 fraction. This method of analyzing the 514nm spectra infers

the sp^3 configuration of the sample from the behavior of the sp^2 Raman peaks. A more direct observation of sp^3 band is only available using UV excitation where the D-band becomes relatively less intense due to decreased resonance. With 325nm excitation and very high sp^3 ratio some T band and diamond peaks may be visible though this did not occur in any of our samples.

Raman spectroscopy using a several wavelengths of excitation was employed to confirm the general results of the 514nm analysis. Depending on the plasma discharge conditions, films with varying properties and varying Raman spectra could be deposited. The observed spectra contained signatures of the underlying silicon substrate, the disorder and graphitic bands of carbon and a significant fluorescence background due to the presence of hydrogen in the deposits. Fluorescence was most significant using the 633 nm laser. As mentioned analysis of the sp^2 bands in the 514nm excitation give some indirect indication of the sp^3 structure but are not completely conclusive; though some trends could be noted. The disorder and graphitic bands indicate the presence of sp^2 bonded carbon and do not directly correlate to the sp^3 content or 'diamond like carbon' nature of the deposited films. UV Raman decreases the intensity of the visibly resonant D band; however, in our samples at 325nm the disorder band of the amorphous carbon is too intense and overlaps with and conceals any sp^3 bands which may be present. The Raman analysis thus was not conclusive but it was able to identify the deposits as either graphite like amorphous carbon or a low quality diamond like amorphous carbon.

8.4.5. Film Characterization

In addition to Raman analysis some basic tests on the films hardness and attachment to the substrate were performed such as wiping, solvent cleaning, scratching, and scotch tape testing. Only films which were intact after wiping, solvent cleaning, and the scotch tape test are presented here. Film thickness measurements were measured using a stylus profilometer, optical profilometer (Zygo NewView 6000) and using the diffractive properties of the transparent thin films and a modified isochromatic color fringe chart.[138] Several of the thin films produced were additionally characterized using common nano-indentation techniques[139, 140] and Nanoindenter XP systems (MTS Systems). Modulus and hardness were determined from the analysis of the load displacement curve using a Berkovich tip at a penetration depth of about 50 nm.

8.5. Results and Discussion

8.5.1. Discharge Stability

Stabilization of the plasma discharges was the most important step toward successful uniform thin film deposition. Stable atmospheric pressure non-thermal plasmas in general are difficult to create due to the onset of the ionization overheating instability and similar instabilities at higher pressures which can lead to undesirable self-pulsing, filamentation, and glow to arc transitions in the discharge. The ionization

overheating instability is indicated by this closed-loop chain:[1, 127]

$$\uparrow n_e \Rightarrow \uparrow T_o \Rightarrow \downarrow n_o \Rightarrow \uparrow E/n \Rightarrow \uparrow T_e \Rightarrow \uparrow n_e$$ (details of course can be found in the

preceding chapter). A perturbation in electron density, n_e, leads through collision to an

increase in gas temperature, T_o, and at constant pressure to a decrease in density, n_o. This

in turn can cause an increase in the reduced electric field, E/n and electron temperature T_e

(at constant electric field). Increased T_e through ionization leads to an additional increase

in n_e and an instability. Low pressure systems are stabilized by wall cooling which

prevents the increase in gas temperature which can lead to such instabilities. Such

temperature cooling is insufficient for discharges such as the DC microplasmas

investigated here. These one atmosphere discharges are non-thermal but warm with gas

temperatures in the range of 300K to 1500K depending on the discharge power and

gas.[109] As detailed in chapter 7[127] the DC microplasmas can be stabilized by decreasing

the response time of the external circuit such that E can change within the timeframe of

the instability and the $\uparrow n_e$ causes $\downarrow E$ and $\downarrow E/n_o$ such that the closed-loop is broken.

Using this method of stabilization DC discharges in the PECVD gas mixtures

could be stabilized as shown in Fig. 8.4. A voltage current characteristic for the discharge

is shown in figure 8.4a and insets show images of the discharge in unstable (8.4b) and

stable (8.4c) modes. In general operation with 1% methane was very similar to operation

in pure hydrogen. The exception is that depending on discharge conditions, over the first

few minutes the discharge would change as a layer was formed on the cathode surface.

Operation up to concentrations of about 10% CH_4 were generally similar. Above this

10% threshold the discharge would begin to appear greenish in color (on account of C_2

swan bands) and a carbonaceous wire ~50 μm in diameter would grow from the anode

wire shorting the discharge gap within 10's of seconds.
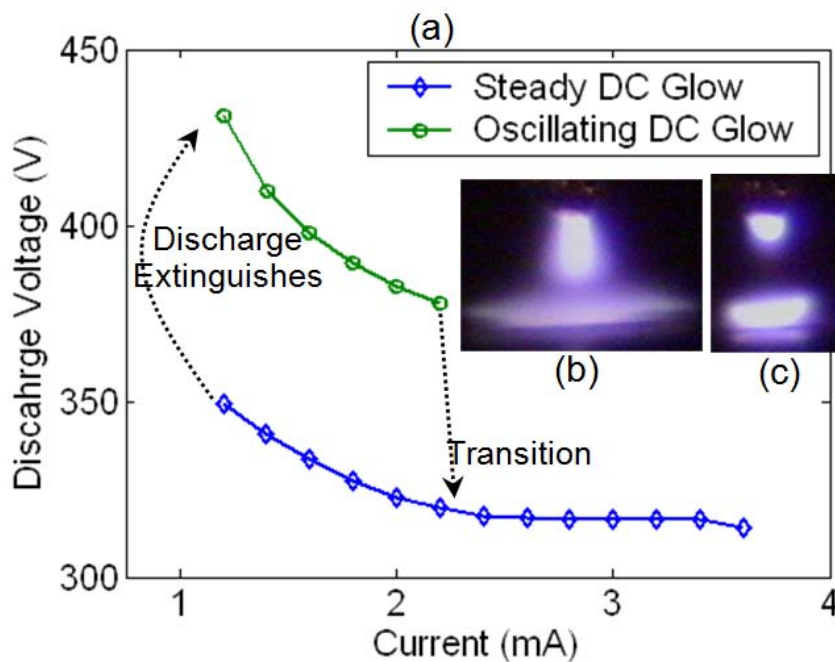
Figure 8.4: (a) voltage current characteristics for an atmospheric pressure H_2/CH_4

(99%/1%) discharge. Electrode gap is 200 μm. Insets show images of the discharge in (b)

unstable/oscillating and (c) stable modes at a current of 1.6 mA.

Figure 8.5 shows images of the deposits which occur on the negatively biased

silicon substrate for an unstable discharge. Figure 8.5a shows the micrograph for a 2 mA

discharge, 5 minutes of deposition and with H_2/CH_4 ratio 99%/1%. Figure 8.5b shows the

micrograph for a 3.8 mA discharge, 15 minutes of deposition and with H_2/CH_4 ratio

99%/1%. Figure 8.5c shows optical profilometry corresponding to a region of figure 8.5b.

Here we see the deposit has some 10-20 μm smooth peaks protruding from a rough

graphitic (as determined by Raman) background. This rough background did not properly track the interference fringes necessary for the optical profilometer analysis and is shown in black in Figure 8.5c. Exactly how these structures are formed is not clear. During the unstable operation what occurs is the discharge ignites, then rapidly thermalizes and contracts as part of the thermal overheating instability. As the discharge current increases all of the energy stored in the stray capacitance is consumed and the discharge extinguishes only to reignite in the same manner with a repetition rate of about 10-100 kHz. Each small dot in figure 8.5a corresponds to a single discharge contraction. When prolonged deposition occurs, the patterned structures as in figure 8.5b occur. It is interesting to note that in figure 8.5a there is a rainbow halo corresponding to the size of the negative glow of the discharge. This rainbow of colors corresponds to the diffraction of various thicknesses of transparent film being deposited on the outer rim of the discharge. As the unstable discharge is thermalizing it first begins in a non-thermal regime with normal cathode layer in which this apparently uniform outer film is deposited. The possibility of thin film deposition is thus indicated if the low temperature regime can be stabilized.
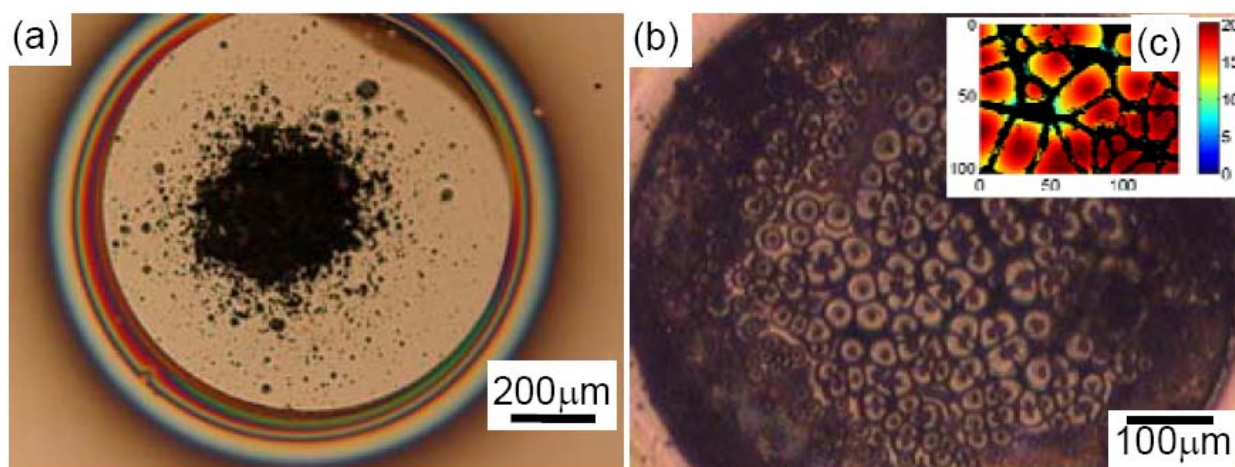
Figure 8.5: Images of deposits using (a) 5 minutes at 2 mA and 15 minutes at 3.8 mA for H_2/CH_4 mixtures 99%/1%. Inset (c) shows optical profilometer results corresponding to a region of 15 minute case. Dimensions and color scale in (c) indicate μm.

In comparison to the depositions with unstable discharges those with stabilized external circuit were considerably more uniform than figure 8.5. Figure 8.6 shows an image of the discharge (Fig. 8.6a) and deposition region (Fig. 8.5b) for a 3.8 mA discharge, at 0.8 mm electrode spacing and with and H_2/CH_4 ratio of 98%/2% and after deposition for 5 minutes. Initially this discharge had similar structure to that in Figure 4c; however, within the first minute as the deposited layer changed the conductive characteristics of the cathode, the discharge spread out laterally. The deposited layer has a lower conductivity such that it limits the current density at any point effectively generating a DC resistive barrier discharge.[141] The final deposit had a diameter of about 1 mm indicating a current density of 0.48 A/cm^2 this is compared to about 16 A/cm^2 for the DC normal glow discharge with conducting cathode. Closer inspection of the film,

Fig. 8.6c, reveals that the deposited film is not a thin film but actually comprised of uniformly deposited nano-particles about 800 nm in diameter.
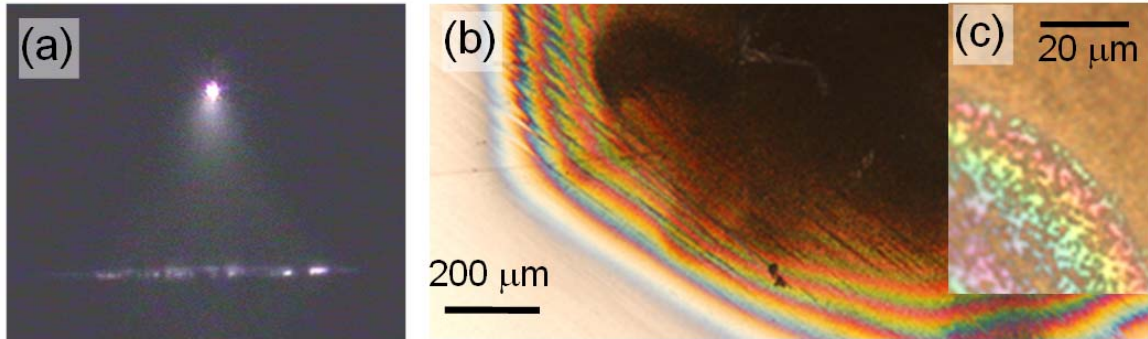
Figure 8.6: (a) Image of stabilized discharge after depositing a resistive layer. (b) Low magnification deposited film indicating general uniform and (c) higher magnification indicating 0.8 μm particle constituents of film.

8.5.2. Particle Formation

If conditions are inappropriate particles will nucleate and aggregate in the discharge volume and finally fall onto the substrate. The formation of particles in volume from the precursors arises in AP-PECVD is due to the increased collisions and the increase in gas temperature for the higher pressure discharges. Two approaches were pursued to stop the formation of particles. First was to reduce the relative methane concentration thus reducing the number of collisions. Second was to reduce the

temperature which was done by two approaches: 1) decreasing the discharge power, and 2) adding atomic gases to the mixture.

Figure 8.7 shows the affect of a reduction in the methane concentration. These images show a high magnification view near the edge of the deposition circle. Discharge current was 2mA, discharge gap was 500 μm, silicon substrate was cathode, and deposition time was 30 seconds. As can be seen the lower methane concentration results in smaller particle sizes. For the 2% methane case (Fig. 8.7a) the particles are relatively uniform in size and about 900 nm in diameter. The particles are more densely concentrated towards the center of the discharge zone. For the 0.4% methane case the particles are almost indistinguishable and the film appears quite uniform. Close inspection of the edge of the film (LHS of Figure 8.7b) where it becomes thinner reveals small particles <500nm in diameter. A reduction in particle size is to be expected considering that the volumetric collision leading to particle formation and growth will decrease proportional to the square of the methane concentration.
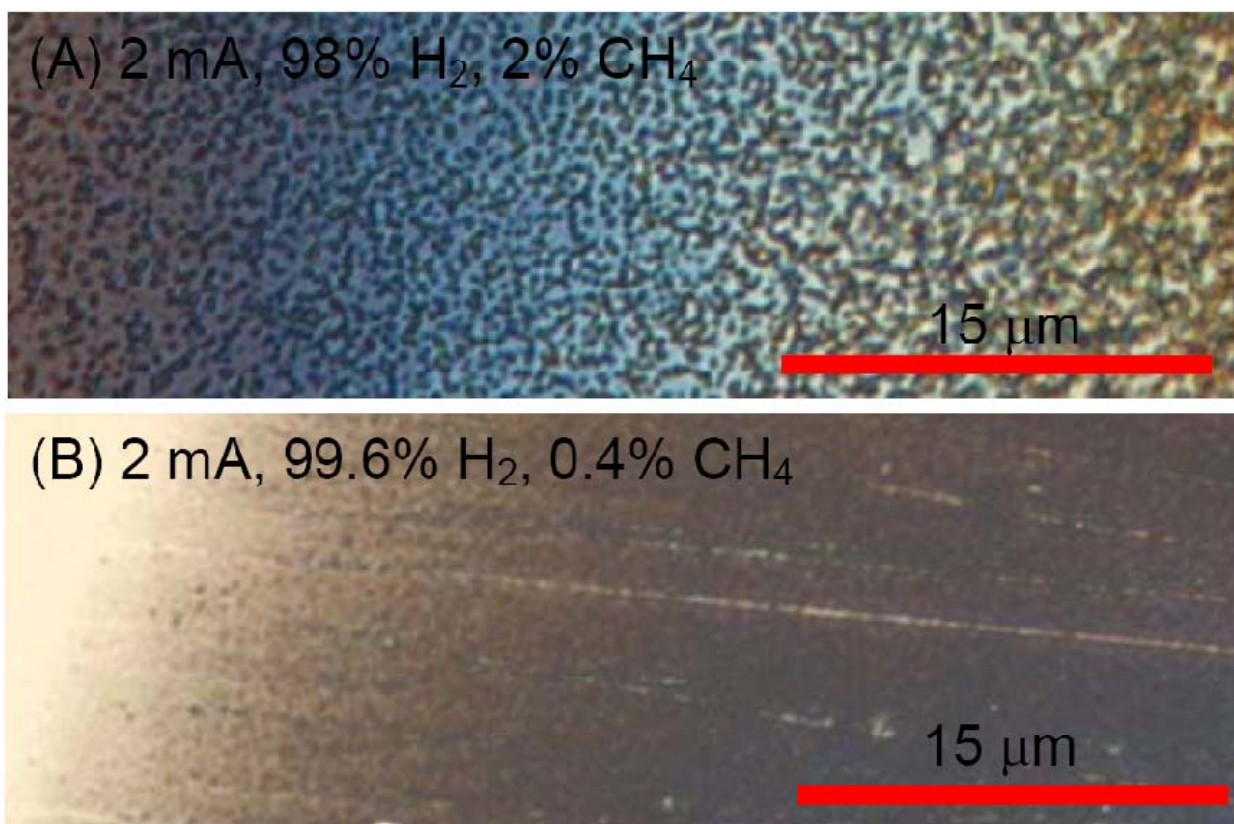
Figure 8.7: Micrograph of films deposited using hydrogen mixtures with (a) 2% methane and (b) 0.4% methane indicating decrease in particle size with reduction of methane concentration.

The formation of particles and higher hydrocarbons from acetylene is a thermally driven process and it is not surprising that the reduction in methane concentration only served to reduce the particle size and number. In contrast the thin film deposition mechanism is governed by the presence of radicals and active species which are generated through electron impact dissociation, vibrational stimulation of endothermic reactions[2] and similar non-thermal processes. These discharges in hydrogen operate at a gas temperature of about 750K and vibrational temperature of about 5000K[109]. This gas

temperature is sufficiently high to drive particle nucleation. This is because above about 400°C the pyrolysis of acetylene will start.[3, 142] The most successful route to remove the particles is thus to reduce the gas temperature. This will reduce the pyrolysis of acetylene but the film deposition processes which are dependent on T_e and T_{vib} will not be affected.

The first approach to reduce the gas temperature is to decrease the discharge current. Since the power density of these discharges is relatively constant, there is little sensitivity to the gas temperature with changes in discharge current (see Chapter 4). An exception to this is for extremely low discharge currents which are also susceptible to instabilities. As an extreme low current one might also consider stable negative corona discharges, however these will typically have too low power density to generate high densities of reactive species and thus will have very low deposition rates. As expected thus there was no dramatic change in the particle formation during deposition by operating at lower discharge currents down to 0.8 mA and staying in the normal micro-glow discharge mode.

To more decisively control the discharge temperature helium was added to the gas mixture. As was shown in reference [109] when there are no chemical reactions between the additional species and intermediate operating temperatures proportional to the additions of other gases can be achieved. Argon and helium atomic gases were available as additions to operate at lower temperatures. Argon which operates nominally at 680K is not expected to be low enough in temperature and at 50% addition did not significantly affect particle formation. Helium which operates at about 420K is an appropriate buffer gas to add (neon may also be a viable lower-cost alternative but was not tested). A 50%/50% helium/hydrogen mixture should thus operate at a temperature of about 585K.

Figure 8.8 shows comparative images of the deposited films taking into account helium addition and circuit stabilization. Figure 8.8a shows that by reducing the discharge temperature a particle free uniform thin film can be deposited. Figure 8.8b is for the same conditions without Helium and the micron size roughness due to particles is visible. Figure 8.8c is from a deposit taken without using the external circuit discharge stabilization and shows non-uniformities on the scale of 10's of microns. Together these images indicate the progress made in this research to develop thin film plasma processing techniques with atmospheric pressure microplasmas. Though helium is used to create the uniform films significantly less helium is used in this microplasma PECVD as compared with DBD, RF, and VHF discharges which are also able to produce uniform films. The reason for this is that in this case helium is used for temperature control not for discharge stabilization. In stabilizing discharges the electrical benefits of helium are only significant when the concentration is >95%, however this discharge is stabilized without helium and the thermal benefits are present proportional to concentration. In fact other methods of temperature control such as convective cooling may even be able to replace the need for helium.
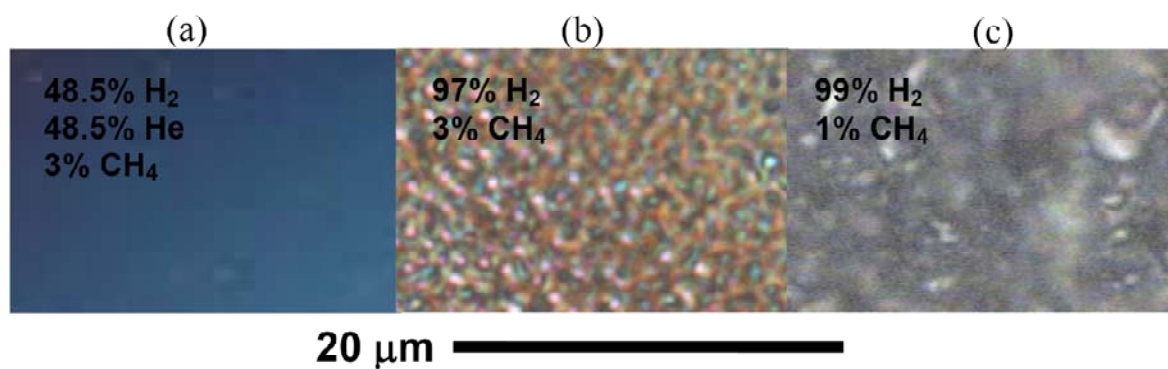
Figure 8.8: Micrographs of films deposited during 10 seconds with 2 mA atmospheric pressure micro-glow discharge in various hydrogen, methane mixtures. (a) circuit stabilized discharge with helium addition. (b) circuit stabilized discharge without helium buffer. (c) unstable circuit. All films are shown at the same magnification.

8.5.3. Uniformity

By stabilization of the discharges and lowering of the temperature uniform thin films could be deposited within the discharge region. The use of microplasma for thin film deposition though by many accounts may be considered undesirable because the inherently small size of the discharge (~100 μm) cannot treat large areas uniformly. This wide area uniformity could be solved by using arrays of microplasma and rastering, rotating or vibrating the substrate. In fact many of these techniques are currently used in RF afterglow techniques[57] where the gas jets can cause non-uniformities over wide area.

An alternative is to use the small size of the discharge to advantage in creating micropatterns without the use of traditional masks. Figure 8.9a shows patterns created by igniting a 0.5 mA DC normal glow microplasma in air over a silicon substrate and then programmatically moving the substrate to create the patterns. Deposition of amorphous carbon lines could also be performed using hydrogen methane mixtures as shown in Figure 8.9b. The stage was moving at 66 μm/s, corresponding to about 4.2 seconds of deposition at each location along the line. The minimum feature size of the deposition is directly determined by the diameter of the discharge region which in turn is determined by the normal current density and minimum current. Considering typical minimum currents in normal glow mode of about 0.5 mA this corresponds to ~25 μm. The feature size of ~25 μm may not be desirable for use in modern IC nano-manufacturing; however, applications may be available for MEMs devices, micro-circuits, or printing technologies. Also this feature size and scale of the plasma may be reduced by considering the use of denser media for the discharges such as high pressure gases and liquids. Applying such principles we have created non-thermal discharges less than 2.5 μm is diameter in liquids[143] though the materials deposition characteristics are still being investigated.
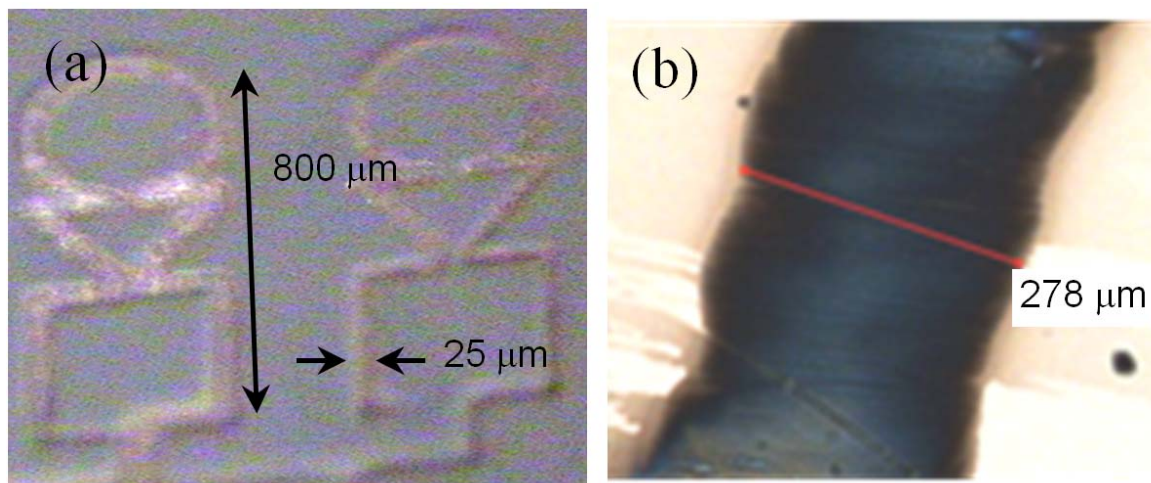
Figure 8.9: (a) Patterned oxide formed on silicon using DC microplasma in air and programmable substrate positioning system. (b) Line drawn in 2 mA, at 99.6% H_2, and 0.4% CH_4.

The possibility that the duration of the deposition also has an effect on particle generation and discharge uniformity was also addressed. In the consideration of particles a fundamental change with respect to deposition time was not expected since establishment of the conditions for particle formation within the plasma occurs on the timescale of microseconds. Even when the deposition time was reduced to as little as 1 second, sparsely distributed particles were still apparent when helium was not used.

Some other temporal changes in the deposition characteristics and uniformity though may be expected considering for example changes in the conductive properties of the cathode. An example of how the changes in the surface properties affect the discharge which in turn affects the deposition is shown in figure 10. Here the discharge was 2 mA in a 48.5% He, 48.5% H_2, and 3 % CH_4 mixture and (a) thru (d) correspond to deposition

times of 2 s, 10 s, 30 s, and 300 s. The substrate was 150ºC. Initially a uniform thin film is deposited. As the film gets thicker the cathode spot begins to wander somewhat looking for the most favorable location. The anode spot is fixed so the film thickness increases. Eventually, in this case after about 280 seconds when the thickness was about 600 nm the change in cathode properties causes the discharge to become unstable. Such deposition/discharge interactions could possibly be solved by arranging the discharge laterally over the substrate as was attempted by Ito[13] and as is discussed in future design improvement in chapter 10.
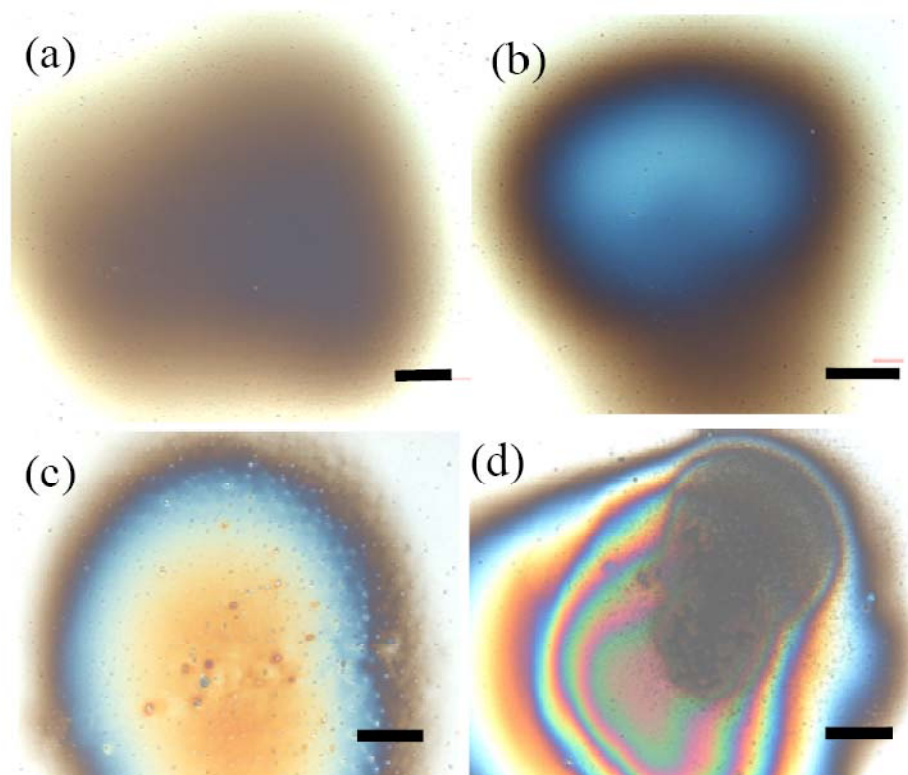
Figure 8.10: Deposition at a single spot using 2mA discharge and helium buffered hydrogen methane mixture for (a) 2 sec, (b) 10 sec, (c) 30 sec, and (d) 5 minute. Respective scale bars are 50 μm, 50 μm, 50 μm, and 100 μm.

8.5.4. *Deposition Characterization*

An illustrative set of results on the materials characterization of the thin films deposited is shown here to verify that the films deposited are sufficiently similar to LP-PECVD and other AP-PECVD results. Also some general trends and characteristics are discussed.

8.5.4.1. *Deposition Rates*

The results shown in figure 8.10 can also be used to estimate the film thickness and changes in the deposition rate. The principle is simply to match the observed color fringe with an isochromatic chart. An unknown is the film index of refraction but a value of about 1.5 is common for polymers and makes the thicknesses corresponds with our profilometry measurements. Thicknesses assuming an index of refraction n=1.5 are about 20 nm, 70 nm, 140 nm, and 590 nm for (a)-(d) respectively. Though this is a rough estimate errors are less 50% due to both interpretation of the color fringes and assumption of the index of refraction. From the rough estimates of thicknesses, rates of deposition thus start at about 10 nm/s and decreases to about 1.8 nm/s. This decrease could be due to both surface changes and the increase area over which deposition is occurring.

8.5.4.2. *Nanoindentation*

For a 500 nm thick film deposited for 4 minutes using 3% CH_4, 48.5% H_2 and 48.5% He mixture a nanoindentation analysis was performed to determine the modulus

and hardness of the film. Figure 9.11 shows the load displacement curve including the loading, holding, and unloading phases of the test. During the holding phase some creep occurs and properties are determined from the unloading phase. Hardness is determined by force / tip area at the maximum load during the unload phase, and modulus is calculated from the slope of a linear fit to the initial unloading line. The indentation was only 10% of the film thickness so the properties of the substrate were not taken into account. For this sample the modulus was 9.7 GPa and the Hardness was 0.37 GPa. These values are in the range common to PLCH.[136]
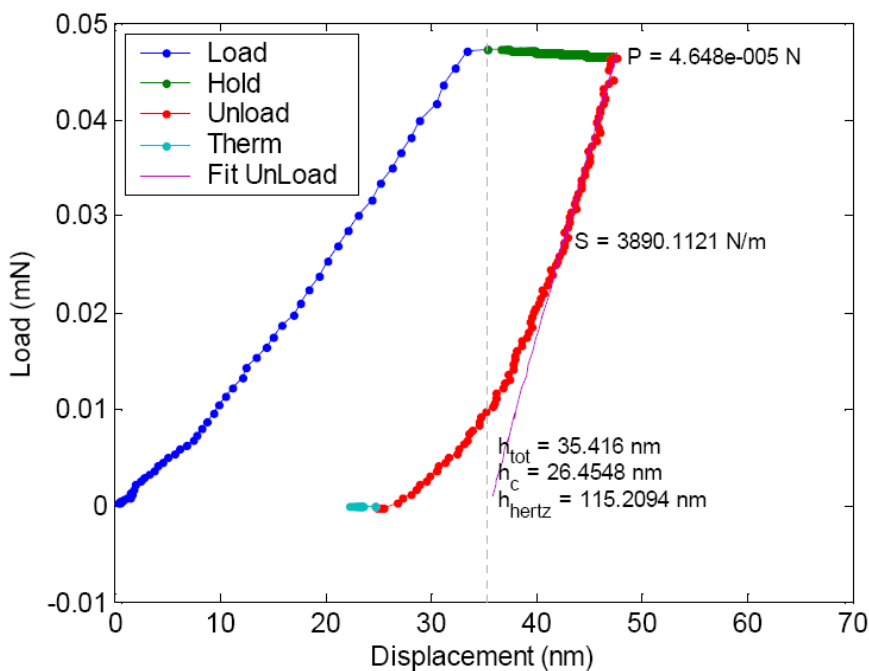
Figure 8.11: Load displacement curve for nanoindentaion analysis.

8.5.4.3.   Raman Spectra

A feature in the deposition of a-C:H is the different forms; polymeric, graphitic, or diamond like which can be deposited. Raman spectroscopy was used to investigate the deposits. In low pressure systems the deposition quality is highly dependant on ion bombardment and the presence of H atoms. By using microplasmas which are in direct contact with the substrate (rather than an afterglow) we hope to have the same control over the form of the deposit in atmospheric pressure systems as in low pressure systems.

Raman spectra were acquired using 738nm, 633nm, 514nm, and 325nm laser excitation as shown in figure 8.12. We see from these spectra that there is a peak in the fluorescence signal at around 633nm. In both the 633nm and 738nm spectra the fluorescence signal level is too high to get any reasonable information. For 514 nm excitation we see the characteristic D and G peaks of a-C:H and the peaks of the silicon substrate at $520cm^{-1}$ and $975cm^{-1}$ too. For 325 nm excitation which is in the UV we see that the D peak is decreased in height relative to the G peak. However the D peak is still significantly high and hides any sp^3 features. Future work using 244nm laser excitation may clarify the presence of sp^3 bonded carbon.
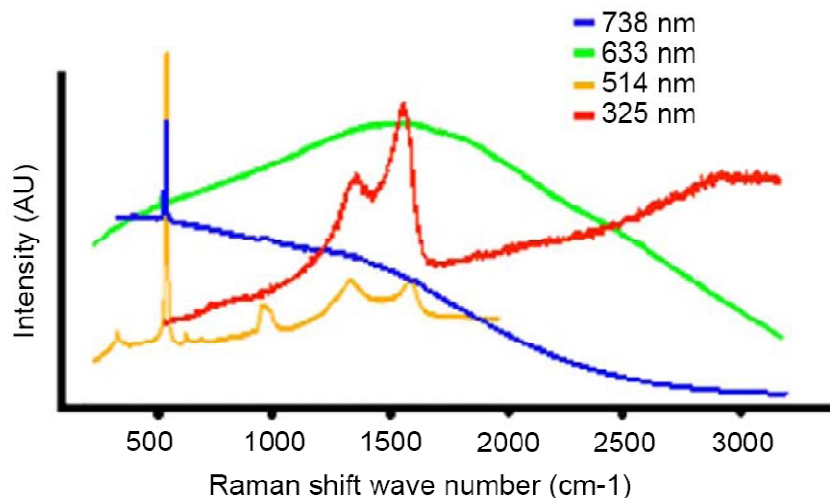
Figure 8.12: Raman spectra of a-C:H sample using various laser excitation.

Figure 8.13, 8.14, and 8.15 are Raman spectra using 514nm excitation. Figure 9.13 was deposited using a plasma with 30 mA discharge current while figure 8.14 and 8.15 were deposited using a 3.8 mA discharge current. During deposition both electrodes were stationary though the discharge moved some on its own, duration was 3 minutes for all cases. In these depositions the substrate temperature was 400°C. The deposit in figure 8.13 annealed at that temperature for 10 minutes after the deposition was complete. The slope of the fluorescence background signal is significantly higher in the high discharge current discharge. The normalized background slopes were 6.6, 4.5, 3.2 respectively. Using the methods of reference[67] (figure 8.10 in their paper) this corresponds to hydrogen contents of about 38%, 35%, and 30%. These hydrogen levels are similar to those received by low pressure PECVD techniques. Lower discharge currents thus result in less hydrogenated films. We believe this is due to a lower gas temperature in the discharge at these conditions. References [67, 131] [137]were used to analyze the G peak

location. The G-peak location of both the high current and annealed samples indicates a nano-crystalline graphite with little or no sp^3 content. The less annealed sample shows a sp^3 content of at least 15%. This indicates that the use of a heated substrate and annealing during deposition may have deleterious effects on the level of sp^3 bonding. This result is actually consistent with annealing studies performed in the literature. The lack of any recognizable sp^3 features when using 325nm excitation indicate that the sp^3 content is probably less than 30% in all samples.
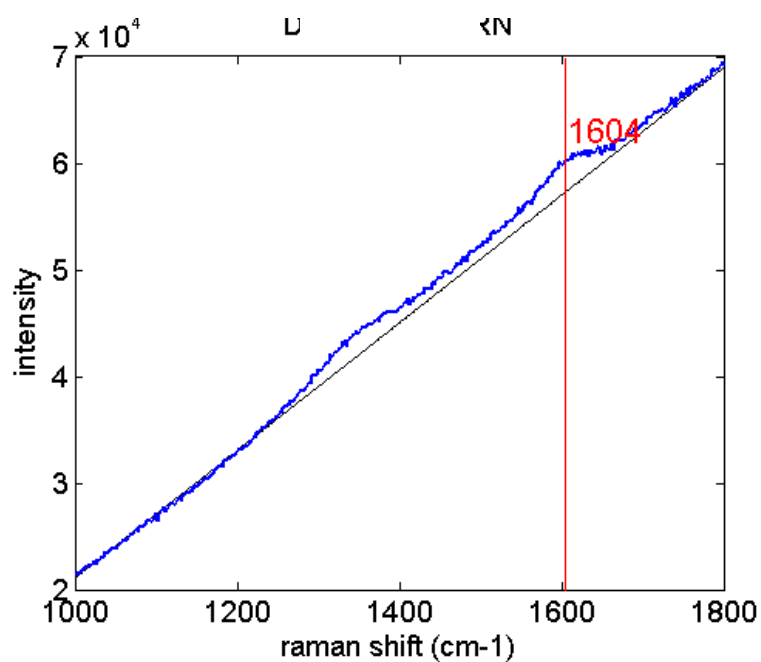
Figure 8.13: 514nm Raman spectra of a-C:H deposited at 30 mA discharge current.
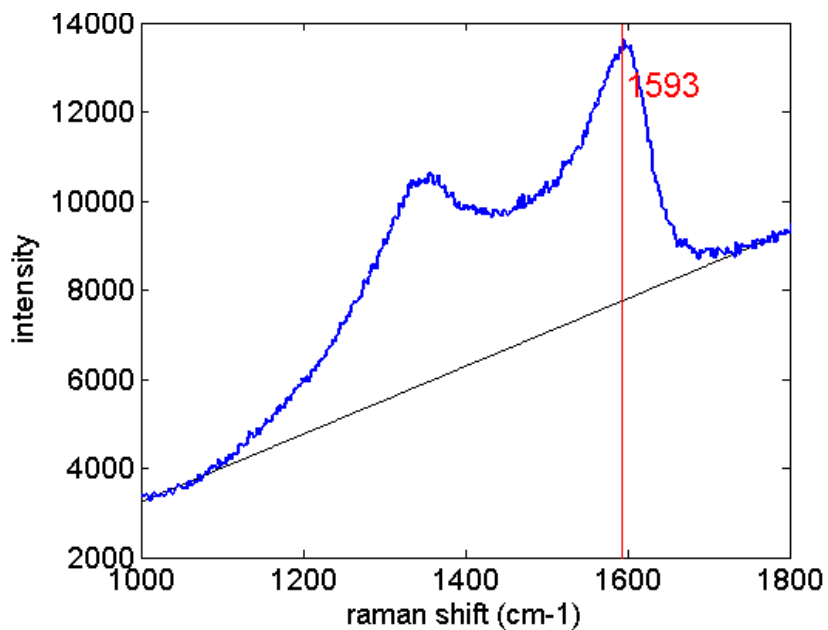
Figure 8.14: 514nm Raman spectra of a-C:H deposited at 3.8mA discharge current.

Annealed in hydrogen atmosphere at 300°C for 10 minutes after deposition.
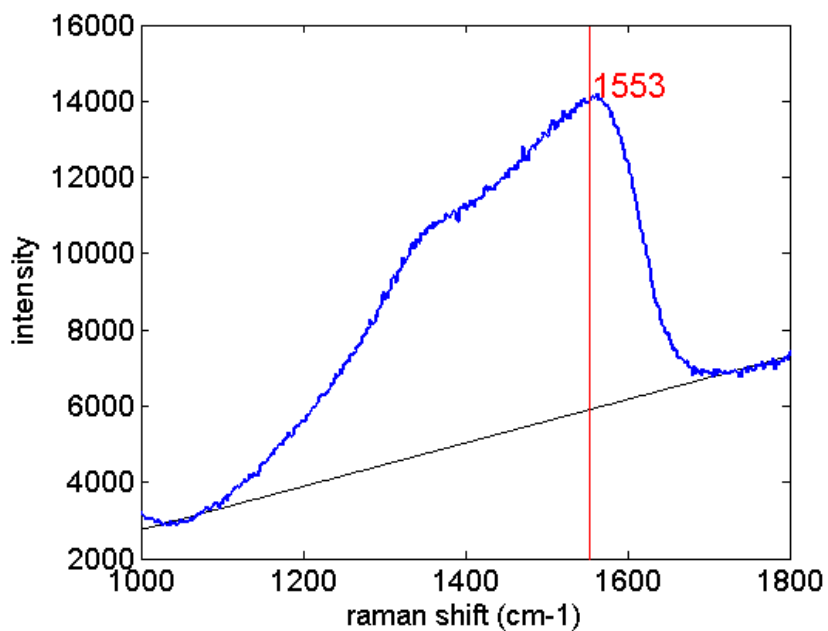
Figure 8.15: 514nm Raman spectra of a-C:H deposited at 3.8mA discharge current.

These Raman spectral results confirm the general understanding that these films are similar in characteristics to the PLCH and slightly DLC films currently studied from low pressure systems. Whether truly hard DLC films can be produced remains to be discovered. In low pressure systems it is typically the ion energy which most greatly determines the film hardness; low ion energies produce PLCH, higher energies DLCH, and the highest energies GLCH.[49] A major challenge will be that the sheaths in these high pressure systems are highly collisional and the ions will lose a significant amount of their energy through momentum transfer and charge transfer collisions. Typical ion kinetic energies at the cathode in atmospheric pressure glow discharge may be only 1eV-5eV even though the cathode potential fall is 250V. In comparison in a low pressure system ion typically gain almost all of the cathode potential fall as kinetic energy.

8.5.5. *Parametric Study*

A brief parametric study of the films deposited and their Raman signatures is presented in table 8.1. Varied here are discharge current, polarity, substrate temperature and methane concentration, and annealing time. Not all of these conditions lead to uniform thin films none-the-less the deposits were characterized using the Raman analysis with 514 nm excitation. In generally the following trends can be noted which will lead to more diamond like films. These are 1) decrease methane %, 2) decrease current, 3) increase substrate temperature, and 4) decrease annealing. No significant polarity difference is noted in the quality of the films. However with the anode as substrate the discharge is more likely to wander and or jump around.[144] For variations in substrate temperature by reviewing the literature from low pressure deposition techniques it was noted that there is often an optimal substrate temperature for processing. Too hot a

substrate will cause the films to graphitized with time or increased temperature. As is seen too high gas temperature cause gas more gas phase polymerization and deposition of more polymeric films. A more detailed study of the film properties and sensitivities to discharge conditions would of course be worthwile but beyond the scope of this dissertation. The trends seem promising and ideal operating conditions may be found. The potential for high quality diamond films though is in question due to the low ion energy considerations already discussed.

Table 8.1: Summary of conditions and analysis of several deposited films. Multiple G peak locations listed indicate multiple experiments at the same operating conditions.

#	Ch4%	I (mA)	Bias	Sub. (^{o}C)	G Peak Loc (cm-1)	Analysis
1	20	3.5	Anode	20	1603	GLC
2	20	3.5	Anode	400	1602, 1598	GLC
3	2	3.5	Anode	20	1599, 1595	GLC
4	2	3.5	Cathode	20	1607	GLC
5	2	30	Cathode	20	1604	GLC
6	2	20	Cathode	400	NA – Fluorescence too strong	PLC
7	2	30	Anode	400	NA – Fluorescence too strong	PLC
8	2	3.5	Cathode	400 – annealed 10 minutes.	1593	GLC
9	2	3.5	Cathode	400	1548, 1552	DLC

8.6. Chapter Conclusions

Atmospheric pressure DC microplasma discharges in methane-hydrogen mixtures were used to create thin films of amorphous carbon coatings on silicon substrates. Several challenges were overcome to achieve this goal. First was plasma stabilization which showed to greatly improve the uniformity of the deposits. Second was controlling the formation of particles. Discharge temperature was determined to be the controlling parameter for the formation of particles. Through helium addition of only 50% the temperature could be made sufficiently low. The films deposited are transparent hydrogenated amorphous carbon thin films more polymer like than diamond like. Some control of film characteristics is possible through substrate temperature and annealing and in general is similar to low pressure PECVD amorphous carbon films. Deposition rates are about 10 nm/s. Though uniform, the deposition is localized to the small region of the discharge and this may be used to advantage in applications such as maskless micropatterning.

9. Comparison of DC and RF Thin Film Deposition

9.1. Context

This is the last chapter which presents results. As the endpoint of the research it serves to compare the film deposition results using the DC microplasma to other state of the art techniques for atmospheric pressure thin film deposition. As we are currently the only research group actively pursuing DC non-thermal discharges for deposition a RF deposition system similar to those more widely studied by others was designed and implemented. As such this chapter serves to put the knowledge gained in the context of existing and parallel research efforts into AP-PECVD. This chapter for the most part reproduces the material in a paper currently in preparation for journal publication, "Comparison of film deposition using DC and RF atmospheric pressure normal glow discharges."[145]

9.2. Summary

Amorphous carbon (a-C:H) films are deposited from $He/H_2/CH_4$ mixtures using atmospheric pressure DC microplasmas and RF (13.6 MHz) glow discharges. Characterization of the plasmas show that both discharges operate as density scaled version of, respectively, the γ-mode and α-mode normal glow discharges well studied in low pressure systems. The RF discharge is stabilized in the α-mode using significant amounts (>95%) of helium as a buffer gas. The DC discharge is stabilized by its external circuit; however, helium (~50%) is also used to decrease the discharge's temperature.

Both particle (volume dominated) and thin film (surface dominated) regimes of deposition could be attained in either discharge. Characterizations of the films show the DC deposits to be harder and less hydrogenated. This may be due to the higher power density and ion energies in the γ-mode discharge. Deposition rates in the DC discharge were also significantly higher, ~10 nm/s in comparison with ~0.1 nm/s, this is partially due to the RF discharge's stability requirement to operate at significantly lower partial pressures of methane. The RF system is able to treat significantly larger areas more uniformly though the γ-mode discharge can deposit very locally. As tested the RF configuration is significantly better for depositing non-conducting films and depositing on dielectric substrates. The DC discharge has higher deposition rates and improved film properties.

9.3. Introduction

Most thin film plasma enhance chemical vapor deposition (PECVD) processes[4] take place in vacuum-based plasma reactors. Performing PECVD at atmospheric pressure has several advantages: firstly, microfabrication is less expensive as there is no need for expensive vacuum pumps; secondly, the process uses less energy and is more environmentally-friendly because operating at ambient pressure and temperature satisfies "Green Chemistry"[9] principles; thirdly, free from the constraints of a vacuum chamber, the processing can take place in continuous rather batch mode and can treat any size shape or object. Similarly, non-vacuum compatible or biological substrates can be treated by operating at an atmospheric pressure. Lastly, due to the higher operating gas densities, the deposition rate is likely be higher allowing for more rapid processing.

There are several challenges to atmospheric pressure deposition. These are mostly related to operation at higher gas number densities, n, in which volumetric processes ($\sim n^2$) begin to overwhelm surface processes which are dependent on surface fluxes ($\sim n$). These volumetric processes can lead to higher gas temperatures and instabilities such as the overheating instability and glow to arc transition. Also volumetric reactions leading to particle formation and the degradation of thin film quality are more likely.[3, 4, 6]

There are several different approaches currently being researched to remedy these problems mainly relying on novel plasma discharges and deposition systems and comparisons of low pressure and atmospheric pressure deposited films indicate many similarities.[54] Films have been deposited by several different types of discharges including 1) helium glow DBDs,[12, 33, 55, 62, 63] 2) non-helium continuous wave DBDs,[56] 3) helium RF (13-27 MHz) afterglows (so called APPJs and cold torches),[57, 59] 4) helium RF (13.6MHz) CCPs,[58] and 5) helium VHF (150MHz) CCPs,[61]. In most of these systems the deposition of uniform thin films without patterns, granules, particles, globules or significant (> 50nm) surface roughness requires significant use of helium buffer gas to maintain discharge uniformity and stability. In these helium based systems typically precursor concentrations are around 0.1% with typical deposition rates in the 0.2 to 2 nm/s range for the lower frequency DBD systems and as high as 15 nm/s for the RF and VHF CCPs and jets. This higher deposition rate in the RF and VHF systems may partially be due to higher gas flow rates used to help with discharge cooling.

In this chapter we compare a system similar to these helium based RF deposition systems with a recently developed DC microplasma for PECVD.[130] Though DC microplasma have been used in atmospheric pressure deposition previously[13, 64] progress

toward depositing thin films has only recently been demonstrated.[127, 130] The microplasmas are small in scale and thus may not be useful for all applications. There are however potential advantages in that the microplasma is not stabilized by helium and thus can operate over a larger range of precursor mixtures. Additionally with DC operation, rather than RF, insight into the role of ion energies, sheaths and power densities on the quality of the deposited films can be gained.

9.4. Experimental Setup

Two reaction chambers were designed and built to test the methods of amorphous carbon film deposition using atmospheric pressure plasmas. Both of these systems are parallel plate reactors and the discharges were excited by either RF or DC electric fields. A set of mass flow controllers in the range of 0.01 to 10 SLPM for helium, hydrogen and methane was used to control the precursor gas mixture. The feed gases were mixed before entering the reactor. Methane to hydrogen ratios of 1% to 3% were generally maintained for stable not excessively sooting deposition. A silicon wafer was used as substrate. The substrate temperature in both cases was generally kept at 150°C. In the case of the DC discharge this was provided by external heating and some variation in temperature was studied. In the RF case heating occurred through self heating due to the system power. The PECVD reactors operated at or slightly above atmospheric pressure. Other conditions varied as per the discharge excitation.

The deposited films were characterized with optical microscope and Raman spectroscopy. Optically the uniformity and thin film quality of film could be ascertained by inspection. Also estimation of film thickness could be made from the diffraction

caused by the thin transparent films.[138] The amorphous carbon films deposited could take many forms including polymeric, graphitic, and diamond like carbon.[49] Also depending on the conditions the films may also contain significant hydrogen content. The Raman spectroscopy utilized a 514nm excitation laser and analyzed the observed fluorescence back ground, and broad peaks of disordered and graphitic sp2 carbon at around 1350 cm^{-1} and 1600 cm^{-1} respectively. Interpretation of these peaks in consultation with existing literature [67, 135, 137] on the subject gives a rough quantitative estimate of the hydrogen content and relative presence of sp^3 and sp^2 bonded carbon in the deposited film though it cannot be conclusive.

The specific discharge reactors are detailed below.

9.4.1. DC Microplasma

Figure 9.1 schematically shows the reactor system used for DC AP-PECVD and is identical to the system recently used for thin film characterization.[130] A power supply is connected in series to a set of ballast resistors and the discharge gap. The resistors are placed physically close to the discharge to stabilize the system from the ionization overheating instability.[127] Because of the small diameter of the discharge ~200 μm relative to the anode wire diameter, 1mm, the discharge is effectively in a parallel plate configuration. The discharge is maintained in a 25 cm cube with windows for optical access and a gas inlet and exhaust. During deposition the discharge was operated at about 3.5 mA and with an electrode gap of 0.5 mm to 1 mm.
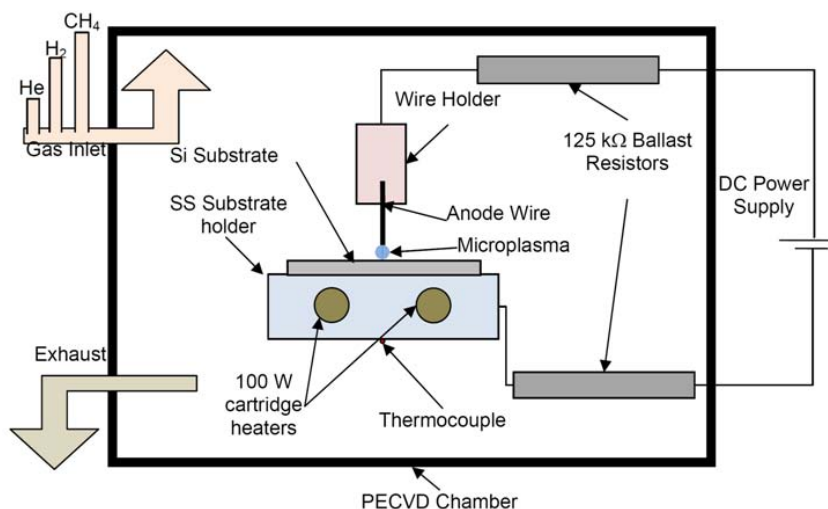
Figure 9.1: Schematic of the DC AP-PECVD reactor.

9.4.2. RF CCP Plasma

A parallel plate capacitevly coupled plasma (CCP) configuration previously used in low pressure PECVD[146] was modified for use at atmospheric pressure. The power system consisted of a 500W 13.56 MHz RF generator (Plasma Therm HFS 500E) and L-type matching network with variable tuning and loading capacitors (Plasma Therm AMNS 500E) typical for generating alpha mode CCP discharges.[7] A schematic of the circuit is shown in figure 9.2. The axis symmetric reactor is also show schematically in figure 9.2. Gas entered through a 12.7 cm diameter shower head gas distributor. The second electrode was spaced at 1 mm to 3 mm away with a 7.5 cm diameter silicon wafer substrate on top. A glass disk or microscope slide could also be used as substrate. A glass tube with rubber gasket formed the walls of the reactor chamber. The gas exited to ambient air through the 5 mm slot between the glass wall and shower head. Either electrode could be powered with no significant change in operation, though here the substrate holder was powered and the showerhead electrode was grounded. During

deposition the discharge were operated at a forward power of about 50W to 200W and though the matching network was adjusted to minimize reflected power the system is not optimized for the impedance of atmospheric pressure plasmas and typically the system operated with 50W to 100W of reflected power. For some of the initial characterizations of the RF-CCP operation a discharge setup similar to that shown in the DC configuration (Fig. 9.1 was used) with the modifications of: 1) replacement of the DC power supply and ballasts with the RF circuit, and 2) removal of the anode wire and use of the ~1cm diameter wire holder as the powered electrode.
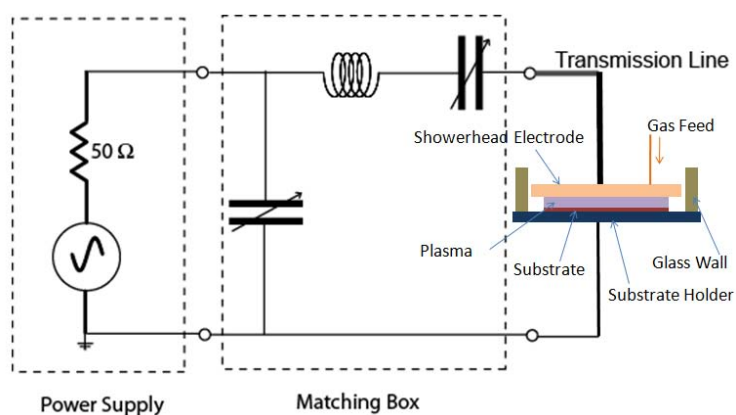
Figure 9.2: Schematic of RF electronic circuit and discharge reactor.

9.5. Results and Discussion

9.5.1. Discharge Characterization

9.5.1.1. RF

All of the intricacies in the operation of atmospheric pressure CCP discharges are not currently understood though some progress has been made in their understanding

over the past decade. [11, 147] It is generally though that the discharges operate as an alpha mode CCP discharge with the possibility of alpha to gamma transition occurring as the power density is increased similar to moderate pressure CCP discharges.[2, 148, 149] This alpha mode operation is only maintain is high concentrations >95% of noble gases helium and argon. Small additions of molecular gases cause transition to gamma mode, overheating of the electrode, transition to an arc and unstable operation. The discharge is thus stabilized from alpha to gamma transition by use of the noble gases. Whether this stabilization is due to mainly thermal effects (lower discharge temperature and less chance of the ionization overheating instability) or is due to different plasma physics in noble gases (such as dependence of the critical current density for alpha to gamma transition on the gas properties)[2] is a current topic of research and is not yet known.

These characteristics were confirmed in the operation of this AP-RF-CCP setup. Figure 9.3 shows images of the AP-RF-CCP operating in pure helium, argon, hydrogen, nitrogen, and air. In the noble gases the discharge could be initiated in the alpha mode at a gap of about 1.5 mm. At higher power the discharge transitions to gamma mode. A distinct visual change is apparent as the discharge goes from volume dominated in the alpha mode to sheath dominated in the gamma mode. In the alpha mode a dim glow is observed throughout the discharge gap and diminishes towards the electrodes. The gamma mode is significantly brighter and has the brightest sheaths directly in contact with the electrodes. There is also a change in the color of the discharge as the increase in electron energies in the sheaths excites higher energy electronic states to emit. In the molecular gases alpha mode operation could not be attained and the discharge could only be ignited in the gamma mode by touching and then separating the powered electrodes. A

reason for this is likely the higher breakdown voltages in the molecular gases which could not be attained with the current RF matching network. Using previously developed techniques for temperature measurement using the N_2 2nd positive system[83] gas temperatures in the helium alpha mode, and air gamma mode as shown in figure 9.3 were measured to be 370K, and 2500K respectively.
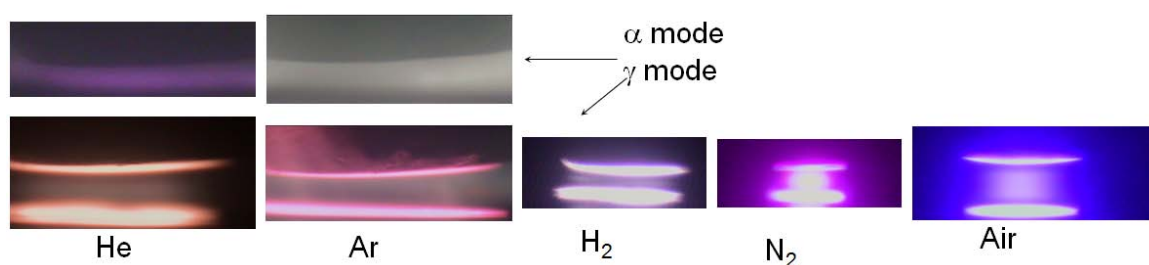
Figure 9.3: Modes of AP-RF-CCP operation in atmospheric pressure atomic and molecular gases.

The operation of the RF-CCP as a normal alpha mode discharge was verified by the micrograph images of the discharge in operation shown in Figure 9.4. The gas mixture in these images was 95% helium with 5% air and a glass plate covered the lower electrode. Initially as the discharge power was increased the size of the discharge proportionally increases such that the indicated power density was constant at about 50 W/cm^2. Discharge powers were measured using the indicator for forward power on the power supply, equipment for verification of these measurements was not available and actual discharge powers may be a fraction of these. Once the discharge covered the entire area of the upper electrode the power density increased with further increase of discharge

power with a transition to gamma mode occurring at an indicated power of about 80 W/cm². It should be noted that this α–γ transition is highly dependant on the discharge gas mixture, external circuit parameters, and discharge geometry. Also, I do not trust the value of discharge power reported here in comparison with later verified power measurements in the RF deposition reactor. The discrepancy in power measurement is likely due to transmission line and geometric losses when the RF power was connected to the DC-AP-PECVD reactor. The labels in figure 9.4 are thus indicated power. Dependence of the transition on power density and not power was confirmed using a larger sized upper electrode in which case the transition occurs at higher indicated powers and similar power densities.
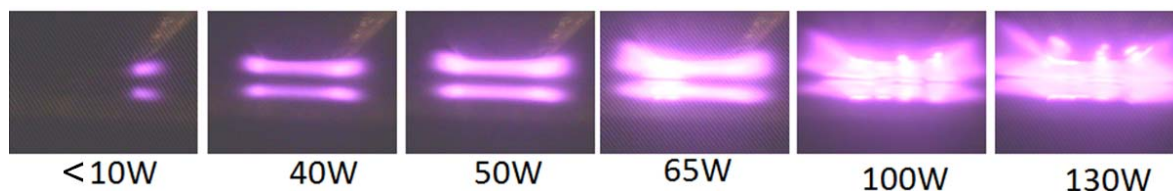
Figure 9.4: Alpha to gamma mode transition with increasing power in an air-helium mixture. Upper electrode is stainless steel and lower electrode is glass. Electrode gap is 1.5 mm and transition occurs at an indicated input power of ~65W. In these images the upper portion is the actual discharge and the lower is a reflection of the discharge in the substrate.

An image of the discharge during operation in the configuration with shower head electrode (Fig 9.2) as used during deposition is shown in figure 9.5. The glass wall was removed for better imaging. Gas mixture flow rates are 5 SLPM He, 500 SCCM H_2, and

5 SCCM CH$_4$. Percentages are 90.8%, 9.1%, and 0.1% for helium, hydrogen and methane and the CH$_4$/H$_2$ fraction is approximately 1%. Discharge power was 200W and power density was 1.3 W/cm^2 and was verified by measurements of the current and voltage using a current transformer, high voltage probe and oscilloscope.
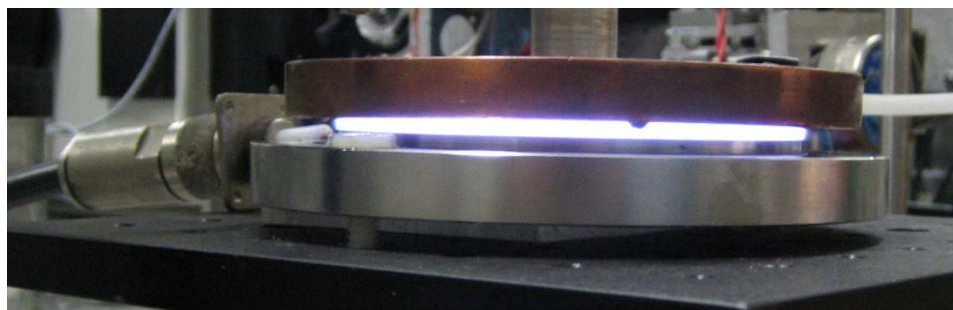
Figure 9.5: Alpha mode RF-CCP operation with shower head upper electrode.

9.5.1.2.   DC

The DC discharge operation in various gases and in the PECVD reactor has been described in detail elsewhere (also chapters 6 and 8).[109, 130] For comparison to the RF deposition the DC discharge was operated with a gas mixture that had similar methane to hydrogen fractions. Because the DC discharge is stabilized by the external circuit rather than by the addition of Helium the percentage of helium used was not maintained. Some helium was used in the DC discharges to lower the operating gas temperature. In comparison to the RF discharges the DC discharges operate in a gamma mode with sheath potentials at the cathode of about 250V. As such they are also significantly high power density ~3 kW/cm^2 for the DC in comparison with ~1.5 W/cm^2 to for the RF discharges.

9.5.2. Film Deposition

9.5.2.1. RF Films

Figure 9.6 shows a micrograph of the films deposited using the atmospheric pressure RF-CCP plasma enhanced chemical vapor deposition reactor. Both were deposited with alpha mode discharges at 200W. In the case shown in Figure 9.6A the gas mixture was 90% He, 10% H_2 , 0.1% CH_4 in Figure 9.6B the gas mixture was 95% He, 3% H_2 , 2% CH_4 with total flow rates of 5 SLPM. The films were deposited over two hours. The case of lower methane concentration deposited a uniform transparent thin film. From the diffraction pattern of the film and stylus profilometry the maximum thickness is estimated to be 480 nm. This corresponds to a deposition rate of 0.067 nm/s. The higher methane concentration deposited both a film and particles onto the substrate.
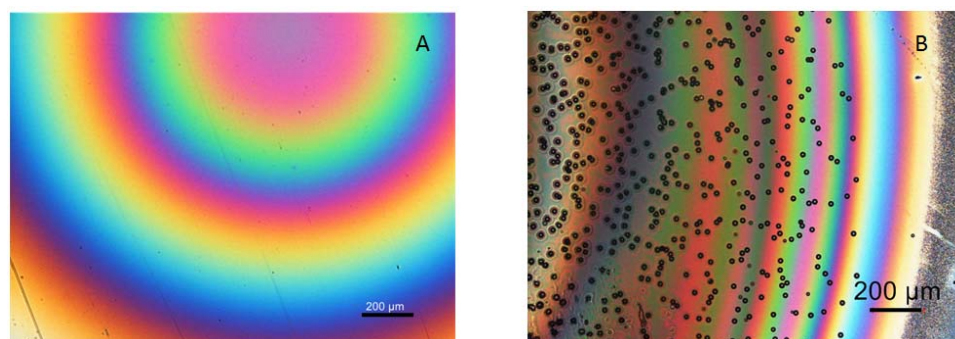
Figure 9.6: Micrographs of deposited films using AP-RF-CCP-PECVD. Scale bars for both images in 200 μm.

The film produced in Figure 9.8A was not uniformly distributed over the substrate. Spots of deposition were located corresponding to the shower head pattern shown in Figure 9.7. Closer inspection of the discharge in this region reveals a slightly intensified plasma emanating from the discharge holes. Operation in pure helium

confirmed that the intensification is likely due to holes of the shower head (at 1 mm in diameter) being larger than the plasma sheaths. As such, the plasma actually extends to inside of the gas supply hole as illustrated in Figure 9.9. This problem was corrected by placing a tightly woven stainless steel mesh (Twill Dutch Weave, 200×1400 wires/inch, .0.0028" × 0.0016" diameter wires) over the top of the gas supply to more uniformly distribute the gas flow. The film deposited using the mesh was no longer localized at the hole and significantly more uniform. The deposition rate was significantly lower ~ 0.003 nm/s, and in eight hours of deposition only ~100 nm thick film was produced. Some broad scale (~3cm) non-uniformities of about 20% of thickness were observed likely due to sagging of the mesh away from the showerhead surface and thus non-uniform spacing between the electrodes. This deposition rate is somewhat lower than observed in other deposition studies[6] and is due to different precursors and the relatively low flow rate per unit area of deposition used here.
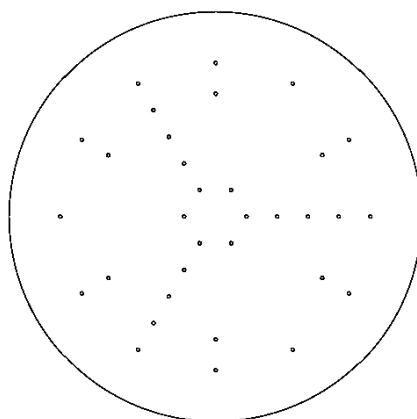
Figure 9.7: Shower head gas supply hole pattern
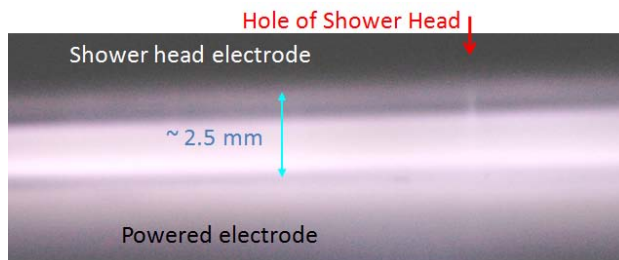
Figure 9.8: Micrograph of alpha mode RF discharge showing intensified plasma emanating from gas supply hole in showerhead electrode. 2.5 mm electrode spacing, 95% He, 5% H_2 0.05% CH_4, 10 SLPM
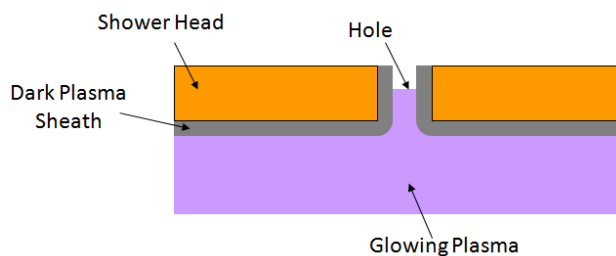
Figure 9.9: Illustration of glowing plasma, and sheath in vicinity of shower head gas supply holes.

The particles deposited as shown in Figure 9.6B are uniformly 20 microns in diameter. This is not coincidence and very interesting. This is likely a 'dusty plasma' phenomenon.[2] Particles formed in the volume of the discharge will become charged due to transient behavior in the relative rates of electron and ion fluxes to the particles. The floating potential and charge on the particles is typically negative when the particles are above a size of about 20 nm. These negative particles are in the balance of forces due to gravity and the Lorentz force in the oscillating electric fields. The Lorentz force will dominate for small particles and the particles will be trapped in RF field unable to overcome the negative sheath potential at the substrate and be levitated in the discharge.

As the particles get larger their charge to mass ratio decreases and at a particular size and q/m gravitational forces will overcome the sheath potential. The particles which fall from plasma will thus be uniform in size and weight.

The films deposited by the RF discharge were generally not very robust and quite soft. Generally few of the films passed the fingernail scratch test resulting in detaching from the substrate and balling up. A micrograph of the film shown in figure 9.6B after scratch testing is shown in figure 9.10. Regimes with higher CH_4/H_2 ratios were also were found in which the deposit was a viscous oily residue removable by wiping. The Raman spectra of the particles in figure 9.6B and figure 9.10 was taken and the particles were identified as PLCH and shows general similarities to polyactelyene plastics like latex though with significant bond disorder. The most robust film tested (capable of surviving wiping with a solvent) was that shown in figure 9.6. Raman spectra for this film was also attained however the film was found to be sensitive to heating by the laser as shown in figure 9.12 and holes could be burned in the film, Figure 9.12 inset. In figure 9.12 we see that the film decomposes from a polymer to disordered graphitic soot with continued application of the laser.
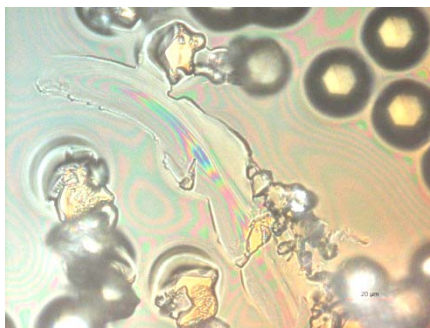
Figure 9.10: RF deposited film/particle after scratch testing with precursor

mixture 95% He, 3% H_2 , 2% CH_4.
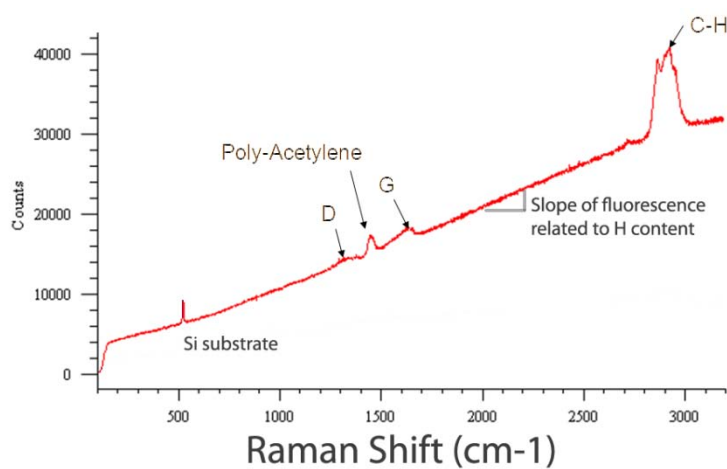
Figure 9.11: Raman spectra of particle deposited in RF plasma identifying it as a

polymeric particle.
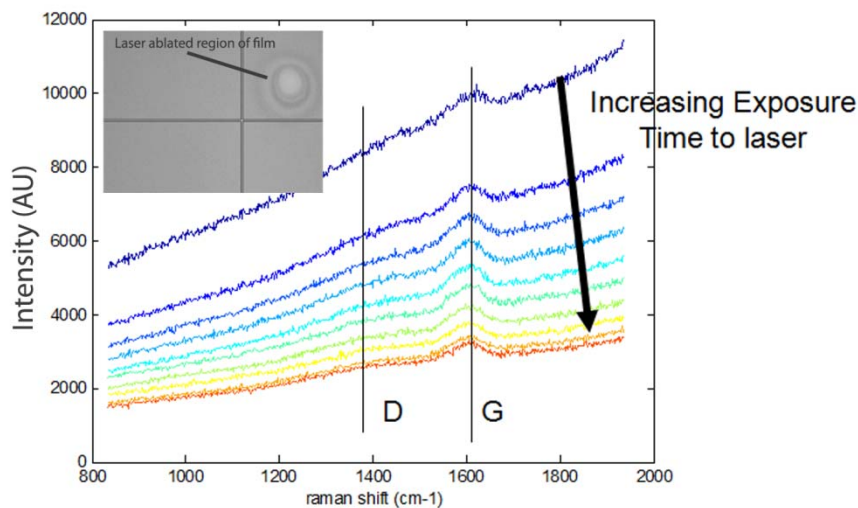
Figure 9.12: Raman spectra of RF deposited thin film showing ablation of film by laser.

Initially film is PLCH and becomes disordered GLCH with exposure.

9.5.2.2. DC Films

Some details on the deposition of DC films were provided in chapter 8[130] and a summary is presented here. Figure 9.13 shows a range of DC deposit films. Gas mixtures He/H$_2$/CH$_4$ were A) 48.5%/48.5%/3%, B) 0%/97%/3%, C)0%/98%/2% D) 0%/99.6%/0.4%. Particle free films were only attained by using Helium to lower the discharge gas temperature as in Figure 9.13A, although a decrease in particle size with decreasing methane concentration and no helium addition was also apparent. Though particle free films is one goal, uniform deposition of submicron particles can also form useful coatings.[150]

In general these DC deposited film were quite robust resistant to scratching by soft metals, wiping with common solvents, and heating by the Raman laser. The DC

films were deposited at about 10nm/s for a 3% methane concentration and other thing

equal scaling approximately linearly with methane concentration. This higher deposition

rate than RF discahrges is likely due to both the high partial pressure of methane and

higher power densities attainable in DC discharges. Some trends in terms of Raman

characterization observed in the DC deposition were also observed in the RF discharges.

Namely lower hydrogen/methane ratios resulted in higher hydrogen content in the

deposits. Although in general all of the RF films had higher hydrogen content than a DC

film with similar hydrogen/methane ratios.
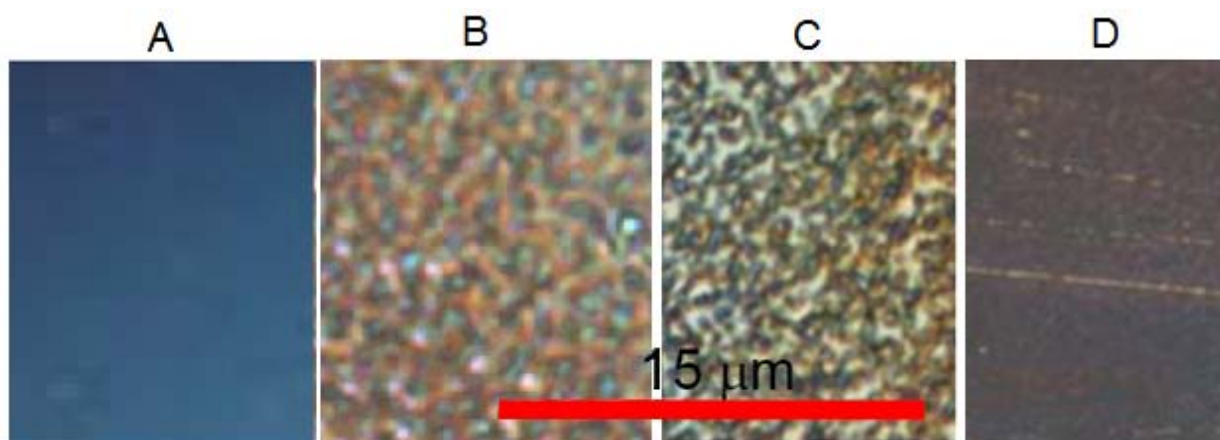
Figure 9.13: Micrographs of deposited films us DC microplasma. Substrate is cathode

and current was 2ma. Gas mixtures He/H_2/CH_4 were A) 48.5%/48.5%/3%, B)

0%/97%/3%, C)0%/98%/2% D) 0%/99.6%/0.4%. Scalebar is the same for all images.

9.6. Chapter Conclusions

In comparison to the alpha mode helium based RF discharges used here and in the

literature the DC discharges operates in drastically different regime, sustained in a

gamma mode and with sheath potentials at the cathode of about 250V. They have significantly high power density ~3 kW/cm^2 for the DC in comparison with 1.5 W/cm^2 for the RF discharges. The RF discharges are stabilized by helium buffering and as such the partial pressure of methane precursor is quite low resulting in lower deposition rates. The DC discharges are stabilized by their external circuit and do not require helium though it can be used to advantage in decreasing the discharge temperature and avoiding particle formation.

The obvious differences in RF and DC deposition is that the RF is more versatile in treating a variety of substrate (conducting or dielectric) and is not very sensitive to changes in the substrate conductivity during deposition. The RF discharge is also significantly more uniform over large areas. The DC discharge only deposits on an area approximately 300 μm in diameter. The RF discharge was able to deposit relatively uniformly over an area of several centimeters in diameter and possibly larger.

However, the DC discharges appear to deposit higher quality films than their RF counterpart. The problem of low film quality with atmospheric pressure RF films is generally known and has been attributed to the noble gas dilution resulting in the coated films having nano-scale powder-like structures showing poor mechanical properties and very low carbon density.[150] Higher quality low pressure films are attained without dilutants. Some of these improvements may be due to the lower helium content in the gas mixture though some features are also likely due to the DC discharges being more intense and also having higher ion energies in the sheath. The higher intensity of the DC discharges may improve film quality because there will be an increase in the flux of atomic hydrogen to the film during deposition. Atomic hydrogen is known to chemically

etch polymeric amorphous carbon from the surface and improve film quality.[49] The higher voltage sheath may also improve film quality because energetic ion bombardment is known to provide energy for stiching of the carbon atoms into 3D sp3 bonded carbon structures. In low pressure systems for PECVD of a-C:H films increasing the ion energy is the main way to improve the DLC characteristics of PLCH films. Excessively energetic ion bombardment is also known to create the GLC films and optimization of this parameter is warranted. An effect that was not properly controlled for or measured for each case presented here was the difference in discharge gas temperatures. In general the DC discharge operated between 450K and 700K where as the RF alpha mode discharges were in the range of 350K to 500K so some overlapping conditions may be further studied.

The combined use of RF and DC powering in low pressure PECVD systems is well studied and great benefit can be gotten from controlling the ion energy through the DC component. Technically such applications at atmospheric pressure would help in combining the benefits of more uniform treatment from RF discharge and better film quality with DC discharge. A problem though at atmospheric pressure is that energetic ion bombardment onto the substrate will facilitate alpha to gamma transition and instabilities due to the increased secondary electron emission and breakdown of the sheath. A future solution may be to tailor the RF external circuit to operate stably in gamma mode as in the case of the DC external circuit.

10. Conclusions

10.1.   Overall Summary

Returning to the thesis statement of chapter 1, the results present in this dissertation show that *"atmospheric pressure DC microplasmas can be stable, non-thermal and used in thin film deposition."* Chapters 3, 4, 5, and 6 focused on the characteristics, thermodynamics and classification of these microplasmas to show that they are density scaled versions of low pressure normal glow discharges and thus appropriate for thin film deposition applications. Chapter 7 analyzed how these discharges are stabilized. Chapters 8 and 9 demonstrated thin film deposition with these discharges and comparison to other state of the art atmospheric pressure techniques. The results presented can be broken up into three areas 1) fundamental characterization (Chapters 3-6), 2) stability analysis (Chapter 7), and 3) AP-PECVD demonstration (Chapter 8-9). The first two are fundamental science and the last is applied but relies on the knowledge gained by the fundamental studies. Mores specifics summaries and discussions of the impact and limitations in these three sub-areas of the research are discussed below. Those discussions lead to ideas for continuing and future work.

10.2.   Specific Summaries, Impacts and Limitations

10.2.1. Fundamental Characterization

The fundament microplasma characterizations presented relied upon: A) measurements of the electrical characteristics of the discharges, B) microscopic manipulation of the discharges, C) microscopic imaging of the discharges, D) analysis of

images to determine size, shape, and structure of the discharges, E) microscopic optical

emission spectroscopy measurements, and F) development, use, and analysis of

spectroscopic models to measure non-equilibrium temperatures and identify species. The

following list of observed and measured characteristics was completed initially for air

and later in nitrogen, hydrogen, helium and argon DC microplasmas:

1) Structure of the microplasma discharge consisting of negative glow, faraday dark space, and positive column. Standing striations in the positive column are observed under some conditions.
2) Discharge operation with flat voltage current characteristics.
3) Discharge operation with constant current density.
4) Constant electric field in the positive column.
5) Breakdown characteristics in agreement with Paschen behavior.
6) Electronic, vibrational and rotational temperatures are measured with $T_{elex} \approx T_{vib} > T_{rot}$.
7) Values of cathode sheath voltage, reduced electric field, and scaled current density agree with Engle-Steinbeck and Townsend theories.
8) Variations of temperatures in molecular and atomic gases are consistent with theories of energy relaxation.
9) Gas temperatures in discharges can be significantly above ambient temperature.
10) Diameter of contracted positive column and temperature of discharge are related by requirements for thermal balance.
11) Variations in temperature with current explain negative V-I characteristics and some other anomalous behaviors.
12) Variations in temperature with current are explained by changes in the relative rates of cooling to electrodes and by diffusion due to changes in discharge size with current.
13) Significant micro-scale variations in temperature exist.
14) Conditions in the anode sheath are very sensitive to electrode surface conditions.

A very important conclusion is drawn from these results namely that: "DC

microplasmas are density scaled version of low pressure normal glow discharges." This

conclusion is based on results 1-8 above. Some deviations from 'ideal' normal glow behavior were also noted and in some cases explained (points 9-14). This conclusion serves to define DC microplasmas within the context of other plasma discharges. The DC normal glow discharge, to which the microplasma is related, is the most well studied and understood plasma discharge. Such a classification helps in predicting the behavior of microplasma discharges in new applications and situations. This work was not the first to suggest that atmospheric pressure microplasma were 'pd' scaled[5] version of low pressure discharges. But it was the first to clearly document all of these normal glow behaviors in a variety of situations and circumstances. As such this characterization and classification of the DC microplasma serves to expand these types of discharges from the narrow definition of 'novel' microplasmas to one of the most basic and fundamental regimes relevant to all atmospheric pressure non-thermal plasmas.

The techniques developed and the fundamental work defining microplasmas has been well accepted by the plasma research community and the four papers published on the subject corresponding to chapters 3[68], 4[83], 5[100] and 6[109] have already been well cited. The articles citing these works have generally fallen into two categories 1) those referring to the fundamental behavior of atmospheric pressure plasmas in general and 2) those referring to the spectroscopic techniques developed for temperature measurements. The reasons for the first impact are related to the nature of the microplasma classification as already discussed. The impact with regards to optical emission spectroscopy likely occurred due to the extensive and detailed use of the spectroscopic technique for such a

---

[5] *'pd'* here refers to pressure*distance between electrodes as discussed in chapter 2. *'pd'* scaling is the fundamental feature of the Paschen curve. Maintaining constant *'pd'* is essentially the same as operation at a constant Knudsen number. The size of the discharge should be maintained the same in relation to the number of collisions within the discharge to achieve similar operation.

variety of conditions. To put this in perspective in the review on microplasma written by Becker[36] (which was completed just days prior to the first of these publications and gives a good review of the prior state of the art) temperatures had been measured in microplasmas for five conditions. In the four papers published as part of this work temperature measurements are presented for 122 different operating conditions of the microplasma. Prior to this work the spectroscopic technique using the N_2 2nd positive system was only beginning to be implemented for atmospheric pressure non-thermal plasmas. Previously it had been applied in low pressure non-thermal systems and atmospheric pressure thermal systems. These publications with their many results gave additional credence to the technique and also specifically the 2nd publication (Chapter 4) analyzed in detail some of the inaccuracies, and assumptions in applying the methods. The ability to operate in non-thermal regimes with low temperatures is the most important feature of a variety of non-thermal atmospheric pressure plasmas applications ranging from biomedical applications to PECVD processing. Thus the continued development of non-equilibrium temperature measurement techniques is a very important impact of this research. Locally the methods and techniques have already been taught to several other researchers at Drexel.

The limitations and deficiencies in this area of my dissertation research are as might be expected in any such a characterization based study. Though many questions were answered, many were not, and new ones arose. The two most important measurements which were not made were direct measurements of the plasma density, n_e, and electron temperature, T_e. These are two of the most fundamental plasma properties

and yet are very difficult to measure at atmospheric pressure. Further discussion on this is given in the future work section on improved diagnostics.

10.2.2. Discharge Stabilization

The operation of these microplasmas at gas temperatures significantly above ambient and possible operation as 'warm discharges' gives rise to the question: why are they stable? In this section of the dissertation it was shown that these discharges should not be stable with respect to the ionization overheating instability (IOI) if only the traditionally considered wall cooling stabilization is considered. The electron density will grow exponentially in ~0.1 μs for discharges operating with current densities on the order of 1 A/cm^2 (consistent with gamma mode operation). It is shown both analytically and experimentally that specifically in atmospheric pressure plasmas the external circuit plays an important role in stabilizing the discharge. If the characteristic (RC) response time of the external circuit is comparable to the instability increment, Ω, time the discharge can operate stably.

This result has been submitted for publication and is currently under review and I can only guess as to its impact in the research community. I see that for those working with DC atmospheric pressure discharges some insight into specific operation will be gained. Also particularly for my applications in AP-PECVD this suppression of instabilities was essential to successful deposition of thin films. I hope that for those plasma researchers working in atmospheric pressure non-thermal plasmas a more general understanding of instabilities will also be gained. Though the IOI and its relation to glow

to arc transition is generally known this is the first calculation of the rates of such instabilities for atmospheric pressure systems.

There are limitations of this stabilization mechanism. First, unlike other methods of stabilization such as operation in helium and convective cooling this method does not prevent heating of the gas. In our approach the IOI is suppressed but the plasma is still warm. The potential applications of warm stable non-thermal plasma are significantly less than those for cold stable non-thermal plasmas. Though having separate stabilizing mechanism (external circuit) and cooling mechanism (helium and convection) enables more control. AP-PECVD is one of the more demanding applications with respect to temporal and spatial uniformity. In many less sensitive applications like volume gas reactions for fuel conversion and medical application uniformity is less of a concern and the 10's of microseconds pulsing as observed for unstable operation here to many might be considered inconsequential. Thus not all applications require this level of stabilization.

10.2.3. AP-PECVD Demonstration

The final sections of this dissertation demonstrate the significant progress made toward thin film deposition with atmospheric pressure plasmas. By controlling instabilities and excessive gas temperatures amorphous carbon deposits could be deposited with nano-scale surface uniformity. Some preliminary work is also presented showing that by tailoring the precursor gas mixture and discharge conditions various desirable forms of a-C:H can be attained. In comparison to existing technologies for helium based AP-RF-PECVD the films deposited can be more durable likely due to the

larger role of ions in deposition and the increased power densities from operating in a gamma mode.

This more applied aspect of this research has the potential for broader direct impacts. However, I do not believe that Intel is going to come knocking on my door asking about microplasmas anytime soon. Even in the nascent field of AP-PECVD with its various potential applications, I do not think DC microplasmas as shown here will gain much traction. Although the microplasmas were able to successfully deposit thin films the downsides with regard to treatment of only conducting surfaces and changing in discharge parameters with extent of deposition will limit their adoption. Though the improved deposition characteristics with DC operation does reveal some concerns and solutions solutions for attaining better quality thin films in more generally applicable AP-RF discharges. Also although the DC microplasmas are able to perform PECVD with nano-scale uniformity at the macroscale (~0.1 to 0.5 mm) there are of course significant non-uniformities due to the inherent small size of the plasma. Some of these deficiencies may be addressed through improved device design as discussed in the future works sections. Also one important future impact as presented in chapter 8 is that the inherent size of the discharge could be a great advantage in mask-less micro-patterning applications for MEMs, simple circuit and detectors which do not require nano-scale patterning like IC manufacturing.

10.3.   Future and Continuing Work

Following is a list of avenues of research which this dissertation research has lead to or may lead to in the future. Some of these address limitations in the current research and some are expansion of the research in various directions. In several cases some preliminary work has been completed and is presented. In a few cases extensive work has been completed and is referred to by publication.

10.3.1. Improved Diagnostics

As mention in the summary techniques to directly measure two very important plasma's properties, namely the electron density, n_e, and temperature, T_e, are lacking. The low cost, tried and true method of Langmuir type probes used in low pressure plasma systems is difficult to apply at atmospheric pressure. While this has been attempted in large scale atmospheric pressure helium DBD's [151], the small size of the plasma, sheaths, and mean free paths encountered in atmospheric pressure microplasmas, the presence of a probe can cause significant perturbations to the plasma in addition to complications associated with the analysis of collisional sheaths. This small size is inherent to atmospheric pressure plasma systems due to '*pd*' scaling.[37] The electrode gap '*d*' is typically about 1 mm, and characteristic features such as sheaths are <10 μm. Laser techniques for plasma property measurements such as Thompson scattering [152], heterodyne interferometry[97] are expensive, complex, indirect (only in the case of interferometry), hindered by the small discharge size, and/or not well tested at atmospheric pressure. Microwave techniques are complicated by discharge size and proximity of the collision frequency with microwave frequency [153, 154].

As part of my research though not presented in this dissertation a technique was developed and applied to measure the electron densities in atmospheric pressure non-

thermal DC micro-plasmas from the Stark broadening of the atomic Hydrogen Balmer α and β lines. A publication on this subject was submitted to Spectrochimica Acta B, in June 2008.[155] Such an emission spectroscopy technique is one of the few available to measure the electron density in atmospheric pressure micro-scale plasmas. In atmospheric pressure plasmas the overall broadening is due to both Stark and Van der Waals effects and proper estimation of the Van der Waals broadening is essential to determine the electron density in the microplasma. Since the plasmas are non-thermal, estimation of the Van der Waals contribution is non-trivial. We use the broadening of multiple lines, to accurately determine both the Van der Waals and Stark broadening. The efficacy of the technique relies upon the fact that the Van der Waals broadening varies only slightly from one line to another while the Stark broadening varies significantly from line to line for the hydrogen Balmer α and β lines. The technique was applied to measure electron density in atmospheric pressure DC normal glow microplasma in helium as $n_e=4.8 \times 10^{13}$ cm^{-3}.

Another avenue to make measurements is micro-scale probe diagnostics. However, there are several significant challenges. To be non-perturbing to the plasma the probes could be several microns in size or even smaller. These small probes would have to be able to withstand high heating loads in the 1000K+ plasmas as well. The probe measuring circuit would also have to be specially made. Stray capacitance should not be introduced by the probe, and the probes impedance to ground should be significantly higher than the plasma resistance. Technically if such a robust probe could be made Langmuir type diagnostics including measurement of voltage current characteristics for single and double probe could be used to determine the electron temperature, ion density,

and even the electron energy distribution function. However, in additional to the advances in probe construction significant advancements in probe operational theory would have to be made as well. Atmospheric pressure plasmas, which are very collisional in comparison to low pressure plasmas, will have additional reactions such as negative ion formation, charge exchange, and ionization within the sheaths which will significantly affect the interpretation of the probe measurements.

A third measurement which would be both fundamentally interesting and also relevant to many applications is measurement of the kinetic energy of the ions in the cathode sheath. In a low pressure glow discharge the cathode sheath potential is about 250V and the ions gain almost all of this energy as kinetic energy since there are few collisions within the length of the sheath. These high energy ions are very good at creating anisotropic structures and for physical sputtering of material. The voltage drop in the cathode sheath of the atmospheric pressure plasmas is similar to that for low pressure plasmas but the ions experience significantly more collisions. Much of their kinetic energy can be lost in charge exchange processes (some of which have very high cross sections due to resonant charge exchange). Since the ion mean free path (<.2 μm) is much less than the sheath dimensions (~20 μm), these processes should lead to a large number of neutrals and ions with moderate kinetic energy rather than the few very high energy ions in the case of low pressure plasmas. This can be modeled[156], and expected energies are 1 eV to 10 eV though no experimental verification has ever been performed. Laser induced fluorescence and measurement of the Doppler shift of absorption lines in the most viable method to measure the ion kinetic energies. The energy of the ions is

important to understand if anisotropic processing can occur at atmospheric pressure[6]. Energetic ions can also change film properties as in the case of ion stitching in a-C:H films. Sputtering is also a deposition method for metals requiring energetic ions. A quick test of sputtering with a copper wire as cathode in an argon DC microplasma was performed. Sputtered Copper was collect on a silicon wafer anode as shown in Figure 10.1. Only a very thin <50nm layer was deposited after 2 ½ hrs of sputtering. These preliminary results indicated a sputter yield at the cathode of significantly less than 1 and a ion energy $\ll$ 100 eV.[157]
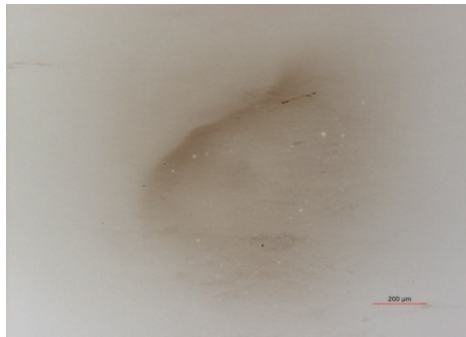
Figure 10.1: Sputtered copper redeposited from cathode onto silicon wafer anode after 2 ½ hours of operation with argon DC microplasma.

10.3.2. Expanded Materials Characterization

A limitation in this research with possible avenue for further explorations (though perhaps by a materials scientist and not a mechanical engineer) is the quality and variety of materials which may be deposited using the AP-PECVD. The Raman analysis placed an upper bound on the sp^3 content of about 30% for the best condition tested. There is no inherent reason why higher quality DLC films could not be attained. In fact, though not

---

[6] The ratio of depth to width and thus anisotropy is on the order of $(KE_{ion}/T_{ion})^{1/2}$. Which is simply the ratio of the directed velocity to the thermal velocity of the ions.

rigorously pursued, some of the materials deposited with the unstable plasma discharge when subject to the scratch test actually scratched into the stainless steel screw driver used for scratching indicating high hardness. Such high quality DLC films have been deposited in low pressure PECVD systems and should be attainable in the AP-PECVD systems especially the DC systems developed in which ions can help to harden the surface.

Another future task is a more detailed materials characterization of the produced films. SEM and AFM could be used to determine the nano-scale features of the thin film at resolutions better than the approximately 250 nm limit of the optical diffraction technique used here. Elipsometry could be used to measure the dielectric properties of the thin films. UV raman using 244 nm which was in disrepair at the time of these analyses is currently operational at the Drexel materials characterization facility and could be used to more accurately measure the sp^3 content of the DLC films. Fourier transform infra-red (FTIR) spectroscopy could be performed on the films to determine some of the C-H bonding, surface bonds and surface functional groups. X-ray photoelectron spectroscopy (XPS) could also be used to investigate the elemental composition and bond structure in the films.

Some preliminary FTIR and XPS results were attained though only for the RF deposited films (the region of deposition on the DC-deposited film was too small to properly interrogate). Figure 10.2A shows the ATR-FTIR spectra attained for the sample. In this wavenumber range H-C bonding in either: 1) H-C-C sp^3 hybridized (2850 cm^{-1} to 2970 cm^{-1}) Alkanes, 2) H-C=C sp^2 hybridized (3010 cm^{-1} to 3095 cm^{-1}) Alkenes or 3) H-C≡C sp hybridized (~ 3300 cm^{-1}) Alkynes can be identified. This spectra indicates that

all of the carbon bonds are hydrogenated and is consistent with other diagnostics and our expectations. The lack of peaks corresponding to C double and triple bonds also indicates no significant sooting. Figure 10.2B shows an XPS spectra. Peaks corresponding to O1s, C1s, Si2s, Si1s are visible. The elemental constants of the film can be estimated from this as shown in the inset (though H content is not observable by this diagnostic). As expected significant carbon content (~88%) is indicated as is some of the substrate. Significant contamination from the counter electrode (copper in this case) is not observed. The oxygen content is likely due to aging effects or wiping with alcohol both of which are known to terminate dangling or weak bonds on the surface of the film with C-O and similar bonds. The XPS technique only probes the top ~10nm from the surface.
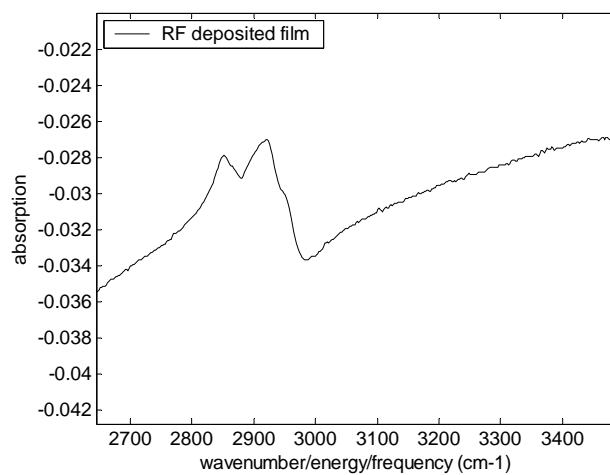
(A)
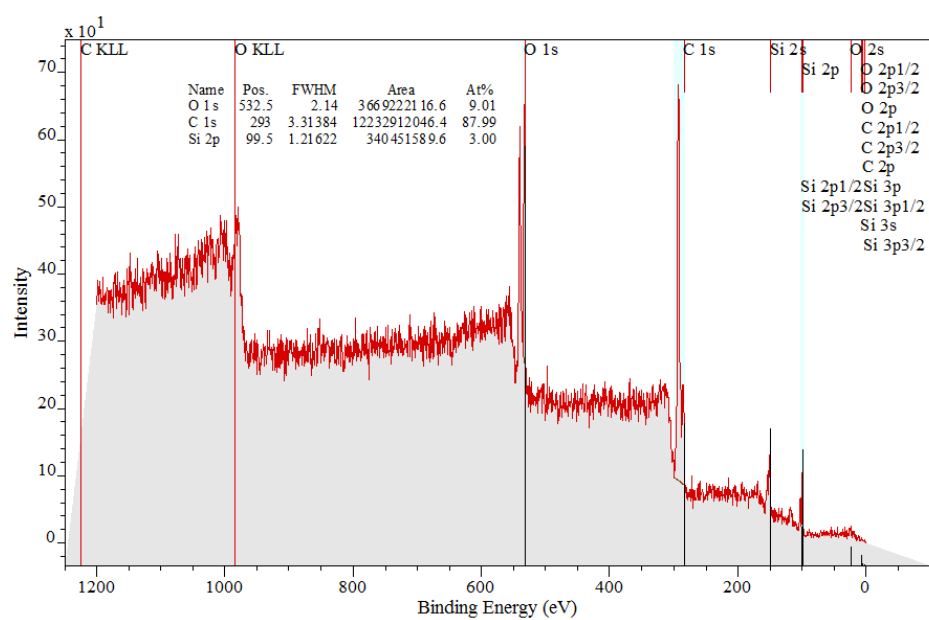
(B)

Figure 10.2: Preliminary ATR-FTIR (A) and XPS (B) measurements of the AP-RF-

PECVD thin films.

10.3.3. Micro patterning

The small size of the microplasma is perhaps one of its most interesting features. The ability to move the discharge around and to directly write small features for applications in MEMs, simple circuit and detectors which do not require nano-scale patterning seems very promising. Such application should be explored in future work. Table 10.1 summarizes the expected sizes of the discharges based upon their measured operating power densities and range of minimum operating powers. The gamma mode discharges are able to create the smallest plasmas and the alpha mode are more appropriate for uniform treatment of large areas.

Table 10.1: Summary of measured current densities and discharge sizes for atmospheric pressure discharges operating in several different gases and modes.

Gas and Sheath Mode	Measured Normal Current Density	Diameter of 0.1 W to 2 W Discharge
Hydrogen γ-mode	20 A/cm^2	36 μm to 160 μm
Air γ-mode	6 A/cm^2	65 μm to 291 μm
Helium γ-mode	0.5 A/cm^2	226 μm to 1.0 mm
Helium α-mode	~ 0.003 A/cm^2	2.9 mm to 13 mm

Shown in chapter 8 were results for patterning using PECVD. Localized etching and surface functionalization can also be achieved with the microplasma. Figure 10.3A shows the modification of the contact angle on a silicon wafer by application of a low

current microplasma in air. The plasma treated area has a lower surface energy and the water wets the surface with lower contact angle and spreads out. In the untreated areas the condensed water beads up. The treated area appears to be about 100 μm in width indicating that for surface functionalization the treatment area is large than the discharge. In constrast for PECVD the treatment area was the same size as the discharges. Shown in Figure 10.3B is the patterned etching of material from a surface, in this case dried ink from a glass microscope slide. This was done with the DC microplasma in a bent configuration for treating dielectrics as to be discussed in the improved device design section.
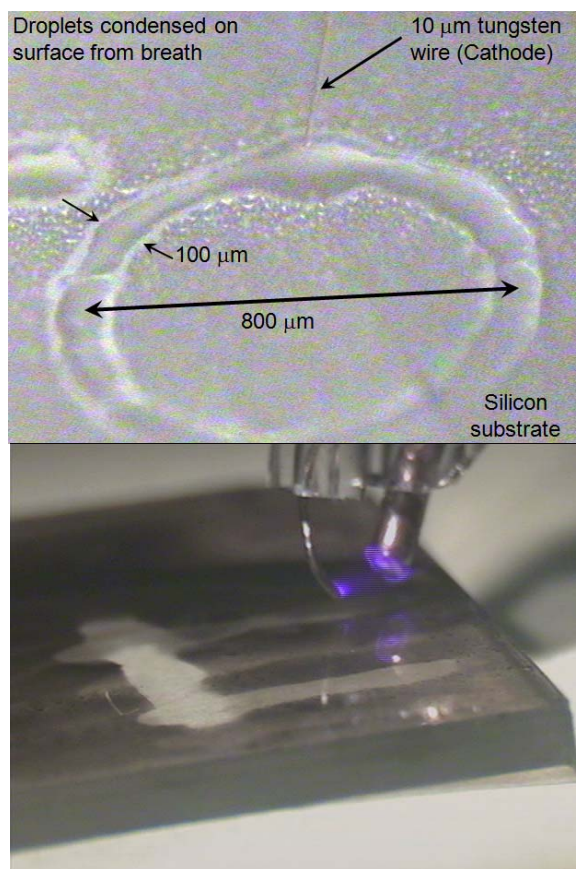
Figure 10.3: Patterned (A) surface modifications affecting wettability and (B) etching of ink from a glass substrate using the side of a bent discharge.

Several significant issues occur when trying to consistently perform this patterning. Motion of the anode and cathode spot independent of the substrate motion often occurs. These are due to both changes in the conducting properties of the electrode surface and the volumetric chemical changes within the discharge volume. These surface effects are much more prevalent at the anode as discussed in chapter 5.[7] I investigated many of these phenomena in conjunction with an undergraduate student as part of a NSF-REU related to this project and a journal paper on these self-induced motions was published.[144] While investigating the various possible sources for self-induced discharge motions no specific solutions to stopping the motions were given and should be an avenue of future research. Some ideas for doing this are presented in the improved device design section.

10.3.4. Improved Device Design

The configuration of microplasma studied here (a wire over a planar electrode in a parallel plate configuration) was chosen because of its simplicity and fundamental nature. Without significant gas flows, odd geometries or other spurious effects the fundaments of these microplasma could be more easily studied. However, this configuration is not necessarily the best for effective application. Microfabricated arrays of discharges and jets have been investigated.[36] Many of these configurations though serve to additionally destabilized the discharges. For example in jet configuration the gas flow would cause the

---

[7] The reason for this is that the anode sheath is governed by electron dynamics whereas the cathode sheath is governed by ion dynamics. Ions are massive and slow to change electrons are light and easy to move. As a consequence the anode sheath is much more significantly affected by small changes in electrode properties. For this reason most PECVD studies were performed using the substrate as cathode which was more stable.

discharge to blow-out and reignite leading to a pulsing discharge behavior unsuitable for thin film PECVD. These instability effects should be taken into account in designing an appropriate system.

Towards the end of this research a method of using the DC microplasma to treat dielectric surfaces and in which the electrodes were independent of the substrate was proposed. This configuration was not fully implemented because a sufficiently small system could not be contrived to fit inside the existing PECVD reactor chamber. This configuration is shown in Figure 10.4 and uses the side of the positive column to interact with the substrate. The positive column is bent using a magnetic field. Typically the microplasma discharge will occur in a straight line between the anode and cathode. By apply a magnetic field perpendicular to the direct of current flow, see figure 10.4B, there is a magnetic Lorentz Force on the charged particles in the plasma resulting in a bending of the positive column. The intensity of the magnetic field should be chosen to bend but not break the positive column. Figure 10.4C shows an implementation of this using a small neodymium magnet to generate a magnetic field of about 1000 G in the vicinity of the microplasma. Dielectric surfaces could be treated using the side of the positive column as was shown in Figure 10.3B.
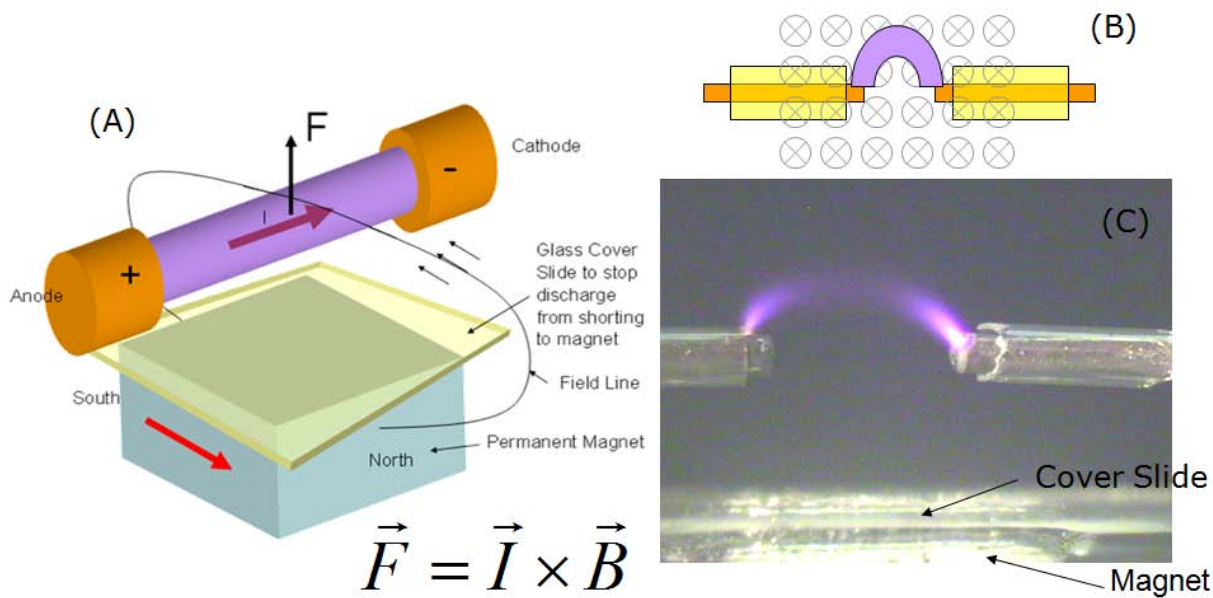
Figure 10.4: (A) Schematic, (B) magnetic field configuration, and (C) micrograph of DC glow discharge operating in a traverse magnetic field to bend the discharge such that dielectric surfaces can be laterally treated.

10.3.5. VHF Discharges

The DC microplasmas showed several advantages in comparison to alpha mode helium based CCP atmospheric pressure discharges with regards to the properties of the deposited films. These stem from the ability of the discharge to operate stably in the gamma mode in a variety of gases. The AP-RF-CCP[8] were limited to operation in significant amount of helium due to alpha to gamma transition and the instability of the RF gamma mode operation. The ideal discharge would operate stability in either gamma

---

[8] Atmospheric-pressure radio-frequency capacitively-coupled-plasmas

or alpha mode and in a variety of gases. This possibility may exist in VHF (30 MHz to 300 MHz) and UHF (300MHz to 3GHz) frequency operation. In VHF the oscillations of the electric field may be faster than the ionization overheating instability. This may lead to external circuit stabilization of the gamma mode as was observed in the DC microplasmas with reduced stray capacitance. Thus the gamma mode VHF-CCP may be stable allowing for more energetic ions to improve deposition quality. The higher frequency operation will also affect the alpha to gamma transition (refer to section 2.2.8). In air at frequencies above about 122MHz the critical current density for $\alpha-\gamma$ transition is greater than the gamma mode normal current density. Thus hopefully both alpha and gamma mode operation will be available in complex gas mixtures without significant helium at VHF operating frequencies. In some respects VHF operation is similar in principles and possibilities to nanosecond pulsed operation for DBDs (though with 100% duty cycle).

Some preliminary experiments were performed with VHF discharges in pure helium. These were done using a variable frequency generator (HP 8656B), VHF amplifier (OPHIR 5124RF), and the same matching network as used in the RF-CCP studies. As shown in Figure 10.5 in the alpha mode at higher frequency operation the sheaths become a smaller portion of the discharge volume. This is consistent with the belief that $\alpha-\gamma$ transition will be delayed at higher frequencies. Figure 10.6 shows the measured power density as a function of power for several operating frequencies. The power density is apparently constant with increase power and operating frequency. Inaccurate measurements of the power density at low powers are likely due to flow of the transmitted power to loads other than the plasma discharge. This keeps alive the

possibility that at higher frequencies the operating current density of alpha mode discharges in air and similar complex gases will be below the critical current density for $\alpha-\gamma$ transition (which should increase with frequency).
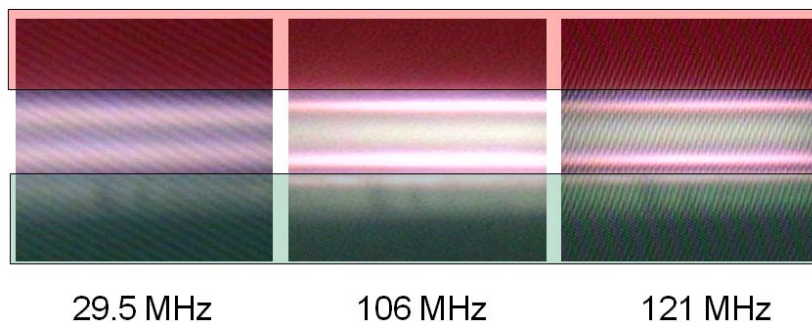
Figure 10.5: Variable freuqnecy operation of VHF CCP discharges in atmospheric pressure helium. Parallel electrodes are sketch over the top of micrographs of the discharges.
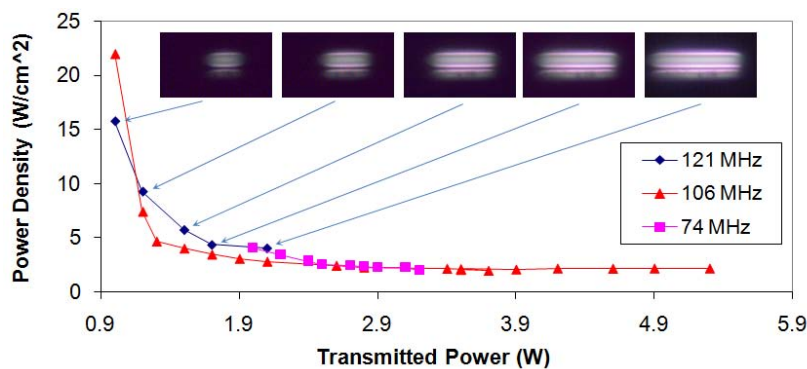
Figure 10.6: Variation in power density with discharge power for various frequencies of operation of VHF CCP in atmospheric pressure helium. Inset images show the images used to perform the analysis for 121 MHz operation.

Significant future work could be done in the fundament plasma physics of atmospheric pressure VHF CCP discharges with the goal of uniform alpha or gamma mode discharges in atmospheric pressure complex gases. One challenging aspect

encountered here was that the matching network for the system should be completely redesigned to work with the high frequencies and higher impedances of atmospheric pressure discharges.

10.3.6. Deposition of Various Materials

This dissertation has shown that DC microplasmas can be appropriate glow discharges for thin film deposition. In future work any of the hundreds of PECVD precursors and deposited films used in low pressure systems could be tested. Such efforts should proceed with a clear application in mind. Amorphous carbon deposition was studied here because of its relative safety and yet challenging requirements for high quality deposition. Future studies on the mechanism of deposition should focus on deposition of solely dielectric materials on dielectric substrates using the side of the discharge. Evaporated TEOS or a similar precursor for SiO_2 deposition would be appropriate. If considering direct deposition with the microplasma, the deposition of conducting materials and metals should be considered for example using evaporated metallic salts such as $TiCl_4$ or organo-mettalic precursors (though safety will be a consideration with these toxic substances).

10.3.7. Nanoscale-plasmas

Again, the small size of the microplasma is one of its most interesting features. This small size is achieved by the *'pd'* Knudsen number scaling which indicates that as the number density is increase the size of the discharge will decrease. These results beg

the question: how small can a plasma be made? The minimum size is determined by the Debye length and size of the sheath and quasi-neutral region (recall Chapter 2, $\lambda_D = 743\sqrt{T_e/n_e}$). A plasma cannot be smaller than it boundary layers. At atmospheric pressure the Debye length is on the order of 1μm and sheaths are several (~5) Debye lengths. The pre-sheaths and quasi-netural regions should also be at least several debye lengths indicating a minimum discharge size of about 20 μm at atmospheric pressure similar to what was observed in our microplasma studies.

To explore smaller plasmas by *'pd'* scaling, the plasma should be generated in denser media than atmospheric pressure air. Two possibilities present themselves, high pressure gases (or super critical gases), and liquids. The use of high pressure systems is somewhat complicated but liquids are high density ambient media. The challenge in generating plasma discharges in liquids is understand how the plasma will be affected by and influence the generation of bubbles in the media. I have performed some research in the direction of nano-scale plasma in liquids as part of my doctoral work but not a part of this dissertation. A aspect of this work titled "Nanoscale Corona Discharge in Liquids, Enabling Nanosecond Optical Emission Spectroscopy" has recently been published.[143] In this work it is shown that non-thermal plasmas as small as 2μm in diameter can be generated in liquids using 10 ns duration voltage pulses on 50 nm sharp electrodes. Several images of the small discharges created from nanoscale electrodes along with the emission spectra of plasma corresponding to the solution which they were immersed are shown in Figure 10.7. One of the greatest impacts of this microplasma research may be how it gave insight into how to push the envelope for development of even smaller scale plasmas. The potential for great impact and advancement exists for these nano-scale

discharges in the areas of spectroscopy, elemental analysis, materials fabrication, micro-fluidics, micro-scale diagnostics, cellular surgery and fundamental physics. This research into nanoscale plasmas as a small scale optical emission spectroscopy diagnostic was recently covered as a news and views article in the journal Nature.[158]
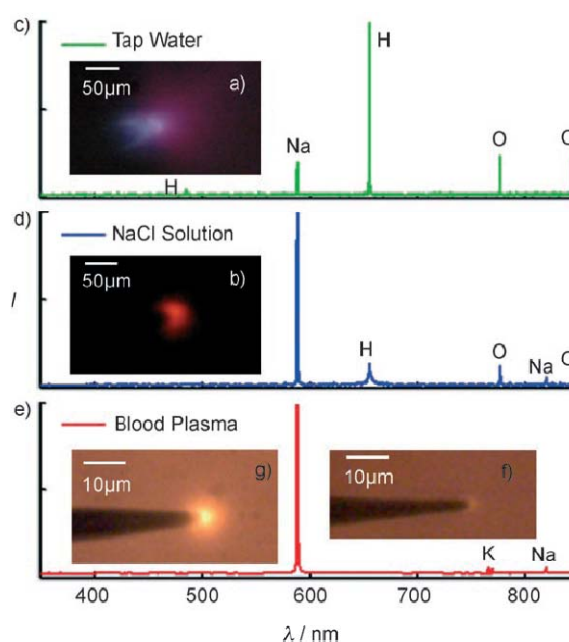
Figure 10.7: OES and corona discharges produced using 5 kV stepped and pulsed voltage excitation in liquids. a, b) Demonstration of color changes as a function of the composition of the solution. c, d) OES from tap water (c) and 0.5M NaCl (d). e) OES for 5 kV, 20 ns duration pulses in blood plasma; this spectrum does not show oxygen and hydrogen peaks and indicates that for longer discharges, light emission is due to recombined ions and decomposition of the liquid, whereas in short discharges, light emission is due solely to recombined ions. Optical micrographs indicate that the short-duration pulsed coronas (f) are less than 3 μm in diameter and are significantly smaller than discharges from microsecond-duration pulses (g), for which a larger discharge and bubble formation is seen.

11. Bibliography

[1]   Y. P. Raizer, "Gas Discharge Physics," Berlin: Springer, 1991.

[2]   A. Fridman and L. A. Kennedy, *Plasma Physics and Engineering*. New York: Taylor and Francis, 2004.

[3]   A. Fridman, *Plasma Chemistry*. New York: Cambridge University Press, 2008.

[4]   D. Graves, "Plasma Processing," *IEEE Transactions on Plasma Science,* vol. 22, pp. 31-42, 1994.

[5]   Semiconductor Industry Association, Press Release: September Semiconductor Sales up 1.6 Percent Year-on Year, 2008, http://www.sia-online.org/cs/papers_publications/press_release_detail?pressrelease.id=1507

[6]   R. d'Agostino, P. Favia, C. Oehr, and M. R. Wertheimer, "Low-Temperature Plasma Processing of Materials: Past, Present and Future," *Plasma Processing and Polymers,* vol. 2, pp. 7-15, 2005.

[7]   M. A. Leiberman and A. J. Lichtenberg, *Principles of Plasma Discharges and Materials Processing*. New York: Wiley-IEEE, 1994.

[8]   M. J. Madou, "Fundaments of Microfabrication," Florida: CRC Press, 2002.

[9]   M. Poliakoff and P. Licence, "Sustainable Manufacturing: Green Chemistry," *Nature,* vol. 450, pp. 810-812, Dec. 6 2007.

[10]   E. E. Kunhardt, "Generation of Large-Volume Atmospheric-Pressure Nonequilibrium Plasmas," *IEEE Transactions on Plasma Science,* vol. 28, pp. 189-200, 2000.

[11]   S. E. Babayan, "Deposition of Silicon Dioxide Films with an Atmospheric-Pressure Plasma Jet " *Plasma Sources Science and Technology,* vol. 7, p. 286, 1998.

[12]   S. Kanazawa, M. Kogoma, T. Morowaki, and S. Okazaki, "Stable Glow Plasma at Atmosherpic Pressure," *Journal of Physics D: Applied Physics,* vol. 21, pp. 838-840, 1988.

[13]   T. Ito, T. Izaki, and K. Terashima, "Application of Microscale Plasma to Material Processing," *Thin solid films,* vol. 386, pp. 300-304, 2001.

[14]   J. C. T. Eijkel, H. Stoeri, and A. Manz, "An Atmospheric Pressure DC Glow Discharge on a Microchip and Its Application as a Molecular Emission Detector " *Journal of Analytical Atomic Spectrometry,* vol. 15, pp. 297-300, 2000.

[15]   K. H. Schoenbach, A. El-Habachi, W. Shi, and M. Ciocca, "High-Pressure Hollow Cathode Discharges," *Plasma Sources Science and Technology,* vol. 6, pp. 468-477, 1997.

[16]   R. J. Goldston and P. H. Rutherford, *Introduction to Plasma Physics*. Philadelphia: IOP Publishing, 1995.

[17]   Public Domain Photo, 2008, http://en.wikipedia.org/wiki/Image:Polarlicht_2.jpg

[18]   G. Herzberg, *Spectra of Diatomic Molecules*. New York: Van Nostrand Reinhold Co., 1950.

[19]   A. G. Engelhardt, A. V. Phelps, and C. G. Risk, "Determination of Momentum Transfer and Inelastic Collision Cross Sections for Electrons in Nitrogen Using Transport Coeficients," *Physical Review,* vol. 135, pp. 1566-1574, 1964.

[20]   Lifshitz, "Correlation of Vibrational De-Excitation Constant (K0-1) Od Diatom Molecules," *Journal of Chemical Physics,* vol. 61, p. 2478, September 1974.

[21]   A. A. Barmin, A. P. Glinoc, and G. A. Shoumova, "Overheating Instability of an Electric Discharge Stabilized by Nonisothermal Walls," *High Temperature (Teplofizika Vysokikh Temperatur),* vol. 25, pp. 626-632, Mar. 1988.

[22]   T. V. Rakhimova and A. T. Rakhimova, "Effect of High-Frequency Electromagnetic Field on Development of Overheating Instability in a Weakly Ionized Gas Discharge Plasma," *High Temperature (Teplofizika Vysokikh Temperatur),* vol. 14, pp. 1174-1177, Nov-Dec 1976.

[23]   B. Shokri and A. R. Niknam, "Discharge Plasma Instabilites in the Presence of an External Constant Electric Field," *Physics of Plasmas,* vol. 10, pp. 4153-4161, October 2003.

[24]   W. L. Nigham and W. G. Wiegand, "Influence of Negative-Ion Processes on Steady-State Properties and Striations in Molecular Gas Discharges," *Physical Review A,* vol. 10, pp. 922-945, Sept 1974.

[25]   Y. Sintov and S. A., "Thermal-Instability Considerations for Pulsed Microwave-Excited Co2 Slab Lasers," *Journal of Physics D - Applied Physics,* vol. 33, pp. 2125-2132, 2000.

[26]   R. A. Haas, "Plasma Stability of Electric Discharge in Molecular Gases," *Physical Review A,* vol. 8, pp. 1017-1043, 1973.

[27]   W. L. Nighan, "Causes of Thermal Instability in Externally Sustained Molecular Discharges," *Physical Review A,* vol. 15, pp. 1701-1720, April 1977.

[28]   P. Chabert, A. J. Lichtenberg, M. A. Lieberman, and A. M. Marakhtanov, "Instabilities in Low-Pressure Electronegative Inductive Discharges," *Plasma Source Science and Technology,* vol. 10, pp. 478-489, July 2001.

[29]   J. R. Roth, *Industrial Plasma Engineering, Vol. 1 - Principles*. PHialdelphia: IOP Publishing, 1995.

[30]   S. E. Babayan, "Deposition of Coatings Using an Atmospheric Pressure Jet". vol. 6194036, U. P. Office, Ed. USA, 2001.

[31]   Surfx Technologies LLC, 2008, http://www.surfxtechnologies.com/

[32]   U. Kogelschatz, "Dielectric-Barrier Discharges: The History, Discherge Physics, and Industrial Applications," *Plasma Chemistry and Plasma Processing,* vol. 23, pp. 1-46, March 2003.

[33]   F. Fanelli, R. d'Agostino, and F. Fracassi, "Atmospheric Pressure Pe-Cvd of Fluorocarbon Thin Films by Means of Glow Dielectric Barrier Discharges," *Plasma Processes and Polymers,* vol. 4, pp. 797-805, 2007.

[34]   H. Ayan, G. Fridman, A. Gutsol, V. Vasilets, A. Fridman, and G. Friedman, "Nanosecond Pulsed Uniform Dielectric Barrier Discharge," *IEEE Transactions on Plasma Science,* vol. 36, pp. 504-508, 2008.

[35]   W. M. Yen, S. Shionoya, and H. Yamamoto, *Phosphor Handbook*. Boca Raton: CRC Press, 2006.

[36]   K. Becker, K. Schoenbach, and J. Eden, "Microplasmas and Applications," *Journal of Physics D - Applied Physics,* vol. 39, pp. R55-R70, FEB 7 2006.

[37]   M. Kushner, "Modeling of Microdischarge Devices: Plasma and Gas Dynamics," *Journal of Physics D: Applied Physics,* vol. 38, pp. 1633-1643, 2005.

[38]   H. Y. Fan, "The Transition from Glow Discharge to Arc," *Physics Review* vol. 55, p. 769, April 15 1939.

[39]   W. A. Gambling and H. Edels, "The High-Pressure Glow Discharge in Air," *Br. J. Appl. Phys.,* vol. 5, p. 36, 1956.

[40]   W. A. Gambling and H. Edels, "The Properties of High-Pressure Steady State Discharges in Hydrogen," *Br. J. Appl. Phys.,* vol. 7, p. 376, November 1956.

[41]   R. Foest, M. Schmidt, and K. Becker, "Microplasmas, an Emerging Field of Low-Temperature Plasma Science and Technology," *International Journal of Mass Spectrometry,* vol. 248, pp. 87-102, 2006.

[42]   A. Koutsospyros, S. M. Yin, C. Christodoulatos, and K. Becker, "Destruction of Hydrocarbons in Non-Thermal, Ambient-Pressure Capillary Discharge Plasmas," *International Journal of Mass Spectrometry,* vol. 233, pp. 305-315, 2004.

[43]   D. Hsu and D. Graves, "Microhollow Cathode Discharge Stability with Flow and Reaction," *Journal of Physics D - Applied Physics,* vol. 36, pp. 2898-2907, 2003.

[44]   R. M. Sankaran and K. P. Giapis, "High Pressure Micro-Discharges in Etching and Deposition Applications," *Journal of Physics D - Applied Physics,* vol. 36, pp. 2914-2921, 2003.

[45]   Y.-B. Guo and F. C.-N. Hong, "Radio-Frequnecy Microdischarge Arrays for Large-Area Cold Atmoshperic Plasma Generation," *Applied Physics Letters,* vol. 82, pp. 337-339, 2003.

[46]   R. Block, O. Toedter, and K. H. Schoenbach, "Gas Temperature Measurement in High Pressure Glow Discharges in Airs," in *Proceeding of the 30th AIAA Plasma Dynamics and Laser Conference* Norfolk VA, 1999, pp. AIAA-99-3434.

[47]   P. Kurunczi, N. Abramzon, M. Figus, and K. Becker, "Measurements of Rotational Temperatures in High-Pressure Microhollow Cathode Mhc and Capillary Plasma Electrode Cpe Discharges," *Acta Physica Slovaca,* vol. 54, pp. 115-124, 2004.

[48]   C. Penache, M. Miclea, A. Brauning-Demian, O. Hohn, S. Schossler, T. Jahnke, K. Niemax, and H. Schmidt-Bocking, "Characterization of a High-Pressure Microdischarge Using Dionde Laser Absorption Spectroscopy," *Plasmas Source Science and Technology,* vol. 11, pp. 476-483, 2002.

[49]   J. Robertson, "Diamond-Like Amorphous Carbon," *Material Science and Engineering R,* vol. 37, pp. 129-281, 2002.

[50]   K. Bera, B. Farouk, W. J. Yi, and Y. H. Lee, "Simulation of Thin Carbon Film Deposition in a Radio-Frequency Methane Plasma Reactor," *Journal of the Electrochemical Society,* vol. 146, pp. 3264-3269, 1999.

[51]   S. E. Alexandrov and M. L. Hitchman, "Chemical Vapor Deposition Enhanced by Atmospheric Pressure Non-Thermal Non-Equilibrium Plasmas," *Chemical Vapor Deposition,* pp. 457-468, Dec. 2005 2005.

[52]   V. Hopfe and D. W. Sheel, "Atmospheric Pressure Plasmas for Wide Area Thin Film Deposition and Etching," *Plasma Processes and Polymers,* vol. 4, pp. 253-265, 2007.

[53]   V. Hopfe and D. W. Sheel, "Atmospheric-Pressure Pecvd Coating and Plasma Chemical Etching for Continuous Processing," *IEEE Transactions on Plasma Science,* vol. 35, pp. 204-214, 2007.

[54]   F. Truica-Marasescu, P.-L. Girard-Lauriault, A. Lippitz, W. E. S. Unger, and M. R. Wertheimer, "Nitrogen Rich Plasma Polymers: Comparison of Films Deposited in Atmospheric- and Low- Pressure Plasmas," *Thin solid films,* vol. 516, pp. 7406-7417, 2008.

[55]   R. Foest, F. Adler, F. Sigeneger, and M. Schmidt, "Study of an Atmosheric Pressure Glow Discharge (Apg) for Thin Film Deposition," *Surface and Coating Technology,* vol. 163-164, pp. 323-330, 2003.

[56]   K. Schmidt-Szalowski, Z. Rzanek-Boroch, J. Sentek, Z. Rymuza, Z. Kusznierewicz, and M. Misiak, "Thin Film Deposition from Hexamethyldisiloxane and Hexamethyldisilazane under Dielectric-Barrier Discharge (Dbd) Conditions," *Plasmas and Polymers,* vol. 5, pp. 173-190, 2001.

[57]   G. R. Nowling, M. Yajima, S. E. Babayan, M. Moravej, X. Yang, W. Hoffman, and R. F. Hicks, "Chamberless Plasma Deposition of Glass Coating on Plastic," *Plasma Sources Science and Technology,* vol. 14, pp. 477-484, 2005.

[58]   H. Yoshiki and T. Saito, "Preparation of TiO_2 Films on the Inner Surface of a Quartz Tube Using a Atmospheric-Pressure Microplasma," *Journal of Vacuum*

Science and Technology A - Vacuum, Surfaces and Films, vol. 26, pp. 338-343, 2008.

[59]   H.-K. Ha, M. Yoshimoto, and H. Koinuma, "Open Air Plasma Chemical Vapor Deposition of Highly Dielectric Amorphous Tio2 Films," *Applied Physics Letters,* vol. 68, pp. 2965-2967, 1996.

[60]   M. Matsumoto, Y. Inayoshi, M. Suemitsu, T. Yara, S. Nakajima, T. Uehara, and Y. Toyoshima, "Low Temperature Growth of Polycrystalline Si on PET Films Using Pulsed-Plasma Cvd under near Atmospheric Pressure," *Thin solid films,* vol. 516, pp. 6673-6676, 2007.

[61]   Y. Mori, K. Yoshii, K. Yasutake, H. Kakiuchi, H. Ohmi, and K. Wada, "High-Rate Growth of Epitaxial Silicon at Low Temperature (530-690 Oc) by Atmospheric Pressure Plasma Chemical Vapor Deposition," *Thin solid films,* vol. 444, pp. 138-145, 2003.

[62]   J. L. Hodkinson, D. W. Sheel, H. M. Yates, and M. E. Pemble, "Atmospheric Pressure Glow Discharge Cvd of Al2o3 Thin Films," *Plasma Processes and Polymers,* vol. 3, 2006.

[63]   F. Fanelli, F. Fracassi, and R. d'Agostino, "Deposition of Hydrocarbon Films by Means of Elium-Ethylene Fed Glow Dielectric Barrier Discharges," *Plasma Processes and Polymers,* vol. 2, pp. 688-694, 2005.

[64]   T. Ito and K. Terashima, "Multiple Microscale Plasma Cvd Apparatuses on a Substrate," *Thin solid films,* vol. 390, pp. 234-236, 2001.

[65]   K. Okazaki and T. Nozaki, "Ultrashort Pulsed Barrier Discharges and Applications," *Pure Applied Chemistry,* vol. 74, pp. 447-452, 2002.

[66]   Y. Lifshitz, "Diamond-Like Carbon - Present Status," *Diamond and Related Materials,* vol. 8, pp. 1659-1676, 1999.

[67]   C. Casiraghi, A. C. Ferrari, and J. Robertson, "Raman Spectroscopy of Hydrogenated Amorphouse Carbons," *Physical Review B,* vol. 72, 2005.

[68]   D. Staack, B. Farouk, A. Gutsol, and A. Fridman, "Characterization of a DC Atmoshperic Pressure Normal Glow Discharge," *Plasma Source Science and Technology,* vol. 14, pp. 700-711, 2005.

[69]   L. Yu, C. O. Laux, D. M. Packan, and C. H. Kruger, "Direct-Current Glow Discharges in Atmospheric Pressure Air Plasmas," *Journal of Applied Physics,* vol. 91, pp. 2678-2686, March 1 2002.

[70]   R. M. Sankaran and K. P. Giapis, "Maskless Etching of Silicon Using Patterened Microdischarges," *Appl. Phys. Lett.,* vol. 79, pp. 593-595, 2001.

[71]   R. M. Sankaran and K. P. Giapis, "Hollow Cathode Sustained Plasma Microjets: Characterization and Application to Diamond Deposition," *Journal of Applied Physics,* vol. 92, pp. 2406-2411, 2002.

[72]   R. M. Sankaran, K. P. Giapis, M. Moselhy, and K. H. Schoenbach, "Argon Excimer Emission from High-Pressure Microdischarges in Metal Capilleries," *Appl. Phys. Lett.,* vol. 83, pp. 4728-4730, 2003.

[73]   R. H. Stark and K. H. Schoenbach, "Direct Current Glow Discharges in Atmospheric Air," *Applied Physics Letters,* vol. 74, pp. 3770-3772, Jun 21 1999.

[74]   K. H. Schoenbach, M. Moselhy, W. Shi, and R. Bentley, "Microhollow Cathode Discharges," *J. Vac. Sci. Technol, A,* vol. 21, pp. 1260-1265, 2003.

[75]   R. H. Stark and K. H. Schoenbach, "Electron Heating in Atmospheric Pressure Glow Discharges," *Journal of Applied Physics,* vol. 89, pp. 3568-3572, Apr 7 2001.

[76]   Z. Yu, K. Hoshimiya, J. D. Williams, S. F. Polvinen, and G. J. Collins, "Radio-Frequency-Driven near Atmospheric Pressure Microplasma in a Hollow Slot Electrode Configuration," *Appl. Phys. Lett.,* vol. 83, pp. 854-856, 2003.

[77]   Y. Akishev, M. Grushin, I. Kochetov, V. Karal'nik, and A. Napartovich, "Negative Corona, Glow and Spark Discharges in Ambient Air and the Transitions between Them," *Plasma Sources Science and Technology,* vol. 14, pp. S18-S25, May 2005 2005.

[78]   Z. L. Petrovic and A. V. Phelps, "Oscillations of Low-Current Electrical Dischaerges between Parallel-Plane Electrode. I. Dc Discharges," *Physics Review E,* vol. 47, pp. 2806-2815, April 1993.

[79]   R. R. Laher and F. R. Gilmore, "Improved Fits for the Vibrational and Rotational Constants of Many States of Nitrogen and Oxygen," *Journal of Physical Chemical Reference Data,* vol. 20, p. 685, April 1991.

[80]   C. O. Laux, T. G. Spence, C. H. Kruger, and R. N. Zare, "Optical Diagnostics of Atmospheric Pressure Air Plasmas," *Plasma Sources Science and Technology,* vol. 12, pp. 125-138, May 2003.

[81]   C. Laux, "Specair Simulation," *Personal communication,* 2005.

[82]   C. L. Tien and J. H. Leinhard, *Statistical Thermodynamics*. New York: Taylor and Francis, 1979.

[83]   D. Staack, B. Farouk, A. Gutsol, and A. Fridman, "Spectroscopic Studies and Rotational and Vibrational Temperature Measurements of Atmospheric Pressure Normal Glow Plasma Discharges in Air," *Plasma Source Science and Technology,* vol. 15, pp. 818-827, Nov. 2006.

[84]   A. Mohamed, R. Block, and K. Schoenbach, "Direct Current Glow Discharges in Atmospheric Air," *IEEE Transactions on Plasma Science,* vol. 30, pp. 182-183, 2002.

[85]   L. Yu, L. Pierrot, C. Laux, and C. H. Kruger, "Effects of Vibrational Nonequilibrium on the Chemistry of Two--Temperature Nitrogen Plasma," *Plasma Chemistry and Plasma Processing,* vol. 21, pp. 483-503, 2001.

[86]   C. Laux, "Radiative and Non-Equilibrium Collisional-Radiative Models," in *von Karman Institute Special Course on Physico-chemical Modeling of High Enthalpy and Plasma Flows*, Rhose-Saint-Genesem Belgium, 2002.

[87]   A. Chelouah, E. Marode, and G. Hartmann, "Measuremetns of Rotational and Vibrational Temperatures in a Low-Pressure Plasma Device Using the Abel Transform and a Spectral Slit Function," *Journal of Physics D - Applied Physics,* vol. 27, pp. 770-780, 1994.

[88]   A. Chelouah, E. Marode, G. Hartmann, and S. Achat, "A New Method for Temperature Evaluation in a Nitrogen Discharge," *Journal of Physics D - Applied Physics,* vol. 27, pp. 940-945, 1994.

[89]   V. M. Donnelly and M. V. Malyshev, "Diagnostics of Inductively Coupled Chlorine Plasmas: Measurements of the Neutral Gas Temperature," *Applied Physics Letters,* vol. 77, pp. 2467-2469, Oct. 6, 2000.

[90]   A. Rahman, A. P. Yalin, V. Surla, O. Stan, K. Hoshimiya, Z. Yu, E. Littlefield, and G. J. Collins, "Absolute Uv and Vuv Emission in the 110-400 Nm Region

from a 13.56 Mhz Driven Hollow Slot Microplasmas Operating in Open Air," *Plasma Source Science and Technology,* vol. 13, pp. 537-547, 2004.

[91] F. Iza and J. A. Hopwood, "Rotational, Vibrational, and Excitation Temperatures of a Microwave-Frequency Microplasma," *IEEE Transactions on Plasma Science,* vol. 32, pp. 498-504, April 2004.

[92] J. C. Langarias, J. A. Reeds, M. H. Wright, and P. E. Wright, "Convergence Properties of the Nelder-Mead Simplex Method in Low Dimensions," *SIAM Journal of Optimization,* vol. 9, pp. 112-147, 1998.

[93] D. I. Slovetsky, *Mechanisms of Chemical Reactions in Non-Equilibrium Plasma.* Moscow: Nauka (Science), 1980.

[94] E. Stoffels, A. J. Flikweert, W. W. Stoffels, and G. M. W. Kroesen, "Plasma Needle: A Non-Destructive Atmospheric Plasma Source for Fine Surface Treatment of (Bio) Materials," *Plasma Source Science and Technology,* vol. 11, pp. 383-388, 2002.

[95] J. A. M. van der Mullen, "Excitation Equilibria in Plasmas; a Classification," *Physics Reports,* vol. 191, pp. 190-220, 1990.

[96] W. J. M. Brok, M. D. Bowden, J. v. Dijk, J. J. A. M. v. d. Muller, and G. M. W. Kroesen, "Numerical Description of Discharge Characteristics of the Plasma Needle," *Journal of Applied Physics,* vol. 98, p. 013302, 2005.

[97] F. Leipold, R. H. Stark, A. El-Habachi, and K. H. Schoenbach, "Electron Density Measurements in an Atmospheric Pressure Air Plasma by Means of Infrared Heterodyne Interferometry," *Journal of Physics D - Applied Physics,* vol. 33, pp. 2268-2273, 2000.

[98] R. N. Varney, "Drift Velocity of Ions in Oxygen, Nitrogen and Carbon Monoxide," *Physical Review,* vol. 89, pp. 708-711, Feb. 15, 1953.

[99] M. Kaviany, *Princples of Heat Transfer.* New York: John Wiley & Sons, Inc., 2002.

[100] D. Staack, B. Farouk, A. Gutsol, and A. Fridman, "Spatially Resolved Temperature Measurements of Atmospheric-Pressure Normal Glow Microplasmas in Air," *IEEE Transaacations on Plasma Science,* vol. 35, pp. 1448-1455, 2007.

[101] Q. Wang, I. Koleva, V. M. Donnelly, and E. D. J., "Spatially Resolved Diagnostic of an Atmospheric Pressure Direct Current Helium Microplasma," *Journal of Physics D - Applied Physics,* vol. 38, pp. 1690-1697, Jun 7 2005.

[102] T. Farouk, B. Farouk, D. Staack, A. Gutsol, and A. Fridman, "Simulation of Dc Atmospheric Pressure Argon Micro Glow-Discharge," *Plasma Source Science and Technology,* vol. 15, pp. 676-688, Nov. 2006.

[103] Edmund Optics, Personal Communication, Simulation of Chromatic Aberations, 2005,

[104] F. Druyts, J. Fays, and C. H. Wu, "Interaction of Plasma-Facinf Materials with Air and Stream," *Fusion Engineering and Design,* vol. 63-64, pp. 319-325, 2002.

[105] B. Koslowski, H. G. Boyen, C. Wilderotter, G. Kastle, P. Ziemann, R. Wahrenberg, and P. Oelhafen, "Oxidation of Preferentially (111)-Orient Au Films in an Oxygen Plasma Investigated by Scanning Tunneling Microscopy and Photoelectron Spectroscopy," *Surface Science,* vol. 475, pp. 1-10, 2001.

[106] I. Saeki, H. Konno, and R. Furuichi, "The Initial Oxidation of Type 430 Stainless Steel in O2-H20-N2 Atmospheres at 1273 K," *Corrosion Science,* vol. 38, pp. 19-31, 1996.

[107] A. von Engle, "Ionized Gases," vol. 1965d, p. Sec. 8.1, 1965.

[108] L. Dorf, Y. Raitses, and N. J. Fisch, "Experimental Studies of Anode Sheath Phenomena in a Hall Thruster Discharge," *Journal of Applied Physics,* vol. 97, pp. 103309 (1-9), 2005.

[109] D. Staack, B. Farouk, A. Gutsol, and A. Fridman, "DC Normal Glow Discharges in Atmospheric Pressure Atomic and Molecular Gases," *Plasma Sources Science and Technology,* vol. 17, p. 025013, 2008.

[110] T. Farouk, B. Farouk, D. Staack, A. F. Gutsol, and A. A. Fridman`, "Modeling of Direct Current Micro-Plasma Discharges in Atmospheric Pressure Hydrogen," *Plasma Source Science and Technology,* vol. 16, pp. 619-634, Aug. 2007.

[111] D. Staack, B. Farouk, A. Gutsol, and A. Fridman, "Thin Film Deposition Using Atmospheric Pressure Microplasmas," in *IEEE Pulsed Power and Plasma Science Conference*, Albuquerque NM, 2007.

[112] Princeton Instruments INC. , Supplied Quantum Efficency Graphs for the Gratings and Camera Used, 2007,

[113] R. W. B. Pearse and A. G. Gaydon, *The Identification of Molecular Spectra*. New York: John Wiley and Sons Inc, 1963.

[114] Z. Navratil, D. Trunec, R. Smid, and L. Lazar, "A Software for Optical Emission Spectroscopy - Probelm Formulation and Application to Plasma Diagnostics," *Chechoslovak Journal of Physics,* vol. 56, pp. B944-B951, May 2006.

[115] Y. Ralchenko, A. E. Kramida, J. Reader, and N. I. S. T. A. S. D. Team, "Nist Atomic Spectra Database (Version 3.1.5), [Online]. ," National Institute of Standards and Technology, Gaithersburg, MD, 2008.

[116] J. Henriques, E. Tatarova, F. M. Dias, and C. M. Ferrerira, "Wave Driven N2-Ar Discharge Ii. Experiment and Comparison with Theory," *Journal of Applied Physics,* vol. 91, pp. 5632-5639, May, 1 2002.

[117] A. Chingsungnoen, J. I. B. Wilson, V. Amornkitbamrung, C. Thomas, and T. Burinprakhon, "Spatially Resolved Atomic Excitation Temperatures in Ch4/H2 and C3h8/H2 RF Discharges by Optical Emission Spectroscopy," *Plasma Source Science and Technology,* vol. 16, pp. 434-440, May 1, 2007.

[118] S. Darwiche, M. Nikravech, S. Awamat, D. Morvan, and J. Amouroux, "Optical Emission Spectroscopic Investigation of Hydrogen Plasma Used for Modification of Electrical Properties of Multi-Crystalline Silicon," *Journal of Physics D - Applied Physics,* vol. 40, pp. 1030-1036, Feb. 2, 2007.

[119] M. Capitelli, R. Celiberto, F. Esposito, A. Laricchiuta, K. Hassouni, and S. Longo, "Elementary Processes and Kinetics of H2 Plasma for Different Technological Applications," *Plasma Source Science and Technology,* vol. 11, pp. A7-A25, Aug. 19 2002.

[120] V. I. Kolobov, "Striations in Rare Gas Plasmas," *Journal of Physics D - Applied Physics,* vol. 39, pp. R487-R506 Dec 21 2006.

[121] V. Y. Kozhevnikov, A. V. Kozyrev, and Y. D. Korolev, "Theory of a Normal High-Pressure Glow Discharge," *Russian Physics Journal,* vol. 49, pp. 199-206, 2006.

[122] V. I. Arkhipenko, A. A. Kirillov, L. V. Simonchik, and S. M. Zgirouski, "Influence of the Nitrogen-Helium Mixture Ratio on Parameters of a Self-Sustained Normal Dc Atmospheric Pressure Glow Discharge," *Plasma Source Science and Technology,* vol. 14, pp. 757-765, Oct. 24 2005 2005.

[123] V. I. Arkhipenko, S. M. Zgirovskii, A. A. Kirillov, and V. Simonchik, "Cathode Fall Parameters of Self-Sustained Normal Glow Discahrge in Atmoshperic Pressire Helium," *Plasma Physics Reports,* vol. 28, pp. 930-938, 2002 2002.

[124] K. Takaki, D. Taguchi, and T. Fujiwara, "Voltage Current Characteristics of High-Current Glow Discharges," *Applied Physics Letters,* vol. 78, p. 2646, 2001.

[125] G. M. Petrov and C. M. Ferreira, "Numerical Modeling of the Constriction of the Dc Positive Column in Rare Gases," *Physical Review E,* vol. 59, pp. 3571-3582, March 1999.

[126] Y. Kabouzi, M. D. Calzada, M. Moisan, K. C. Tran, and C. Trassy, "Radial Contraction of Microwave-Sustained Plasma Columns at Atmospheric Pressure," *Journal of Applied Physics,* vol. 91, pp. 1008-1019, Febuary 1 2002.

[127] D. Staack, B. Farouk, A. Gutsol, and A. Fridman, "Stabilization of the Ionization Overheating Instability in Atmospheric Pressure Microplasmas," *Journal of Applied Physics,* Submitted 2008.

[128] J. Winter, H. Lange, and Y. B. Gulubovskii, "Gas Temperature in the Cathode Region of a Dc Glow Discharge with a Thermionic Cathode," *Journal of Physics D - Applied Physics,* vol. 41, p. 085210, 2008.

[129] G. Ecker, W. Kroll, and O. Zoller, "Thermal Instability of the Plasma Column," *PHysics of Fluids,* vol. 7, pp. 2001-2006, 1964.

[130] D. Staack, B. Farouk, A. Gutsol, and A. Fridman, "Realization of Thin Film Deposition Using Atmospheric Pressure DC Microplasmas," in progress 2008.

[131] A. C. Ferrari and J. Robertson, "Resonant Raman Spectroscopy of Disordered, Amorphous, and Diamondlike Carbon," *Physical Review B,* vol. 64, p. 075414, 2001.

[132] K. W. R. Gilkes, S. Prawer, K. W. Nugent, J. Robertson, H. S. Sands, Y. Lifshitz, and Z. Shi, "Direct Quantitative Detection of the Sp3 Bonding in Diamond-Like

Carbon Flims Using Ultraviolet and Visible Raman Spectroscopy," *Journal of Applied Physics,* vol. 87, pp. 7283-7289, May 15 2000.

[133]   J. Birrell, J. E. Gerbi, O. Auciello, J. M. Gibson, J. Hohnson, and J. A. Carlisle, "Interpretation of Raman Spectra of Ultrananocrystalline Diamond," *Diamond and Related Material,* vol. 14, pp. 86-92, 2005.

[134]   J. Shiao and R. Hoffman, "Studies of Diamond-Like and Nitrogen-Containing Diamond-Like Carbon Using Laser Raman Spectroscopy," *Thin solid films,* vol. 283, pp. 145-150, 1996.

[135]   A. C. Ferrari and J. Robertson, "Origin of the 1150 Cm-1 Raman Mode in Nanocrystalline Diamond," *Physical Review B,* vol. 63, p. 121405, 2001.

[136]   C. Casiraghi and F. Piazza, "Bonding in Hydrogenated Diamond-Like Carbon by Raman Spectroscopy," *Diamond and Related Material,* vol. 14, pp. 1098-1102, 2005.

[137]   A. C. Ferrari and J. Robertson, "Interpretation of Raman Spectra of Disordered and Amorphous Carbon," *Physical Review B,* vol. 61, pp. 14095-14107, May 15 2000.

[138]   R. K. Roeder and E. B. Slamovich, "Measuring the Critical Thickness of Thin Metalorganic Precursor Films," *Journal of Materials Research,* vol. 14, pp. 2364-2368, 1999.

[139]   B. Bushan, *Handbook of Micro/Nanotribology*. Boca Raton FL: CRC PRess, 1995.

[140]   K. Herrmann, K. Hasche, F. Pohlenz, and R. Seemann, "Characterization of the Geometry of Indenters Used for the Micro- and Nano- Indentation Method," *Measurement,* vol. 29, pp. 210-207, 2001.

[141]   M. Laroussi, I. Alexeff, J. P. Richardson, and F. F. Dyer, "The Resistive Barrier Discharge," *IEEE Transactions on Plasma Science,* vol. 30, pp. 158-159, 2002.

[142]   T. Farouk, "Simulation of Atmospheric Pressure Methane-Hydrogen Microdischarge for Diamond Like Carbon (Dlc) Film Deposition," in *IEEE 34th International Conference on Plasma Science* Alberquerque NM, 2007, p. 508.

[143] D. Staack, A. Gutsol, A. Fridman, Y. Gogotsi, and G. Friedman, "Nanoscale Corona Discharge in Liquids, Enabling Nanosecond Optical Emission Spectroscopy," *Angewandte Chemie,* vol. 42, pp. 8020-8024, 2008.

[144] A. Wilson, D. Staack, T. Farouk, A. Gutsol, A. Fridman, and B. Farouk, "Self-Rotating Dc Atmoshperic-Pressure Discharge over a Water-Surface Electrode: Regime of Operation " *Plasma Source Science and Technology,* vol. 17, p. 045001, 2008.

[145] D. Staack, B. Farouk, A. Gutsol, and A. Fridman, "Comparison of Film Deposition Using DC and RF Atmospheric Pressure Normal Glow Discharges," in progress 2008.

[146] J. W. Yi, Y. H. Lee, and B. Farouk, "Low Dielectric Fluorinated Amorphous Carbon Thin Film Grown from C6f6 and Ar Plasma," *Thin Solid Films,* vol. 374, pp. 103-108, 2000.

[147] X. Yang, M. Moravej, G. R. Nowling, J. P. Change, and R. F. Hicks, "Operating Modes of an Atmospheric Pressure Radio Frequency Plasma," *IEEE Transactions on Plasma Science,* vol. 33, pp. 294-295, 2005.

[148] S. M. Levitsky, "Potential of Space and Electrode Sputtering under High-Frequency Discharge in the Gas," *Soviet Physics Technical Physics,* vol. 27, pp. 1001-1011, 1957.

[149] T. Farouk, B. Farouk, A. Gutsol, and A. Fridman, "Atmospheric Pressure Radio Frequency Glow Discahrges in Argon: Effects of External Matching Circuit Parameters," *Plasma Sources Science and Technology,* vol. 17, p. 035015, 2008.

[150] H. Kodama, A. Shirakura, A. Hotta, and T. Suzuki, "Gas Barrier Properties of Carbon Flims Synthesized by Atmospheric Pressure Glow Plasma," *Surface Coatings and Technology,* vol. 201, pp. 913-917, 2006.

[151] A. K. Srivastava, M. K. Garg, K. S. G. Prasad, V. Kumar, M. B. Chowdhuri, and R. Prakash, "Characterization of Atmospheric Pressure Glow Discharge in Helium Using Langmuir Probe, Emission Spectroscopy and Discharge Resistivity," *IEEE Transactions on Plasma Science,* vol. 35, pp. 1135-1142, 2007.

[152] J. J. A. M. v. d. Mullen, M. J. v. d. Sande, N. d. Vries, B. Broks, E. Iordanova, A. Gamero, J. Torres, and A. Sola, "Single-Shot Thomson Scattering on Argon

Plasma Created by the Microwave Plasma Torch; Evidence for a New Plasma Class," *Spectrochimica Acta Part B,* vol. 62, pp. 1135-1146, 2007.

[153]   Z. Jiang, X. Hu, M. Liu, C. Lan, S. Zhang, Y. He, and Y. Pan, "Attenuation and Propagation of a Scattered Electromagnetic Wave in Two-Dimension Atmospheric Pressure Plasma," *Plasma Source Science and Technology,* vol. 16, pp. 97-103, 2007.

[154]   S. Zhang and X.-W. Hu, "New Microwave Diagnostic Theory for Measurement of Electron Density in Atmospheric Plasmas," *Chinese Physics Letters,* vol. 22, pp. 168-170, 2005.

[155]   D. Staack, B. Farouk, A. Gutsol, and A. Fridman, "A Multi-Line Technique for Stark Broadening and Van-Der Waals Measurements of the Electron Density in Atmospheric Pressure Non-Thermal DC Micro-Plasmas," *Spectrochemica Acta B,* Submitted June 2008.

[156]   J. Choi, F. Iza, J. K. Lee, and C.-M. Ryu, "Electron and Ion Kinetics in a DC Microplasma at Atmoshperic Pressure," *IEEE Transaacations on Plasma Science,* vol. 35, pp. 1274-1278, 2007.

[157]   P. Sigmund, "Theory of Sputtering," *Physical Review,* vol. 184, pp. 383-416, 1968.

[158]   J. A. C. Broekaert, "Analytical Chemistry: Plasma Bubble Detect Elements," *Nature,* vol. 455, pp. 1185-1186, October 30, 2008.

12. Appendix

12.1. SPECAIR algorithms and graphical user interface

SPECAIR [80] is a FORTRAN program which can simulate the emission spectra of air in the ultra-violet (UV), visible, and near infared (NIR). The emission spectra are a function of the temperature of the air and the relative population of different atomic/molecular species within the air mixture. SPECAIR is able to simulate air in non-equilibrium conditions. This is done by allowing the temperatures of translational, rotational, vibrational, and electronic states (T_{trans}, T_{rot}, T_{vib}, T_{el}) to be arbitrarily specified. Also the relative population of the different species within air can be also be specified.

A powerful application of SPECAIR is to use it to compare simulated spectra and experimentally attained emission spectra from air. The parameters of the simulated spectra can be varied until the simulated and experimental spectra are nearly equal. The parameters, T_{trans}, T_{rot}, T_{vib}, T_{el}, and species mole fractions, used in the model that corresponds to the "best fit" can typically be taken as the properties of the air that was the source of the experimental spectra. Thus SPECAIR in conjunction with experimentally measured spectra can be used to measure T_{trans}, T_{rot}, T_{vib}, T_{el}, and species mole fractions. The accuracy to which T_{trans}, T_{rot}, T_{vib}, T_{el} and the species mole fractions can be determined depend on the specific spectrum attained and the sensitivity of the spectrum to the parameter of interest. In practice, so far I have been able to determine the parameters listed in table 1, the sensitivities listed are approximate. Technically SPECAIR and the experimental spectra are sensitive to more parameters but efficient and practical methods of elucidating all of those sensitivities have not been discovered.

Table 12.1: Parameters I have used SPECAIR to measure.

Parameter	Species	Sensitivity
T_{rot}	N_2	50 K
T_{rot}	NO	50 K
T_{vib}	N_2	< 500 K
T_{vib}	NO	< 500 K
T_{el}	NO	< 300 K
n_{N2+}/ n_{N2}	N_2, N_2^+	< 1 order of magnitude

12.1.1. SPECAIR Program Overview

SPECAIR is a FORTRAN program for calculating emission spectra from air; Obtained from C.O. Laux. The executable is rad.exe in the C:\Specair\radiation\SPECAIR directory. It can be run from a MS-DOS command line. Modifiable input files are:

1. input.inp: parameters of the code such as what transitions to use

2. gas.inp: mole fractions of the different species and temperatures of the emitting gas

The input files are in the same directory as the executable. The output file spec.dat is written to C:\Specair\radiation\results and is a file containing columns of wavelength and corresponding intensity for the simulated spectra. Rad.exe will calculate the spectra for the conditions given in the input files.

Rad.exe was compiled using Visual Fortran 6.0. The Visual Fortran project workspace file RAD.dsp was also obtained from C.O. Laux. In order to compile rad.f into rad.exe the existing RAD.dsp was opened and the compile button was clicked, nothing additional needed to be done. Other fortran compilers such as Salford FTN95, and g95 could not compile the rad.f without errors.

1. input.inp

The contents of the input file input.inp are listed below. Lines which were modified are highlighted; all other lines should not be modified unless you know what you are doing.

```
1         MSTART
1          MSTEP
1          IGAS
2         NPRT1  atomic, molecular andradiation data (ATOMIN,MOLIN,RADIN)
1         NPRT2  excitation calculation data (EXCTAM,MOLEXT)
2         NMETH  calculation method
65536     NARRAY array size for spectral computation (must be power of 2)
3         NAS    # of atomic species
9         NMS    # of molecular species
34        NBS    # of electronic band systems( 30 + NO-IR + CO-R +NH)
1         NLAYER # of layers (NX maximum)
0         D      medium thicknes
2000      WAVELS short wave length
4500      WAVELL long wave length
0         N Bound-Bound
0         N Bound-Free
0         N Free-Free
0         O Bound-Bound
0         O Bound-Free
0         O Free-Free
0         C Bound-Bound
```

```
0         C Bound-Free
0         C Free-Free
0         N2+ (1-)
0         N2  (1+)
1         N2  (2+)
0         N2 Birge-Hopfield 2
0         NO Beta
0         NO Gamma
0         O2 Schumann-Runge
0         CN Violet
0         CN Red
0         C2 Swan
0         CO (4+)
0         NO Delta
0         NO Epsilon
0         OH (A-X)
0         NO Beta prime
0         NO Gamma Prime
0         N2 Birge-Hopfield
0         N2 Carrol-Yoshino
0         NO (C-A)
0         NO (D-A)
0         N2+ Meinel
0         NO B'-B
0         NO E-C
0         NO F-C(3)
0         NO H-C
0         NO H'-C
0         NO E-D(5)
0         NO F-D(3)
0         NO H-D
0         NO H'-D
0         NO IR
0         CO IR
0         NH (A-X)
0         OH IR
0.0003        CUTOFF
0         ISLIT (0 for no slit function, 1 for convolution, 2 for cumulative)
0         IOPT option for the radiative transport (0 thin, 1 abs.)
0         IO2 (0 if no extra room air slab, 1 otherwise)
500       WO2 (length of the room air slab, in cm)
0         AbsH2O (1 if H2O vapor absorption in optical path, 0 otherwise)
9.2E+006        WH2O (length of the optical path in cm)
0.002   XH2O (mole fraction of H2O in room air)
0         AbsCO2
9.2E+006        WCO2
0.00033        XCO2
0         IAIRLAMBDA (0 for vacuum wav., 1 for air wav. (default is 1))
0         IWAVEL (0 for angstroms, 1 for nanometers, 2 for wavenumbers)
0         IOTHER (0 nothing, 1 transm., prof., 2 absorpt. coeff) MONOLAYER
1         DTHETA angle increment (in degrees)
1         NANGLE # of lines of sight
0         NFIRST (first slab position: 0 or 1 means along diameter)
Molecular species (molecules and ions)
N2+
N2
NO
O2
CN
C2
CO
OH
NH
1,2,2,2,3,3,4,5,5,6,7,3,3,8,3,3,2,2,3,3,1,3,3,3,3,3,3,3,3,3,3,7,9,8
Atomic species (atoms and ions)
N
N+
O
O+
C
C+
```

```
1       IEQ
0       INO
```

NARRAY is the length of the simulated spectra file. WAVELS and WAVELL are the lower and upper wavelength bounds in angstroms over which the spectrum is calculated. The resolution of the calculated spectra is (WAVELL-WAVELS)/NARRAY and should always be smaller than the resolution of the spectrometer. Rad.exe runs faster if the wavelength range is shorter and NARRAY is smaller. WAVELL and WAVELS should cover a range slightly larger than the experimental data.

The next 43 lines correspond to which molecular and atomic transitions should be calculated in the simulated spectra. Transition corresponding to species and transitions which may be present in the experimental range should be included. If you do not know which transitions are important; a) check the literature, or b) turn them all on and then selectively turn them off and compare spectra to discover which are important.

ISLIT determines whether the output file contains a natural spectrum or spectrum that has been convolved with the slit function specified in slit.inp. I set ISLIT to 0 inorder to obtain a natural spectra.

2. gas.inp

The contents of the input file gas.inp are shown below. All of the lines in this file have been modified. The file is essential 3 columns. Column 1 is the conditions at X=0cm and column 2 at X=1cm. The emitting region is a slab in this case 1cm thick. The conditions at either end of the slab are identical so a uniform emitting region is simulated.

If the output spectra are normalized the size of the region does not matter. The first 16 rows correspond to the density fractions of the species as listed in column 3 (Do not change which species are listed or their order). In this case only N_2 is considered to be present (this may not always be the case). Increasing the number density of the other species will not always change the spectra this is because; a) the transitions corresponding to that species need to be turned on in input.inp and b) That species may not have any transitions in the region over which is being calculating. Row 17 is the total number density, if the output spectra are normalized this value does not matter. Rows 18-21 are the Translational, Rotational, Vibrational, and Electronic temperatures respectively. These temperatures have significant effect upon the spectra as noted in Appendix A.

```
1 1 N2
1e-019 1e-019 O2
1e-019 1e-019 NO
1e-019 1e-019 N
1e-019 1e-019 O
1e-019 1e-019 C
1e-019 1e-019 N2+
1e-019 1e-019 N+
1e-019 1e-019 O+
1e-019 1e-019 C+
1e-019 1e-019 CN
1e-019 1e-019 OH
1e-019 1e-019 NH
1e-019 1e-019 C2
1e-019 1e-019 CO
1e-019 1e-019 E-
2.5e+019 2.5e+019 #dens(/cm3)
300 300 Ttran
3000 3000 Trot
10000 10000 Tvib
10000 10000 Tel
0 1 X(cm)
```

12.1.2. Matlab program overview

A Matlab program was written by D. Staack, to interface to the FORTRAN executable and automate fitting experimental to simulated spectra. The Matlab function is RunSpecAir.m and the graphical user interface (GUI) is RunSpecAir.fig. Both are in the

C:\Specair\radiation\results\GUI directory. The GUI can be run by typing RunSpecAir from the Matlab command line when C:\Specair\radiation\results\GUI is in the Matlab path. A screen capture of the GUI created is shown in figure 12.1.
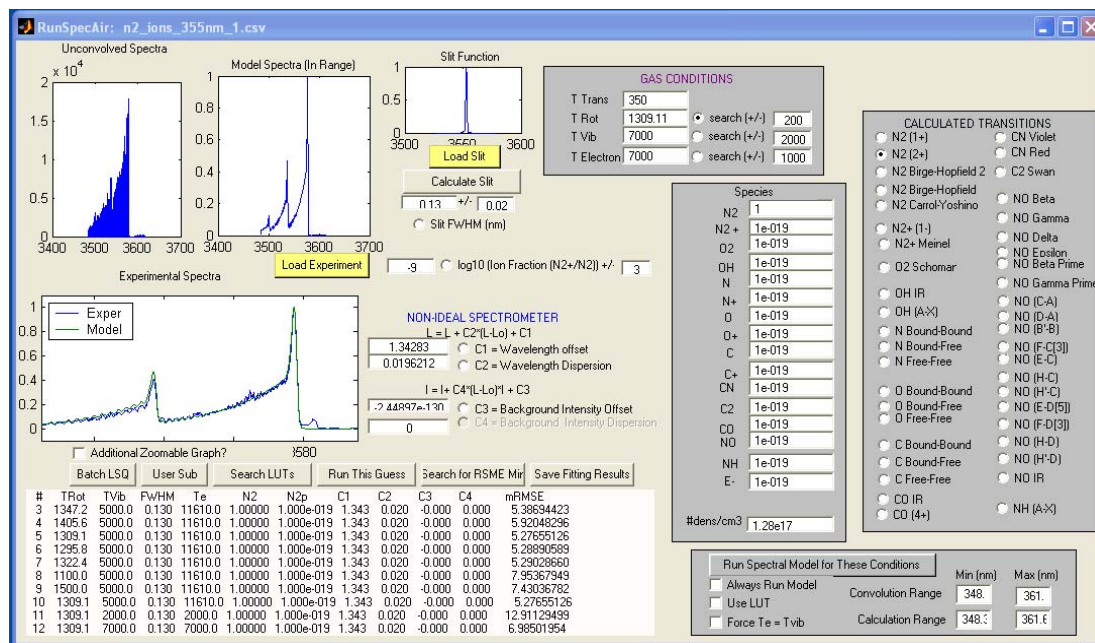
Figure 12.1: Screen shot of Matlab SPECAIR user interface

This GUI allows the user to:

1. Change most of the parameters in the gas.inp and input.inp files. The box on the right entitled *'Calculated Transitions'* has radio buttons for turning on or off each of the transitions in input.inp. The box entitled *'species'* allows the user to specify the fraction and gas density of each of the species in gas.inp. The box entitled 'Gas Conditions' allows the user to change the temperatures specified in gas.inp. The

calculation range in the low right corresponds to WAVELS and WAVELL. NARRAY is automatically calculated so that the resolution of the calculated spectra is 0.05 angstroms.

2. Load experimental spectra from a text file (using the *'load experiment button'* for comparison to experimental spectra. The experimental spectra is normalized and displayed on the axes entitled 'Experimental Spectra'. The data file should be two comma separated columns the first column contains the wavelength in nm, and the second column contains the intensity in any unit.

3. Load the slit function from a text file (using the *'load slit'* button) or calculate a Gaussian slit function (using the *'calculate slit'* button) with a given '*slit FWHM'* (full width at half maxium). The slit function is displayed in the axes entitled *'slit function'*. The data file should be two comma separated columns the first column contains the wavelength in nm, and the second column contains the intensity in any unit.

4. Calculate simulated spectra using the *'Run Spectral Model for These Conditions'* button. This calls a function which goes through the following steps:

   a) Read the gas conditions, species, and calculated transitions data from the GUI and write the input.inp and gas.inp files.

   b) Run the command line code rad.exe.

c) Load the SPECAIR output file spec.dat.

d) Truncate the simulated spectrum to only correspond to the range specified by *'convolution range'*.

e) Convolve the natural spectra with the slit function and normalize the spectra. f) The natural spectrum is shown in the axes entitled *'unconvolved spectra'*, the convolved spectrum is shown in the axes *'Model Spectra'*.

5. Compare simulated and experimental spectra using the *'Run This Guess'* button. This calls a function which goes through the following steps:

   a. If the specified gas conditions have changed *'Run Spectral Model for These Conditions'* is called to recalculate the simulated spectrum. However if the *'use LUT'* box is checked then rad.exe is not called instead the spectrum is attained from look up tables containing pre-calculated spectra for a range of Trot, Tvib, and FWHM rounding to the nearest values in the table. The LUT are not very extensive only corresponding to wavelength ranges each about 10nm wide centered at 296nm, 313nm, 334nm, and 374nm, covering Trot from 300K to 2000K, Tvib from 2000K to 8000K, and slit function FWHM from 0.02nm to 0.09nm. If the specified gas conditions have not changed the previous simulated spectra is used.

   b. The experimental data is corrected based upon the parameters *C1, C2, C3*, and *C4* under the title *'non-ideal spectrometer'*. *C1* shifts the experimental data left and right. *C2* spreads out the data horizontally. *C3* shifts the data up and down by a constant value. *C4* shift the data up and down by a linear sloped value. Non-zero values of *C1, C2, C3*, and *C4* may be necessary to account for any mis-calibration,

and background noise of the spectrometer. The correction formula used are:

$$\lambda_{corrected} = \lambda + C1 + C2 * (\lambda - \lambda_0), \text{ and } I_{corrected} = I + C3 + C4 * (\lambda - \lambda_0).$$

c. After the correction is applied the modeled spectra is interpolated so that the modeled intensities and experimental intensities correspond to exactly the same wavelengths. Then the experimental spectra are normalized. I = I/max(I), and the root mean square error is calculated (RMSE). The RMSE is defined as:

$$RMSE = \frac{\sqrt{\sum_{i=1}^{N}\left(I_{\exp_i} - I_{\text{mod}_i}\right)^2}}{N}$$, where I_{exp} and I_{mod} are the experimental and modeled intensities at a given wavelength, and N is the number of wavelength points in the experimental data.

d. The parameters of the fit and the RMSE*1000 (mRMSE) are displayed in the text box on the lower left of the GUI. The experimental and modeled spectra are also shown together in the axis labeled *'Experimental Spectra'*. If the box, *'additional zoomable graph?'* is checked then the experimental and modeled data will also be plotted in a standard Matlab figure external from the GUI. This external figure is zoomable, can have the colors altered, the axes labeled, be printed, or saved as any standard Matlab figure.

6. All of the fitting results can be saved in a text file by clicking *'Save Fitting Results'*. This saves all the parameters of each fit and the resulting RMSE that have been attempted since the last experimental file was loaded in a text file. The Modeled spectra is not save in a text file. If access is needed to the modeled spectra it can be found in the \Specair\radiation\results\spec.dat file.

7. An automated search for the minima of the RMSE can be initiated by clicking the *'Search for RMSE min'* button. In general the possible parameter space to search is: Trot, Tvib, Tel, FWHM, C1, C2, C3 , and Ion Fraction (searches for C4 and T_{trans} have not been implemented). The 8 dimensional parameter space is too large to randomly search in an efficient manner. In addition the specific spectra being investigated may not be sensitive to all of these parameters. The fitting parameters can be broken down into two groups the model parameters, Trot, Tvib, Tel, FWHM and Ion Fraction, and the experimental corrections C1, C2, and C3. In the current implementation the model parameters cannot be search in a coupled manner they can only be search individually. The experimental parameters can be search all three together or individually.

The function used to find the RMSE minimum when searching the experimental parameters (C1, C2, C3) is the Matlab function **fminsearch**. **fminsearch** is a multidimensional unconstrained nonlinear function minimization using the simplex search method (see Matlab online documentation for a full description). The function being minimized is the RMSE calculated by the *'Run This Guess'* button. Since changing these parameters does not change the modeled spectra, and thus SPECAIR is not run, this search can be quite quick.

The model parameters (Trot, Tvib, Tel, FWHM, and Ion Fraction) can only be search independently of each other. This is a weakness of the current fitting routines, however in many cases two parameters may be orthogonal to one another when minimizing the RMSE and thus can be search independently (this however is not

always the case and care should be taken). The function used to find the RMSE minimum in the built in Matlab function **fminbound**. **fminbound** is a scalar bounded nonlinear function minimization. The algorithm used is based on golden section search and parabolic interpolation.[2] The bounds of the search are given in the GUI by the +/- value to the right of the parameter. For example; for a Trot of 1000K and a +/- Trot of 200K, fminbound will search between 800K and 1200K for the minimum RMSE. The programs is hardwired such that Trot<250K is not even attempted. The resolution of the search is such that approximately 20 points cover the range. Thus the Trot could be determined to higher precision (though not necessarily any more accurately) by decreasing the range.

Searches for the minimum RMSE coupling one of the model parameters with the experimental parameters is possible. In this situation up to 4 parameters can be search and the experimental parameter search is nested inside of the model parameter search. For example is searching using the parameters Trot, C1, C2, and C3 for each Trot the C1, C2, and C3 which minimize it would be found. This is done since the experimental parameter search is so much quicker than the model parameter search.

Choosing which parameters are searched is done by using the radio buttons adjacent to that parameter. You will note that more than one model parameter cannot be chosen.

8. The *'Search LUTs'* button allows for a quick although rough estimate of the Trot, Tvib, and FWHM. This function compares the correct experimental spectra to

modeled spectra which has been stored in a look-up-table (LUT) and calculates the RMSE. The LUTs corresponding to wavelength ranges each about 10nm wide centered at 296nm, 313nm, 334nm, and 374nm, covering Trot from 300K to 2000K, Tvib from 2000K to 8000K, and slit function FWHM from 0.02nm to 0.09nm. If this function is used and a LUT in the appropriate wavelength range doesn't exist the function will fail. The RMSE is a function of Trot, Tvib, and the slit function. The Trot, Tvib, FWHM corresponding to the minimum RMSE are set as the current Trot, Tvib, and FWHM on the GUI. RMSE = f(Trot, Tvib, FWHM) is a 4D plot and cannot be visualized; however, Figure 12.2 shows RMSE = f(Trot, Tvib) for a given FWHM of 0.04 nm. The rotational and vibrational temperature range corresponding to the best fit (minimum RMSE) is represented by the dark blue region near the middle of the image. We also see from this image that the semi-major and semi-minor axes of the elliptical iso-RMSE contours are nearly parallel to the Trot and Tvib axes indicating that Trot and Tvib are not tightly coupled. It should be noted that in reality RMSE = f(Trot,Tvib, FWHM, C1, C2, C3) for this transitions and so this graph may change slightly for different C1, C2, C3.
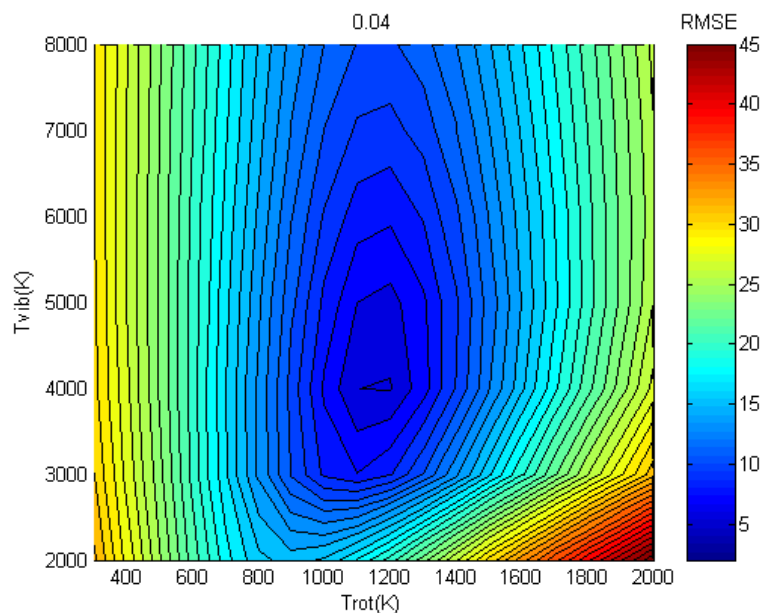
Figure 12.2: RMSE and a function of Trot and Tvib for a typical N_2 experimental

spectrum at 374 nm.

9. The *'Batch LSQ'* button automatically loads all of the experimental files in a given

directory and determines the best fit temperatures for each file. For each file the best

fit temperatures are determined in the following steps.

    a. The file is loaded and C1 is determined by matching the experimental and

       modeled peak location.

    b. *'Search LUTs'* is run to roughly guess the Trot, Tvib, and FWHM of the slit.

    c. *'Search for RMSE min'* is run using the search parameters C1, C2 and C3 to

       correct the experimental data. Steps b and c are looped until the rough guess is

       determined to be the same.

    d. T_{rot}, FWHM, and T_{vib} are used as search parameters in consecutive runs of

       'Search for RMSE min'. The series of searches is as follows in table 2. The

searches are repeated incase there was any coupling between the model

parameters. After the completion of this series of searches the results are

saved using the *'Save Fitting Results'* function.

Table 12.2: The series of RMSE minimum searches done by Batch LSQ search function

Search #	Search Parameters	+/- Range of Model Parameter
1	T_{rot}	2*LUT spacing (+/- 200K)
2	C1, C2, C3	-
3	FWHM	2*LUT spacing (+/- 0.02nm)
4	C1, C2, C3	-
5	T_{vib}	2*LUT spacing (+/-2000K)
6	T_{rot}, C1, C2, C3	2*LUT spacing (+/- 200K)
7	FWHM, C1, C2, C3	2/3*LUT spacing (+/- 0.007nm)
8	T_{vib}, C1, C2, C3	2/3*LUT spacing (+/- 666K)
9	T_{rot}, C1, C2, C3	2/3*LUT spacing (+/- 66K)

10. The *'User Sub'* button calls the function UserSub_SpecAir.m, in

    C:\Specair\radiation\results\GUI\. This Matlab function provides a backdoor into the

    function calls of the GUI and specair. Through Matlab programming all of the loaded

variables and functions can be accessed. This enables any degree of required sophistication. For examples the LUTs, and figure 12.2 was generated by programming this function to do the task.

11. Additional features which may be useful in more complicated fitting searches are the *'Force Trot=Ttrans'* and *'Force Telec=Tvib'* check boxes. When checked the programs will make sure either Trot is the same as Ttrans or Tel is the same as Tvib respectively. Trot=Ttrans should be on for most searches. Tvib=Telec is not always true and should only be used is special circumstances.

12.1.3. Spectroscopy Primer

A spectrum is the intensity of light as a function of wavelength. Figure 12.3 is an experimental spectrum from a glow discharge plasma in air.[68] Visible in the spectrum are many peaks. A peak is due to a change in state (a.k.a. transition) of a molecule or atom from some initial high energy level to a lower energy level with the emission of a photon. The change in energy corresponds to the wavelength of the peak, $\Delta E = h\nu = hc/\lambda$. Each and every transition is due to a different combination of initial energy, final energy, and is due to a specific molecular or atomic species.
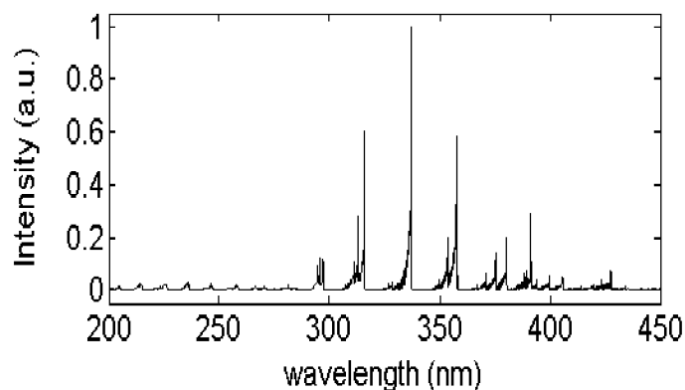
Figure 12.3: Optical emission spectra from a glow discharge in air

The intensity of one particular transition, I_i, is proportional to the number of atoms/molecules in the initial high energy level, $n_{\varepsilon i}$, $I_i = kn_{\varepsilon_i}$. The constant of proportionality, k, is calculated in SPECAIR for each transition, and is a function of the probability that transition will occur.[1] Each transition is due to a specific molecule/atom, A, and a specific initial energy level. Each initial energy level is quantized and can characterized by three quantum numbers n, v, and J, corresponding to the electronic, vibrational, and rotational quantum numbers.[2] Atoms because they consist of only one atom do not have vibrational or rotational quanta. The number of molecules/atoms in any state, $n_{A,n,v,J}$, is given by statistical thermodynamics.

An important concept in understanding why spectra can be used to measure temperature is the concept of the energy distribution function. The energy distribution function gives the population of a given energy level. The energy distribution function, f, is typically normalized by a total population as shown in equation 1 and 2. For each

---

[1] Many details are beyond the scope of this brief explanation but can be found in C. Laux's lecture notes on SPECAIR, and textbooks on statistically thermodynamics and spectroscopy.
[2] Translational energy is also quantized but the quantization is too fine to observe and the effects of translational energy are taken into account in the model by thermal doppler broadening.

energy mode (Rotational, Vibrational, and Electronic Excitation) an assumption is made

in SPECAIR that the energy distribution functions , f_{Rot}, f_{Vib}, and f_{el} is Maxwell-

Boltzmann at temperatures T_{Rot}, T_{Vib}, and T_{el} respectively as shown in equations 3 and 4.

Thus, the different energy modes do not need to be at equilibrium $T_{Rot} \neq T_{Vib} \neq T_{el}$, but

within each energy mode a Maxwell-Boltzmann equilibrium is assumed.[3]

$$\frac{n_{A,n,v,J}}{\sum\limits_{v} n_{A,n,v,J}} = \frac{n_{A,n,v}}{n_{A,n,J}} = f_{Vib}(\varepsilon_v) \qquad \text{Eq. 1}$$

$$\frac{n_{A,n,v,J}}{\sum\limits_{n}\sum\limits_{v}\sum\limits_{J} n_{A,n,v,J}} = \frac{n_{A,n,v,J}}{n_A} = f(\varepsilon_{n,v,J}) \qquad \text{Eq. 2}$$

$$f_{vib}(\varepsilon_v) = \frac{g_v e^{\frac{-\varepsilon_v}{T_{Vib}}}}{\sum\limits_{v} g_v e^{\frac{-\varepsilon_v}{T_{vib}}}} \qquad \text{Eq. 3}$$

$$f(\varepsilon_{n,v,J}) = \frac{g_J e^{\frac{-\varepsilon_J}{T_{Rot}}} g_v e^{\frac{-\varepsilon_v}{T_{Vib}}} g_n e^{\frac{-\varepsilon_n}{T_{el}}}}{\sum\limits_{n}\sum\limits_{v}\sum\limits_{J} g_J e^{\frac{-\varepsilon_J}{T_{Rot}}} g_v e^{\frac{-\varepsilon_v}{T_{Vib}}} g_n e^{\frac{-\varepsilon_n}{T_{el}}}} \qquad \text{Eq. 4}$$

The change in the relative population with temperature is the sensitivity that is

exploited when determining temperature from spectra. Figure 12.4 shows the vibrational

distribution function of N_2 in the $C^3\Pi_u$ state approximating it as a harmonic oscillator

which has a characteristic vibrational energy, θ_{vib} = 2933K, and degeneracy, g_v, of 1.[4]

When shown in a semi-log plot vs. energy, Fig 2b, the slope of the line = $-1/T_{vib}$. Using

the previous equations if we can solve for the relative intensities of two transitions with

---

[3] This assumption is definitely accurate for rotational modes, is probably accurate for vibrational modes, and is questionable but okay for electronic modes.
[4] In SPECAIR more accurate calculations of distribution functions are done taking into account anharmonicity and coupling of different modes.

different vibrational quantum numbers, v=0, and v=1, as a function of vibrational temperature as shown in equations 5 and 6. Alternatively if the intensities were measured experimentally the vibrational temperature could be determined as shown in equation 7. The values of $k, \varepsilon, g,$ are constants which are either tabulated or calculated from quantum mechanics within SPECAIR. In reality the situation is significantly more complicated than as shown in equation 7. First, the transitions may be from different species, with different initial quantum numbers, in which case the temperatures and mole fractions of different species are coupled as shown in equation 8. Second, two lines often cannot be isolated for comparison[5], and the spectra may be the overlapping of several hundred transitions. Third, the actual spectra are modified by the measurement device and are actually a convolution of the narrow actual narrow spectra and the apparatus/slit function as shown in Figure 12.5. Luckily for us SPECAIR takes all these effects into account when simulating emission spectra.

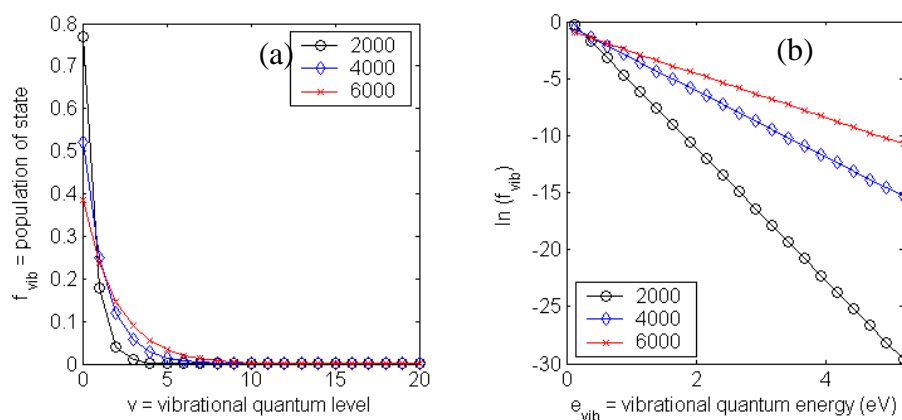**Figure 12.4:** Vibrational distribution function for N_2-$C^3\Pi_u$ state at 3 different vibrational temperatures (2000K, 4000K, 6000K).

---

[5] This is especially true for rotational transitions. The spacing between different rotational transitions is typically less than the resolution of the spectrometer. For vibrational and electronic transitions separate transitions can often be resolved.

$$\frac{I_{A,n,J,v=1}}{I_{A,n,J,v=0}} = \frac{k_{A,n,J,v=1}}{k_{A,n,J,v=0}} \frac{n_{A,n,J,v=1}}{n_{A,n,J,v=0}} = \frac{k_{A,n,J,v=1}}{k_{A,n,J,v=0}} \frac{f_{vib}(\varepsilon_{A,n,J,v=1})}{f_{vib}(\varepsilon_{A,n,J,v=0})} \quad (EQ.5)$$

$$\frac{I_{A,n,J,v=1}}{I_{A,n,J,v=0}} = \frac{k_{A,n,J,v=1}}{k_{A,n,J,v=0}} \frac{\dfrac{g_{v=1}e^{\frac{-\varepsilon_{v=1}}{T_{Vib}}}}{\sum_{v} g_{v}e^{\frac{-\varepsilon_{v}}{T_{vib}}}}}{\dfrac{g_{v=0}e^{\frac{-\varepsilon_{v=0}}{T_{Vib}}}}{\sum_{v} g_{v}e^{\frac{-\varepsilon_{v}}{T_{vib}}}}} = \frac{k_{A,n,J,v=1}}{k_{A,n,J,v=0}} \frac{g_{v=1}e^{\frac{-\varepsilon_{v=1}}{T_{Vib}}}}{g_{v=0}e^{\frac{-\varepsilon_{v=0}}{T_{Vib}}}} \quad (EQ.6)$$

$$T_{Vib} = \frac{-(\varepsilon_{v=1} - \varepsilon_{v=0})}{\ln\left(\dfrac{I_{A,n,J,v=1}}{I_{A,n,J,v=0}} \dfrac{k_{A,n,J,v=0}}{k_{A,n,J,v=1}} \dfrac{g_{v=0}}{g_{v=1}}\right)} \quad (EQ.7)$$

$$\frac{I_{A,n,J,v}}{I_{B,m,K,w}} = \frac{n_A}{n_B} \frac{k_{A,n,J,v}}{k_{B,m,K,w}} \frac{\dfrac{g_{J}e^{\frac{-\varepsilon_{J}}{T_{Rot}}} g_{v}e^{\frac{-\varepsilon_{v}}{T_{Vib}}} g_{n}e^{\frac{-\varepsilon_{n}}{T_{el}}}}{\sum_{n}\sum_{v}\sum_{J} g_{J}e^{\frac{-\varepsilon_{J}}{T_{Rot}}} g_{v}e^{\frac{-\varepsilon_{v}}{T_{Vib}}} g_{n}e^{\frac{-\varepsilon_{n}}{T_{el}}}}}{\dfrac{g_{K}e^{\frac{-\varepsilon_{K}}{T_{Rot}}} g_{w}e^{\frac{-\varepsilon_{w}}{T_{Vib}}} g_{m}e^{\frac{-\varepsilon_{m}}{T_{el}}}}{\sum_{m}\sum_{w}\sum_{K} g_{K}e^{\frac{-\varepsilon_{K}}{T_{Rot}}} g_{w}e^{\frac{-\varepsilon_{w}}{T_{Vib}}} g_{m}e^{\frac{-\varepsilon_{m}}{T_{el}}}}} \quad (EQ.8)$$
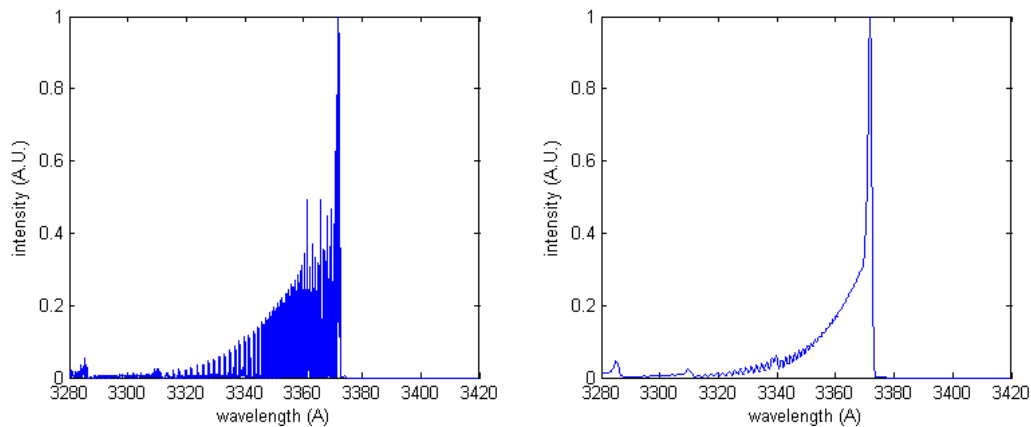

Figure 12.5: Calculated spectra for N2 ($C^3\Pi_u$- $B^3\Pi_g$) transitions without (a) and with (b) spectrometer apparatus function (FWHM = 0.1nm) taken into account.

12.1.4. Additional SPECAIR features not explored

1. Absorption of light between the emitting source and the spectrometer detector can be taken into account.
2. Absolute spectra are actually calculated with the size of the emission source listed in the gas.inp file. I normalize the spectra and so ignore this additional calculation.
3. The gas can also be non-uniform and have temperature and density gradients. This can be done by specifying the properties as a function of X in gas.inp.
4. SPECAIR can be used to convolve the slit function with the natural spectra. I did not use this option but rather used matlab for the convolution.
5. It may be possible to deviate from a Boltzmann distribution for the vibrational levels using the file noneqvib.inp.
6. Also see measurements done in Ref [80].

12.1.5. SPECAIR Program Directory Structure

Specair: Contains only subdirectories

radiaton: Contains only subdirectories

data: Contains only subdirectories

extrans: contains FORTRAN files of unknown use

debug: contains complied FORTRAN files of unknown use

radtrans: contains FORTRAN files of unknown use

radtrans: contains complied FORTRAN files of unknown use

results: contains text file with output from SPECAIR

GUI: contains Matlab files for user interface

296nm_LUT: Contains Matlab lookup table data for N_2 spectra near 296 nm

313nm_LUT: Contains Matlab lookup table data for N_2 spectra near 313 nm

334nm_LUT: Contains Matlab lookup table data for N_2 spectra near 334 nm

374nm_LUT: Contains Matlab lookup table data for N_2 spectra near 374 nm

SPECAIR: Contains data files, FORTRAN files, and executable needed to run SPECAIR

Debug: contains debugger files used while compiling SPECAIR

12.1.6. Runspecair.m code

Below is a listing of the MATLAB code used for the graphical interface and search routines. About half of this code is related to the user interface and about half to the search algorithms. In total there are 3217 lines of code. Below is only listed the sections of code relating the search algorithms for getting the best fit temperature and the code for interfacing with the SPECAIR executable from MATLAB.

12.1.6.1. Search Look-Up-Tables

```matlab
% --- Executes on button press in pushbutton19.
function pushbutton19_Callback(hObject, eventdata, handles)
%% search LUTS
try
    here = cd;
    SpecAirDir = get(handles.frame6,'userdata');
    cd(SpecAirDir)

    ExpData = get(handles.pushbutton9,'userdata');
    CW = ExpData.CW;
    CI = ExpData.CI;

    ExpTrans = mean(CW);

    tables = dir('*LUT');
    for j=1:length(tables)
        cd(tables(j).name)
        load('LutConds.mat')
        cd(SpecAirDir)
        if (ExpTrans>Wlims(1))&(ExpTrans<Wlims(2))
            WaveDir = ['\',tables(j).name]
        end
    end

    cd([SpecAirDir,WaveDir])
    load('LutConds.mat')

    TableDataHolder = get(handles.pushbutton19,'userdata');
    try
        if TableDataHolder.WaveDir == WaveDir
            LoadEm = 0;
```

```matlab
        else
            LoadEm = 1;
        end
    catch
        LoadEm = 1;
    end
    tic

    Er = NaN*Sls;
    for k=1:length(Sls)
        FWHM = Sls(k);
        filename =
[SpecAirDir,WaveDir,'\SpecAir_LUT_SL',num2str(FWHM*1000),'.mat'];
        if ~LoadEm
            TheAnswer = TableDataHolder.Ans{k};
            %'use stored tables'
        else
            load(filename)
            TableDataHolder.Ans{k} = TheAnswer;
            TableDataHolder.WaveDir = WaveDir;
        end
        W1 = TheAnswer.ModelWave;
        RMSE = ones(length(Tvs),length(Trs))*NaN;
        for i = 1:length(Trs)
            for j = 1:length(Tvs)
                NI = TheAnswer.ModelInt{i,j};
                NI_int = interp1(W1,NI,CW);
                NI_int = NI_int./max(NI_int);
                LSQ = 1e2*sqrt(sum((NI_int-CI).^2)/length(CI));
                ErEr = sum(abs(NI_int-CI))/length(CI);
                RMSE(j,i) = LSQ;
                %[i,j,min(min(RMSE)),RMSE(j,i)]
                %            if LSQ == min(min(RMSE))
                if abs(LSQ-min(min(RMSE))<1e-9)
                    Tr(k) = Trs(i);
                    Tv(k) = Tvs(j);
                    Er(k) = RMSE(j,i);
                end
            end
        end
    end
    'Here'
    toc
    TableDataHolder.WaveDir = WaveDir;
    set(handles.pushbutton19,'userdata',TableDataHolder)

    ClosestMatch = find(Er==min(Er));

    FWHM = Sls(ClosestMatch);
    TRot = Tr(ClosestMatch);
    TVib = Tv(ClosestMatch);
    RMSE = Er(ClosestMatch);


    set(handles.edit8,'String',sprintf('%g',TRot))
    if get(handles.checkbox6,'value')
```

```matlab
        set(handles.edit7,'String',sprintf('%5.1f',TRot))
    end
    set(handles.edit9,'String',sprintf('%g',TVib))
    if get(handles.checkbox5,'value')
        set(handles.edit10,'String',sprintf('%5.1f',TVib))
    end
    set(handles.edit41,'String',sprintf('%g',FWHM))
    RunSpecAir('pushbutton17_Callback',handles.pushbutton17,[],handles)

    set(handles.edit39,'String',sprintf('%g',2*mean(diff(Trs))))
    set(handles.edit40,'String',sprintf('%g',2*mean(diff(Tvs))))
    set(handles.edit42,'String',sprintf('%g',2*mean(diff(Sls))))

    cd(here)
end
```

12.1.6.2.   Calculate Slit

```matlab
function [SW,SI] = CalcSlit(handles)
SlitWidth = str2double(get(handles.edit41,'String'))*10;
SlitWidth2 = str2double(get(handles.edit46,'String'))*10;
SlitFraction = str2double(get(handles.edit47,'String'));
SWid = max([SlitWidth2,SlitWidth]);
SWim = max([SlitWidth2,SlitWidth]);

Wmin = str2double(get(handles.edit30,'String'))*10;
Wmax = str2double(get(handles.edit31,'String'))*10;
Center = mean([Wmin,Wmax]);
SW = [max(Center-20*SWid,Wmin-10):SWim/50:min(Center+20*SWid,Wmax+10)];
SW = [Wmin-10:SWim/50:Wmax+10];

%%% gaussian approximation
sigma = SlitWidth/(2*sqrt(2*log(2)));
SIG = exp(-(SW-Center).^2/(2*sigma.^2));
SIG = SIG./max(SIG);

%%% lorentzian approximation
SIL = 1/pi*0.5*SlitWidth2./((SW-Center).^2+(.5*SlitWidth2)^2);
SIL = SIL./max(SIL);
SI = SIG*SlitFraction+SIL*(1-SlitFraction);


SW = [min(Wmin-11,min(SW-1)),SW,max(Wmax+11,max(SW+1))];
SI = [0,SI,0];
SI = SI./max(SI);
```

12.1.6.3.   Batch Fitting

```matlab
function pushbutton14_Callback(hObject, eventdata, handles)
%%% BATCH Fitting
try
```

```matlab
    cd('C:\Documents and Settings\dstaack\My
Documents\Experiments\2007')
end
a = uigetdir(cd)
here = cd;
cd(a)
b = dir('*.csv')
mkdir('results')
cd(here)
c = {b.name};

for i = 1:length(c)
    LoadSt{1} = c{i};
    LoadSt{2} = a;
    pushbutton9_Callback(handles.pushbutton9, eventdata,
handles,LoadSt)
    pushbutton19_Callback(handles.pushbutton11, eventdata, handles)
    pause(.1)
    LookIon = 0;
    if ~LookIon
        %% this is for trot tvib and slit
        sequences =
{[0,0,0,1,1,1],[0,1,0,0,0,0],[0,0,0,1,1,1],[1,0,0,0,0,0],[0,0,0,1,1,1],
[0,0,1,0,0,0],[0,0,0,1,1,1],[0,1,0,1,1,1],[1,0,0,1,1,1],[0,0,1,1,1,1],[
0,1,0,1,1,1]};
        set(handles.edit44,'String','-19')
        edit44_Callback(handles.edit44, [], handles)
    else
        %% this is for tro, tvib, slit, and ion
        sequences =
{[0,0,0,1,1,1],[0,1,0,0,0,0],[0,0,0,1,1,1],[1,0,0,0,0,0],[0,0,0,1,1,1],
[0,0,1,0,0,0],[0,0,0,1,1,1],[0,1,0,1,1,1],[1,0,0,1,1,1],[0,0,1,1,1,1],[
0,1,0,1,1,1],[0,0,0,0,0,1],[0,0,0,1,1,1,1],[0,1,0,1,1,1],[0,0,0,1,1,1
,1],[0,1,0,1,1,1],[0,0,0,1,1,1,1],[0,1,0,1,1,1]};
        set(handles.edit44,'String','-19')
        edit44_Callback(handles.edit44, [], handles)
    end
    ocond = [0,0,0];
    for j=1:length(sequences)
        seq = sequences{j};
        seq
        set(handles.radiobutton60,'value',seq(1)) % Slit
        set(handles.radiobutton53,'value',seq(2)) % Trot
        set(handles.radiobutton54,'value',seq(3)) % Tvib
        set(handles.radiobutton55,'value',seq(4)) % C1
        set(handles.radiobutton56,'value',seq(5)) % C2
        set(handles.radiobutton57,'value',seq(6)) % C3
        if length(seq)>6
            set(handles.radiobutton62,'value',seq(7)) % Ion Fract
        else
            set(handles.radiobutton62,'value',0)
        end
        if j==12&LookIon
            set(handles.edit44,'String','-11')
            edit44_Callback(handles.edit44, [], handles)
            set(handles.edit45,'String','6')
        end
```

```matlab
        if j==13&LookIon
            set(handles.edit45,'String','3')
        end
        if j==15&LookIon
            set(handles.edit45,'String','1')
            dtr = str2double(get(handles.edit39,'String'));
            set(handles.edit39,'String',sprintf('%g',dtr/2))
        end
        pushbutton11_Callback(handles.pushbutton11, eventdata, handles)
        if j==1;
            set(handles.edit36,'String','.1')
            cond =
[str2double(get(handles.edit8,'String')),str2double(get(handles.edit9,'
String')),str2double(get(handles.edit41,'String'))];
            while cond~=ocond
                ocond = cond;
                pushbutton19_Callback(handles.pushbutton11, eventdata,
handles)
                pushbutton11_Callback(handles.pushbutton11, eventdata,
handles)
                cond =
[str2double(get(handles.edit8,'String')),str2double(get(handles.edit9,'
String')),str2double(get(handles.edit41,'String'))]
            end
        end
        if j==8
            %% set ranges to 1/3 what they currently are
            dtr = str2double(get(handles.edit39,'String'));
            dtv = str2double(get(handles.edit40,'String'));
            dsl = str2double(get(handles.edit42,'String'));
            set(handles.edit39,'String',sprintf('%g',dtr/3))
            set(handles.edit40,'String',sprintf('%g',dtv/3))
            set(handles.edit42,'String',sprintf('%g',dsl/3))
        end
    end
    pushbutton12_Callback(handles.pushbutton12, eventdata,
handles,[a,'\results'])
end
```

12.1.6.4.   Fitting and search for minimum RSME

```matlab
% --- Executes on button press in pushbutton11.
function pushbutton11_Callback(hObject, eventdata, handles)
%% search for minimum RSME
set(handles.frame10,'userdata',1) %% so other function know we are
doing a Search and don't graph

%%%%
FixWaveOffset = get(handles.radiobutton55,'Value');
FixWaveDispersion = get(handles.radiobutton56,'Value');
FixIntOffset = get(handles.radiobutton57,'Value');
TRotSearch = get(handles.radiobutton53,'Value');
TVibSearch = get(handles.radiobutton54,'Value');
```

```matlab
SlitSearch = get(handles.radiobutton60,'Value');
TeSearch = get(handles.radiobutton61,'Value');
IonFractSearch = get(handles.radiobutton62,'Value');

C1 = str2double(get(handles.edit34,'String'));
C2 = str2double(get(handles.edit35,'String'));
C3 = str2double(get(handles.edit36,'String'));
C4 = str2double(get(handles.edit38,'String'));

if TRotSearch
    options = optimset('fminbnd');
    options.TolFun = 1e-6;
    TRot = str2double(get(handles.edit8,'String'));
    RangeStep = str2double(get(handles.edit39,'String'));
    TRot_range = [TRot-RangeStep,TRot+RangeStep];
    TolR = min(diff(TRot_range)/10,50);
    options.TolX = TolR; %% tolerance on temperature
    TRot_range(TRot_range<150)=150;
    X = TRot;
    %%% origionally used matlab search but I think we can do it with
less calls to SPECAIR on our own
    X =
fminbnd(@ParamSearch_TRot,min(TRot_range),max(TRot_range),options,handl
es);
    %X =
SearchMinFunTr('ParamSearch_TRot',min(TRot_range),max(TRot_range),optio
ns,handles);
    % the one I made is a little less reliable but takes less time
    TRot = X(1);
    set(handles.edit8,'String',sprintf('%g',TRot))
    if get(handles.checkbox6,'value')
        set(handles.edit7,'String',sprintf('%5.1f',TRot))
    end
end

if TVibSearch
    options = optimset('fminbnd');
    options.TolFun = 1e-6;
    TVib = str2double(get(handles.edit9,'String'));
    RangeStep = str2double(get(handles.edit40,'String'));
    TVib_range = [TVib-RangeStep,TVib+RangeStep];
    TolV = min(diff(TVib_range)/10,200);
    options.TolX = TolV; %% tolerance on vibrational temperature
    TVib_range(TVib_range<250)=250;
    X = TVib;
    %%% origionally used matlab search but I think we can do it with
less calls to SPECAIR on our own
    X =
fminbnd(@ParamSearch_TVib,min(TVib_range),max(TVib_range),options,handl
es);
    %X =
SearchMinFunTr('ParamSearch_TRot',min(TRot_range),max(TRot_range),optio
ns,handles);
    % the one I made is a little less reliable but takes less time
    TVib = round(X(1));
    set(handles.edit9,'String',sprintf('%g',TVib))
```

```matlab
    if get(handles.checkbox5,'value')
        set(handles.edit10,'String',sprintf('%5.1f',TVib))
    end
end

if TeSearch
    options = optimset('fminbnd');
    options.TolFun = 1e-6;
    Te = str2double(get(handles.edit10,'String'));
    RangeStep = str2double(get(handles.edit43,'String'));
    Te_range = [Te-RangeStep,Te+RangeStep];
    TolTe = min(diff(Te_range)/10,100);
    options.TolX = TolTe; %% tolerance on electronic temperature
    %% Te should generally have a small temperature tolerance since the
    %% sentivity is exponential
    Te_range(Te_range<250)=250;
    X = Te;
    %%% origionally used matlab search but I think we can do it with
less calls to SPECAIR on our own
    X =
fminbnd(@ParamSearch_Te,min(Te_range),max(Te_range),options,handles);
    Te = round(X(1));
    set(handles.edit10,'String',sprintf('%g',Te))
    if get(handles.checkbox5,'value')
        set(handles.edit9,'String',sprintf('%5.1f',Te))
    end
end

if IonFractSearch
    options = optimset('fminbnd');
    options.TolFun = 1e-6;
    Zeta = str2double(get(handles.edit44,'String'));
    RangeStep = str2double(get(handles.edit45,'String'));
    Zeta_range = [Zeta-RangeStep,Zeta+RangeStep];
    options.TolX = diff(Zeta_range)/10; %% tolerance on electronic
temperature
    Zeta_range(Zeta_range<-19)=-19;
    Zeta_range(Zeta_range>0)=0;
    X = Zeta;
    %%% origionally used matlab search but I think we can do it with
less calls to SPECAIR on our own
    X =
fminbnd(@ParamSearch_Zeta,min(Zeta_range),max(Zeta_range),options,handl
es);
    Zeta = X(1);
    set(handles.edit44,'String',sprintf('%g',Zeta))
    edit44_Callback(handles.edit44, [], handles)
end

if SlitSearch
    options = optimset('fminbnd');
    options.TolFun = 1e-6;
    FWHM = str2double(get(handles.edit41,'String'));
    RangeStep = str2double(get(handles.edit42,'String'));
    Slit_range = [FWHM-RangeStep,FWHM+RangeStep];
    Slit_range(Slit_range<1e-6)=1e-6;
```

```matlab
    options.TolX = diff(Slit_range)/10; %% tolerance on slit FWHM
    X = FWHM;
    %%% origionally used matlab search but I think we can do it with
less calls to SPECAIR on our own
    X =
fminbnd(@ParamSearch_FWHM,min(Slit_range),max(Slit_range),options,handl
es);
    %X =
SearchMinFunTr('ParamSearch_TRot',min(TRot_range),max(TRot_range),optio
ns,handles);
    % the one I made is a little less reliable but takes less time
    FWHM = X(1);
    set(handles.edit41,'String',sprintf('%g',FWHM))
    pushbutton17_Callback(handles.pushbutton17,[],handles)
end

if max([FixIntOffset,FixWaveOffset,FixWaveDispersion])==1
    fixoffsets(handles)
end

pushbutton10_Callback(handles.pushbutton10,[],handles)
set(handles.frame10,'userdata',0)

function fixoffsets(handles)
FixWaveOffset = get(handles.radiobutton55,'Value');
FixWaveDispersion = get(handles.radiobutton56,'Value');
FixIntOffset = get(handles.radiobutton57,'Value');
C1 = str2double(get(handles.edit34,'String'));
C2 = str2double(get(handles.edit35,'String'));
C3 = str2double(get(handles.edit36,'String'));
C4 = str2double(get(handles.edit38,'String'));
options = optimset('fminsearch');
options.TolFun = 1e-5;
options.TolX = 1e-5;
X = fminsearch(@ParamSearch_C1_C2_C3,[C1,C2,C3],options,handles);
SetCs(handles,X)

function SetCs(handles,X)
FixWaveOffset = get(handles.radiobutton55,'Value');
FixWaveDispersion = get(handles.radiobutton56,'Value');
FixIntOffset = get(handles.radiobutton57,'Value');
if FixWaveOffset
    if FixWaveDispersion
        if FixIntOffset
            [1,1,1];
            set(handles.edit34,'String',sprintf('%g',X(1)))
            set(handles.edit35,'String',sprintf('%g',X(2)))
            set(handles.edit36,'String',sprintf('%g',X(3)))
        else
            [1,1,0];
            set(handles.edit34,'String',sprintf('%g',X(1)))
            set(handles.edit35,'String',sprintf('%g',X(2)))
        end
    else
        if FixIntOffset
            [1,0,1];
```

```matlab
                set(handles.edit34,'String',sprintf('%g',X(1)))
                set(handles.edit36,'String',sprintf('%g',X(3)))
            else
                [1,0,0];
                set(handles.edit34,'String',sprintf('%g',X(1)))
            end
        end
    else
        if FixWaveDispersion
            if FixIntOffset
                [0,1,1];
                set(handles.edit35,'String',sprintf('%g',X(2)))
                set(handles.edit36,'String',sprintf('%g',X(3)))
            else
                [0,1,0];
                set(handles.edit35,'String',sprintf('%g',X(2)))
            end
        else
            if FixIntOffset
                [0,0,1];
                set(handles.edit36,'String',sprintf('%g',X(3)))
            else
                [0,0,0];
                % do nothing
            end
        end
    end
end

function LSQ = ParamSearch_C1_C2_C3(X,Params)
%% this function can be called by a matlab fminsearch
handles = Params;
SetCs(handles,X)
pushbutton10_Callback(handles.pushbutton10,[],handles)
Fitting = get(handles.pushbutton10,'userdata');
LSQ = Fitting.LSQ;
pause(.01)

function LSQ = ParamSearch_TRot(x,Params)
%% this function can be called by a matlab fminbnd
handles = Params;
TRot = x(1);
set(handles.edit8,'String',sprintf('%g',TRot))
if get(handles.checkbox6,'value')
    set(handles.edit7,'String',sprintf('%5.1f',TRot))
end
FixWaveOffset = get(handles.radiobutton55,'Value');
FixWaveDispersion = get(handles.radiobutton56,'Value');
FixIntOffset = get(handles.radiobutton57,'Value');

if max([FixIntOffset,FixWaveOffset,FixWaveDispersion])==1
    fixoffsets(handles)
end

pushbutton10_Callback(handles.pushbutton10,[],handles)
Fitting = get(handles.pushbutton10,'userdata');
LSQ = Fitting.LSQ;
```

```matlab
pause(.01)


function LSQ = ParamSearch_TVib(x,Params)
%% this function can be called by a matlab fminbnd
handles = Params;
TVib = x(1);
set(handles.edit9,'String',sprintf('%5.1f',TVib))
if get(handles.checkbox5,'value')
    set(handles.edit10,'String',sprintf('%5.1f',TVib))
end
FixWaveOffset = get(handles.radiobutton55,'Value');
FixWaveDispersion = get(handles.radiobutton56,'Value');
FixIntOffset = get(handles.radiobutton57,'Value');

if max([FixIntOffset,FixWaveOffset,FixWaveDispersion])==1
    fixoffsets(handles)
end
pushbutton10_Callback(handles.pushbutton10,[],handles)
Fitting = get(handles.pushbutton10,'userdata');
LSQ = Fitting.LSQ;
pause(.01)


function LSQ = ParamSearch_Te(x,Params)
%% this function can be called by a matlab fminbnd
handles = Params;
Te = x(1);
set(handles.edit10,'String',sprintf('%5.1f',Te))
if get(handles.checkbox5,'value')
    set(handles.edit9,'String',sprintf('%5.1f',Te))
end
FixWaveOffset = get(handles.radiobutton55,'Value');
FixWaveDispersion = get(handles.radiobutton56,'Value');
FixIntOffset = get(handles.radiobutton57,'Value');

if max([FixIntOffset,FixWaveOffset,FixWaveDispersion])==1
    fixoffsets(handles)
end

pushbutton10_Callback(handles.pushbutton10,[],handles)
Fitting = get(handles.pushbutton10,'userdata');
LSQ = Fitting.LSQ;
pause(0.01)


function LSQ = ParamSearch_Zeta(x,Params)
%% this function can be called by a matlab fminbnd
handles = Params;
Zeta = x(1);

set(handles.edit44,'String',sprintf('%g',Zeta))
edit44_Callback(handles.edit44, [], handles)

FixWaveOffset = get(handles.radiobutton55,'Value');
FixWaveDispersion = get(handles.radiobutton56,'Value');
```

```
FixIntOffset = get(handles.radiobutton57,'Value');

if max([FixIntOffset,FixWaveOffset,FixWaveDispersion])==1
    fixoffsets(handles)
end
pushbutton10_Callback(handles.pushbutton10,[],handles)
Fitting = get(handles.pushbutton10,'userdata');
LSQ = Fitting.LSQ;
pause(0.01)




function LSQ = ParamSearch_FWHM(x,Params)
%% this function can be called by a matlab fminbnd
handles = Params;
FWHM = x(1);
set(handles.edit41,'String',sprintf('%g',FWHM))
pushbutton17_Callback(handles.pushbutton17,[],handles)
FixWaveOffset = get(handles.radiobutton55,'Value');
FixWaveDispersion = get(handles.radiobutton56,'Value');
FixIntOffset = get(handles.radiobutton57,'Value');

if max([FixIntOffset,FixWaveOffset,FixWaveDispersion])==1
    fixoffsets(handles)
end
pushbutton10_Callback(handles.pushbutton10,[],handles)
Fitting = get(handles.pushbutton10,'userdata');
LSQ = Fitting.LSQ;
pause(.01)
```

12.1.6.5.   Calculate Spectra for Given Conditions

```
% --- Executes on button press in pushbutton10.
function pushbutton10_Callback(hObject, eventdata, handles)
%%% Run This Guess
Fitting = get(handles.pushbutton10,'userdata');
Fitting.Trot = str2double(get(handles.edit8,'String'));
Fitting.Tvib = str2double(get(handles.edit9,'String'));
Fitting.C1 = str2double(get(handles.edit34,'String'));
Fitting.C2 = str2double(get(handles.edit35,'String'));
Fitting.C3 = str2double(get(handles.edit36,'String'));
Fitting.C4 = str2double(get(handles.edit38,'String'));
Fitting.FWHM = str2double(get(handles.edit41,'String'));
Fitting.Te = str2double(get(handles.edit10,'String'));
Fitting.N2 = str2double(get(handles.edit13,'String'));
Fitting.N2p = str2double(get(handles.edit14,'String'));
Fitting.ModParams = [
Fitting.Trot,Fitting.Tvib,Fitting.FWHM,Fitting.Te,Fitting.N2,Fitting.N2
p];
Fitting.SpecParams = [ Fitting.C1,Fitting.C2,Fitting.C3,Fitting.C4];

try
    RunModel=1;
```

```matlab
    if Fitting.ModParams == Fitting.OldModParams;
        RunModel=0;
    end
    if get(handles.checkbox4,'value')
        RunModel=1;
    end
catch
    RunModel = 1;
end




try
    ExpData = get(handles.pushbutton9,'userdata');
    W = ExpData.W;
catch
    uiwait(errordlg('No Experimental Data Loaded','ERROR','modal'));
    pushbutton9_Callback(handles.pushbutton9, [], handles)
    pause(.1)
    ExpData = get(handles.pushbutton9,'userdata');
end


W = ExpData.W;
I = ExpData.I;
%% apply spectrometer corrections to experimental data
C1 = Fitting.C1;
C2 = Fitting.C2;
C3 = Fitting.C3;
C4 = Fitting.C4;
Lo = mean(W(I==max(I))); %%%
W_ni = W + C2*(W-Lo) + C1;
Lo_2 = mean(W_ni(I==max(I)));
I_ni = I+C4*(W_ni-Lo_2).*I+C3;
I_ni2 = I_ni./max(I_ni);
CW = W_ni;
CI = I_ni2;
ExpData.CW = CW;
ExpData.CI = CI;
set(handles.pushbutton9,'userdata',ExpData);

if RunModel
    %%% Set the range min and max
    RMx = max(CW) + 20;
    RMn = min(CW) - 20;
    set(handles.edit30,'string',num2str(RMn/10))
    set(handles.edit31,'string',num2str(RMx/10))
    UseLUT = get(handles.checkbox3,'value');
    if ~UseLUT
        pushbutton7_Callback(handles.pushbutton7, [], handles);
    else
        try
            'need to incorporate look up table here'
            [Lut_W,Lut_I] = loadnearestslit(handles,Fitting.ModParams);
            ModData.W = Lut_W;
            ModData.I = Lut_I;
```

```matlab
            ModData.W1 = Lut_W;
            ModData.NI = Lut_I;
            set(handles.pushbutton7,'userdata',ModData);
        catch
            pushbutton7_Callback(handles.pushbutton7, [], handles);
        end
    end
    Fitting.OldModParams = Fitting.ModParams;
    set(handles.pushbutton17,'userdata','OldSlit')
end

set(handles.pushbutton10,'userdata',Fitting);

ModData = get(handles.pushbutton7,'userdata');

W1 = ModData.W1;
NI = ModData.NI;

NI_int = interp1(W1,NI,CW);
if max(NI_int)>0
    NI_int = NI_int./max(NI_int);
end

LSQ = 1e2*sqrt(sum((NI_int-CI).^2)/length(CI));
ErEr = 1e2*sum(abs(NI_int-CI))/length(CI);

Fitting.LSQ =LSQ;

FitResult = [Fitting.ModParams, Fitting.SpecParams, Fitting.LSQ];

try
    OldFit = get(handles.text63,'userdata');
catch
    OldFit = [];
end

FitResults = [OldFit;FitResult];

b = size(FitResults);

m=0;
maxview = 9; %% number of lines which fits in the fitting results
window
rangestart = max([b(1)-maxview,1]);
for j = rangestart:b(1);
    m=m+1;
    lines{m} = sprintf('%4.0d    %4.1f    %5.1f    %5.3f   %6.1f
%1.5f   %1.3e   %5.3f    %5.3f    %5.3f    %5.3f
%13.8f',[j,FitResults(j,:)]);
end

textwords = sprintf('   %s       %s       %s     %s      %s             %s
%s         %s           %s          %s          %s
```

```matlab
%s','#','TRot','TVib','FWHM','Te','N2','N2p','C1','C2','C3','C4','%RMSE
');
for j=1:length(lines)
    textwords = sprintf('%s\n%s',textwords,lines{j});
end

Fitting.TheFit = [CW,CI,NI_int];

set(handles.text63,'String',textwords)
set(handles.pushbutton10,'userdata',Fitting)
set(handles.text63,'userdata',FitResults)

set(handles.text63,'fontsize',5)


Searching = get(handles.frame10,'userdata');
Searching,RunModel
if ~Searching|RunModel
    axes(handles.axes4)
    try
        plot(CW/10,CI,CW/10,NI_int)
        xlim([min(CW)/10,max(CW)/10])
        ylim([-.1,1.1])
        legend('Exper','Model',2)
    end
    if get(handles.checkbox2,'Value')
        try
            figure(get(handles.checkbox2,'userdata'))
        catch
            f = figure;
            set(handles.checkbox2,'userdata',f)
        end
        'plot case 3'
        try
            p1 = plot(CW/10,CI,'-',CW/10,NI_int,':')
            xlim([min(CW)/10,max(CW)/10])
            ylim([-.1,1.1])
            legend('Exper','Model',1)
            set(p1,'linewidth',1)
            set(gca,'fontsize',16)
            set(gca,'position',[  0.1300    0.1500    0.7750
0.8150])
            xlabel('wavelength (nm)')
            ylabel('Intensity (A.U.)')
            pause(.1)
        end
    end
end

set(handles.text63,'fontsize',7)
```

12.1.6.6.   Run SPECAIR

```matlab
% --- Executes on button press in pushbutton7.
function pushbutton7_Callback(hObject, eventdata, handles)
%% Run Spectral Code Button

fromdir = cd;
cd(get(handles.frame6,'userdata'))

'Now we run the code'

Searching = get(handles.frame10,'userdata');

if ~Searching
    w = waitbar(0,'Begin Spectral Calculation --> Reading
Variables','position',[250,300,400,50]);
    set(get(w,'children'),'position',[15,10,370,15]);
    pause(.1)
end

%% text boxes
T_Trans = str2double(get(handles.edit7,'String'));
T_Rot = str2double(get(handles.edit8,'String'));
T_Vib = str2double(get(handles.edit9,'String'));
if get(handles.checkbox5,'value')
    T_e = T_Vib;
    set(handles.edit10,'String',num2str(T_e));
else
    T_e = str2double(get(handles.edit10,'String'));
end

MinLambda = str2double(get(handles.edit11,'String'));
MaxLambda = str2double(get(handles.edit12,'String'));

f_N2 = str2double(get(handles.edit13,'String'));
f_N2p = str2double(get(handles.edit14,'String'));
f_O2 = str2double(get(handles.edit15,'String'));
f_OH = str2double(get(handles.edit16,'String'));
f_N = str2double(get(handles.edit17,'String'));
f_Np = str2double(get(handles.edit18,'String'));
f_O = str2double(get(handles.edit19,'String'));
f_Op = str2double(get(handles.edit20,'String'));
f_C = str2double(get(handles.edit21,'String'));
f_Cp = str2double(get(handles.edit22,'String'));
f_CN = str2double(get(handles.edit23,'String'));
f_C2 = str2double(get(handles.edit24,'String'));
f_CO = str2double(get(handles.edit25,'String'));
f_NO = str2double(get(handles.edit26,'String'));
f_NH = str2double(get(handles.edit27,'String'));
f_E = str2double(get(handles.edit28,'String'));
numdens = str2double(get(handles.edit29,'String'));
f = [f_N2, f_N2p, f_O2 , f_OH, f_N, f_Np,f_O, f_Op, f_C , f_Cp, f_CN ,
f_C2 , f_CO, f_NO, f_NH ,f_E ];
%f = [1 f_N2, 2 f_N2p, 3 f_O2 , 4 f_OH, 5 f_N, 6 f_Np,7 f_O, 8 f_Op, 9
f_C , 10 f_Cp, 11 f_CN , 12 f_C2 , 13 f_CO, 14 f_NO, 15 f_NH ,16 f_E ];
f(f<=1e-19) = 1e-19;
f = f./sum(f);
```

```matlab
for i = 1:length(f)

eval(['set(handles.edit',num2str(i+12),',''String'',',num2str(f(i)),');
']);
end
relevant = find(f>1e-15);

if ~Searching
    waitbar(.1,w,'GUI Inputs Loaded --> writing gas.inp');
end
%%%%%%%%%%%%
List =
{'N2','O2','NO','N','O','C','N2+','N+','O+','C+','CN','OH','NH','C2','C
O','E-','#dens(/cm3)','Ttran','Trot','Tvib','Tel','X(cm)'};
ValC1 =
[f(1),f(3),f(14),f(5),f(7),f(9),f(2),f(6),f(8),f(10),f(11),f(4),f(15),f
(12),f(13),f(16),numdens,T_Trans,T_Rot,T_Vib,T_e,0];
ValC2 =
[f(1),f(3),f(14),f(5),f(7),f(9),f(2),f(6),f(8),f(10),f(11),f(4),f(15),f
(12),f(13),f(16),numdens,T_Trans,T_Rot,T_Vib,T_e,1];

for i = 1:length(List)
    line{i} = sprintf('%g %g %s',ValC1(i),ValC2(i),List{i});
end

here = cd;

there = [here(1:strfind(here,'results')-1),'Specair'];

cd(there);
fid = fopen('gas.inp','w');
for i = 1:length(List)
    fprintf(fid,'%s\n',line{i});
end
fclose(fid);
cd(here);

if ~Searching
    waitbar(.2,w,'Gas.inp SPECAIR input file written --> writing
input.inp');
end
%%% radio buttons
%%%% change input.inp file to run different transitions
pause(.1)

here = cd;
there = [here(1:strfind(here,'results')-1),'Specair'];
cd(there)
WAVELS = str2num(get(handles.edit11,'string'))*10;
WAVELL = str2num(get(handles.edit12,'string'))*10;
wavestep = .05; %% units are angstroms should be less than spectrometer
resolution
narraypow = ceil(log2((WAVELL-WAVELS)/wavestep));
NARRAY = 2^narraypow;
```

```matlab
[a,b] = textread('input_origonal.inp','%n %[^\n]',74);
[c] = textread('input_origonal.inp','%[^\n]');


a(7) = NARRAY;
a(13) = WAVELS;
a(14) = WAVELL;


a(15) = get(handles.radiobutton16,'value'); % 0.    N Bound-Bound
a(16) = get(handles.radiobutton17,'value');% 0. N Bound-Free
a(17) = get(handles.radiobutton18,'value');% 0.    N Free-Free
a(18) = get(handles.radiobutton19,'value');% 0. O Bound-Bound
a(19) = get(handles.radiobutton20,'value');% 0. O Bound-Free
a(20) = get(handles.radiobutton21,'value');% 0. O Free-Free
a(21) = get(handles.radiobutton22,'value');% 0. C Bound-Bound
a(22) = get(handles.radiobutton23,'value');% 0. C Bound-Free
a(23) = get(handles.radiobutton24,'value');% 0.    C Free-Free
a(24) = get(handles.radiobutton11,'value');% 1.  N2+ (1-)
a(25) = get(handles.radiobutton4,'value');% 0.  N2  (1+)
a(26) = get(handles.radiobutton5,'value');% 1.  N2  (2+)
a(27) = get(handles.radiobutton7,'value');% 0.  N2 Birge-Hopfield 2
a(28) = get(handles.radiobutton29,'value');% 0.  NO Beta
a(29) = get(handles.radiobutton30,'value');% 0.  NO Gamma
a(30) = get(handles.radiobutton13,'value');% 0.  O2 Schumann-Runge
a(31) = get(handles.radiobutton25,'value');% 0.  CN Violet
a(32) = get(handles.radiobutton26,'value');% 0.  CN Red
a(33) = get(handles.radiobutton27,'value');% 0.  C2 Swan
a(34) = get(handles.radiobutton28,'value');% 0.  CO (4+)
a(35) = get(handles.radiobutton31,'value');% 0.  NO Delta
a(36) = get(handles.radiobutton32,'value');% 0.  NO Epsilon
a(37) = get(handles.radiobutton15,'value');% 0.  OH (A-X)
a(38) = get(handles.radiobutton33,'value');% 0.  NO Beta prime
a(39) = get(handles.radiobutton34,'value');% 0.  NO Gamma Prime
a(40) = get(handles.radiobutton8,'value');% 0.  N2 Birge-Hopfield
a(41) = get(handles.radiobutton9,'value');% 0.  N2 Carrol-Yoshino
a(42) = get(handles.radiobutton35,'value');% 0.  NO (C-A)
a(43) = get(handles.radiobutton36,'value');% 0.  NO (D-A)
a(44) = get(handles.radiobutton12,'value');% 0.  N2+ Meinel
a(45) = get(handles.radiobutton37,'value');% 0.  NO B'-B
a(46) = get(handles.radiobutton38,'value');% 0.  NO E-C
a(47) = get(handles.radiobutton39,'value');% 0   NO F-C(3)
a(48) = get(handles.radiobutton40,'value');% 0.  NO H-C
a(49) = get(handles.radiobutton41,'value');% 0.  NO H'-C
a(50) = get(handles.radiobutton42,'value');% 0.  NO E-D(5)
a(51) = get(handles.radiobutton44,'value');% 0.  NO F-D(3)
a(52) = get(handles.radiobutton45,'value');% 0.  NO H-D
a(53) = get(handles.radiobutton46,'value');% 0.  NO H'-D
a(54) = get(handles.radiobutton47,'value');% 0.  NO IR
a(55) = get(handles.radiobutton49,'value');% 0.  CO IR
a(56) = get(handles.radiobutton48,'value');% 0.  NH (A-X)
a(57) = get(handles.radiobutton14,'value');% 0.  OH IR


for i= 1:length(c)
    if i<=74;
        if i==1
            str = sprintf('%G  \t%s',a(i),b{i});
        else
```

```matlab
            str = sprintf('%s\n%G  \t %s',str,a(i),b{i});
        end
    else
        str = sprintf('%s\n%s',str,c{i});
    end
end

fid = fopen('input.inp','r+');
fprintf(fid,'%s',str);
fclose(fid);
cd(here)

if ~Searching
    waitbar(.3,w,'input.inp SPECAIR input file written (NA)--> Running
SPECAIR ...');
    pause(.1)
end
%%%%%%% Run Spec Air
here = cd;
there = [here(1:strfind(here,'results')-1),'Specair'];
cd(there)
!rad.exe
cd (here)
if ~Searching
    waitbar(.6,w,'SPECAIR Complete --> Loading Results ...');
end
'SPECAIR Complete'
%%%% Load SPECAIR spectra
there = [here(1:strfind(here,'results')-1),'results'];
cd(there)
a=dlmread('spec.dat');
cd(here)
W = a(:,1);
I = a(:,2);
%%% narrow down the window

RangeMin = str2double(get(handles.edit30,'String'));
RangeMax = str2double(get(handles.edit31,'String'));

W1 = W(W>RangeMin*10&W<RangeMax*10);
I1 = I(W>RangeMin*10&W<RangeMax*10);
if max(I1)>0
    I1 = I1./max(I1);
end

badinds = find(isnan(I1));

if badinds
    RangeMin
    RangeMax
    figure
    plot(W,I)
    return
end
```

```matlab
if ~Searching
    waitbar(.65,w,'SPECAIR output Loaded --> Loading Slit ...');
end
%%% Load experimental Slit Function


try
    SlitData = get(handles.pushbutton8,'userdata');
    SW = SlitData.SW;
    SI = SlitData.SI;
catch
    cd(there)
    %    Sf2 = dlmread('SlitFun_Raw.csv');
    'Failed Slit File Loading -- '
    pause(1)
    cd(here)
    SW = Sf2(1:end,1)*10; %% slit function wavelength A
    SI = Sf2(1:end,2); %% slit function intensity
    SI = SI./max(SI);
end

%% set the slit function to this region

wsmax =mean(SW(SI==max(SI)));
SW2 = SW - wsmax + mean(W1);
%% interpolate and extrapolate slit function over the region
SI2 = interp1(SW2,SI,W1);
SI2(isnan(SI2))=min(SI2);

if ~Searching
    waitbar(.7,w,'Slit Function Loaded --> Convolving ...');
end

 im = round(mean(find(SI2==max(SI2))));
 SI2a = [SI2(im:end);SI2(1:im-1)]; %% make slit symetric for fast
convolve
% figure
 % plot(W1,SI2,W1,SI2a)

%%% Convolve Slit and Specair Data
%%% THis is the slowest process
%NI = convn(SI2,I1,'same');
NI = fastconv(SI2a,I1);
if max(NI)>0
    NI = NI./max(NI);
end
'Convolution Complete'

if ~Searching
    waitbar(.95,w,'Convolution Complete --> Plotting ...');
end
ModData.W = W;
ModData.I = I;
ModData.W1 = W1;
ModData.NI = NI;
```

```matlab
set(handles.pushbutton7,'userdata',ModData);


% plotting
ax1 = handles.axes1;
axes(ax1)
plot(W,I)

ax2 = handles.axes2;
axes(ax2)
plot(SW,SI)

ax3 = handles.axes3;
axes(ax3)
plot(W1,NI)

if get(handles.checkbox2,'Value')
    % Zoomable plot
    try
        figure(get(handles.checkbox2,'userdata'))
    catch
        f = figure;
        set(handles.checkbox2,'userdata',f)
    end
    try
        ExpData = get(handles.pushbutton9,'userdata');
        W = ExpData.W;
        I = ExpData.I;
    catch
        W = [];
        I = [];
    end
    try
        plot(W/10,I,'-',W1/10,NI,':')
        set(gca,'fontsize',16)
        xlim([min(W)/10,max(W)/10])
        legend('Exper','Model')
        ylim([-.1,1.1])
        pause(.1)
        xlabel('wavelength (nm)')
        ylabel('Intensity (A.U.)')
    end
end
if ~Searching
    waitbar(1,w,'Completed Modeled Spectra');
    pause(.1)
    close(w)
end

cd(fromdir)
'End RunSpecAir'
```

12.2.   Algorithms for image analysis to determine discharge size

The size and shape of the discharge was an important parameter to determine from the micrographs taken of the discharges. This size was then used for determining current densities, and sizes of the various structures within the discharge. Since several hundred images were analyzed this was done using a computer program to facilitate the handing of the large amounts data and to prevent human error. The code ran rather quickly, about 30 sec to 60 second per image and displayed the results graphically so that the user of the program could visually check that there were no computer errors. The code is listed below and a representive figure is also shown.

```
Currents = [1.1:.1:3.5]
GlowFigs = dir('*mA.bmp');
m=0;
c = {GlowFigs.name}
SpatialCal = 1.96 %% microns per pixel
FirstPeak = NaN*Currents;
SecondPeak = NaN*Currents;
ThirdPeak = NaN*Currents;
FirstValley = NaN*Currents;
SecondValley = NaN*Currents;
ThirdValley = NaN*Currents;
plotit = 1;
for filename ={c{1}};
    m=m+1;
    A = imread(filename{1},'bmp');
    if plotit
        image(A)
        xlabel('pixel')
        ylabel('pixel')
        figure
    end
```
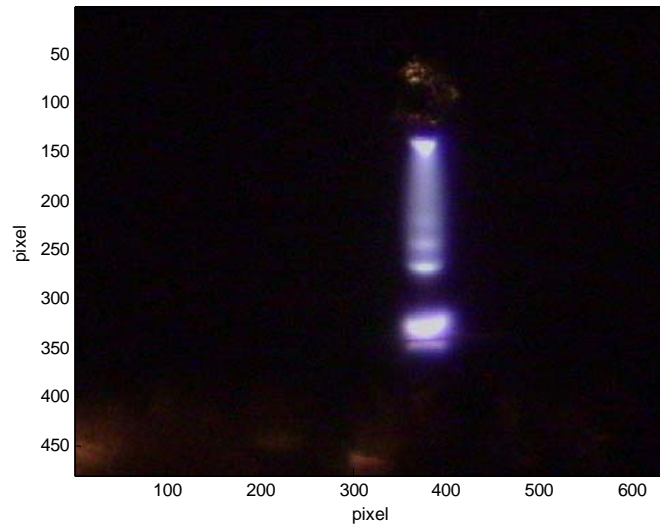
Figure12.6: Image of glow discharge to be analyzed

```matlab
R = double(A(:,:,1));
G = double(A(:,:,2));
B = double(A(:,:,3));
Gr = R+G+B;
Gr = Gr./max(max(Gr));
ss = size(Gr);
y = 1:ss(1);
ym = y'*ones(1,ss(2));
x = [1:ss(2)];
xm = (x'*ones(1,ss(1)))';
if 1 %% turn this on to set inspect val
    imagesc(Gr)
    for val = [.55:.1:.95]
        eg1 = find(Gr>val);
        ymax = max(ym(eg1));
        ymin = min(ym(eg1));
        xmax = max(xm(eg1));
        xmin = min(xm(eg1));
        rectangle('position',[xmin,ymin,xmax-xmin,ymax-ymin])
        text(xmax,ymin+(ymax-ymin)*val,num2str(val))
        pause(.1)
        xlabel('pixel')
        ylabel('pixel')
    end
    xlim([300,425]);
    ylim([40,380]);
    figure
end
```
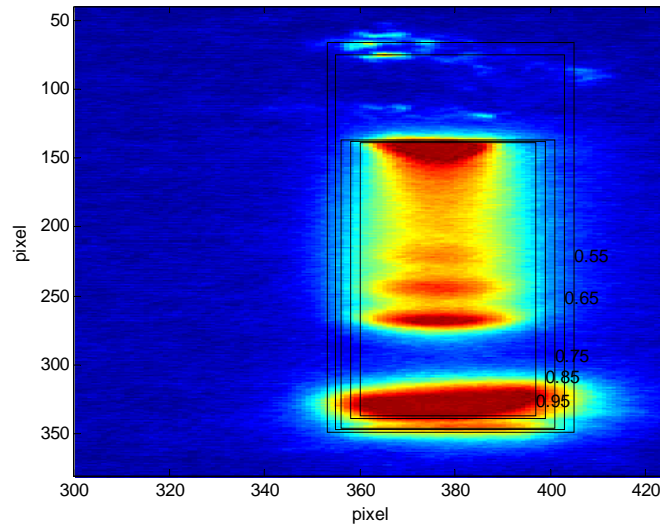
Figure 12.7: Pseudo-color grayscale image of region of interests corresponding to threshold percentage of peak value.

```matlab
    inspectval = 0.9; %% value of region of interest selected by the
user
    eg1 = find(Gr>inspectval);
    ymax = max(ym(eg1))+20;
    ymin = min(ym(eg1))-10;
    xmax = max(xm(eg1))+20;
    xmin = min(xm(eg1))-20;
    rangeX = find(x>xmin&x<xmax);
    rangeY = find(y>ymin&y<ymax);
    X = xm(rangeY,rangeX);
    Y = ym(rangeY,rangeX);
    I = Gr(rangeY,rangeX);
    Iup = Gr(rangeY+1,rangeX);
    Idown = Gr(rangeY-1,rangeX);
    Ileft = Gr(rangeY,rangeX-1);
    Iright = Gr(rangeY,rangeX+1);
    IupLeft = Gr(rangeY+1,rangeX-1);
    IupRight = Gr(rangeY+1,rangeX+1);
    IdownLeft = Gr(rangeY-1,rangeX-1);
    IdownRight = Gr(rangeY-1,rangeX+1);
    ISmooth = I + .5*Iup + .5*Idown + .5*Ileft + .5*Iright +
.15*IupLeft + .15*IupRight + .15*IdownLeft + .15*IdownRight;
    ISmooth = ISmooth./max(max(ISmooth));
    Ir = R(rangeY,rangeX);
    Ig = G(rangeY,rangeX);
    Ib = B(rangeY,rangeX);
    %%% which to use
    %    I = I;
    I = ISmooth;
    %%% Find axis
    IavgY = mean(I);
    XavgY = mean(X);
    X = X-XavgY(find(IavgY==max(IavgY)));
    XavgY = mean(X);
```

```matlab
%%% Outline the discharge
YavgX = mean(Y');
AlongAxis = I(:,XavgY==0)';
Cat = YavgX(max(find(diff(AlongAxis)>0)));
Y = -Y+Cat;
YavgX = mean(Y');
%%
  if plotit

      imagesc(XavgY,YavgX,I)
      axis equal
      axis tight
      xlabel('pixel from cathode')
      ylabel('pixel from centerline')


  end
%%
NearAxis = mean(I(:,abs(XavgY)<=10)')';
AcrossRadius = mean(I');
%%
FDScenter = YavgX(AlongAxis==min(AlongAxis));
PCAxis = AlongAxis./max(AlongAxis(YavgX<FDScenter));
NGAxis = AlongAxis./max(AlongAxis(YavgX>FDScenter));
FDSTop = min(YavgX(PCAxis>.5&YavgX>FDScenter))-1;
FDSBot = max(YavgX(NGAxis>.5&YavgX<FDScenter));
Anode = max(YavgX(PCAxis>.5&YavgX>FDScenter));
Abot = max(YavgX(PCAxis<.95&YavgX<Anode-10));
%%%
DisR = find(YavgX>=-5&YavgX<=Anode+5)+ymin;
IMAxis(1:length(DisR),m,:) =
mean(A(DisR,find(abs(XavgY)<=10)+xmin,:),2);
%%%
NAS = smooth(NearAxis,5).*(YavgX>FDSTop)';
dNAS = derivative(YavgX,NAS');
[P,V] = FindPeak(NAS,0.01);
PV = [];
if isempty(V)
    %% No Stiations
    AnodePeak = P(1);
    StriationDist = 0;
else
    AnodePeak = P(1);
    P = P(2:end); %%% the first peak is the anode glow
    Ploc = YavgX(P);
    Vloc = YavgX(V);
    for i = 1:length(Ploc)
        PV(2*i-1) = Vloc(i);
        PV(2*i) = Ploc(i);
    end
    PV = sort(PV);
    StriationDist = mean(diff(PV))*2
end
for i=1:length(PV);
    if i==1
        FirstPeak(m) = PV(i);
    elseif i==2
```

```matlab
                FirstValley(m) = PV(i);
            elseif i==3
                SecondPeak(m) = PV(i);
            elseif i==4
                SecondValley(m) = PV(i);
            elseif i==5
                ThirdPeak(m) = PV(i);
            elseif i==6
                ThirdValley(m) = PV(i);
            end
        end
    LongData{m} =
{FDSBot,FDScenter,FDSTop,PV,StriationDist,AnodePeak,Anode};
    AllCat(m) = 0;
    AllFDSBot(m) = FDSBot;
    AllFDSTop(m) = FDSTop;
    AllStriDist(m) = StriationDist;
    AllAnode(m) = Anode;
    AllAbot(m) = Abot;
    NAS = smooth(NearAxis,5);
    AB(m,1:length(NAS)) = NAS';

    %%% Radial
    NGR = mean(I(YavgX<FDSBot&YavgX>0,:),1);
    NGR = NGR./max(NGR);
    XLNG = XavgY(min(find(NGR>.85)));
    XRNG = XavgY(max(find(NGR>.85)));
    WidthNG(m) = length(find(NGR>.85));
    PCR = mean(I(YavgX>FDSTop&YavgX<Anode,:),1);
    PCR = PCR./max(PCR);
    WidthPC(m) = length(find(PCR>.85));
    XLPC = XavgY(min(find(PCR>.85)));

    if plotit
        R1 = rectangle('position',[XLNG,0,WidthNG(m),FDSBot]);
        set(R1,'linestyle',':')
        R2 = rectangle('position',[XLPC,FDSTop,WidthPC(m),Anode-
FDSTop]);
        set(R2,'linestyle','--')
```
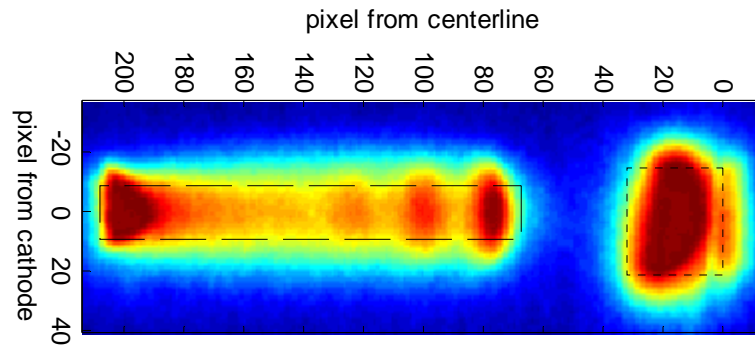
Figure 12.8: Pseudo color grayscale image with location of cathode region and positive column regions outlined.

```
 figure
plot(YavgX,NAS+m,YavgX(P),NAS(P)+m,'x',YavgX(V),NAS(V)+m,'o')
hold on
xlabel('pixel from cathode')
ylabel('Intensity')
pause(.1)
    end
end
```
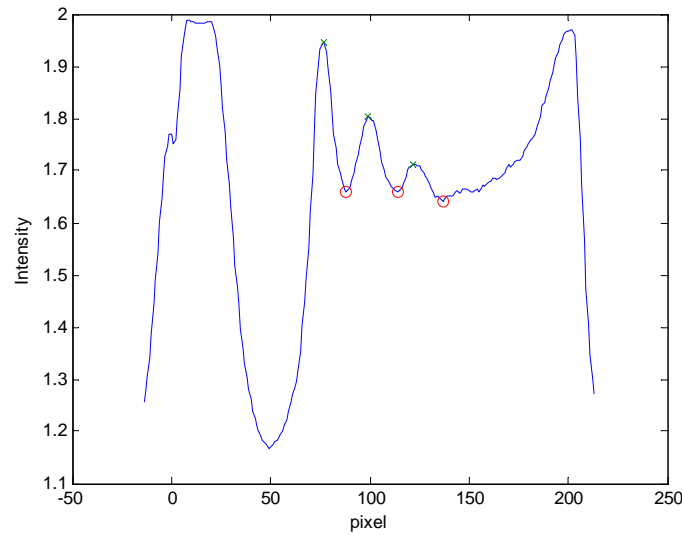
Figure 12.9: On axis intensity plot showing location of striations.

12.3. Detailed derivation of ionization overheating instability

The ionization overheating instability in atomic gases is indicated in the causal chain shown in expression (A) and can be initiated at any step. An incremental increase, δ, in the electron density n_e leads through collision to an increase in gas temperature, T_o. The T_o increase corresponds with a decrease in neutral density, n_o, by the equation of state at constant pressure. The decrease in density corresponds to an increase in the reduced electric field, $E/n,$ assuming a constant electric field, E. The electron temperature, T_e is largely determined by E/n and an increase in E/n causes and increase in T_e. At slightly higher T_e the ionization rate constant, k_i, increases dramatically and causes a further increase in n_e. The chain thus is closed and provides positive feedback.

$$\uparrow \delta n_e \Rightarrow \uparrow \delta T_o \Rightarrow \downarrow \delta n_o \Rightarrow \uparrow \delta \frac{E}{n_o} \Rightarrow \uparrow \delta T_e \Rightarrow \uparrow \delta k_i \Rightarrow \uparrow \delta n_e \quad \text{(A)}$$

Here we consider a simple case wherein just the IOI can be described by the perturbation analysis of a system of three equations (1), (2), (3) for the electron density, n_e and gas temperature, $T_o,$ and applied voltage V. As discussed in chapter 7 the inclusion of the applied voltage in the formulation is a break from typical analyses. Additional terms in these equations are: time, t, neutral gas density, n_o, ionization rate constant, k_i, ambipolar diffusion, D_a, characteristic discharge size, Λ, recombination rate constant k_r, current density, j, Boltzmann constant, k, ratio of specific heats, γ, voltage on the plasma, V_p, ambient temperature, T_a, and gas diffusion, D, applied power supply voltage, V_1, ballast resistance R_b, circuit capacitance, C_1, and effective plasma resistance, R_p. For now we will consider $k_r=0$.

$$\frac{\partial}{\partial t}n_e = n_e n_o k_i - n_e \frac{D_a}{\Lambda^2} - n_e^2 k_r \tag{1}$$

$$\frac{\partial}{\partial t}T = \frac{\gamma-1}{\gamma}\frac{jV_p}{nk} - (T-T_a)\frac{D}{\Lambda^2} \tag{2}$$

$$\frac{\partial}{\partial t}V_p = \frac{V_1-V_p}{R_b C_1} - \frac{V_p}{R_p C_1} \tag{3}$$

The increases in T_o, n_e, and V_p can be expressed as perturbation from a stable case with exponential growth in time and space, r, for example as equations (4), where ω is the growth rate in time, k is the wave vector. Here, as in some past studies, for simplification we have considered only inhomogeneities with wave vector perpendicular to the applied electric field which will lead to catastrophic instabilities and discharge contraction. The perturbation can thus be described solely in time as in equations (5), (6) and (7).

$$T_o = T_o^{(0)} + \delta T_o \exp[i(\omega t - \vec{k} \cdot \vec{r})] \qquad (4)$$

$$n_e = n_e^{(0)} + \delta n_e \exp(i\omega t) \qquad (5)$$

$$T_o = T_o^{(0)} + \delta T_o \exp(i\omega t) \qquad (6)$$

$$V_p = V_p^{(0)} + \delta V_p \exp(i\omega t) \qquad (7)$$

Variations with respect to the electron energy (steps 4,5, and 6 in (A)) are assumed fast and represented by algebraic equations, (8), (9). These correspond to eq. 4.90 and 2.21 in reference [Fridman's Book]. Addition terms taken as constants: e, electron charge, σ_{en}, electron neutral collisional cross section, and δ the average fraction of electron energy lost in a collision[6], m is the mass of the atom, σ_o is the atomic cross section, I is the ionization energy. Similarly sound modes or pressure equilibration (step 3 in (A)) for small magnitude, bounded wavelength perturbations is negligible and density is calculated using the equation of state equation (10). Traditionally E is taken as constant; though we allow is to change and $E = V_p/d$ where d is the discharge gap length. This is a simple representation of E. A more accurate $E = (V_p - V_n)/d$ where V_n is the normal cathode sheath potential drop was also considered but did not significantly alter the results.

$$T_e = \left(\frac{E}{n_o}\right) \frac{e}{\langle \sigma_{en} \rangle} \sqrt{\frac{\pi}{12\delta}} \qquad (8)$$

$$k_i = \sqrt{\frac{8T_e}{\pi m \sigma_o}} \exp(-I/T_e) \qquad (9)$$

$$n_o = p/kT_o \qquad (10)$$

---

[6] This symbol is the same as used for the incremental increments in eq. (1) however is kept here for consistency with the external reference and is distinguishable by context.

The first step in the perturbation analysis is to cast equations (1-3) into a canonical form in which all of the various terms in the equation are written in terms of the variables, n_e, T_o and V_p, or parameters p, E, Λ, T_∞, C_1, R_b, V_1 universal constants k, e, and gas specific constants I, m, σ_o, σ_{ne}, δ. Algebraic expressions for D_a, D, j, and Λ are given in equations 11, 12, 13, and 14 respectively. The ion mobility D_i, is calculated using the Langevin model since the radial electric field is low. D_i is proportional to $1/p$ and thus is constant in our case (eq. 4.117 in ref Fridman). The ion and neutral gas temperatures are assumed equal. For the discharge current, j, the electron drift velocity, v_{de}, is calculated from the product of the applied E and electron mobility, μ_e. For mobility, the similarity parameter $(\mu_e n_o)_{nom}$ is considered as a gas specific constant and μ_e is calculated from the pressure and temperature. The characteristic diffusion length of the discharge is taken as a constant and is given by equation (14) which is for a cylindrical discharge of radius R and length L. R and L were taken from experiment. The IOI does eventually lead to radial contract of the discharge and R will change but during the initial small perturbation which we are studying R is essentially constant.

$$D_a = D_i \frac{T_e}{T_o} \quad (11)$$

$$D = \frac{3T_o^{\frac{3}{2}}}{64 p \sigma_o} \sqrt{\frac{k}{m}} \quad (12)$$

$$j = e n_e v_{de}, \quad j = e n_e \left[(\mu_e n)_{nom} \frac{kT_o}{p} \right] E \quad (13a, 13b)$$

$$\frac{1}{\Lambda^2} = \left(\frac{2.4}{R} \right)^2 + \left(\frac{\pi}{L} \right)^2 \quad (14)$$

Substituting the above equations into equation 1-3 and grouping some of the large constants groups together as K_1 to K_4 we get equations 15-17. From these equations it is obvious almost by inspection what the results of the substitution of the perturbed solutions 5-7 will be. The power of the term will end up as a coefficient of the perturbed variable. The term k_i is given special treatment because unlike all the other terms it is non-linear and thus in not accurately depicted by a algebraic expression. k_i is exponentially dependant on E/n and thus exponentially dependant on the gas temperature T and discharge voltage V_p. To account for this the proper treatment is to use the logarithmic sensitivity.

$$\frac{\partial}{\partial t} n_e = n_e k_i \frac{p}{kT} - \{K_1\}(n_e - n_{e_a})T^{\frac{5}{2}}(V_p - V_n)^2 \tag{15}$$

$$\frac{\partial}{\partial t} T = \{K_2\}n_e(V_p - V_n)T^2 V_p - \{K_3\}(T - T_a)T^{\frac{3}{2}} \tag{16}$$

$$\frac{\partial}{\partial t} V_p = \frac{V_1 - V_p}{R_b C_1} - \frac{n_e T(V_p - V_n)}{\{K_4\}C_1} \tag{17}$$

Equation 1-3 are more easily understood and manipulated if they are written in term of the frequencies of the relevant processes. Equations 18-20 shows this recasting. The relevant frequencies are the ionization frequency, v_i, the electron loss frequency v_{ew} (the $_{ew}$ refers to electron wall diffusion losses, in the case of atmospheric pressure plasma the electron loses are not to the walls but actually to the attachment which occurs directly outsize the high temperature region), and v_r the recombination frequency. v_h is the heating frequency, v_{nw} is the neutral diffusion loss frequency. v_c is the stray capacitance

charging frequency, v_D is the capacitance discharge frequency through the discharge. Definitions of these frequencies can easily be found by comparing equation 1-3 with 18-20.

$$\frac{\partial}{\partial t} n_e = n_e v_i - n_e v_{ew} - n_e v_r \tag{18}$$

$$\frac{\partial}{\partial t} T = T v_h - (T - T_a) v_{nw} \tag{19}$$

$$\frac{\partial}{\partial t} V_p = v_C (V_1 - V_p) - v_D V_p \tag{20}$$

Results of substituting the perturbed equations in 5-7 into equations 15-17 and simplifying the notation in terms of frequencies is given in equations 21-23. Also here Ω is used for the specific ω perturbation, and ε_T is the strength of the perturbation $\delta T_o/T_o^{(0)}$.

$$\Omega \varepsilon_{n_e} = (v_i - v_{ew}) \varepsilon_{n_e}$$
$$+ (v_i(\frac{d \ln k_i}{d \ln T} - 1) - \tfrac{5}{2} v_{ew}(1 - \frac{n_{ea}}{n_e})) \varepsilon_T$$
$$+ (v_i \frac{d \ln k_i}{d \ln V_d} - 2 v_{ew} \frac{V_p}{V_p - V_n}(1 - \frac{n_{ea}}{n_e})) \varepsilon_{V_d} \tag{21}$$

$$\Omega \varepsilon_T = v_h \varepsilon_{n_e}$$
$$+ (2 v_h - (\tfrac{5}{2} - \tfrac{3}{2}\frac{T_a}{T}) v_{nw}) \varepsilon_T$$
$$+ (1 + \frac{V_p}{V_p - V_n}) v_h \varepsilon_{V_d} \tag{22}$$

$$\Omega \, \varepsilon_{V_p} = -V_D \varepsilon_{n_e} - V_D \varepsilon_T - \left(V_C + \frac{V_p}{V_p - V_n} V_D\right) \varepsilon_{V_p}$$

(23)

These equations can be conveniently written in matrix notation for the system of 3 equations. The solution of this system is only relevant (i.e. non-trivial) when the determinant of the 3x3 matrix is zero. This is written in equation (24). As is typical of these types of analyses Ω is the eigen value of the system.

$$\begin{vmatrix} V_i - V_{ew} - \Omega & V_i\left(\frac{d\ln k_i}{d\ln T} - 1\right) - \frac{5}{2}V_{ew}\left(1 - \frac{n_{ea}}{n_e}\right) & V_i\left(\frac{d\ln k_i}{d\ln V_d}\right) - 2V_{ew}\frac{V_p}{V_p - V_n}\left(1 - \frac{n_{ea}}{n_e}\right) \\ V_h & 2V_h - \left(\frac{5}{2} - \frac{3}{2}\frac{T_a}{T}\right)V_{mw} - \Omega & \left(1 + \frac{V_p}{V_p - V_n}\right)V_h \\ -V_D & -V_D & -V_C - \frac{V_p}{V_p - V_n}V_D - \Omega \end{vmatrix} = 0$$

(24)

To proceed with the solution it is important to understand the size of some of these terms. Table 12.4 summarizes these coefficients for typical discharge conditions. In atmospheric pressure plasmas we are dealing with warm discharges which are generally longer in size.

Table 12.4: Typically values of coefficients in matrix equations

Electron density

$$\hat{n}_{e_a} = \frac{n_{e_a}}{n_e}$$

$$\nu_i = \nu_{ew}(1 - \hat{n}_{e_a})$$

$$\hat{n}_{e_a} \approx 0 \rightarrow 1x10^{-6}$$

Gas temperature

$$\hat{T}_a = \frac{T_a}{T}$$

$$\nu_h = \nu_{nw}(1 - \hat{T}_a)$$

$$\hat{T}_a \approx .2 \rightarrow .9999$$

Warm discharge   Cool discharge

Voltage

$$\hat{V}_c = \frac{(V_p - V_n)}{V_p}$$ ← Positive Column Voltage

← Discharge Voltage

$$\hat{V}_c \approx 0.05 \rightarrow 0.5$$

Sheath Dominated

Longer Discharge

Technically a 3rd order solution for the perturbation's growth can be found from equation 24; however, this doesn't give any insight into the problem. To address the necessary simplifications let's consider a system without any time variations in the external circuit. This constant E solution is often done in the literature. This system corresponds to the upper left (rows 1-2 and columns 1-2) of the matrix shown in equation 24. To simplify this further the following approximations are made: $\Omega < \nu_i$, ν_i-ν_{ew} is of order -ν_i[7], $\frac{d \ln k_i}{d \ln T} > 1$, and terms of order 1 are equal to 1 for simplifications. Also the relationships between the steady state frequencies as shown in table 2.4 are utilized. This gives us the matrix should in equation (26).

$$\begin{matrix} \nu_i - \nu_{ew} - \Omega & \nu_i(\frac{d \ln k_i}{d \ln T} - 1) - \frac{5}{2}\nu_{ew}(1 - \frac{n_{e_a}}{n_e}) \\ \nu_h & 2\nu_h - (\frac{5}{2} - \frac{3}{2}\frac{T_a}{T})\nu_{nw} - \Omega \end{matrix} \quad (25)$$

$$\begin{vmatrix} -\upsilon_i & \frac{d \ln k_i}{d \ln T}\upsilon_i \\ \upsilon_h & -\upsilon_{nw} - \Omega \end{vmatrix} = 0 \quad (26)$$

---

[7] This assumption may seem a bit strong, but makes sense physically as loses rates are always faster. Another way to consider this assumption is to also include recombination, even a little bit. ν_r is ~n_e^2 so the losses term will always have a factor 2(from the exponent) and be slightly larger.

Solution of equation 26 is trivial and gives the important solution found in the literature and textbooks[1,2]. The ramifications and applications of this equation (27) are given in chapter 7.

$$\Omega = v_h \frac{dlnk_i}{dlnT} - v_{nw} \quad (27)$$

Taking a similar simplifying approach and considering only columns 1,3 and rows 1,3 we get the matrix equation (28). This ignores the temperature change and only shows the instability with respect to the external circuit. As expected the solution is always stable, but this solution gives the term caused by the stabilization of the external circuit as discussed in chapter 7.

$$\begin{vmatrix} -v_i & \frac{dlnk_i}{dlnVd} v_i \\ -v_D & -v_D - \Omega \end{vmatrix} = 0 \quad (28)$$

$$\Omega = -v_D \frac{dlnk_i}{dlnVd} \quad (29)$$

DAVID STAACK

859 N. Ringgold St. · Philadelphia, PA 19130
(215) 787-0470 · dstaack@drexel.edu

EDUCATION

Drexel University, *Philadelphia, PA*
Ph.D. Candidate Mechanical Engineering, September 2004 – Expected Fall 2008

Princeton University, *Princeton, NJ*
M.E. Mechanical and Aerospace Engineering, January 2001 – August 2004

University of Virginia, *Charlottesville, VA*
M.S. / B.S., Aerospace Engineering, September 1995 – January 2001

EXPERIENCE

Graduate Research Assistant, *Drexel University, Philadelphia, PA, Fall 2004 – Present*
*Advisors: Bakhtier Farouk, Alexander Fridman, Gary Friedman, Yury Gogotsi, Alexander Gutsol (DrexelUniversity).*Development and utilization of micro- and nano-scale plasmas for materials synthesis, biomedical; and energy applications. Research focuses on understanding the scaling, control, and stabilization of microplasma and nanoplasma discharges using spectroscopy and non-intrusive diagnostic techniques. Work includes experience with: DC, RF and pulsed plasma discharges, micro-fabrication, optical emission spectroscopy, nonequilibrium thermodynamics and chemistry, plasma enhanced chemical vapor deposition, Raman and FTIR material characterization, optical microscopy, CFD of chemically reacting flows, biological decontamination and sterilization, gas chromatography, thermal gravimetric analysis and fuel reforming.

Adjunct Instructor, *Drexel University Goodwin College, Philadelphia, PA, Fall 2006 – Spring 2007*
Course Taught: MEM 311 Thermal and Fluid Sciences Laboratory - Junior level undergraduate mechanical engineering course consisting of lectures and laboratory experience in thermodynamics, heat transfer, fluid dynamics, and experimental methods. Responsible for all aspects of the course including: lecturing; preparation of lectures, quizzes and exam; grading; and maintenance of laboratory equipment. Also participated in committee to update the course and prepare for ABET review.

Graduate Research Assistant, *Princeton University, Princeton, NJ, Winter 2001 – Summer 2004*
Advisors: Nathaniel Fisch, Yevgeny Raitses (Princeton University).
Study and development of plasma thrusters for spacecraft propulsion. Experiments on the effects of plasma wall interactions on the performance of Hall thrusters. Work includes experience with plasma discharges, spacecraft propulsion, plasma material interactions, rarefied gas dynamics, probe based plasma diagnostic techniques, cryogenic and other high vacuum facilities, multistage high-acceleration positioning systems, electronic measurement circuits, data acquisition software, and data analysis software.

Graduate Research Assistant, *University of Virginia, Charlottesville, VA, Fall 1998 – Fall 2000*
Advisor: James C. McDaniel (University of Virginia).
Research focused on experimental studies of the interaction between rarefied and continuum flow in a reaction control system. Measurements were compared to computer simulations of reaction control systems made by NASA Langley. Work included the building and designing of a vacuum based hypersonic wind tunnel and development of planar laser induced fluorescence (PLIF) techniques to measure temperature, pressure, and velocity in the flowfield.

Undergraduate Research Assistant, *University of Virginia, Charlottesville, VA and Carnegie Mellon University, Pittsburgh, PA, Spring 1996 – Spring 1998*
Advisor: Randy Pausch (Carnegie Mellon University).
Research involved programming virtual reality environments and helping to develop the Alice 3D graphics software. Also developed content for virtual reality experiments for the psychology department to compare human perceptions of real and virtual worlds. Work included programming, animation and CAD/CAM.

ACHIEVEMENTS

Drexel University Invention Disclosure, Fall 2007
Koerner Foundation Fellowship, Fall 2006 – Summer 2007
NSF - IGERT Fellowship in Nanotechnology, Fall 2005 – Summer 2006
Outstanding Teacher Assistant Award, Spring 2005
Princeton Plasma Physics Lab Patent Awareness Program Invention Disclosure, Spring 2003
NASA Graduate Student Researchers Program (GSRP) Fellowship, Fall 1999 – Fall 2001
Virginia Space Grant Consortium Aerospace Graduate Research Fellowship, Fall 1999
Sigma-Gamma-Tau Outstanding Aerospace Graduate Award, Spring 1999
AIAA Regional Student Conference Undergraduate First-Place Paper Winner, Spring 1999
Third Place FAA/NASA Advanced General Aviation Transport Experiment (AGATE), 1998 and 1999

RESEARCH AND TEACHING INTERESTS

Plasma Engineering, Plasma Physics, Plasma Medicine, Microfabrication, Nanotechnology, Spacecraft Propulsion, Green Energy, Reacting Flows, Spectroscopic Diagnostics, Optics and Lasers, Non-equilibrium Kinetics, Statistical Thermodynamics, Experimental Methods, Fluid Dynamics, Thermodynamics.

PROFESSIONAL SERVICES AND ACTIVITIES

Reviewer for the journal IEEE Transactions on Plasma Science
Reviewer for the journal Physics of Plasmas
Member AIAA, Member ASME, Member APS, Member IEEE, Member AAAS, Member ASEE

ACCEPTED/PUBLISHED REFEREED JOURNAL PUBLICATIONS

1. Staack D, Fridman A, Gogotsi Y, Friedman G, *"Nanoscale Corona Discharge in Liquids Enabling Nanosecond Optical Emission Spectroscopy"* Angewandte Chemie International Edition, Oct. 2008. [VIP Paper, Impact Factor 10.03]

2. Wilson A, Staack D, Farouk B, Gutsol A, Fridman A, *"Self-Rotating DC Atmospheric Pressure Discharge over a Water-Surface Electrode"*, accepted Plasma Source Science and Technology, June 2008. [Impact Factor 2.35].

3. Staack D, Farouk B, Gutsol A, Fridman A, *"DC normal glow discharges in atmospheric pressure atomic and molecular gases,"* Plasma Source Science and Technology, Vol. 17, Art. 025013, May 2008 [Impact Factor 2.35, Times Cited 1]

4. Staack D, Friedman G, Gutsol A, Fridman A, *"Preliminary evaluation of a pulsed corona discharges for characterization of biological liquids",* accepted "Plasma Assisted Decontamination of Biological and Chemical Agents", Editors: S. Guceri and V. Smirnov, Springer, NY, 2008. [Refereed Book Article]

5. Staack D, Farouk B, Gutsol A, Fridman A, *"Spatially resolved temperature measurements of atmospheric pressure DC microplasmas,"* IEEE transactions on plasma science, Vol. 35 (5), 1448-1455, Oct. 2007. [Impact Factor 1.14, Times Cites 2]

6. Farouk T, Farouk B, Staack D, Gutsol A, Fridman A, *"Modeling of direct current micro-plasma discharges in atmospheric pressure hydrogen",* Plasma Sources Science and Technology, Vol. 16 (3), 619-634, Aug. 2007. [Impact Factor 2.35]

7. Staack D, Farouk B, Gutsol A, Fridman A, *"Spectroscopic studies and rotational and vibrational temperature measurements of atmospheric pressure normal glow plasma discharges in air,"* Plasma Source Science and Technology, Vol. 15 (4), 818-827, Nov. 2006. [Impact Factor 2.35, Times Cited 4]

8. Farouk T, Farouk B, Staack D, Gutsol A, Fridman A, *"Simulation of dc atmospheric pressure argon micro glow-discharge,"* Plasma Source Science and Technology, Vol. 15 (4), 676-688, Nov. 2006 [Impact Factor 2.35, Times Cited 2]

9. Raitses Y, Staack D, Dunaevsky A, Fisch N J, *"Operation of a segmented Hall thruster with low-sputtering carbon-velvet electrodes,"* Journal of Applied Physics, Vol. 99 (3), Art. No. 036103, Feb. 1, 2006. [Impact Factor 2.32, Times Cited 1]

10. Raitses Y, Smirnov A, Staack D, Fisch N J, *"Measurements of secondary electron emission effects in the Hall thruster discharge,"* Physics of Plasmas Vol. 13 (1), Art. No. 014502, Jan, 2006. [Impact Factor 2.26, Times Cited 3]

11. Staack D, Farouk B, Gutsol A, Fridman A, *"Characterization of a dc atmospheric pressure normal glow discharge,"* Plasma Source Science & Technology, Vol. 14 (4), 700-711, Nov, 2005.[Impact Factor 2.35, Times Cited 16]

12. Raitses Y, Staack D, Smirnov A, Fisch N J, *"Space charge saturated sheath regime and electron temperature saturation in Hall thrusters,"* Physics of Plasmas, Vol. 12 (7), Art. No. 073507, July 2005. [Impact Factor 2.26, Times Cited 24]
13. Raitses Y, Staack D, Keidar M, Fisch N J, *"Electron-wall interaction in Hall thrusters,"* Physics of Plasmas, Vol. 12 (5), Art. No. 057104, May 2005. [Impact Factor 2.26, Times Cited 25]
14. Staack D, Raitses Y, Fisch NJ, *"Temperature gradient in Hall thrusters,"* Applied Physics Letters, Vol. 84 (16), 3028-3030, Apr 19, 2004. [Impact Factor 3.98, Times Cited 15]
15. Staack D, Raitses Y, Fisch NJ, *"Shielded electrostatic probe for non-perturbing plasma measurements in Hall thrusters,"* Review of Scientific Instruments 75 (2), 393-399, Feb 2004. [Impact Factor 1.54, Times Cited 10]
16. Raitses Y, Keidar M, Staack D, Fisch N J, *"Effects of segmented electrode in Hall current plasma thrusters,"* Journal of Applied Physics Vol. 92 (9), 4906-4911, Nov 1, 2002. [Impact Factor 2.32, Times Cited 28]

IN PROGRESS JOURNAL PUBLICATIONS
1. Staack D, Farouk B, Gutsol A, Fridman A, "R*egimes of thin film and particle deposition for atmospheric pressure microplasmas*" in preparation for Plasma Processes and Polymers.
2. Staack D, Farouk B, Gutsol A, Fridman A, *"Stabilization of the ionization overheating instability in atmospheric pressure microplasmas"* in preparation for Journal of Physics D Applied Physics.
3. Ayan H, Fridman G, Staack D, Gutsol A, Vasilets V, Fridman A, Friedman G, *"Heating effect of dielectric barrier discharge for direct medical treatment"* submitted IEEE transactions on plasma science, July 2007.

SELECTED CONFERENCE PUBLICATIONS
1. Staack D, Fridman G, Farouk B, Friedman G, Gutsol A, Fridman A, "*Tubular floating electrode dielectric barrier discharge for applications in sterilization and tissue bonding*", 1st International Conference on Plasma Medicine, Corpus Christi TX, Oct 15-18, 2007.
2. Staack D, Farouk B, Gutsol A, Fridman A, *"Thin film deposition using atmospheric pressure microplasma",* 34th IEEE International Conference on Plasma Science, Albuquerque NM, June 17-22, 2007.
3. Staack D, Farouk B, Gutsol A, Fridman A, *"Atmospheric pressure RF microplasma characterization"*, 18th International Symposium on plasma chemistry, Kyoto Japan, August 26-31, 2007
4. Staack D, Farouk B, Gutsol A, Fridman A, *"Rotational and Vibrational Temperature Measurements of Atmospheric Pressure Normal Glow Plasma Discharges in Air, Nitrogen, Argon, and Helium,"* proceeding of the 3rd International Workshop on Microplasmas, Greifswald, Germany, May 9-11, 2006, p. 102.
5. Staack D, Farouk B, Gutsol A, Fridman A, *"Atmospheric Pressure Normal Glow DC Microplasma in Air,"* proceedings of the 17th International Symposium on Plasma Chemistry, Toronto, Canada, August 7-12, 2005.
6. Staack D, Raitses R, and Fisch N J, "*Control of Acceleration Region in Hall Thrusters,"* the 28th International Electric Propulsion Conference, Toulouse, France, March 17-21 2003, IEPC paper 2003-0273.
7. Staack D, Raitses Y, Fisch N J, *"Investigations of probe induced perturbations in a Hall thruster,"* 38th AIAA/ASME/SAE/ASEE Joint Propulsion Conference and Exhibit, Indianapolis, IN, July 7-10, 2002, AIAA Paper 2002-4109.
8. McDaniel J C, Glass C, Staack D, Miller C, *"Experimental and computational comparison of an under-expanded jet flowfield,"* AIAA Aerospace Sciences Meeting & Exhibit, 40th, Reno, NV, Jan. 14-17, 2002, AIAA Paper 2002-0305.
9. Raitses Y, Staack D, Smirnov A, Litvak A, Dorf A, Graves T, Fisch N J, *"Studies of non-conventional configuration closed electron drift thrusters,"* AIAA/ASME/SAE/ASEE Joint Propulsion Conference and Exhibit, 37th, Salt Lake City, UT, July 8-11, 2001, AIAA Paper 2001-3776.
10. Staack D, McDaniel J C, Glass C E, and Miller C, *"Experimental study of interacting rarefied and continuum flows,"* AIAA Thermophysics Conference, 35th, Anaheim, CA, June 11-14, 2001, AIAA Paper 2001-2762.
11. Staack D and Delvecchio T, *"The Design Building and Calibration of a Hypersonic Wind Tunnel,"* AIAA, Aerospace Sciences Meeting and Exhibit, 38th, Reno, NV, Jan. 10-13, 2000, AIAA Paper 2000-0004. [Winner AIAA Regional Student Conference First-Place Paper Winner]
12. Pierce J, Audia S, Burnette T, Christiansen K, Cosgrove D, Conway M, Hinckley K, Monkaitis K, Patten J, Shochet J, Staack D, Stearns B, Sturgill C, Williams G, Pausch R, *"Alice: Easy to Use Interactive 3D Graphics,"* ACM Symposium on User Interface Software and Technology 1997, .p 77-78.